ANALYSING THE STATUS AND FUTURE CHANGES OF THE CRYOSPHERE AND ITS RELATION WITH CLIMATE CHANGE FOR THE HIMALAYAN REGION

Ph.D. THESIS

by

JAYDEO KUMAR DHARPURE

CENTRE OF EXCELLENCE IN DISASTER MITIGATION AND MANAGEMENT

INDIAN INSTITUTE OF TECHNOLOGY ROORKEE

ROORKEE - 247 667 (INDIA)

MAY, 2022

ANALYSING THE STATUS AND FUTURE CHANGES OF THE CRYOSPHERE AND ITS RELATION WITH CLIMATE CHANGE FOR THE HIMALAYAN REGION

A THESIS

Submitted in partial fulfilment of the
requirements for the award of the degree

of

DOCTOR OF PHILOSOPHY

in

DISASTER MITIGATION AND MANAGEMENT

by

JAYDEO KUMAR DHARPURE

CENTRE OF EXCELLENCE IN DISASTER MITIGATION AND MANAGEMENT

INDIAN INSTITUTE OF TECHNOLOGY ROORKEE

ROORKEE - 247 667 (INDIA)

MAY, 2022

INDIAN INSTITUTE OF TECHNOLOGY ROORKEE

STUDENT'S DECLARATION

I hereby certify that the work presented in the thesis entitled "**ANALYSING THE STATUS AND FUTURE CHANGES OF THE CRYOSPHERE AND ITS RELATION WITH CLIMATE CHANGE FOR THE HIMALAYAN REGION"** is my own work carried out during a period from July, 2018 to May, 2022 under the supervision of Dr. Ajanta Goswami, Associate Professor, Department of Earth Sciences and Joint-Faculty at Centre of Excellence in Disaster Mitigation and Management, Indian Institute of Technology Roorkee, Roorkee and Dr. Anil V. Kulkarni, Distinguished Scientist, Divecha Center for Climate Change, Indian Institute of Science, Bangalore.

The matter presented in this thesis has not been submitted for the award of any other degree of this or any other Institution.

Dated: May 02, 2022

Signature of the Student
(JAYDEO KUMAR DHARPURE)

SUPERVISOR'S DECLARATION

This is to certify that the work mentioned above is carried out under our supervision.

Signature of Supervisor
(ANIL V. KULKARNI)

Signature of Supervisor
(AJANTA GOSWAMI)

Dated: May 02, 2022

ABSTRACT

The Karakoram and Himalayan (KH) cryosphere (in terms of snow and glaciers) plays a significant role in managing the ecosystem and supporting livelihood and economic development. The KH region experiences large variations in snow cover and glaciers in a warming environment. The potential adverse effect of changing cryosphere causes a cascading implication on water availability and generates a condition of water stress in the future. Other than this, the change in water storage with increasing temperature can create drought-like conditions and affect people living in the region. Therefore, monitoring cryospheric changes and their interaction with climate are essential to understanding present climate sensitivity and future water availability. The melting of the cryosphere provides water for the region where the livelihood of millions of people depends upon meltwater of snow and glacier during the summer season. However, the continuous monitoring of snow cover at a large spatial extent is challenging due to harsh climatic conditions and rugged topography. For this, the use of remote sensing presented a great advantage in snow cover monitoring.

This thesis uses satellite observations for spatio-temporal snow cover monitoring at basinal and regional scales. The cloud blocks are the major limitation of optical remote sensing data that hinders the original snow cover information in the high-mountain terrains. To overcome this limitation, a spatially distributed cloud removal methodology is developed to ensure that all the necessary physical-based considerations and topographical variations are correctly incorporated in the method. This non-spectral sequential methodology includes a combination of multi-sensor data, temporal filter, nearest neighborhood filter, zonal snowline filter, and multiday-backward replacement filter. The cloud-gap-filled snow cover outcomes are validated with a direct and indirect approach to assess the accuracy of the methodology over the Chenab River basin. The results suggested that the spatially distributed cloud removal methodology can bridge the gap between regional observation-based snow cover and cloud blocks. After analyzing the methodology performance, the snow cover distribution is assessed at spatio-temporal scale along with topographical parameters. Further, we have established a relationship between snow cover and essential climatic drivers.

After developing a cloud removal methodology, the snow cover distribution and trends have been carried out over the KH region. The methodology-related uncertainties are quantified for understanding the exact error inherent in the cloud gap-filling approach. The cloud-gap-filled Snow Cover Area (SCA) is compared with Landsat-8, and the relationship with in situ observations (snowfall and temperature) is also examined. Then, the Snow Cover Day (SCD) and nine snow cover timing indices have been assessed to explore the snow cover characteristics.

The interconnection between SCA and meteorological variables is evaluated, suggesting a higher correlation with temperature as well as shortwave radiation. Other than this, a sensitivity analysis is performed, indicating a higher sensitivity with radiations towards SCA than other selected variables.

On the other hand, we have explored the variation of energy balance components and then measured the point-scale Surface Energy Balance (SEB) for the Phuche glacier, upper Ganglass catchment, Ladakh range. The meteorological variables are recorded at 5600 m a.s.l., altitude, which is mounted at the ridge of the glacier. And the point-scale SEB ablation is validated with the stake measured total melt. Despite this, we have also quantified the point-based and glacier-wide Mass Balance (MB) calculated using the stake measurement for Phuche and Khardung glaciers, Ladakh range during 2014–2017. The Equilibrium Line Altitude (ELA) and Accumulation Area Ratio (AAR) are calculated to assess the year-wise glacier changes for the hydrological year. The result suggests that the Khardung glacier experienced 3.7 times more mass loss relative to the Phuche glacier. In the glacier mass variation, the cold-arid region is considered because this region comes under climatic zone (western Himalayas) where mass variation is large and the majority of the glaciers (~79%) of this region have a smaller surface area (< 0.75 km^2), and only 4% of glaciers are > 2 km^2. Due to the smaller glacier area and scarce precipitation, we have selected these two glaciers to understand the glacier's direct response to climate fluctuation. It was noted that the small size glaciers are a good indicator of climate change.

Another objective of this thesis is to present the water storage change over the major river basin of India in order to assess the water availability and water stress in the future. We have used the twin satellite gravimetric data to analyze the total water storage change, groundwater recharge and also quantify the condition which causes drought. The total water storage change and groundwater recharge are measured over the Ganga River basin from 2003 to 2016. In this study, various groundwater recharge estimation methods are applied and validated with the in situ observational well. And the best-fitted recharge method with higher accuracy is used to establish the link between the recharge change and hydrometeorological variables. The relationship of ground recharge with other factors (total withdrawal, irrigation-based groundwater abstraction, population density (domestic factor), and overall water stress) are established to conclude the exact picture of groundwater reduction.

Further, a new drought index is developed to map the drought occurrence and severity that incorporate meteorological and hydrological conditions in drought identification. The generated index is applied over the Indus, Ganga, and Brahmaputra river basins. Results are compared with

the past drought occurrence and other well-established drought indices. The model output suggested that the index has the capability to map the agricultural, meteorological, and hydrological droughts to a broader area.

The last component of the study in this thesis presents a comprehensive approach for predicting the discharge over the Sutlej River basin using different Long Short-Term Memory (LSTM) deep learning models. The combination of best-suited variables (climatic and SCA) is selected based on their correlation and recursive feature elimination techniques. After finalizing the dataset, the hyperparameter tuning was done and set the best parameters to enhance the model performance. We have compared five different LSTM model architectures over the selected dataset. The bidirectional LSTM (BLSTM) outperformed other LSTM architectures during the training and testing stages. Further, we have also compared the normal BLSTM with Principle Component Analysis (PCA)-based BLSTM models over the study area. The PCA-based BLSTM performed well during the training stage, and this model was further used for forecasting the discharge over the other selected gauging sites.

To derive the snow cover and glaciers changes, we have used a methodology to connect the cryosphere changes with the spatial extent and climatic interaction. We have utilized remote sensing data; however, the in situ observation is used to calibrate and validate the obtained results. The cloud removal methodology development and their variation with terrain parameters are presented in objective-1. The snow cover distribution and their trend are discussed in objective 2.1. In comparison, the glacier energy balance and mass balance variation are quantified in objective 2.2. And water storage change, recharge modeling, and identification of drought occurrence in objective 2.3. Finally, the discharge prediction model is developed in objective 3. Overall, the outcomes and model development in this thesis is likely to be important for the research community to understand the snow cover and glacier variation in the present and their implication on discharge in the future. This thesis can also be a benchmark for modelers working in the high-mountain region and facing challenges in terms of cloud blocks. The present work also produces a solution for the drought modeling (hydrological and meteorological) which can be mapped using the remote sensing-based index. In a broader context, the results of this thesis can be used for predicting the snow cover changes and their interaction with climate change. It also helps to manage the water availability and even reduce the condition of water stress in the future by designing laws by the decision-maker for balancing the ecosystem.

Keywords: Basin; Drought; Climate change; Energy balance; Glacier; Himalayas; Mass balance; Recharge; Remote Sensing; Snow cover variability; Water resources.

ACKNOWLEDGEMENT

First and foremost, I offer my sincerest gratitude to my supervisors, Prof. Ajanta Goswami, Associate Professor, Centre of Excellence in Disaster Mitigation and Management, Indian Institute of Technology, Roorkee, and Dr. Anil V. Kulkarni, Distinguished Scientist, Divecha Center for Climate Change, Indian Institute of Science, Bengaluru, who have supported me throughout my research work with their invaluable advice, continuous support, and patience. Their immense knowledge and plentiful experience have encouraged me in all the time of my academic research and daily life. One simply could not wish for such encouraging and friendlier supervisors for my PhD study.

Besides my supervisors, I am very thankful to my thesis committee members: Prof. Ravi Kumar (Chairman SRC), Prof. J. D. Das (Internal Expert), and Dr. L. N. Thakural (External Expert), for their insightful comments and encouragement, but also for the questions, which incented me to widen my research from various perspectives.

My work would not have been possible without the financial support provided by National Centre for Polar and Ocean Research, Goa, to carry out the work. I also acknowledge the Ministry of Human Resource Development for the financial support to continue my PhD. My sincere thanks also goes to Dr. Sanjay Jain, Scientist G, and the late Dr. Renoj J. Thayyen, Scientist E, National Institute of Hydrology, Roorkee, for providing the field data. I would like to thank the US Geological Survey, Copernicus programme, and NASA earth observatory for providing satellite data free of cost.

I am also highly grateful to Prof. Sumit Sen, Head of the Centre, and Prof. Mahua Mukherjee, former Head of the Centre, for providing the necessary facilities to carry out the work in a pleasant academic environment and cooperation. I am also thankful to the technical and non-technical staff of the Centre for their assistance. Special thanks to Mr. Tahir, who provided time-to-time guidance for the official work.

During my stay at IITR, I got the company of many friends and my fellow labmates. I wish to extend my warmest thanks to Dr. Vijendra Singh Bramhe, Dr. Pir Mohammad, Dr. Rituraj Nath, Dr. Ashim Sattar, Mr. Nani Das, Mr. Shashi Gaurav Kumar, Mr. Rohit Kumar, Miss. Abhilasha Dixit, Miss. Kumai Sweta, Miss. Priyanka Negi, Mr. Sashikant Sahoo, Mr. Sourav Sundar Das, and Miss Saraah Imran for their valuable suggestion, helpful discussions, and for their company at various stages during the pleasant stay at IITR.

Most importantly, I express my respect and love for my parents, elder brothers, sisters, and in-laws for their great sacrifices to achieve my dreams and success.

Above all, I would like to thank my wife, Dr. Akansha Patel, for her unconditional love and constant support, for all the late nights and early mornings, to complete my PhD thesis with good publications.

Date: May 02, 2022 (**JAYDEO KUMAR DHARPURE**)

TABLE OF CONTENTS

LIST OF FIGURES

CHAPTER - 3

CHAPTER - 4

CHAPTER - 5

CHAPTER – 6

CHAPTER - 7

CHAPTER – 8

LIST OF TABLES

CHAPTER - 7

CHAPTER - 8

CHAPTER 1

INTRODUCTION

1.1. INTRODUCTION

The Hindu-Kush Himalayas (HKH) is the major source of water in South and South East Asia (Arfanuzzaman 2018). The water originate by snow, glacier and rainfall, which fed the major river system in Asia. About 1.9 billion population living in downstream as well as mountainous regions depend upon these rivers for irrigation, hydropower energy, drinking water etc. (Shrestha et al. 2015). The availability of water is under threat due to rapid increase of population, which placed a greater demand of water resources (Cosgrove and Loucks 2015). The climate change affect the snow cover, river flows as well as hydrological cycle in long term (Zhu and Ringler 2012). The change in hydrological cycle may affect the rainfall pattern, cause extreme precipitation events and drought conditions, which in turn affect the hydrological, agricultural and economic planning of the country (Jain and Singh 2020). Therefore, the spatio-temporal cryosphere monitoring and modelling is needed to understand the changing pattern and their related implication.

The changing pattern of snow cover and glaciers in the warming climate poses a serious concern for water resource management and the people living in the area, mainly fed by the snow and glacier meltwater in the summer season (Nie et al. 2021). This snow and glacier melting may contribute to immediate river discharge and also have the potential for groundwater recharge (Vuille et al. 2018). This is why snow cover and glacier mass changes are much more of a concern in the Karakoram and Himalayan (KH) region, at least from a water availability perspective. The KH region comprises the world's largest ice cover outside the polar regions, which lies in the low-latitude and high-altitude (Bolch et al. 2012a). Apart from this, the KH region is considered a natural "climate meter" to understand the sensitivity of climate change (Davaze et al. 2020). Therefore, any significant change in snow and glacier lies in this region would modify the water resources and affect the water needs of millions of population in Asia (Immerzeel et al. 2010).

According to the International Panel on Climate Change (IPCC) 5th Assessment Report (AR5), the glacier retreat and permafrost thaw decrease the stability of the high mountainous slopes and increase the number of glacier lakes as well as their area in recent decades. They have also concluded that the glacier and snow cover changes have contributed to the localized decline in

agricultural yield in the HKH and the tropical Andes region. Wood et al. (2020) have also revealed that the glacier and snowpack loss threaten the seasonal melt contribution to the water supply and domestic water resources. By combining knowledge obtained from published literature on glacier and snow cover and the sensitivity of the KH region, we have selected the KH region to analyze the spatiotemporal distribution of cryosphere and their contribution to total water availability change. For this, the different datasets and approaches are utilized by analyzing the various characteristics of the cryosphere in the recent period.

1.2. IMPORTANCE OF SNOW COVER AND ITS CHANGING PATTERN

Snow cover is a significant component for understanding the earth's climate system and hydrological modelling. The change in Snow Cover Area (SCA) tends to affect the runoff volume and early onset of the melt season (Singh and Bengtsson 2004; Singh et al. 2006). The variability of SCA is a great interest in the context of climate change (Barnett et al. 2005; Yeo et al. 2017). As a change in climate directly altered the snow cover pattern, Snow Cover Days (SCDs), snowmelt and further affected the drought characteristics. According to the IPCC, it was observed that the snow cover extent was decreasing due to a warmer temperature (Bates 2009). In addition, the temperature increase in the future decade was expected due to global warming, which may project the water scarcity condition. Thus, considering the present and future snow cover variability, the investigation of spatio-temporal change in SCA is crucial for proper water resource management and policy adaptation.

The changing pattern of snow cover in the KH region was analyzed by many authors using remote sensing data (Hall and Riggs 2007; Liang et al. 2008; Jain et al. 2008; Xu et al. 2017; Chen et al. 2020). Similarly, numerous authors have experienced a higher glacier melting in different glaciers come under the KH region (Dobhal et al. 2013; Sharma et al. 2016; Vijay and Braun 2016; Bolch et al. 2017; Lin et al. 2017; Tawde et al. 2017; Maurer et al. 2019; Muhammad et al. 2019a; Soheb et al. 2020; Mandal et al. 2020). In this regard, many authors were observed, the snow cover variation over the Indian Himalayan region (Atif et al. 2015; Kumar and Kumar 2016; Murtaza and Romshoo 2017; Singh et al. 2018b). However, few researchers have reported about the temperature, precipitation, snowmelt, and river discharge other than the SCA variability (Tahir et al. 2011, 2015; Mishra et al. 2014b). The reported studies show both increasing and decreasing trend of SCA in different parts of the Himalayas (Mishra et al. 2014a; Tahir et al. 2015; Kour et al. 2016a; Kumar and Kumar 2016) whereas stable or increasing trend in Karakoram region (Hewitt 2005; Tahir et al. 2011, 2016; Bolch et al. 2017). It was also observed that the rapid change in SCA over the high altitude region that directly influences the snow cover

dynamics. The heterogeneous change in SCA offers an opportunity to observe snow cover dynamics in the basinal scale (Figure 1.1). The SCA information on the basinal scale may provide a better understanding of climate change impact on cryosphere.

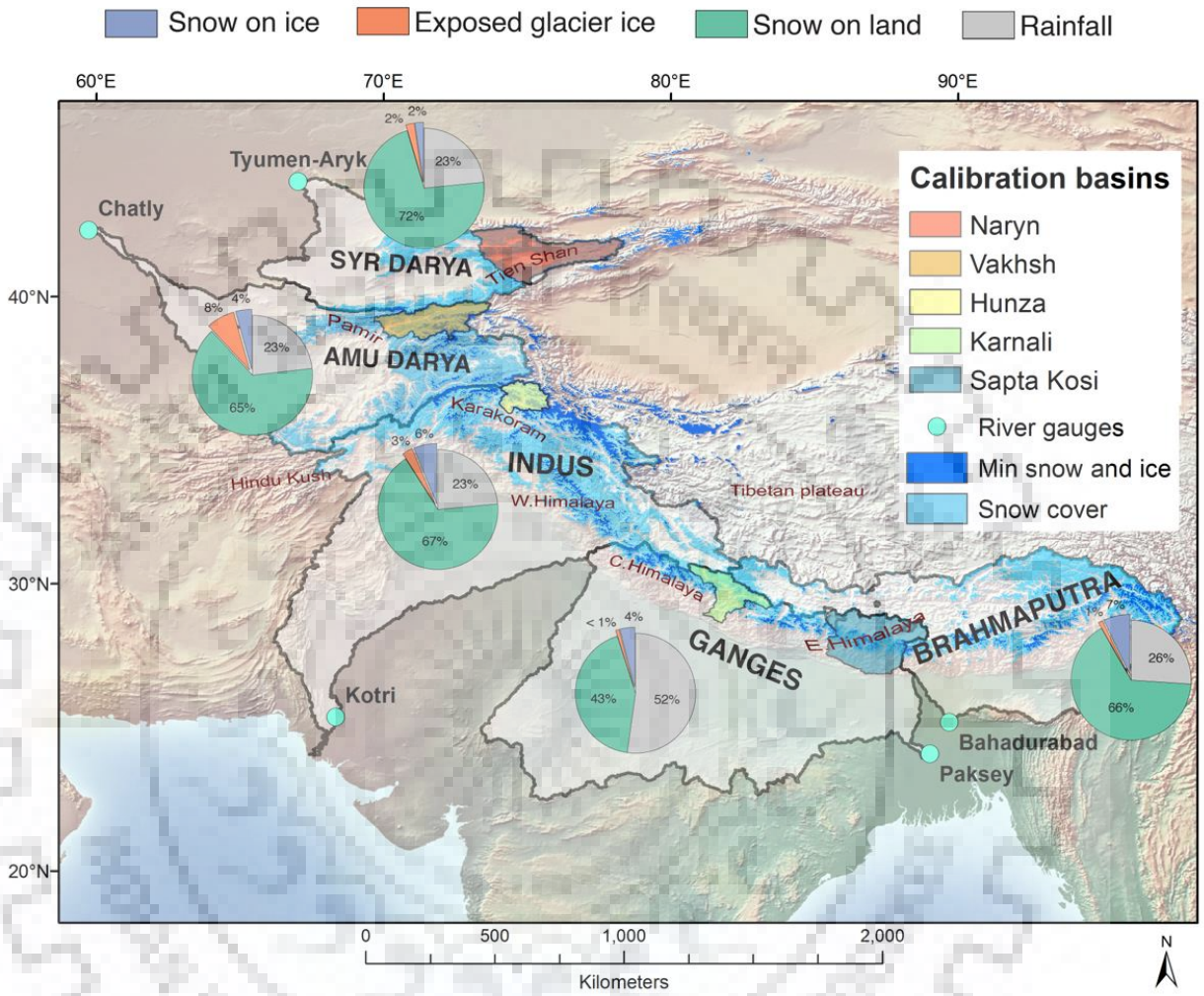

Figure 1.1. Map of five major river basins of High Mountain Asia. Pie charts indicate the mean annual contribution of snow, ice, and rainfall to runoff above 2000 m in the major river basins. This map is obtained from the National Snow and Ice Data Center (NSIDC) (Source: https://nsidc.org/nsidc-monthly-highlights/2018/07/remote-sensing-maps-birth-water-high-asia).

For mapping and monitoring of SCA variation, continuous snowfield observation was important. The in-situ observation failed due to complex topography over the HKH region. Therefore, the majority of stations were installed lower than 2200 m altitude (Anjum et al. 2019). The satellite-based remote sensing data is a good alternative source for spatio-temporal monitoring of SCA. A summary of snow cover variation observed using remote sensing data in the HKH region and its sub-region/basin is illustrated in Table 1.1.

Table 1.1 Review on snow cover changes using remote sensing data over the Himalayan region.

S.No	Location	Data used	Duration	Reference
1	Hindu-Kush Himalayas	MODIS	2002-2010	(Gurung et al. 2011b)
2	Tibet (Qinghai-Xizang)	SMMR	1951-1997	(Qin et al. 2006)
3	Tibet Plate	MODIS	2000-2006	(Pu and Xu 2009)
4	China	SMMR	1978-1987	(Xiao et al. 2007)
5	Tibetan Plateau	MODIS	2000-2009	(Zhang et al. 2010)
6	Tibetan Plateau	SMMR; MODIS	1997-2011	(Shen et al. 2015)
7	Giligit, Hunza, Astore	MODIS	2000-2012	(Tahir et al. 2016)
8	Swat basin	MODIS	2002-2004	(Dahri et al. 2011)
9	Brahmaputra, Indus, Ganga, Amudarya,Syr Darya, Mekong	AVHRR, MODIS	1961-1990; 2001-2010	(Savoskul and Smakhtin 2013)
10	Astore, Gilgit, Hunza, Jhelum, Kabul, Swat, Shigar, Shyok	MODIS	2001-2012	(Hasson et al. 2014b)
11	Indus, Ganga, Brahmaputra	MODIS	2000-2011	(Singh et al. 2014)
12	Brahmaputra, Ganga, Indus, Yangtze, Yellow	MODIS	2000-2008	(Immerzeel et al. 2010)
13	Brahmaputra	MODIS	2000-2010	(Mukhopadhyay 2012)
14	Gangotri glacier	IRS-LISS	Mar-Nov 2000	(Gupta et al. 2005)
15	Sutlej	MODIS; IRS, WiFS, AVHRR	2000-2004	(Jain et al. 2008)
16	Ganga, Sutlej, Chenab, Indus	AWiFS	2004-2007	(Kulkarni et al. 2010)
17	Beas basin	AWiFS	2004-2005	(Negi et al. 2009)

18	Siachen, Gangotri glacier	ERS-1/2 ENVISAT	1996-2004; 1996-2007	(Kumar and Venkataraman 2011)
19	Alaknanda, Bhagirathi, Yamuna sub-basin	AWiFS	2004-2012	(Rathore et al. 2015)
20	Jhelum	MODIS	2005-2009	(Sharma et al. 2013)
21	Sutlej basin	MODIS	2000-2009	(Mir et al. 2015)
22	Bhaga Basin	MODIS	2001-2012	(Snehmani et al. 2016)
23	Kashmir	MODIS	2000-2016	(Shafiq et al. 2018)

1.3. INFLUENCE OF WATER AVAILABILITY CHANGE

The water cycle describes the circulation of water from Earth's surface to the atmosphere and back again (Figure 1.2). This system, governed by energy from the sun, is a continuous exchange of moisture between the oceans, the atmosphere, and the land. Therefore, studying each hydrological component and influence of energy fluxes is needed to understand the changing pattern over the region due to the warming climate. In this thesis, we have analyzed these variables over the KH region.

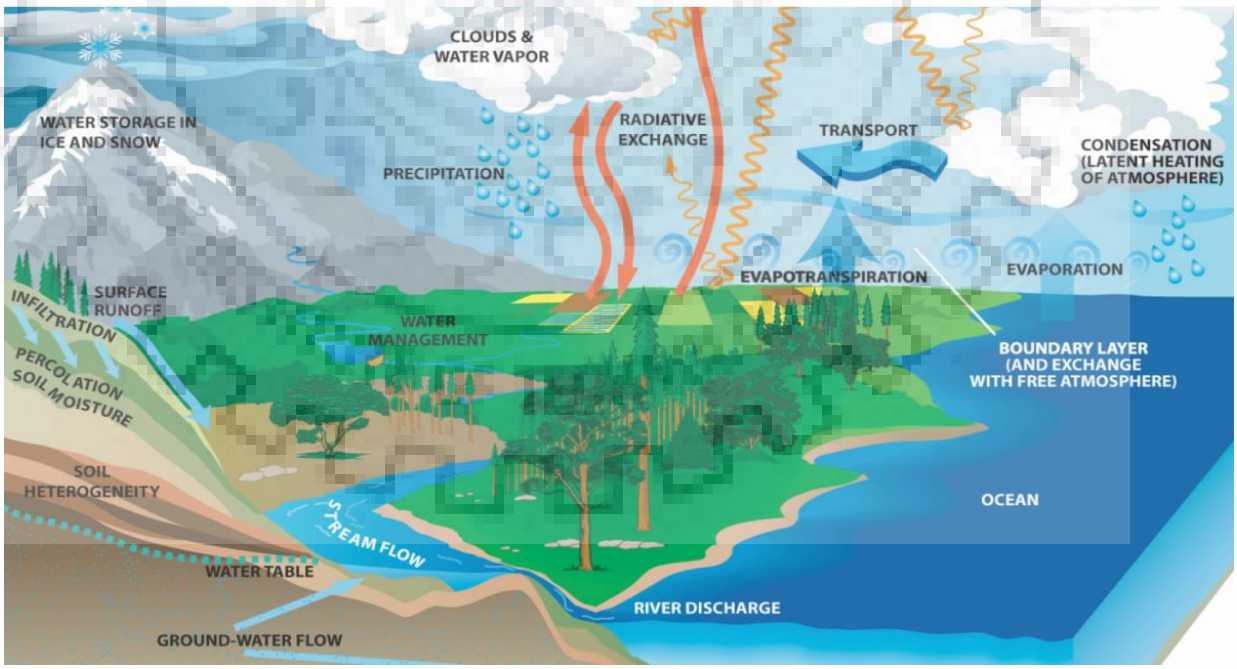

Figure 1.2. Water cycle illustrating the ocean, land, mountains, and rivers returning to the ocean. Processes labeled comprise precipitation, condensation, evaporation, evapotranspiration, radiative exchange, surface runoff, groundwater and streamflow, infiltration, percolation, and soil moisture. This diagram is obtained from NASA Earth

Science: Water Cycle (Source: https://science.nasa.gov/earth-science/oceanography/ocean-earth-system/ocean-water-cycle/).

About one third of the world's population depends upon the largest freshwater reservoirs (Glaciers + Ice caps) on the Earth during the summer season (Brown et al. 2010). Changing patter of snow and glacier can exert a substantial influence on climate by interacting with the atmosphere through a range of feedback mechanisms (Hock 2005). Glacier melt contributes to the discharge of major rivers system (Bajracharya and Shrestha 2011) and feeds endorheic lakes on the HKH region (Bajracharya and Shrestha 2011). The changing pattern of glaciers might also increase the risk of water availability in future and also be responsible for new glacier lake generation and then may alter into Glacial Lake Outburst Flood (GLOF) in future (Ashraf et al. 2012). As a result, the changes in glacier mass are the direct or indirect, influences the water availability of the region and may cause water stress in near future. Other than this, the water availability change can also be quantified by continuous monitoring of ground water recharge and even from total water storage changes. Several authors measured the total water storage change and groundwater recharge on different basins or sub-basins of Indian major rivers (Sakthivadivel 2007; Shah 2008; Mukherjee et al. 2015; CGWB 2017; Prasad and Rao 2018; Senthilkumar et al. 2019; Bhanja et al. 2019). On the other hand, the change in total water storage not only impacted the water availability but also caused the drought-like condition. To model the drought occurrence and measure their severity, specialized drought indices have been developed recently, such as Standardized Precipitation Evapotranspiration Index (SPEI) (Vicente-Serrano et al. 2009), Vegetation Drought Response Index (VegDRI) (Brown et al. 2008), Total Storage Deficit Index (TSDI) (Yirdaw et al. 2008), Standardised Precipitation Index (SDI) (Nalbantis and Tsakiris 2009), Multivariate Standardized Drought Index (MSDI) (Hao and AghaKouchak 2013), Standardised Groundwater level Index (SGI) (Bloomfield and Marchant 2013), etc.

1.4. STREAMFLOW PREDICTION AND THEIR IMPORTANCE

River discharge is the end product of all the hydrological regimes of a river basin and also one of the significant steps for managing water resources. The measured river discharge can be a proxy method for estimating the snow and glacier melting, which also helpful for providing the necessary information relate with the global temperature rise. Therefore, the monitoring and prediction of river discharge at basinal scale is needed to forecast. However, the field based river discharge monitoring and prediction at continuous time scale may be hampered by the terrain properties of Himalayan region as well as the harsh climatic condition. Apart from this, different hydrometeorological variables are used to estimate the amount of river discharge. Therefore, the

machine learning based river discharge prediction at high temporal scale encode the domain knowledge and predict according. Several methods and techniques have been employed for the prediction of various applications based on the dependent and independent variables (Callegari et al. 2015; Kan et al. 2017; Kratzert et al. 2018, 2019; Le et al. 2019; Fan et al. 2020; Lin et al. 2020; Thapa et al. 2020b). However, the advantage of the Long Short-Term Memory (LSTM) deep neural networks on spatial and temporal prediction was previously noted by many authors (Gauch et al. 2020; Hussain et al. 2020; Liu et al. 2020; Zhang et al. 2020; Ajayi et al. 2021; Yao 2021).

1.5. RESEARCH QUESTIONS

- **What is the distribution of snow cover in the KH region?** Can the remote sensing data capture the changing snow cover pattern at a large spatial and temporal scale? Do the snow cover of the KH region declining or progressively increasing? How does the snow cover vary from 2000 onwards?
- **How do the Himalayan glaciers behave in response to concerning climatic variability?** Is the Himalayan glacier retreating or advancing? What are contributing variables responsible for the glacier mass loss? Are any significant changes in small size glaciers observed in the past period? Is any significant change in small glaciers causes imbalance for local communities?
- **What are the implication of snow and glacier changes on runoff on a seasonal time scale?** What are the possible changes observed in the total water storage change and also in groundwater recharge? Is the natural and human-made groundwater storage change to further contribute to drought occurrence? May the remote sensing-based drought indices be able to capture both hydrological and meteorological droughts?
- **What is the possible model for river discharge prediction?** Is any model available that can have the capability for long-term or short-term forecasting? Which model architecture is suited for the selected region in order to predict discharge? Do the developed model is able to perform well for the study location?

1.6. RESEARCH AIM AND OBJECTIVES

This thesis aimed to quantify the snow cover variation, glacier mass changes, and their linkage with meteorological and hydrological variables as well as explain their implication on water availability. It also includes the development of a cloud removal methodology that improves the

estimation by filling the cloud gap with temporal and topographical information. The thesis also comprises a new drought index that can monitor hydrological and meteorological induced droughts. This thesis also contains a prediction model development for river discharge using machine learning and deep learning approaches at high temporal resolution. To pursue this overarching aim, we have addressed the following research objectives:

1. Development of an effective methodology for monitoring the Spatio-temporal pattern of snow characteristics

2. Analyzing the changing pattern of snow cover as well as glaciers and its implication on water availability in a warming climate

    2.1. Assessment of snow cover dynamics and its sensitivity with hydrometeorological factors

    2.2. Quantify the glacier energy and mass balance using the meteorological and glaciological methods

        2.2.1. Modeling of glacier energy and mass budget of the Phuche glacier, Cold-arid Himalayan region, Ladakh range, India

        2.2.2. Estimation of glaciological based mass balance and its interrelationship with climate drivers over the Phuche and Khardung glaciers, Cold-arid Himalayan region, Ladakh range, India

    2.3. Monitoring of water availability change and their impact on extreme event occurrence

        2.3.1. Quantify the combined effect of hydrometeorological and anthropogenic factors on groundwater recharge as well as their variability over the Ganga River basin

        2.3.2. Drought characterization using the Combine Terrestrial Evapotranspiration Index over the Indus, Ganga, and Brahmaputra River basin

3. Predicting the river discharge using the machine and deep learning approaches in order to assess the downstream impacts of hydrological changes on ecosystems

1.7. THESIS STRUCTURE

The whole thesis is organized into nine chapters. A brief description of each chapter is summarized below:

Chapter 1: This chapter includes the general introduction of research and its importance on a global scale. It also presents the varying pattern of snow cover and glaciers with supporting literature. The implication of cryosphere changes and their related problems are highlighted. It also includes the importance of machine learning for river discharge prediction at the basinal scale. This chapter concludes the gap in the literature, research questions, and related objectives.

Chapter 2: This chapter comprises a development of a non-spectral sequential composite methodology for cloud gap filling for daily time series data over the Chenab River basin. The effectiveness of the methodology is calibrated and validated with direct and indirect methods and associates uncertainty. The variation of snow cover with topographical parameters is discussed. This chapter also includes the spatio-temporal distribution of climatic variables and association with snow cover change.

Chapter 3: In this chapter, the snow cover variability and its trend are quantified at monthly, seasonal, and annual scales over a large spatial extent of the KH region. The snow cover days and other snow cover timing indices are quantified. The influence of forcing climatic and radiative fluxes on snow cover variation is established, and their sensitivity in each region is also discussed.

Chapter 4: This chapter analyses the surface energy balance components and mass change at point scale over the Phuche glacier, Ladakh range. The energy balance components are collected from Automatic Weather Station (AWS) data located at 5600 m a.s.l. The outcomes of the surface melting are validated with stake measurements and compared with the help of other studies.

Chapter 5: This chapter describes the Mass Balance (MB) measurement using a glaciological-based method over the Phuche and Khardung glaciers, Ladakh range. The elevation-based MB distribution, shift in Equilibrium Line Altitude (ELA), Accumulation Area Ratio (AAR) at annual time scales are estimated. This chapter compares two glaciers MB lying in the same climatic zone and includes the possible reasons for their contrasting MB.

Chapter 6: This chapter illustrates the quantification of groundwater recharge using different methods over the Ganga river basin. The performance of the methods is analyzed with the observation wells data. It also comprises the impact of climatic variability, and anthropogenic activities for the possible changes in groundwater recharge.

Chapter 7: This chapter describes the development of a new drought index for examining the drought occurrence and their severity of the Indus, Ganga, and Brahmaputra River basins. This

new index is compared with preexisting drought indices as well as in situ data over the region. The relationship between the new drought index and hydrometeorological variables (precipitation, potential evapotranspiration, and land surface temperature) is analyzed.

Chapter 8: This chapter includes the development of a discharge prediction model using the machine and deep learning techniques over the Sutlej River basin. Five different LSTM architectures are implemented, and the best-suited model is considered for time series prediction. Also, the best-suited LSTM model is compared with the Principle Component Analysis (PCA)-based LSTM model. The aim is to ensure the model's reliability and performance for the study area.

Chapter 9: This chapter summarises the new research contribution from this thesis for the cryospheric studies and their related implication. The conclusion of chapters 2 to 8 is described with the necessary limitation of the research. It also includes the direction of future research based on the outcomes of the thesis.

CHAPTER 2

DEVELOPMENT OF AN EFFECTIVE METHODOLOGY FOR MONITORING THE SPATIO-TEMPORAL PATTERN OF SNOW CHARACTERISTICS

2.1. INTRODUCTION

The mountain ranges of the Himalayan region are a great climatic barrier between India and its neighbors (Burbank et al. 2012; Singh et al. 2014), which is mainly known for its frozen freshwater in the form of glaciers and seasonal snow cover (Gao et al. 2019). This region receives a constant supply of fresh water for downstream livelihood from seasonal snowmelt in spring and autumn (Barnett et al. 2005), while peak glacier melts occur during the summer months and peak rainfall runoff occurs in the monsoon season (Immerzeel et al. 2009; Zhang et al. 2019a). Several studies have suggested a changing areal extent of seasonal snow cover, which further influences the melt-runoff (Bookhagen and Burbank 2010; Mukhopadhyay 2012; Thapa et al. 2020a).

Many authors have highlighted the snow cover variability over the Himalayan region (Hasson et al. 2014a; Rathore et al. 2018a; Singh et al. 2018a). However, some researchers have also reported about the change in temperature, precipitation, snowmelt, and river discharge apart from the Snow Cover Area (SCA) variability (Tahir et al. 2015; Snehmani et al. 2016; Azmat et al. 2017; Butt et al. 2019). They reported both increasing and decreasing trends of SCA in different parts of the Himalayas, whereas a stable or increasing trend has been noted in the Karakoram region (Hewitt 2005; Tahir et al. 2016; Lin et al. 2017). It was also observed that the rapid change in SCA over the high-altitude region may be affecting glaciers along with the hydrological behavior of the basin (Singh et al. 2019). Therefore, the continuous monitoring of snow cover distribution at the regional and global scale is not only essential for managing water resources but is also significant for understanding the influence of climatic variability and environmental conservation.

In the Himalayan region, a limited number of in situ observations are present for continuous snowfield measurement due to the complex topography. Therefore, satellite-based snow cover retrieval approaches offer a viable option to overcome this limitation. Several researchers have monitored SCA changes from Thematic Mapper (TM), Landsat Multispectral Scanner System (MSS), and Satellite Pour l'Observation de la Terre (SPOT) data (Dorothy K. Hall et al., 1995; Kumar and Kumar, 2016). However, many studies revealed limitations of these sensors,

including small swath, band resolution, and error in the spatio-temporal estimation of SCA (Dankers and De Jong 2004; Kulkarni et al. 2006). Contrary to this, several authors have used MODIS (Moderate Resolution Imaging Spectroradiometer) Snow Cover Products (SCPs) for daily to monthly SCA monitoring, which shows higher accuracy in certain parts of the world (Hall and Riggs 2007; Liang et al. 2008; Jain et al. 2008; Xu et al. 2017). However, the high cloud contamination in the MODIS SCP is a significant problem in many applications. Hence, there is a need to improve MODIS SCPs using cloud gap-filling approaches before use in SCA characterization. Several authors have developed numerous methodologies for the removal of cloud pixels from the data based on spatial, temporal, and topographical information (Wang et al. 2008; Gafurov and Bárdossy 2009; Parajka et al. 2010; Marchane et al. 2015; Li et al. 2019a; Chen et al. 2020).

2.2. RESEARCH QUESTIONS

- **What are the essential requirements in cloud removal methodology development**- How are the cloud blocks removed in each sequential step? Is the information filled at cloud pixel-accurate?
- **What are the snow cover characteristics over the study region**- What are the snow pattern in time series analysis? Can any shift in snow cover accumulation or melting be observed in the study area?
- **What role does the topography play in snow cover variation of a region -** How important is the topographic information supporting the snow cover distribution across the basins? Does the change in topographic parameters play a significant role in varying snow cover patterns?
- **What are the controlling factors that impact the snow cover pattern of a region**- Are the climatic variables really influential on the selected region, or are radiative fluxes more prevailing?

2.3. OBJECTIVES

- Development and implementation of cloud removal methodology to generate daily snow cover using the remote sensing data
- Analyzing the spatio-temporal distribution of SCA and its trends using different snow cover time-series indices

- Investigation of long-term snow cover characteristics and their changing pattern irrespective of different topographic parameters (elevation, aspect, and slope).
- Establishing the linkage between SCA and essential climatic variables and assessing their contribution to snow cover change

2.4. STUDY SITE

Chenab River is a fourth-order basin of the great Indus River system, located in the foothills and very high rugged mountains of the western Himalayas. The major part of the basin lies in the Indian Territory, whereas its lower part and outfall (into the Indus basin) are situated in Pakistan. In India, this river passes through two states, i.e., Himachal Pradesh and Jammu & Kashmir, covering an area of about 7,873 km^2 and 22,323 km^2, respectively. The upper part of the basin lies between Zanskar and the Pir Panjal ranges, whereas the lower part in Dhauladhar and the outer ranges of the Himalaya (Singh et al. 1997). However, the Chenab basin contributed approximately 50% of the total water supply by snow and glacier melt (Muhammad et al. 2019b).

The Chenab River formed on the confluence of two streams, namely Chandra and Bhaga at Tandi, located in the Lahaul-Spiti district of Himachal Pradesh, India (Figure 2.1). These streams arise from snowfields on the opposite sides of the Baralacha Pass at an elevation of ~4900 m a.s.l. (Singh et al. 1997). It is elongated in shape and covers an area of 30,370 km^2. The total length of the river is about 974 km (Luqman et al. 2018), and it feeds several irrigation canals. The elevation of the basin varies widely from about 242 to 7066 m a.s.l., with an average of 2900 m a.s.l. However, the river gradient is very steep at its source and gradually decreases downstream. Additionally, the land use pattern of the basin involves forest and agriculture at an elevation of about 2500 m a.s.l., whereas higher elevation exists subalpine and alpine conditions (Rao et al. 1997). The basin covers 2645 km^2 glaciers area, which mainly starts from ~4000 m a.s.l. altitude (RGI Consortium 2017). Furthermore, the Chenab basin lies in the boundary between two large-scale circulation patterns, i.e., the western disturbances and the Indian summer monsoon system (Shekhar et al. 2010). Additionally, this basin is not only controlled by precipitation but the change in temperature also. The climate of this basin varies from hot and moist tropical in the lower valley to cold temperature at about 2000 m a.s.l. (Rao et al. 1997). Therefore, we have selected this basin to understand the variability of meteorological variables and the conflicting signal of climate change.

2.5. DATASETS

2.5.1. MODIS SNOW COVER PRODUCTS

In the present study, the MODIS daily SCPs version 6 (V6) of Terra (MOD10A1) and Aqua (MYD10A1) were utilized over the study area from 1 January 2001 to 31 December 2017. We have selected the latest version of MODIS SCPs rather than the old existing one (Version 5) because Zhang et al. (2019) found that V6 has higher accuracy than that of V5. The datasets were obtained from the National Aeronautics and Space Administration (NASA) Earth data gateway customize service (https://search.earthdata.nasa.gov) with sinusoidal projection at 500m grid resolution. The Chenab basin comes under the MODIS tile number h24v05, i.e., horizontal 24 and vertical 5. For the observation period, a total of 6144 images for Terra and 5645 for Aqua were utilized, while 65 and 15 images for Terra and Aqua were missing, respectively. Detailed information of MODIS SCPs retrieved snow mapping algorithm is available at Riggs et al. (2016).

These data sets contain seven parameters (Normalized Difference Snow Index [NDSI] snow cover, raw NDSI, basic QA, algorithm flags QA, snow albedo, orbit pointer, and granule pointer) in Hierarchical Data Format (HDF). The NDSI snow cover parameter of both sensors was used for snow cover mapping and monitoring. For this, we have used the global value of the NDSI threshold 0.4, which is still recommended (Riggs et al. 2016, 2017). The mean yearly percentage of the total geographical area, estimated for three new classes (i.e., cloud, snow, and no-snow) obtained from 9-standard MODIS classes (NDSI snow cover, Missing data, No decision, Night, Inland water, Ocean, Cloud, Detector saturated and Fill). Overall, the mean cloud cover percentage of the total basin area in Aqua (54.9%) is accounted 20.9% higher than the Terra (45.4%) during the study period (Figure 2.2).

2.5.2. LANDSAT-8 OLI SATELLITE IMAGES

Due to scarcity of ground observation, numerous authors have used different high-resolution satellite data for validating the cloud gap-filled MODIS SCPs over various regions of the Himalayas (Hasson et al. 2014a; Stillinger et al. 2019). Therefore, we have considered the Landsat-8 Operational Land Imager (OLI) images to validate the MODIS SCPs over the study period (2013–2017). A total of 47 cloud-free images were acquired (Path-147 and Row-38) from the United States Geological Survey (USGS) EarthExplorer, which is available at 30m grid resolution and 16-day temporal scale (Table 2.1).

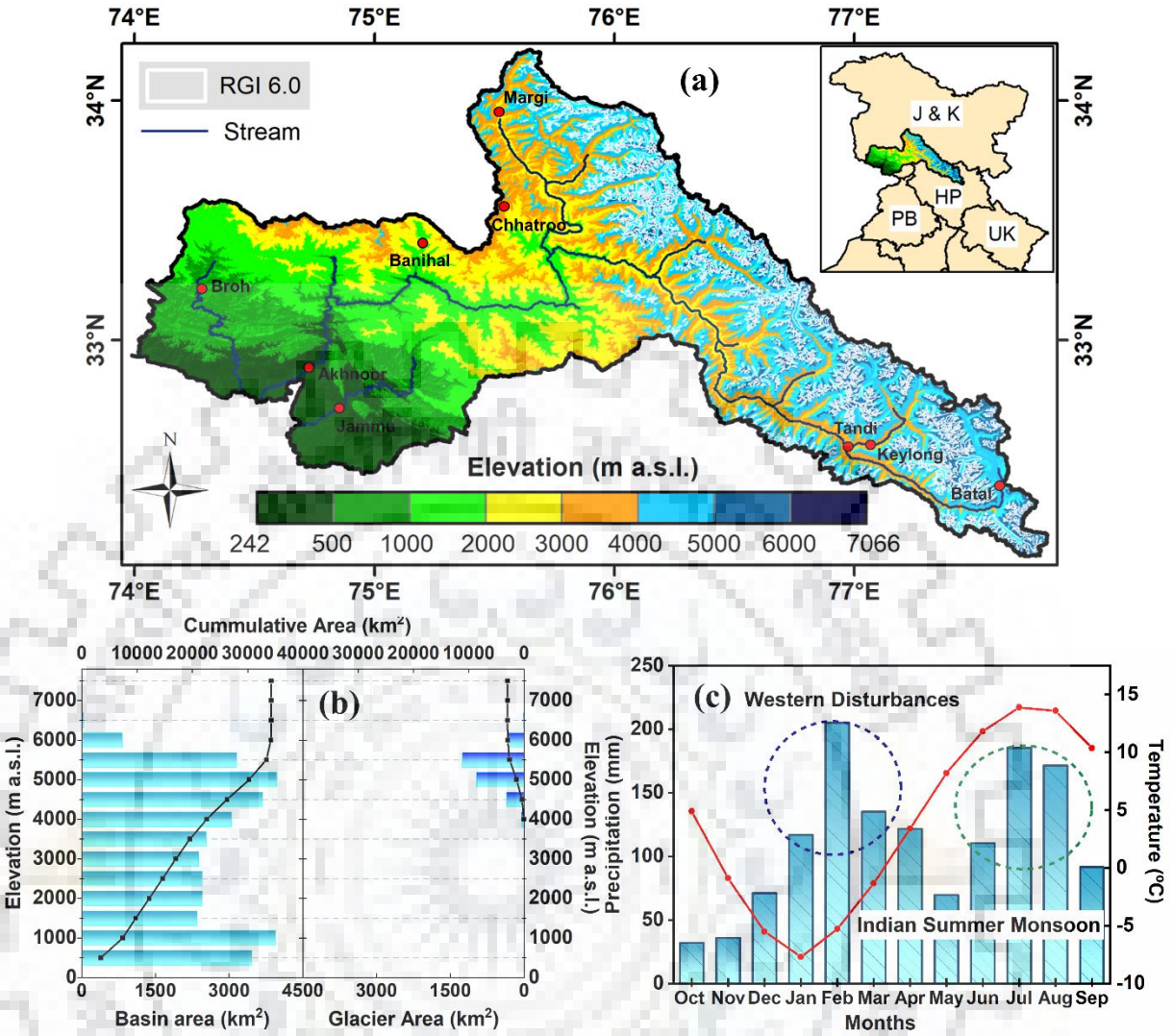

Figure 2.1. (a) Chenab River basin and its location in India that represents the altitude variation, drainage pattern, and glaciers boundary, (b) hypsometry curve of the basin and glaciers area, and (c) mean monthly total precipitation and air temperature of ERA-5 reanalysis data extracted over the study area.

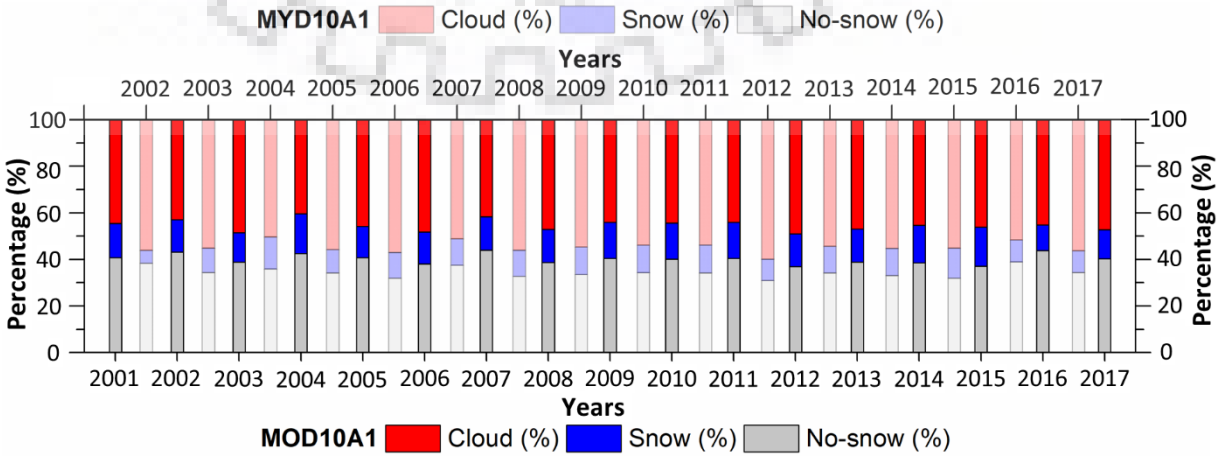

Figure 2.2. Mean yearly percentage of the total geographical area is calculated for cloud,

snow, and no-snow classes during 2001–2017 for MOD10A1 (lower group) and 2002–2017 for MYD10A1 images (upper group).

Table 2.1. Details of the used Landsat-8 OLI data for validating the daily cloud-free MODIS SCA from October 2013 to September 2017.

Year	Date of image acquisition (DD/MM/YYYY)
2013	18/04/2013; 20/05/2013; 05/06/2013; 25/09/2013; 27/10/2013; 28/11/2013
2014	15/01/2014; 16/02/2014; 20/03/2014; 21/04/2014; 07/05/2014; 08/06/2014; 10/07/2014; 11/08/2014; 28/09/2014; 30/10/2014; 15/11/2014; 01/12/2014
2015	18/01/2015; 23/03/2015; 24/04/2015; 27/06/2015; 30/08/2015; 15/09/2015; 01/10/2015; 17/10/2015; 02/11/2015; 04/12/2015
2016	05/01/2016; 22/02/2016; 26/04/2016; 12/05/2016; 13/06/2016; 03/10/2016; 19/10/2016; 06/12/2016
2017	23/01/2017; 24/02/2017; 12/03/2017; 13/04/2017; 15/05/2017; 04/09/2017; 20/09/2017; 06/10/2017; 22/10/2017; 07/11/2017; 09/12/2017

2.5.3. ERA5-LAND REANALYSIS DATA

ERA5 is a fifth-generation European Centre for Medium-Range Weather Forecasts (ECMWF) re-analysis (ERA5)-Land is a global reanalysis dataset covering a period from 1981 to the present at 0.1º × 0.1º grid resolution (~9 km) with a monthly temporal scale. ERA5-Land provides a consistent view of the water and energy cycles at a surface level during several decades (C3S 2019). The performance of ERA-5 datasets was evaluated against the observed gridded datasets from the India Meteorological Department by Mahto and Mishra (2019). They have reported that the ERA-5 performed better than other reanalysis products, and it can be used for hydrological modeling in India. In this study, the total precipitation (P_t), air temperature (T_a), wind speed (u), and net shortwave radiation (SWN) were acquired to identify the influence of these variables on the spatial and temporal SCA over the Chenab basin during the two separate periods, i.e., 1981-2017 and 2001-2017.

2.5.4. DIGITAL ELEVATION MODEL (DEM)

In this study, the void-filled Shuttle Radar Topography Mission (SRTM) Digital Elevation Model (DEM) version 3.0 (~90 m spatial resolution) (Jarvis et al. 2008) was used to assess the topographical effect on SCA variation. The SRTM DEM was interpolated to the MODIS SCPs spatial resolution of 500 m using the bilinear interpolation technique (suggested by Lopez-

Burgos et al., 2013). Vertical absolute and relative height error of the DEM is described to be less than ±16 m and ±6 m, respectively; the circular absolute and relative geolocation error are ±20 m and ±15 m, respectively, at a 90% confidence level (Rabus et al. 2003; Farr et al. 2007).

2.6. METHODOLOGY

2.6.1. CLOUD REMOVAL METHODOLOGY

To overcome the cloud gaps in the daily MODIS SCPs, we have selected and applied rigorous non-spectral cloud removal techniques over the extracted study area (Figure 2.3). The implemented methodology is a combination of high accuracy (> 90%) cloud reduction methods that are introduced (Gafurov and Bárdossy 2009; Wang et al. 2014) and partially adopted by (Parajka et al. 2010; Paudel and Andersen 2011; Hasson et al. 2014a; Tran et al. 2019). These studies presented effective cloud removal techniques with the consideration of topographic and seasonal variability over the different regions. However, these studies include numerous cloud-gap filling steps in which each successive step reduced more cloud coverage, but it introduced a high probability of information loss (Gafurov and Bárdossy 2009; Hasson et al. 2014a). Therefore, we have produced a trade-off between cloud removal and information loss while considering the composite methodology of five different methods. The brief description, theoretical accuracy, and functionality as discussed below.

The first step merged the MODIS Terra and Aqua images of the same day in order to minimize the short-term persistent cloud cover. We have replaced the cloud pixels of the Terra image with the same-day cloud-free pixels of the Aqua image by considering the Terra snow product as a primary image. Because it has experienced relatively less cloud coverage and higher accuracy than the Aqua product (Hall et al. 2019). This step preferred more accurate and adequate snow cover than both observations (Terra and Aqua). This may occur due to a short time difference (~3 – 4 hours at the Equator) between these two sensors (Gafurov and Bárdossy 2009).

The second step comprises the replacement of present-day cloud pixels with a combination of 2-successive images (two forward and two backward). As for the temporal filling, three different temporal iterations were applied sequentially for snow and land pixels. In the first iteration, if both backward (t – 1) and forward (t + 1) images observed the same class (snow or no-snow) for the corresponding cloud pixel of the present image, then the cloudy pixel is replaced by that class. Besides, the second iteration applies a similar logic using images (t – 1) and (t + 2) followed by the third iteration using images (t – 2) and (t + 1). Here, we assumed that no snowmelt or snowfall occurred during the spans of different temporal iterations (Lopez-Burgos et al. 2013). Moreover,

the probability of rapid snowmelt is low because the present-day cloudy pixels limit the incoming shortwave radiation and diffuse the longwave radiation (Gafurov and Bárdossy 2009). However, these assumptions show significant disagreement in the transitions zones as well as the transitional period. These changes are mainly attributed to the varying sun solar angle (Järvinen and Leppäranta 2013; Kahl et al. 2019), wind blow (Mott et al. 2018), and avalanche events (Valero et al. 2018). These sub-daily variation effects are not considered for this step due to the unavailability of sub-daily scale observation.

In the third step, the particular cloud cover pixel was replaced by the information from the eight nearest neighbor pixels, elevation, and aspect of the surrounding pixel. This method is explained by Gafurov and Bárdossy (2009) and modified by Lopez-Burgos et al. (2013). For the spatial filtering, we have considered the two iteration processes sequentially for a 3×3 moving window in order to reduce the cloud cover. Also, numerous studies have suggested that this window size is optimal for cloud gap-filling (Gurung et al. 2011a; Brooks et al. 2018; Chen et al. 2020). The first iteration removes a cloudy pixel; if any of this direct laying eight neighboring pixels covered by snow and their elevation is lower than the cloudy pixel with the same orientation, the cloudy pixel is assigned as snow pixel. Also, if five out of eight neighboring pixels of the cloudy pixel shows snow/no-snow and a cloud pixel elevation is higher/lower from the minimum/maximum adjacent snow/no-snow elevation, then the cloudy pixel is reclassified as snow/no-snow pixel.

In the fourth step, the regional snowline mapping approach (Parajka et al. 2010) utilizes the aspect-wise elevation information to correctly identify the snow/no-snow pixels. For this, the cloudy pixels are assigned as snow or no-snow-based on their elevation, which is compared with the mean elevation of all the snow (μ_s^h) or no-snow (μ_{ns}^h) pixels in each aspect. The assumption of this filter is that at least 70% cloud-free pixel (Gafurov and Bárdossy 2009) are present in a particular aspect; otherwise, this step will be skipped. In this approach, if the elevation of the cloudy pixel is above the μ_s^h classified as snow and elevation is below the μ_{ns}^h assigned as no-snow. However, there will be no change in cloud pixels between the μ_s^h and μ_{ns}^h because the maximum uncertainty occurred in this transitional zone (Wang et al. 2009).

Although most of the cloud pixels were eliminated using the steps mentioned above, the remaining cloud pixels were removed using a multi-day backward replacement method (Wang et al. 2014). In this approach, the cloud pixels on a current-day image were replaced by the cloud-free pixels of the previous day and continued until all the cloud pixels were removed. However, if the cloudy pixels are replaced by cloud-free pixels of more extended previous day images (cloud persistent continue), then the uncertainty of those pixels is increased. Overall, the

sequence of each subsequent step was considered based on their accuracy and their assumptions for cloud removal. Moreover, the combination of these steps was applied, and their outcomes were validated with the accuracy assessment methods.

2.6.2. VALIDATION OF METHODOLOGY AND THEIR ACCURACY ASSESSMENT

The best way to validate the composite cloud removal methodology was based on the in situ measurement or ground truth data. However, the unavailability of continuous records and scarce measurement locations limit the validation with observatory data in the Chenab basin. Therefore, the adopted methodology was validated with the indirect method suggested by Gafurov and Bárdossy (2009) as well as high-resolution satellite data (Figure 2.3).

In an indirect approach, a total of 186 images (157 belongs to Terra and 29 belongs to Aqua) with less than 2% cloud cover from standard MODIS SCPs during 17 years study period were utilized and filled with other dense cloud covered images. Then the cloud-free images were considered as a 'ground truth' observation for the corresponding cloud-filled images. Numerous authors have considered different sets of images for validation (Parajka and Blöschl 2008; Paudel and Andersen 2011; Dariane et al. 2017). Based on this, we have selected a large number of images to understand the accuracy of the composite methodology. However, the accuracy assessment results may depend on the selection of the cloud-free images and their number in each month because the snow cover condition varies in each month of the year. After applying the composite cloud removal methodology to the artificially generated cloud-covered images and comparing them with the corresponding cloud-free images. However, the first step (the combination of Terra and Aqua SCPs) was not validated because the cloud cover differences between these two satellite images were very low within a day (Gafurov and Bárdossy 2009). Further, the accuracy of the methodology was calculated by assessing the number of pixels reclassified correctly (snow to snow and no-snow to no-snow) and the number of pixels that were misclassified (snow to no-snow and no-snow to snow pixels). Additionally, the overall accuracy was estimated by the percentage of correctly reclassified pixels to the total reclassified pixels in each image.

Second, the validation method based on the high-resolution satellite data, the Landsat-8 OLI images, was used to extract the snow region for 2013–2017. A total of 47 images of the different months were considered for the area comparison with corresponding cloud-free MODIS images. Therefore, the binary snow cover maps were generated based on the reflectance bands (band 3 and 6) of the Landsat satellite data with a threshold of NDSI [(band3 – band6)/ (band3 + band6)]

> 0.4 and the reflectance in band 5 (near-infrared) was > 0.11 for avoiding the water body. Then, we have extracted the common snow-covered region from both datasets (MODIS and Landsat images) and compare them. Moreover, the relative error and Mean Absolute Difference (MAD) between these two datasets were calculated in order to assess the agreement (Hasson et al. 2014a).

2.6.3. SNOW COVER INDICES

To investigate the snow cover change, one of the most popular indexes, i.e., Snow Cover Duration (SCD), was derived using the generated MODIS daily cloud-free images over the study period. The SCD is widely used in several studies to understand interannual variations. Additionally, some other indexes were estimated from the daily snow cover timing, utilized by Dariane et al. (2017). The indexes were extracted by plotting the daily time series of SCA over the basin from 1 September to 31 August. Hence, for the Chenab basin, a total of 16 timing snow curves were obtained, one for each year. However, a five-day moving average of daily SCA was used to reduce the short-term snow cover variation. The detail of the indexes used in this study (Figure 2.4) was explained as follows:

- *Snow Accumulation Onset Day (SAOD):* Considered as the day number from which snow accumulation started. The SAOD is estimated when the SCA exceeds 15% and remains above 15%. However, the shift in SAOD mainly occurred due to the precipitation and temperature changes.
- *Snow Melt Ending Day (SMED):* Considered as the day number that snow storage in the study area is depleted. This index is calculated when the SCA goes under 15%. The SMED is dependent on the amount of snow stored in the winter season, variability in solar radiation, and the T_a during the summer season.
- *Accumulation-Ablation Period (AAP):* Considered as the difference between the SAOD and SMED period. It denotes the period of hydrological processes (snowfall and snowmelt) carried out in the basin.
- *Maximum snow cover (MSC):* Considered as the maximum extent of snow cover observed in a year. This index was mainly used to indicate the snow storage in the basin for that particular year.
- *Maximum Snow Cover Day (MSCD):* Considered as the day in which MSC occurred.
- *Snow Accumulation Period (SAP):* Considered as the period from SAOD to the MSCD.
- *Snow Melt Period (SMP):* Considered as the period between the MSCD and SMED. SMP indicated the time is taken by the snow stored in the basin to be depleted.

- *Snow Accumulation Slope (SAS):* Considered as equal to the ratio of MSC to SAP. SAS denotes the rate at which snow accumulation reached its maximum extent (i.e., the slope of the rising limb).

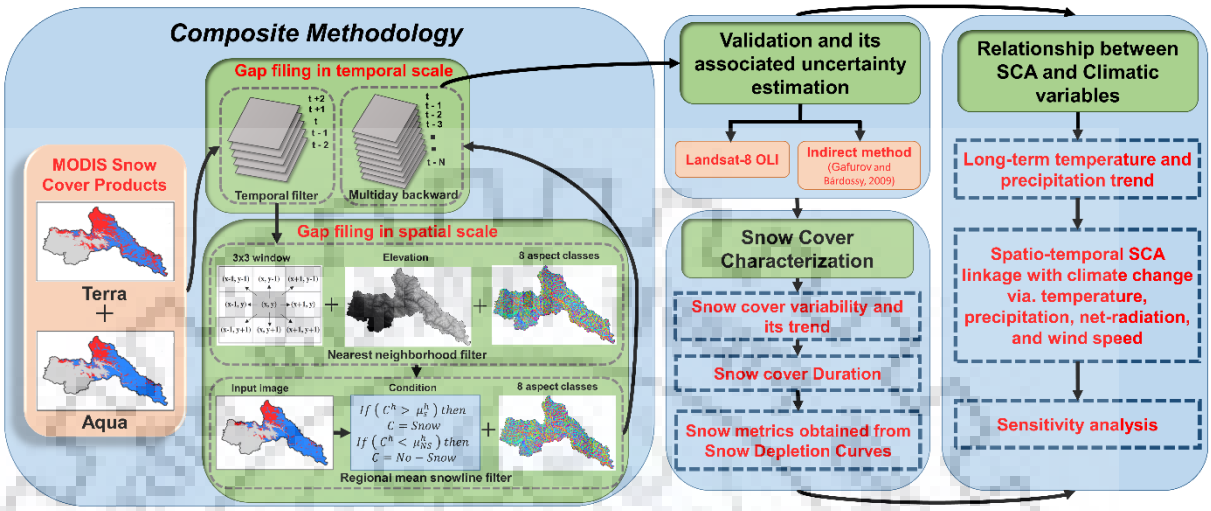

Figure 2.3. Overall workflow of the methodology and analysis structure.

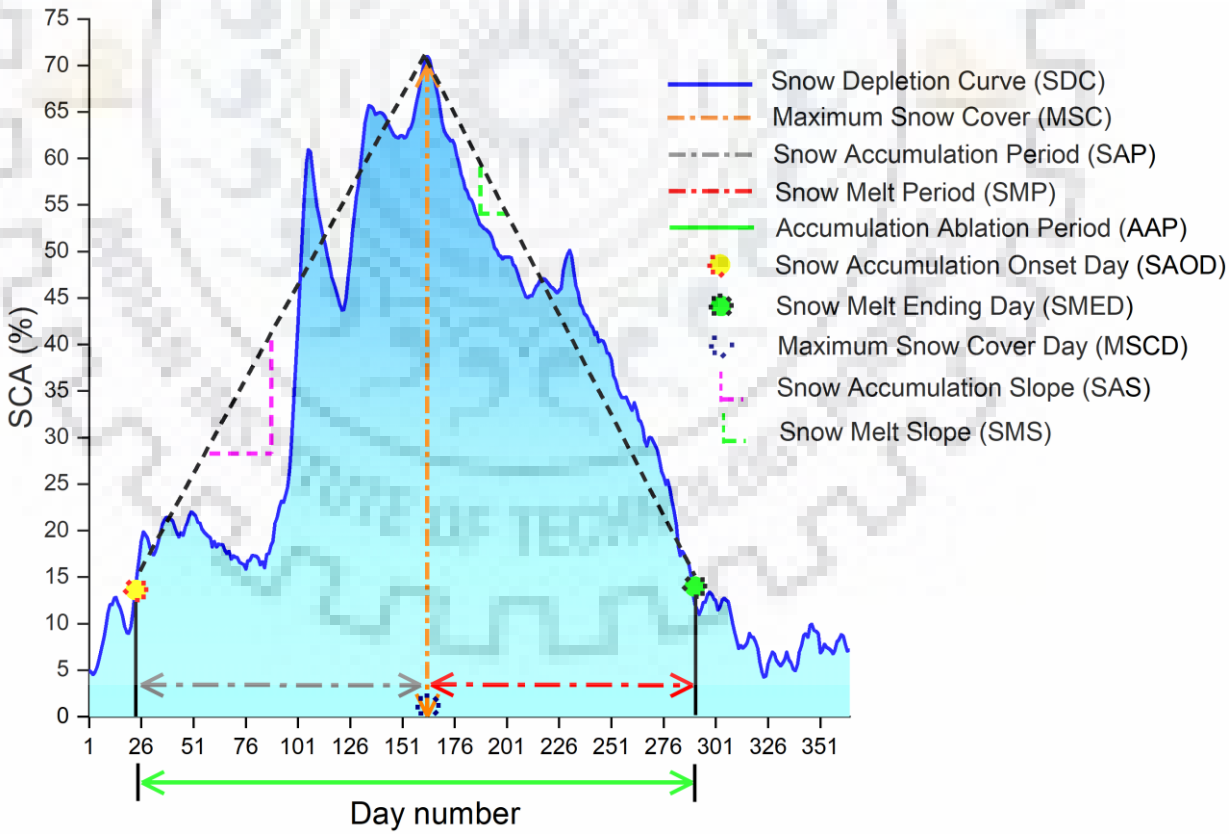

Figure 2.4. Conceptual diagram showing the snow cover timing and defined snow indexes using daily cloud-free SCA between 1 September 2007 (day-1) and 31 August 2008 (day-366).

- *Snow Melt Slope (SMS):* Considered as the ratio of maximum snow cover extent (MSC) to the corresponding SMP. SMS was defined as a melting rate (i.e., the slope of the falling limb).

2.6.4. STATISTICAL ANALYSIS

For the statistical analysis, the non-parametric Mann-Kendall (MK) trend (Mann 1945) and Sen's slope estimator method (Sen 1968) were applied in monthly, seasonal, and annual time-series data of SCA and meteorological variables. Sen's slope provides the rate of change over time-series data, whereas the MK test includes the monotonically increasing or decreasing trend. These trend detection methods are widely accepted in hydrology and meteorology time-series studies (Hamed 2009; Deng et al. 2018b). The relationship of SCA with climatic variables was performed based on the Pearson correlation coefficient (R). Moreover, the daily MODIS SCA was classified into four seasons, i.e., December, January, and February (DJF), March, April, and May (MAM), June, July, and August (JJA), and September, October, and November (SON) to characterize the snow cover distribution in seasonal scale. Figure 2.3 shows the graphical representation of the overall workflow followed, including the cloud gap-filling composite methodology and the relationship between SCA and climatic variables.

2.7. RESULTS

The present study produced cloud-free daily snow cover imageries using standard MODIS daily SCPs (Terra and Aqua) from 2001–2017. Here, we have used preexisting techniques by considering only higher accuracy (> 90%) for cloud removal. Besides, the obtained results were validated by simulating the Gafurov and Bárdossy (2009) method and Landsat-derived snow cover extent. Then, the generated cloud-free images were used to monitor the snow cover variability, dynamics, and its linkage with meteorological variables.

2.7.1. VALIDATION OF THE CLOUD-FREE MODIS SNOW COVER PRODUCT

Firstly, the accuracy assessment was analyzed over 186 cloud-free MODIS images (157 for Terra and 29 for Aqua) by the indirect method. Several authors previously used the adopted methodology for accuracy assessment. The minimum, maximum, and mean accuracy achieved on images were 84.1%, 98.2%, and 93.1%, respectively, for the 157 Terra images, and 81.3%, 97.1%, and 91.3%, respectively, for the 29 Aqua images. The overall mean accuracy of the selected images (186 images) indicated higher efficiency in step-2 while lower in step-5 (Table 2.2). This may have occurred due to the longer time of backward image involvement, which increased the persistent cloud days and produced uncertainty of the land features.

Table 2.2. Accuracy assessment of 186 images calculated for each step (from step 2 to 5) of the cloud removal methodology.

Steps	Minimum	Maximum	Mean	Standard deviation	Kappa coefficient
2	89.1	98.3	94.2	1.21	0.91
3	86.3	96.6	93.3	1.65	0.86
4	84.3	97.6	94.1	1.78	0.83
5	81.2	94.5	89.8	1.61	0.81

The mean monthly accuracy of the selected images and their deviation were analyzed using the adopted methodology. The results indicate that the efficiency starts decreasing from January (94.3%) and attains its minimum in July (90.5%) (Figure 2.5a). This may occur due to the variability of SCA being lower in the winter period compared to other seasons (Gutzler and Rosen 1992). However, a lower accuracy was also observed in the transitional months, i.e., June, July, October, and November, compared to other months. Similar results have been demonstrated by Li et al. (2019) over the Tienshan Mountains using snow depth data. Moreover, a higher deviation was highlighted in July (1.9%). This is possibly due to the monsoonal period that may create a higher variation. The overall mean efficiency was obtained by about 92.8 $\pm$ 1.6%, with a kappa coefficient of 0.85 over the study period.

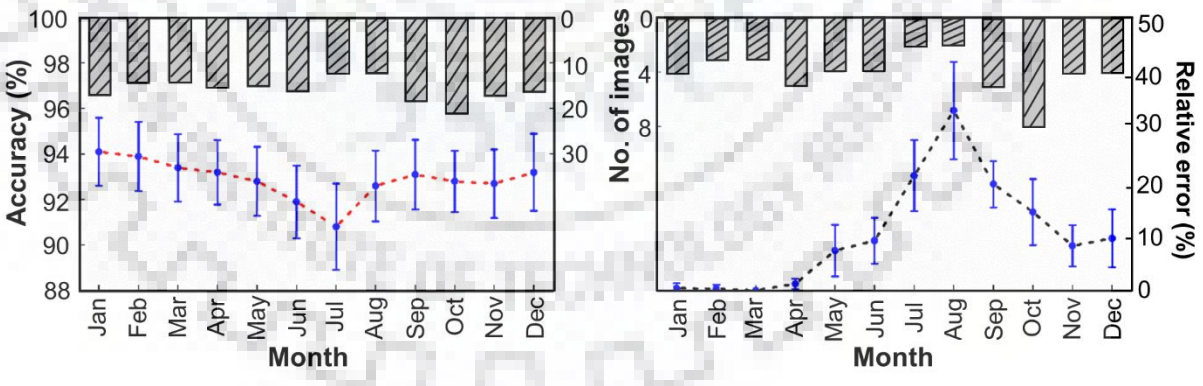

Figure 2.5. (a) Mean monthly accuracy of MODIS SCA using indirect method and (b) relative error between MODIS and Landsat SCA over the study area from 2001 to 2017. The vertical line and bars represent the deviation and number of images, respectively, used for accuracy assessment.

The second approach of cloud-free MODIS data validation included the area comparison between MODIS cloud-free images and Landsat snow cover extent over 2013–2017 (47 images). Validation results show that the Mean Absolute Difference (MAD) between Landsat and MODIS

SCA was approximately 2.4%, while the relative error ranged from –0.3% to 39.2%, with an average of 9.2% (Figure 2.5b). The estimated results indicate that the MODIS snow cover attained maximum overestimation in August (32.9%) and minimum in March (0.0%). Several authors have also reported an overestimation of MODIS snow cover with Landsat in different regions (Tang et al. 2012; Hasson et al. 2014a). However, the underestimation was only slightly observed in January (0.1%). Besides, the MODIS cloud-free snow cover showed a higher correlation ($R = 0.99$, $p < 0.001$) with Landsat data under clear sky conditions.

2.7.2. EFFECTIVENESS OF THE METHODOLOGY

In this study, the effectiveness of individual steps was analyzed over the 17 years of data in order to demonstrate the amount of cloud removal and associated uncertainties. In standard SCPs, the percentage of cloud cover was higher in July and August and lowered in October and May (Figure 2.6). This higher cloud obstruction might have occurred due to the influence of the southwest summer monsoon, while the minimum obstruction may have been caused by the transition of the season (Padma Kumari and Goswami 2010). The mean cloud cover percentage of the basin area in standard MODIS Aqua was 20.9% higher than Terra; however, the mean SCA of Aqua was 30.6% less than Terra SCP. This may have occurred due to the diurnal cycle of cloud cover that varies as well as increases throughout the day (Shang et al. 2018).

In the first step, the combination of Terra and Aqua snow products reduced the mean cloud cover from ~45.4% (Terra) and ~54.9% (Aqua) to 33.9% (combined products) of the total geographical area. However, the mean SCA was increased from 14.5% (for Terra) and 11.1% (for Aqua) to 16.2%. Overall, a five-step composite methodology reduced mean cloud cover by 33.9% (step-1), 20.4% (step-2), 13.4% (step-3), 8.3% (step-4) and ~0.0% (step-5). However, the mean SCA also progressively increased by 16.2%, 21.3%, 25.1%, 28.5%, and 33.6% in each subsequent step. However, in the last step, 30 previous-day images were used to remove almost all cloud pixels for the whole study area. This step removed the mean cloud cover from 8.3% (fourth step) to 5.1% (using first previous-day), 2.2% (using second previous-day), 1.8% (using third previous-day), and ~0.0% (using 30 previous-day images). This step considerably increased the mean SCA during the snow accumulation (December to March) and had no significant changes in the ablation season (July to September). The performance of each subsequent step (from 1 to 5) for cloud removal was observed on a randomly selected date (12 March 2012), as shown in Figure 2.7. The standard Terra SCP observed 94.1% cloud cover (Figure 2.7a), whereas the Aqua satellite observed 99.9% of cloud coverage (Figure 2.7b) after a time difference of ~3-hour.

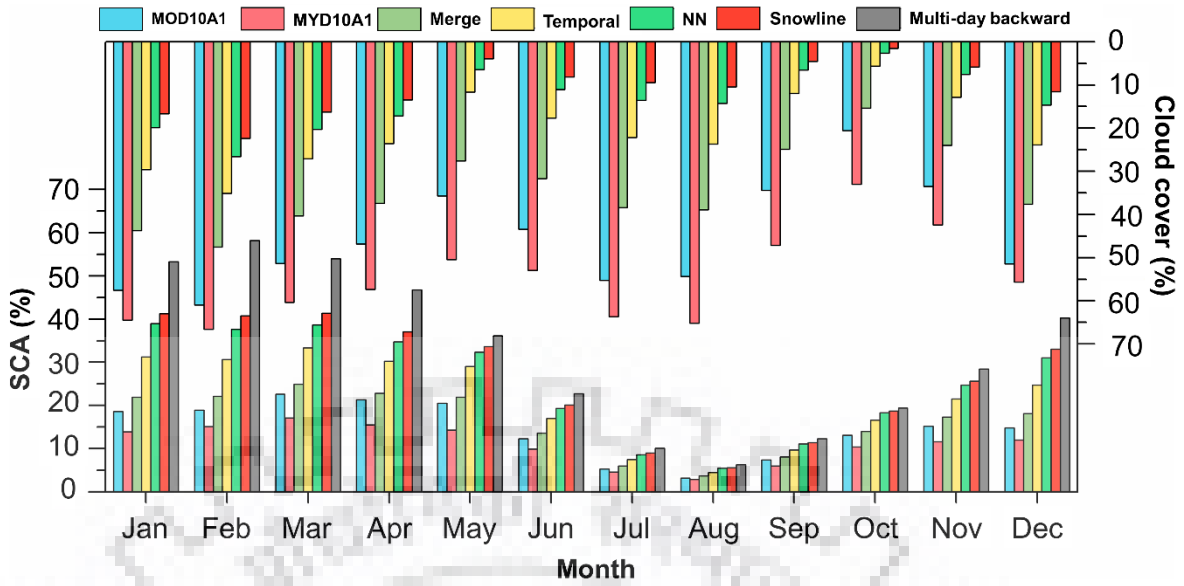

Figure 2.6. Month-wise progressive improvement was obtained in five different consecutive steps. The mean change in SCA and cloud cover percentage in each step are presented of the total study area during 2001-2017.

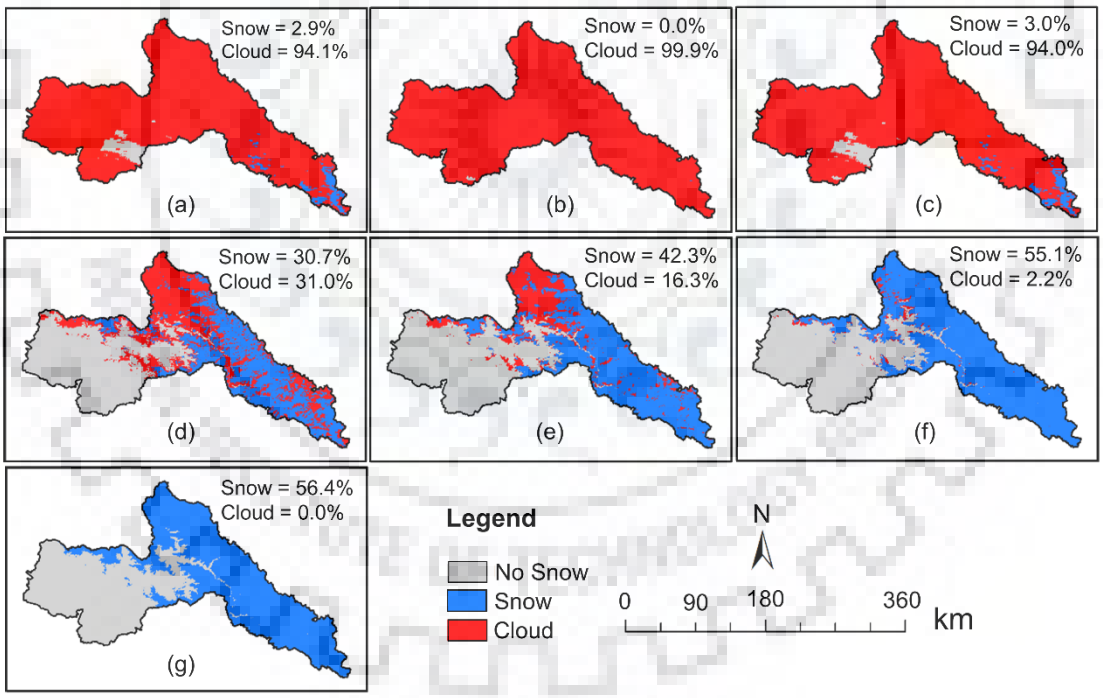

Figure 2.7. Cloud cover percentage of the randomly selected image and produced daily cloud-free image after implementation of the five steps on 12 March 2012. (a) Terra; (b) Aqua; (c) Combination of Terra and Aqua images; (d) Adjacent temporal combination; (f) Nearest neighborhood; (e) Regional mean snow line; and (g) Multi-day backward replacement.

Obliviously, this percentage change in cloud cover reflects the continuous cloud movement dynamics. The implementation of the first step (combine of Terra and Aqua) removed 0.1% cloud

cover from Terra and 5.9% from Aqua, while a total of 94.0% cloud cover remained (Figure 2.7c). The second step removed 63.0% cloud cover, while 31.0% remained (Figure 2.7d). However, the cloud coverage for the previous two and the next two days was observed at 13%, 71%, 19%, and 46%, respectively. The third step removed 14.7% cloud cover, and 16.3% remained (Figure 2.7e). Although this step removed less cloud cover, however, it should still be considered in the part of methodology due to high accuracy and further minimizes the overall error. Many authors reported that the neighboring pixels method attains low error (Gafurov and Bárdossy 2009; Tran et al. 2019). The fourth step, based on a regional snow line, removed 14.1% cloud cover, and 2.2% remained (Figure 2.7f). Finally, the last step removed the remaining 2.2% cloud cover using a multi-day backward replacement approach (Figure 2.7g).

2.7.3. UNCERTAINTY ASSOCIATED WITH CLOUD GAP-FILLING TECHNIQUES

In this study, the standard MODIS SCPs were used as observational data; however, all observational data have some inherent uncertainty. These inherent uncertainties are usually associated with the larger solar zenith angles, which can reduce the accuracy of the product (Li et al. 2016). Additionally, there are other uncertainties associated with the cloud gap-filling algorithm because of the different band considerations in Terra (band 6) and Aqua (band 7) for the NDSI algorithm (Hall and Riggs 2007). Moreover, the MODIS snow product has an advantage for large areas; however, the accuracy of the single-pixel can be influenced by different variables, i.e., acquisition angle, acquisition time, topographic effect, and land cover (Matiu et al. 2020). These factors lower the accuracy, especially at the start and end of the snow season. Therefore, the last multi-day backward replacement filter was used to provide reasonable estimation when averaged over the more extended periods. Hence, special consideration should be given to the daily value of snow cover pixels during the monsoon season.

2.7.4. SNOW COVER VARIABILITY

After a satisfactory assessment of the methodology efficiency, the generated new daily cloud-free MODIS snow cover images were used to understand the intra-annual and inter-annual variability of snow cover over the Chenab basin. Daily distributions of the SCA for each date from 1 January 2001 to 31 December 2017, depicting the annual cycle, are shown in Figure 2.8. The sequence of daily images indicates that the major snowfall events and growth/shrink of snowfall period over one year change from decade to decade. It also suggests that the snow cover extent is highly variable within the observation period, further leading to a shift in the snowfall season.

Figure 2.8. Daily cloud-free snow cover area of the Chenab basin from 1 Jan 2001 to 31 Dec 2017.

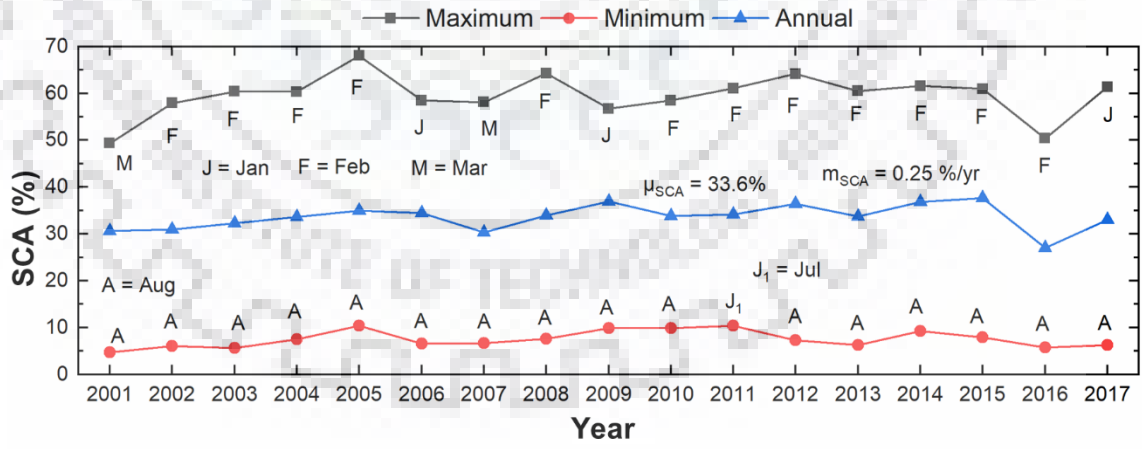

Figure 2.9. Mean annual and monthly minimum and maximum SCA of each year over the Chenab basin from 2001 to 2017.

The annual evolution of snow cover during 2001–2017 was analyzed for the entire basin (Figure 2.9). The mean yearly SCA was 33.6% of the total geographical area. The mean annual minimum and maximum SCA were observed in 2016 (27.0%) and 2015 (37.5%), respectively. The

maximum SCA mostly occurred in February except for the years 2001, 2006, 2007, 2009, and 2017, while the minimum SCA was mostly observed in August except in 2011. Previous studies have also suggested that the maximum and minimum SCA occurred in February and August, respectively, for the western Himalayas (Kripalani et al. 2003; Kour et al. 2016b); thus, this coincided with our results. Also, Dimri et al. (2015) have reported that the major snowfall events occur during December, January, and February were mainly influenced by the western disturbances over the Himalayas. In general, if the maximum SCA occurred in January, this would likely result in a higher rate of melting due to increasing the ablation period and directly contributing to the river system (Barnett et al. 2005).

For the observation period, the mean monthly SCA was more persistent in February (58.2%), followed by January (54.5%), and March (54.0%); while the minimum SCA was observed in August (6.2%), followed by July (10.1%), and September (13.9%). The transitional months of September, October, and November showed the highest inter-annual SCA variability with a Coefficient of Variance (CV) of 0.27, 0.30, and 0.29, respectively, whereas March (CV = 0.07) and April (CV = 0.07) experienced the least variability and were relatively stable.

To evaluate the significant change in snow cover trend, a non-parametric MK and Sen's slope test were performed on monthly, seasonal, and annual time scales in three separate periods, i.e., 2001–2017, 2001–2009, and 2009–2017 (Figure 2.10). It should be noted that a statistical trend for a shorter period than these should be treated carefully. Although the result shows an increasing trend of SCA for the periods 2001–2017 and 2001–2009, it has been slightly decreasing since 2009 and was statistically insignificant. Therefore, an insignificant increasing trend of SCA was observed at a rate of 0.25 % yr^{-1} for the entire period. Moreover, the SCA increased or was stable from January to April during each selected period. This may indicate that the snow accumulation period has changed or is shifting in terms of the seasonal snow cover (Singh et al. 2019). The reduction in mean annual SCA was increased by ~6.8% during 2001–2009; however, recently, it was decreased by ~1.5% of the total basin area during 2009–2017. Moreover, the maximum SCA was reduced (about 10.2%) in SON and was increased (about 1.5%) in DJF during 2009–2017.

2.7.5. SNOW COVER DEPLETION CURVE INDEXES

The Snow Depletion Curve (SDC) was used to extract the different indexes for the entire basin to understand the properties of the snow accumulation- ablation season. Results indicate that the

MSC trend was decreasing (−0.12 % yr^{-1}) for the entire area. Moreover, the SAP was shortened (−1.44 day yr^{-1}), resulting in a stable or no trend of the SAS, which is the ratio of MSC to SAP.

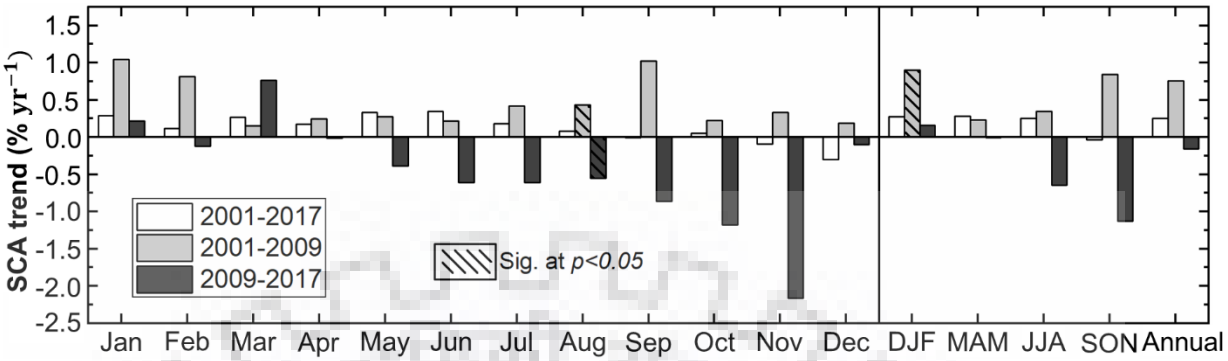

Figure 2.10. Trend analysis of the mean monthly, seasonal, and annual SCA of the Chenab basin during three distinct periods: 2001 to 2017, 2001 to 2009, and 2009 to 2017.

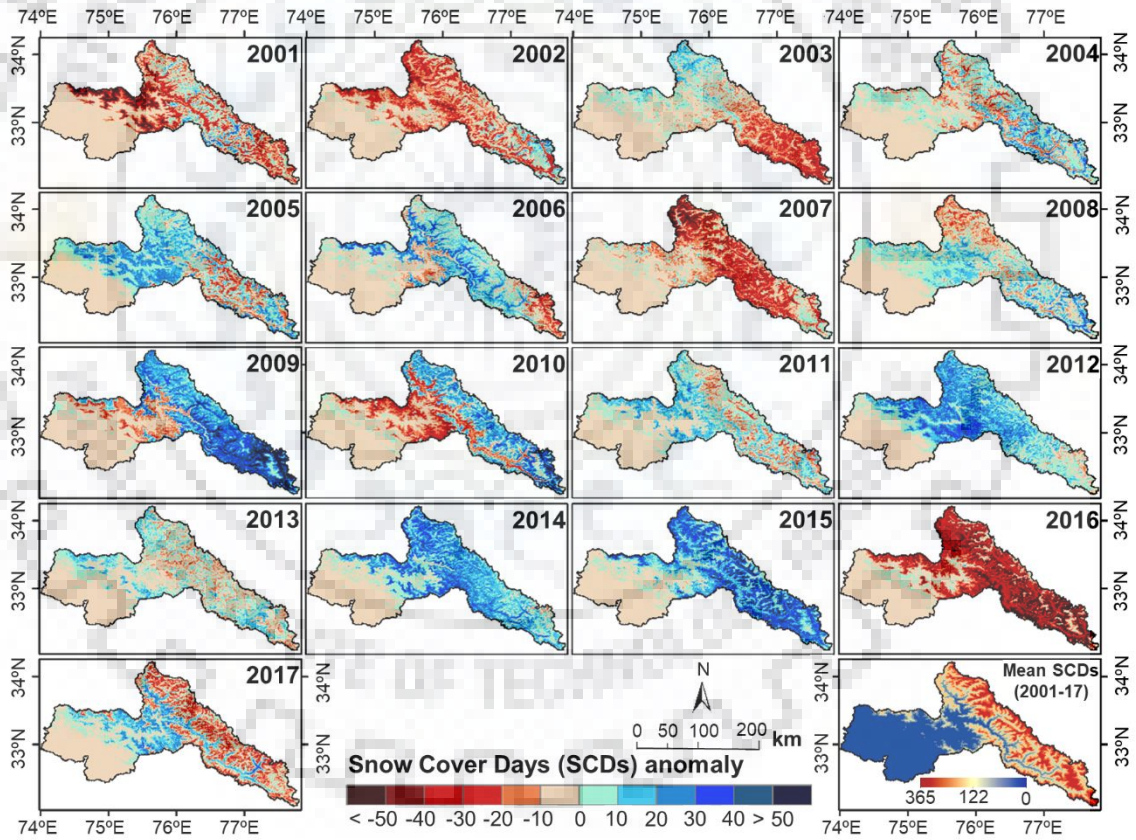

Figure 2.11. Spatial distribution of SCD anomalies (deviation from the mean of the 2001–2017 period) per year and mean SCDs over the Chenab river basin from 2001 to 2017.

In contrast, SMP was elongated by about one day per year with decreasing SMS (–0.004). However, the MSCD was shifting backward at the rate of about one day per year. The trend of SAOD indicated that the snow accumulation started one day earlier, while that of the SMED

showed that the average snowmelt season ended one day earlier in each year. Overall, the AAP indicated a decreasing trend at the rate of –0.92 day yr^{-1}; however, the SAP decreased, and SMP increased at the rates of –1.44 and 1.19 day yr^{-1}, respectively. All indexes showed insignificant trends ($p < 0.05$) during the study period.

2.7.6. SNOW COVER DAYS (SCDS)

The pixel-wise SCDs for each year were calculated based on cloud-free daily snow cover images. The average SCD of the basin was ~122 days during the study period. A 17-year mean SCD was classified into six subsequent classes (Figure 2.11). The SCD of less than 60 days covered the majority of the basin, ~45.0%, which was considered unstable SCA. The other classes, such as 60–120, 120–180, 180–240, and 240–300 days, occupied areas of about 8.4%, 11.3%, 14.6%, and 10.5%, respectively. However, the majority of mountain peaks and glaciers were covered with SCDs above 300 days, with an area of 10.5%. In addition, more SCD values were observed in the higher elevations of the basin (above 5000 m a.s.l.), which received higher snowfall compared to the lower reaches. This region attains most of the Chenab basin glaciers, which have relatively persistent snow compared to the mid-lower and lower elevations. This indicates that the SCD was minimum for areas near 2200 m elevation, and the duration of snow cover became shorter. The spatial distribution of SCD anomalies (deviation from the 17-year mean) of each year is illustrated in Figure 2.11. We observed a relatively shorter SCD than the total mean in 2001, 2002, 2003, 2016, and 2017, particularly in 2016 (23 days). In contrast, 2004, 2010, and 2013 were stable, with the SCD being close to the mean. However, the rest of the years were considered longer than the mean of the SCD, especially in 2015, which indicated that the SCD was 15 days longer than the mean. Randhawa et al. (2016) have found that the SCA reduced significantly during 2015–2016 in comparison to 2010–2014 in almost all basins of the Himachal Pradesh, western Himalayas.

2.7.7. SNOW COVER INFLUENCE BY TOPOGRAPHIC PARAMETERS

The topographical effect on SCA variations was investigated over six different elevation bands (elevation-wise), eight aspect classes (aspect-wise), and five slope classes (slope-wise) over the entire time series of data (Figure 2.12). For this, the classified areas for each elevation zone were 21.5% for 0–1000 m a.s.l., 13.9% for 1000–2000 m a.s.l., 14.2% for 2000–3000 m a.s.l., 16.3% for 3000–4000 m a.s.l., 22.3% for 4000–5000 m a.s.l., and 11.7% for elevations over 5000 m a.s.l. of the total basin area, for which the mean SCA values were about 1.6%, 14.7%, 41.9%, 65.5%, and 84.6%, respectively (Figure 2.12a). Additionally, elevations above 4000 m a.s.l.

covered 34% of the basin area, which included 97.5% of the core glacier area within the basin. However, the SCA for the period 2001–2017 showed an increasing trend at the rate of 0.78% yr^{-1}, whereas a decreasing trend (−1.36 % yr^{-1}) in SCA was observed during 2009–2017 for the elevations above 4000 m a.s.l. This decreasing trend of SCA in higher altitudes could have led to the negative glacier mass balance (Singh et al. 2019) and an increase in streamflow (Lutz et al. 2014) in the recent decade. However, the overall SCA showed a decreasing trend from September to January, whereas an increasing trend was experienced from April to August, which is statistically insignificant above 4000 m a.s.l. It should be noted that the elevation zones between 4000 and 5000 m and above are likely to be most sensitive to climate change as most of the glaciers exist at these elevations, and a significant amount of snow cover remains throughout the year. Therefore, this change in SCA at higher elevations could have a major impact on glacier mass balance and regional water storage.

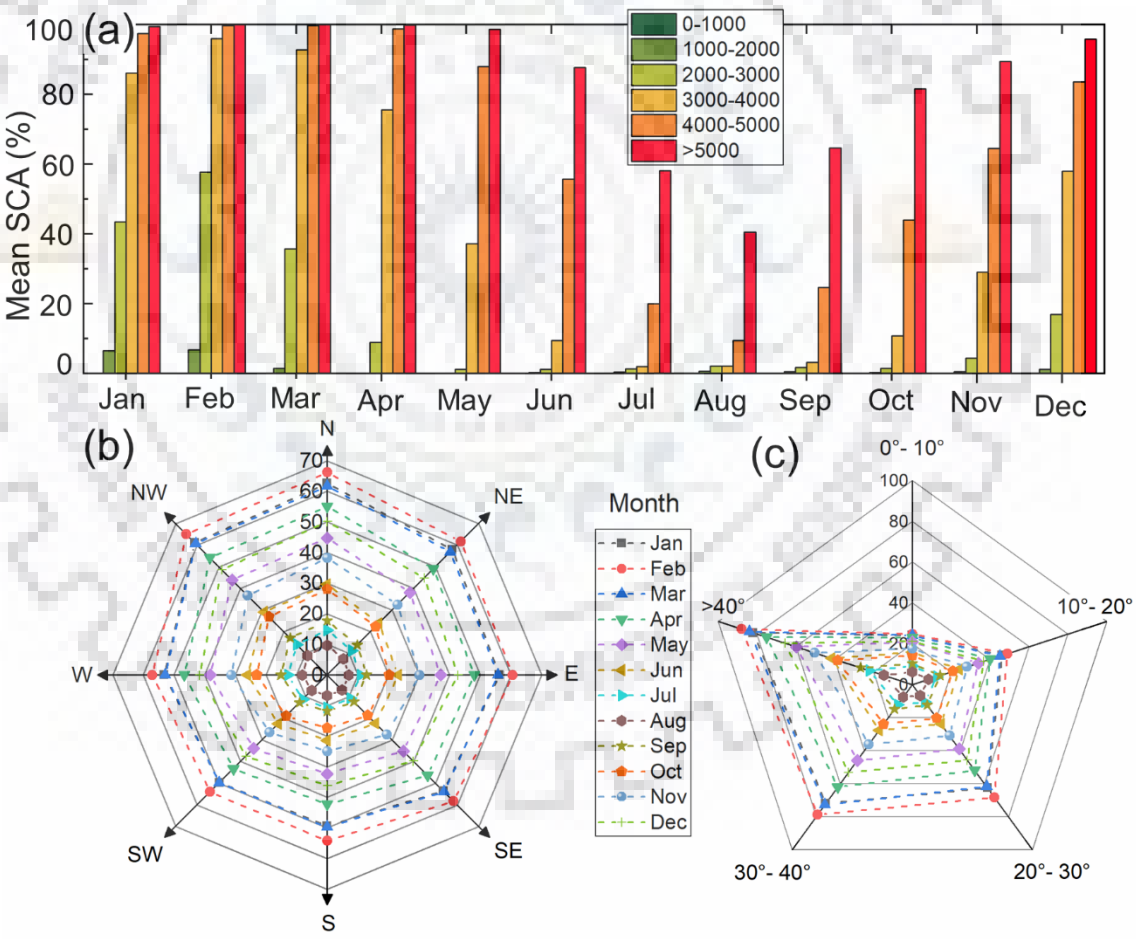

Figure 2.12. Mean SCA distribution from 2001 to 2017 in classified: (a) Elevation; (b) Aspect and (c) Slope of the Chenab basin.

The SCA dependency on aspect-wise varied from location to location because precipitation was influenced by the function of aspect and prevailing wind direction. Therefore, the aspect values

were classified as 7.3% for north (337.5–22.5°), 10.8% for northeast (22.5–67.5°), 10.7% for east (67.5–112.5°), 13.6% for southeast (112.5–157.5°), 17.5% for south (157.5–202.5°), 15.9% for the southwest (202.5–247.5°), 12.5% for the west (247.5–292.5°), and 11.7% for northwest (292.5–337.5°) of the total basin area (Figure 2.12b). It was found that the north and south directions experienced the maximum and minimum SCA in each month, respectively, with the highest occurring in February and lowest in August. By combining the elevation and aspect information, it can be concluded that aspect is not a strong limiting factor for snow persistence in the higher regions during the winter season. However, snowmelt becomes more relevant when the climatic condition is changed or if solid precipitation is weaker in the higher elevations. The slope orientation of the basin has a relatively larger area in the south and southwest, and higher SCAs in the north (40.0%), northeast (35.0%), and northwest (38.9%) during all seasons were observed.

For quantitative snow cover distribution, the slope of the basin was classified into five different categories, i.e., 0–10°, 10–20°, 20–30°, 30–40°, and above 40°, which covered areas of 20.9%, 20.9%, 29.3%, 22.1%, and 6.8% of the total basin area, and mean SCA was observed at 17.5% 29.8%, 36.0% 42.1%, and 53.8% respectively (Figure 2.12c). The basin experienced a maximum and minimum SCA above 40º and 10–20º, respectively, in all months; however, it was highest in February and lowest in August. This could be related to the solar radiation being the largest and smallest on steep south-facing and north-facing slopes, respectively. However, the flatter terrain of lower elevations receives more solar radiation than the steeper slopes. Therefore, the SWN can be influenced by the change in slope and direction, which tends to change in snowmelt (Seyednasrollah and Kumar 2014).

2.7.8. RELATIONSHIP OF SCA WITH CLIMATIC PARAMETERS

To investigate the possible mechanism of snow cover variability, the linkages between the snow cover and climatic variables, i.e., T_a, P_t, SWN, and u, were analyzed. The climatic variables were explained in two ways. First, the long-term spatiotemporal trend of T_a and P_t were analyzed during 1981–2017 to understand the decadal changes, which further linked to regional-scale climate variability. Second, the relationship between SCA and the climatic variables was established using Pearson's correlation coefficient and regression analysis.

2.7.8.1. Temperature and precipitation analysis (1981–2017)

The Annual trend of T_a and P_t were assessed for 1981–2017. Results showed a significant increase in mean annual T_a at the rate of 0.023 °C yr^{-1}, while P_t decreases at the rate of –5.88

mm yr^{-1} (Figure 2.13c). The maximum and minimum temperatures were observed in 2016 (5.19 °C) and 1997 (2.66 °C), respectively, with a mean value of 3.86 °C. Relatedly, 2007, 2010, and 2016 were the warmest year in the Hindu-Kush Himalayan region for the period of 1901–2014 (Ren et al. 2017; Wester et al. 2019). Similarly, the mean maximum and minimum of P_t were observed in 1994 (1978.4 mm) and 2016 (1007.7 mm), respectively, with a mean value of 1452.8 mm. Previous studies have reported that the snow/ice cover area decreased by 0.9% over the Himalayan region between 1990 and 2001 (Menon et al. 2010) due to aerosols. This reduction in snow cover can be supported by our study of the previous decade (1990–2001) that a decrease in P_t (–60.5 mm yr^{-1}, $p < 0.05$) due to a rise in T_a (0.049 ℃ yr^{-1}) over the study area.

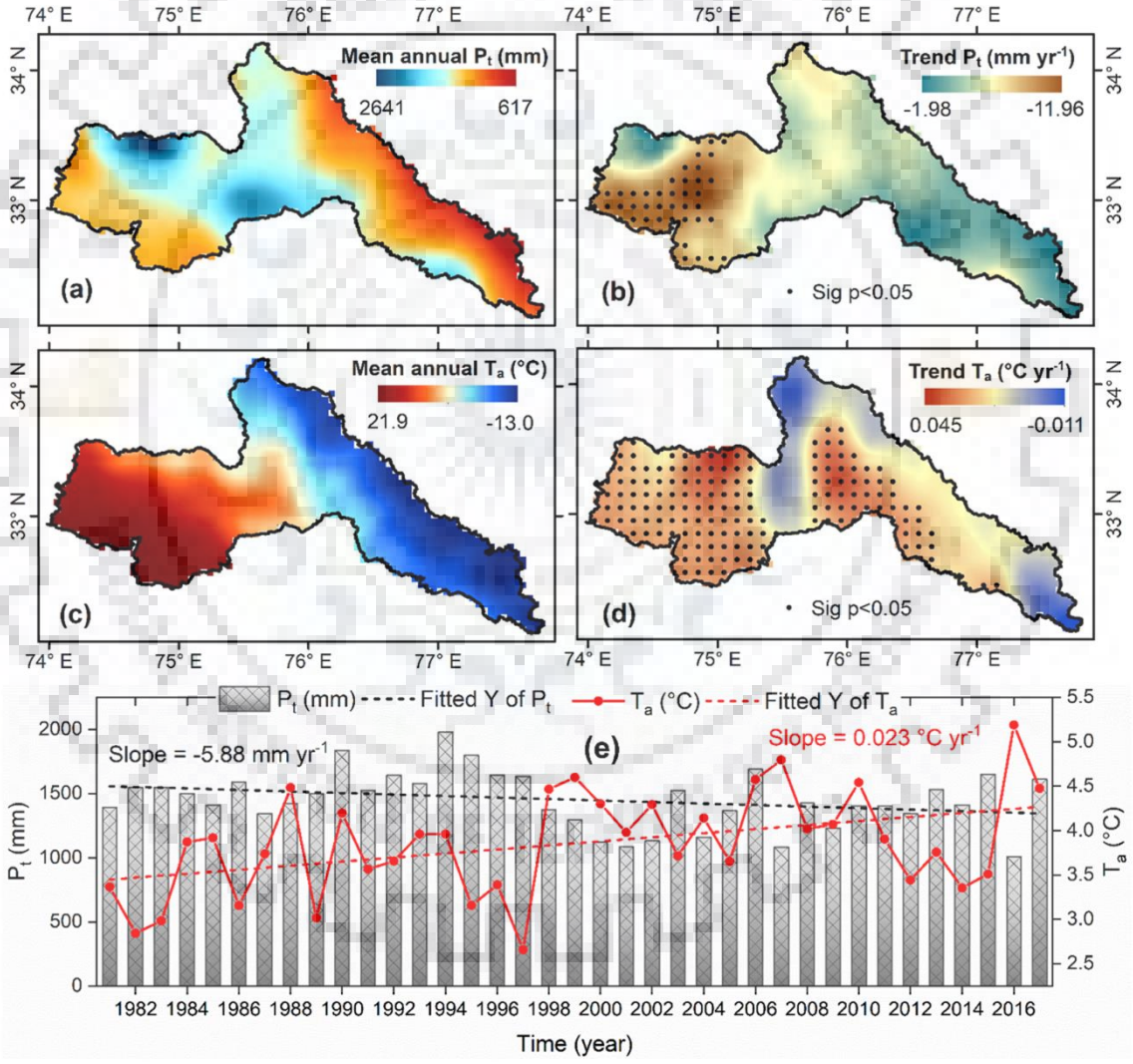

Figure 2.13. Spatiotemporal pattern of a) mean annual air temperature and its trend (b); c) total yearly precipitation and its trend (d); and e) linear relationship between annual temperature and precipitation, derived from gridded data during 1981–2017.

Additionally, the spatial distribution of T_a (Figure 2.13a) and P_t (Figure 2.13b) were observed using MK and Sen' slope test. As identified visually, the rate of change in T_a and P_t varies from location to location. Bhutiyani et al. (2007) have reported that the northwest Himalayan region shows a significant rise in T_a by about 1.6°C during the last century (1901-2001) and winter warming at a faster rate. Also, Jaswal and Rao (2010) have highlighted that a significant increase in the maximum T_a over the Kashmir region and the minimum T_a over the Jammu region during 1976–2007. Furthermore, in this study, the P_t decreases in the southeast region of the Chenab basin with an increase in T_a. However, both P_t and T_a were increased in the northwest region with statistically significant values.

2.7.8.2. Impact of climatic variables on SCA (2001–2017)

The linear relationship between SCA and climatic variables were performed on seasonal and annual data for the period 2001–2017 (Figure 2.14). Results indicate that the SCA has an inverse relation with T_a and a direct relationship with P_t. Additionally, the mean monthly and annual T_a of each year shows an increasing slope except for the MAM and JJA. However, with a higher increase in T_a, the snow cover in later (SON) decreased further. Another effect is that the liquid P_t increased because because P_t occurred as rain in higher T_a conditions; therefore, the SCA dynamics were affected. Moreover, the present study suggested that the rate of SCA attains a higher positive value in MAM compared to DJF. While the T_a rate increases in DJF as compared to MAM (decreasing). This may be occurred due to a shift in the seasonal cycle of climatic variables. A similar pattern was observed by numerous authors (Singh et al. 1997; Kour et al. 2016a; Anjum et al. 2019).

However, these trends are represented for a shorter period of time which cannot fully explain the SCA expansion. Winter P_t and T_a may be considered as key factors for the increasing SCA trends in the Chenab basin and should be studied using more reliable high-altitude data. Also, Rathore et al. (2018) have observed a rising trend of snow cover in all basins of the western and west-central Himalayan regions during 2004–2014, and Negi et al. (2017) have reported that the winter (November to April) mean T_a was decreasing, and the number of snowfall days was increasing insignificantly in the northwest Himalayan region from 2001 to 2014. Furthermore, Gurung et al. (2011) have shown that snow cover trends for the western Himalayan region were positive for all seasons from 2000 to 2010.

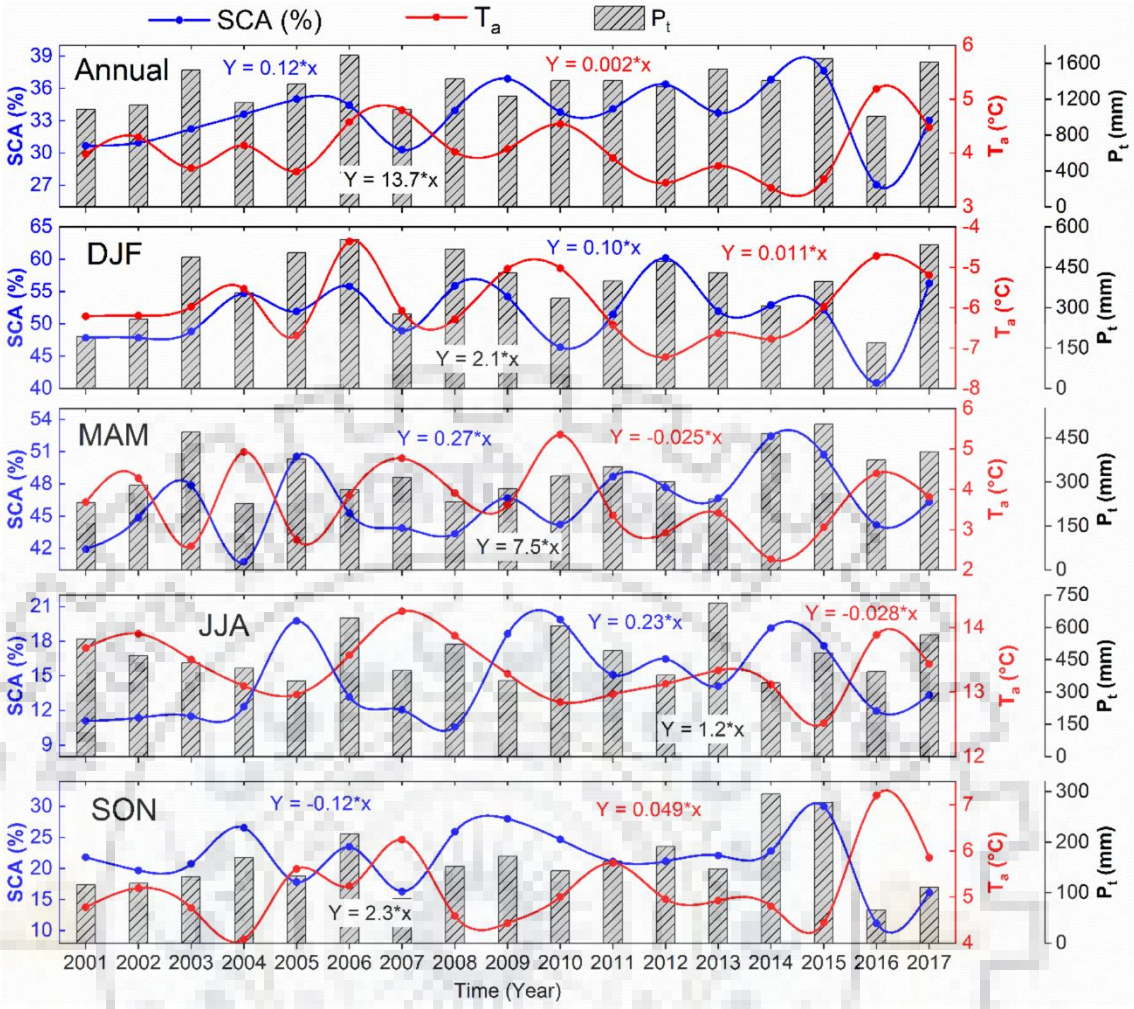

Figure 2.14. Linear variation of mean seasonal and annual SCA, air temperature, and precipitation from 2001 to 2017 over the Chenab basin.

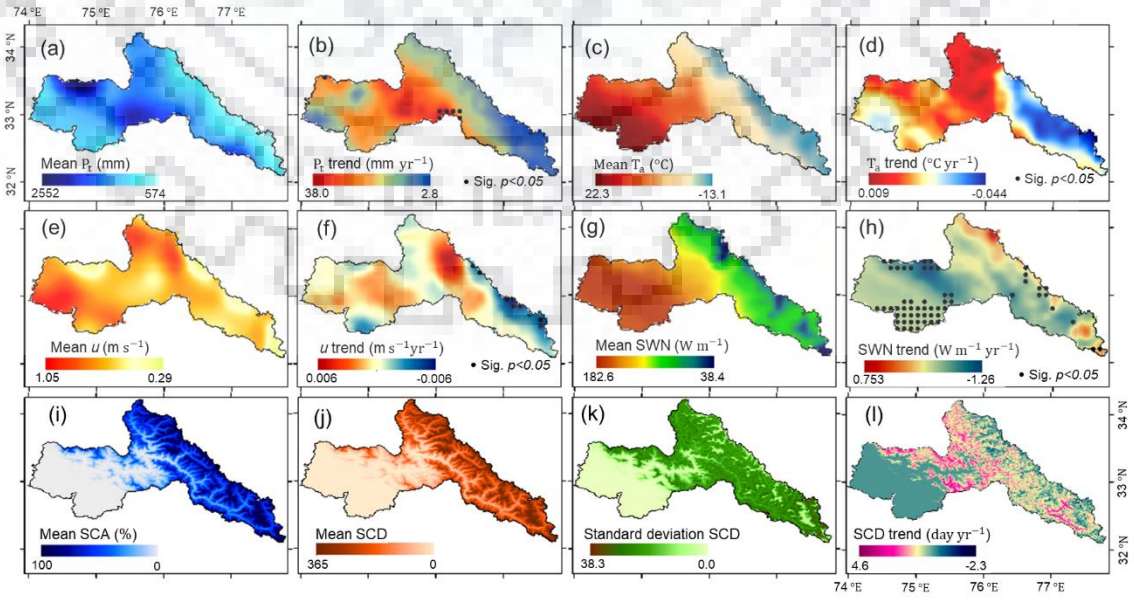

Figure 2.15. Spatial pattern of annual (a, b) precipitation and its trend, (c, d) mean air temperature and its trend, (e, f) wind speed and its trend, (g, h) net shortwave radiation and its

trend, (i) mean SCA, (j) mean annual SCD, (k) SCD standard deviation, and l) SCD trend during 2001-2017.

To evaluate the response of SCA and SCD with the climatic variables and energy flux, the spatio-temporal patterns of P_t, T_a, u, and SWN were assessed over the Chenab basin for the period 2001–2017 (Figure 2.15). Results showed an increasing trend of P_t with a rate of 21.2 mm yr^{-1} for the entire basin. Besides, P_t was found to increase less in the high mountain regions. This result is in good agreement with Dahri et al. (2016) and Rizwan et al. (2019). However, the u, T_a, and SWN rate were also substantially increasing for the low to medium clusters. The analysis demon-strates that the P_t and SWN were increasing in the northeastern region of the basin; however, for T_a and u decreasing trends were observed. In contrast, a decreasing trend of P_t and SWN were observed in the central part of the basin along with the increasing trend of T_a and u.

Additionally, the increasing T_a reduces the SCDs and increases its deviation, which further leads to an earlier onset of snowmelt. This result was previously explained by Rathore et al. (2018b) over the Chenab basin. Also, Shafiq et al. (2018) have reported that the maximum and minimum T_a was decreased while the P_t was increased in the Kashmir valley located in the northwest region of the Himalayas. Furthermore, the SCA variation was influenced by the energy and the mass fluxes of the underlying surface. The regions with higher SCA reflect more solar energy with less absorption, which decreases the SWN over the area. Therefore, the SWN was higher in the snow-free region and lowered in the snow cover. Additionally, the small cluster of SWN was increasing over the region, whereas SCDs decreased. This may have occurred due to the spatial heterogeneity of the SCA and SCDs that varied from location to location. However, the increasing u also helped to increase the mass fluxes, i.e., sensible and latent heat. Moreover, it may have affected the amount of sublimation/re- sublimation in the snow-covered region.

Overall, the changing trends of these climatic variables help in understanding the influence of snow cover distribution and the onset of snowmelt. The inter-relationship between SCA, P_t, T_a, u, and SWN were calculated using Pearson's correlation coefficient for the period 2001–2017 (Figure 2.16). Results indicate that the P_t shows a significant positive correlation with the SCA for all the months except JJA over the basin. This may be because the basin is predominantly influenced by the ISM, which is active during JJA and attains a majority of P_t in the form of rain (Dahri et al. 2016). Similarly, a significant negative correlation was observed between SCA and T_a throughout all months except for DJF. In these months, the T_a shows a low variation (almost negative) as compared to the SCA. Additionally, the SWN was also found to be less negatively correlated with the SCA for the JJA; otherwise, it showed a significant negative correlation for

the rest of the months. This can be evidence of the fact that the SWN usually reaches its maximum from June to July. However, the SCA started decreasing from June and reached a minimum value in August, which may have resulted in a poorer correlation. However, u showed a significantly positive correlation with the mean SCA for the period June–November. Overall, the annual SCA shows a significant positive correlation ($p < 0.05$) with P_t and u, and a negative correlation ($p < 0.01$) with T_a and SWN over the basin. These interrelationships help to identify the contributing factors controlling the spatial and temporal distribution of the SCA. Therefore, further study is recommended to determine exact processes that could contribute to an increase in SCA across the basin.

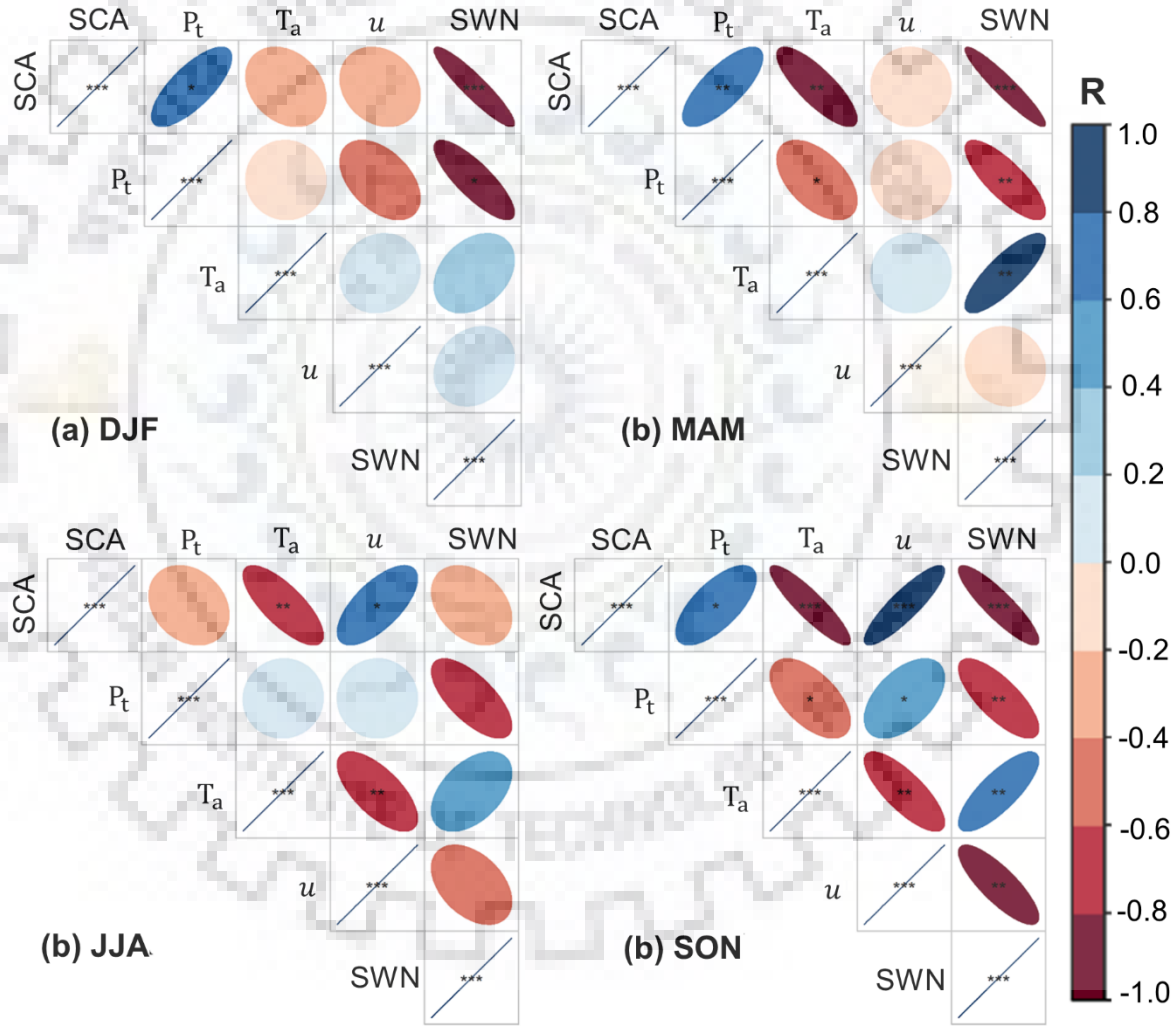

Note: ***, **, & * indicates sig. value at $p<0.001$, $p<0.01$ & $p<0.05$, respectively

Figure 2.16. Seasonal Pearson correlation coefficients between SCA, air temperature (T_a), precipitation (P_t), wind speed (u), and SWN over the Chenab basin from 2001 to 2017.

2.7.9. SENSITIVITY ANALYSIS

The sensitivity analysis was performed by developing a multiple linear regression model between dependent, i.e., SCA, and independent variables, i.e., P_t and T_a during 2001–2017 for the entire basin. The model showed a higher correlation (R = 0.81, $p < 0.001$) between the used variables. The P_t and T_a were altered by $\pm$ 30% and $\pm$ 2ºC, respectively. Results showed that the snow cover response to the warming temperature ($\pm$ 2ºC), reduces the SCA by $\mp$ 11%. In general, the snow cover showed a higher sensitivity to the T_a, which means that the small changes in T_a generate significant variation in the SCA. This obtained result was also highlighted by Rathore et al. (2018b) and Kour et al. (2016). They also found a strong connection between the T_a and SCA variability over the Chenab basin. Our result indicates that the increasing P_t (in this case $\pm$ 30%) had little effect on the snow cover change ($\pm$ 6%); however, a strong influence occurred during the snow accumulation season. A similar result was demonstrated by Brown and Mote (2009) over the Northern Hemisphere. Overall, this analysis suggests that the SCA is more sensitive to T_a; however, is less susceptible to P_t during the melt season for the selected observational period.

2.8. DISCUSSION

Information on spatial distribution and temporal dynamics of snow cover is crucial for understanding the hydrological system within the Chenab basin. In comparison to other regions in the same latitude, the Chenab basin in the western Himalayas is influenced by both P_t, i.e., ISM in summer and Mid-latitude Westerlies in winter (Shekhar et al. 2010). Furthermore, this region has the potential to be the "home to the largest capacity of hydropower project[s]" among all the basins in India (Thakur and Asher 2015). Therefore, seasonal snow cover monitoring at the basin scale is crucial in order to measure the water availability from snowmelt in the summer season. Thus, a reliable estimate of the spatio-temporal snow cover trend and its response to future climatic change is needed. However, ground observations are rare and temporally limited in the high mountainous region of the Chenab basin. The high temporal resolution of the MODIS instrument can overcome this limitation and provide an excellent opportunity to study the snow cover variability. The snow cover result of MODIS data was previously validated over different parts of the world (Hall and Riggs 2007; Gafurov and Bárdossy 2009) within Hindu-Kush Himalayas (Forsythe et al. 2012; Hasson et al. 2014a), and also in the western Himalayas (Jain et al. 2008; Chelamallu et al. 2014).

The higher accuracy (> 90%) methods were combined, and composite methodology was used to remove the cloud cover and maintain the overall accuracy of the selected MODIS snow product. The validation of the methodology suggested that the applied method substantially eliminated the cloud cover with high efficiency over the study area. However, it was also observed that the cloud gap-filling technique was unable to completely remove the clouds from the snow product because of the persistent cloud being longer than the temporal window size, as well as because of more significant cloud cover extent (Hasson et al. 2014a). Therefore, the results suggest that the cloud percentage was higher during JJA. A similar pattern of higher cloud cover in the melt season compared to that of the accumulation season was reported by Maskey et al. (2011) over the central Himalayas. Therefore, the adopted methodology was limited during the respective season, especially for the high mountain glacierized region during the melt season. Still, the overall performance of the methodology was satisfactory in that the importance of gap-filling of cloud cover was highlighted, along with an improvement of SCA.

The variability of the SCA on the Chenab basin was characterized by seasonal and annual changes, which varied with different elevation, slope, and aspect. The study shows that the snow cover has a heterogeneous distribution over the Chenab basin, with more variation in the northeastern region and less snow cover in the western region of the basin. The snow cover extent significantly decreased in the NH, especially in spring (Yeo et al. 2017). Satellite records indicate that during 1967–2012, the SCA reduced considerably, and the most significant change occurred in June (IPCC 2013). Rathore et al. (2018a) have also highlighted the higher variability of snow cover at the sub-basin scale in the Indus, Chenab, Sutlej, and Ganga basins during the accumulation period rather than the ablation. The overall trend of snow cover shows an increasing trend over the basin. However, Sahu and Gupta (2020) have also reported the SCA shrinking at the rate of 0.12% per year over the Chandra basin during 2001–2016. This inconsistency in results may be due to the temporal change in the MODIS snow product (8-day MOD10A2). Additionally, Kour et al. (2016) have demonstrated that the SCA was significantly increased due to a significant increase in snowfall and a decrease in T_a during 2000-2013. The linear relationships between the SCA with the topographic parameters suggested that the SCA trend decreased in September–January for elevations above 4000 m a.s.l., while it increased in April–August. This pattern also was demonstrated by Kour *et al.* (2016b). Additionally, the SCDs and nine snow indexes showed significant shifting movement in and shortening of the snow accumulation period over the basin. An early snow melting was also reported by Ayub et al. (2020) over the upper Indus basin.

Generally, the large interannual variability in snow cover in the Chenab basin is the more striking feature (Kour et al. 2016a; Rathore et al. 2018a), as well as its linkage with climatic variables and energy fluxes necessary for the future prediction and policy adaptation. This analysis shows that the region has experienced an increasing trend of SCA with a statistically significant increase in P_t and T_a during 1981–2017. In addition, there is a high positive correlation observed between the SCA and P_t, and a negative correlation with the T_a. The NW Himalayan region reported a substantial rise in air temperature by about 1.6°C during the last century (1901–2001) and winter warming at a faster rate (Bhutiyani et al. 2007). IPCC (2013) have reported that the mean annual T_a of the Northern Hemisphere during 1983–2012 was considered as the warmest 30-year period of the last 1400 years, and the results of this study agree. Investigation at similar latitudes with longer records of P_t (Rizwan et al. 2019) and T_a trend (Bhutiyani et al. 2010) was observed. Additionally, results showed a significantly negative correlation of T_a with the SCA. SWN directly affects the melt recharge and evaporation, which influences the forest cover and hydrological system (Seyednasrollah and Kumar 2014). Overall, our findings suggest that the SCA over the basin is highly variable and is influenced by climatic variables as well as energy fluxes. Future research on the Chenab basin may focus on the effect of changing SCA on snowmelt and streamflow efficiency and timing. This information could be helpful for informing water resource management if the SCA and SCD decrease.

2.9. CONCLUSIONS

The spatial characteristics and temporal dynamics of snow cover distribution were examined on the daily MODIS snow cover products (MOD10A1 and MYD10A1, version 6) in the Chenab basin for the period 2001–2017 to understand the present state of the snow-cover regime. The period of the dataset is relatively short for the robust conclusion related to the long-term SCA changes and their behavior. Nevertheless, the data provide insight into the shortcoming changes in the SCA and assist in the continuous monitoring of hydrological processes. Results showed that the obtained cloud-free SCA observed ~92.8 ± 1.6%, with a kappa coefficient of 0.85 over the study period using the indirect method (Gafurov and Bárdossy 2009). Additionally, the direct comparison between Landsat and MODIS SCA showed an overestimation (9.3%). However, a higher correlation (R = 0.99, $p < 0.001$) was observed with MODIS SCA under clear sky conditions. Moreover, the effectiveness of the methodology in each subsequent step indicates that the mean cloud cover percentages were removed by 33.9%, 20.4%, 13.4%, 8.3%, and ~0.0%, respectively, and the mean SCA increased about 16.2%, 21.3%, 25.1%, 28.5%, and 33.6% respectively.

Therefore, after a satisfactory assessment of methodology efficiency and its uncertainties, the daily cloud-free snow cover images were used for intra- annual and inter-annual variability of snow cover over the Chenab basin. Results demonstrated an increasing trend of SCA for the period 2001–2017 (at a rate of 0.25 % yr^{-1}), while the rate has been slightly decreasing since 2009 with statistically insignificant values. Furthermore, the SCD and nine other indexes were derived from the SDCs to evaluate the snow cover characterization, indicating that the SAP was shortened while the SMP was elongated by about one day per year. Moreover, the relationships between SCA and topographic parameters indicated that the overall SCA showed a decreasing trend from September to January and an increasing trend from April to August above 4000 m a.s.l. However, these trends were statistically insignificant. The maximum and minimum SCA for all months were experienced in the north for the high-altitude/latitude (4000 m.a.s.l. and above) and south in lower-altitude/latitude (1000–2000 m.a.s.l.), respectively. An insignificant decreasing trend was observed in the elevations of 4000–5000 m a.s.l. (–1.36 % yr^{-1}) and above 5000 m a.s.l. (–1.19 % yr^{-1}) during 2009–2017, compared to the 2001–2009 period. This indicates that the snow accumulation period has changed or is shifting in terms of the seasonal snow cover during the recent decade.

The linear relationship between SCA and climatic variables, as well as energy fluxes, were established to identify the possible influence of snow cover distribution and the onset of snowmelt. The analysis demonstrated that the P_t and SWN were increasing in the northeastern region of the basin; however, the T_a, and u shows a declining trend. In contrast, a decreasing trend of P_t and SWN were observed in the central part of the basin, whereas the increasing trend of T_a and u. Overall, the annual SCA shows a significant positive correlation ($p < 0.05$) with P_t and u, and a negative correlation ($p < 0.01$) with T_a and SWN over the basin. Furthermore, a sensitivity analysis was performed, suggesting that the SCA is more sensitive to T_a; however, is less susceptible to P_t during the melt season for the selected observational period.

It should be noted that 17 years of long-term MODIS information is not sufficient for statements about climate change. Most of the snow cover trends were statistically insignificant during the study period. Therefore, a longer time series of data would be needed to obtain a more definitive conclusion about the spatiotemporal patterns of snow cover and its relationship with climate change. Therefore, quantifying the effects of the climate variables on snow cover is an extraordinary challenge for further studies. Overall, it is concluded that the spatio-temporal characteristics of MODIS SCPs play an essential role in snow cover characterization. Our results

also highlight the potential importance of climatic variables on the snow cover distribution for a proper understanding of the hydrological system.

CHAPTER 3

ASSESSMENT OF SNOW COVER DYNAMICS AND ITS SENSITIVITY WITH HYDROMETEOROLOGICAL FACTORS IN THE KARAKORAM AND HIMALAYAN REGION

3.1. INTRODUCTION

Snow cover extent and its characterization over the Karakoram and Himalayan (KH) region play a significant role in managing water resources as well as understanding regional climate change (Gurung et al. 2011a). Changing SCA can affect river runoff and long-term seasonal freshwater supply (Mukherji et al. 2019). Therefore, the quantification of these changes is crucial to protect and restore the KH region by promoting the sustainable use of the ecosystem. Reliable estimation of snow cover is hindered in terms of data availability over the complex terrain of the KH region (Waqas and Athar 2019; Xue et al. 2019). Long-term snow cover observations are only available from a limited number of weather stations due to the harsh climatic conditions and high maintenance costs. Therefore, comprehensive knowledge of the spatio-temporal snow cover variability over the KH region can be achieved by using remote sensing data and applying advanced modeling techniques at a regional scale.

Over the past few decades, many researchers have examined the changing pattern of SCA from high to low spatial resolution satellite data (Landsat Multispectral Scanner System (MSS) and Thematic Mapper (TM), Linear Imaging Self-Scanning System (LISS) III, LISS IV, Advanced Wide Field Sensor (AWiFS) and Satellite Pour l'Observation de la Terre (SPOT) data) (Hall et al. 1995b; Negi et al. 2009; Kulkarni et al. 2011; Kumar and Kumar 2016). On the other hand, several studies revealed that the small swath, low temporal and spectral resolutions, and associated error in the estimation of snow cover limit the use of these sensors (Dankers and De Jong 2004; Kulkarni et al. 2006). Also, different studies have utilized daily to monthly MODIS (Moderate Resolution Imaging Spectroradiometer) snow products, which shows higher accuracy relative to the ground observation in different parts of the world (Hall and Riggs 2007; Liang et al. 2008; Jain et al. 2008; Xu et al. 2017; Chen et al. 2020). However, the utility of the MODIS data was affected by the presence of cloud blocks, which causes a significant discontinuity in long-term snow cover monitoring, especially in the winter and summer-monsoon seasons.

To resolve the cloud problem, numerous methodologies were developed for cloud removal over the MODIS snow cover products using spatio-temporal pattern and topographical information

(Parajka and Blöschl 2008; Wang et al. 2008; Gafurov and Bárdossy 2009; Gafurov et al. 2015; Li et al. 2017, 2019a). Some studies were also conducted based on multisensor combination approaches which utilize daily MODIS data with cloud transparency of passive microwave data, i.e., Advanced Microwave Scanning Radiometer-Earth Observing System (AMSR-E) (Gao et al. 2010; Huang et al. 2014). These methods displayed less accuracy in the dense forest cover areas (Hall et al. 1982; Foster et al. 1995). Therefore, in this study, we have utilized a composite methodology of five methods, i.e., MODIS Terra and Aqua combination, temporal filter, spatial nearest neighbor filter, regional snowline filter, and multiday backward replacement filter – for accurate measurement of daily snow cover variability over the KH region.

3.2. RESEARCH QUESTIONS

- **What are the snow cover characteristics in the KH region-** How is the snow cover distribution changed from monthly to seasonal and seasonal to annual for the selected period? Is any significant trend of SCA?
- **What are the contributing factors responsible for snow cover variability-** What are the forcing mechanism that causes perturbations in regional-scale snow cover signal? Can certain variables play a direct or indirect role in controlling the seasonal variability over the region?
- **What is the role of topography and climatic condition of a region play-** How important is the topographic and climatic information supporting the snow cover across the KH region? Does the change in topographic and climatic variables play a significant role in varying spatial patterns of snow cover?
- **What are the more dominant factors that influence the snow cover pattern of a region-** Are the climatic variables the main contributor or the energy fluxes on the selected region?

3.3. OBJECTIVES

- Implementation of cloud removal methodology and analyzing their accuracy over daily time series snow cover products using the satellite remote sensing data
- Analyzing the changing pattern of SCA and its trends at different spatial and temporal scales over the KH regions
- Assessing the snow cover characteristic calculation by SCD, and snow cover timing indices
- Establishing the relationships between SCA and hydrometeorological variables to understand the influencing variables on SCA over the study area

3.4. STUDY AREA

The KH region lies between 26.7 and 37.3°N and 72.4 and 95.5°E, in the Hindu-Kush Himalayan region. Primarily, it is recognized as the most significant frozen reservoir of freshwater in the form of perennial snow cover and glacier ice outside the Polar Regions. Consequently, the water availability in these regions substantially influences the upstream and downstream livelihood. The KH region includes 20,812 glaciers, which cover 37,824 km^2 area out of the total area of ~7,13,907 km^2 (Cogley 2011). This region comprises parts of India, Pakistan, Nepal, Bhutan, and China and contains many of the tallest mountain systems in the world.

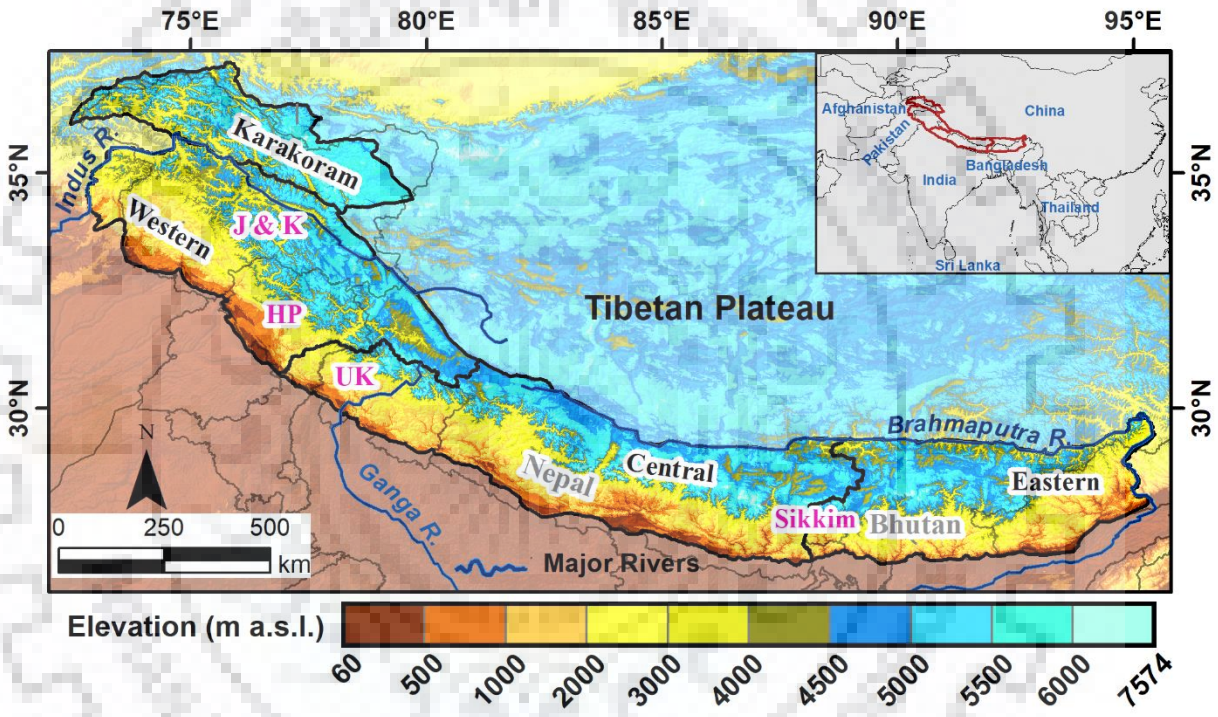

Figure 3.1. Location map of the Karakoram and Himalayan (KH) region showing major rivers and altitude variation using Global Digital Elevation Model (GDEM) of Shuttle Radar Topography Mission (SRTM) v 3.0 at 90-m grid resolution along the region. Abbreviations stand for Jammu & Kashmir (J&K), Himachal Pradesh (HP), and Uttarakhand (UK).

Based on the climate and geographic location, the region is divided into four parts, i.e., the Karakoram (KK), Western (WH), Central (CH), and Eastern Himalayas (EH), covering an area of 56,487, 2,10,389, 2,80,635, and 1,66,397 km^2 respectively previously expressed by Bolch et al. (2012) (Figure 3.1**)**. These regions are characterized based on their terrain properties and global atmospheric circulation pattern. Moreover, the areas are primarily nourished by two sources of precipitation, the Mid-Latitude Westerlies (MLW) and the Indian Summer Monsoon (ISM). The MLW precipitation greatly influences the KK and WH regions during the winter and

spring seasons, according to ~60–70% of the total precipitation annually (Shrestha et al. 2015). In comparison, the ISM has a higher impact on the EH and CH region during the summer. The monsoonal precipitation decreases while moving from the east (~1071 mm annual precipitation in the Brahmaputra basin) to the west (~423 mm in the Indus basin) in the Himalayan region (Immerzeel et al. 2010). Changes in these two precipitation regimes with respect to intensity and frequency cause serious concern regarding the water resources of the downstream region.

3.5. DATA USED

3.5.1. MODIS SNOW COVER PRODUCTS

This study utilizes the daily MODIS snow cover products of Terra (MOD10A1) and Aqua (MYD10A1) level-3 global version 6 (V6) over the KH region from 1 October 2000 to 30 September 2019 (19 hydrological years) (Riggs et al. 2016). The latest version of the MODIS products (V6) was used instead of the previous version 5 (V5). Zhang et al. (2019) found that V6 products have higher accuracy than V5. These snow products are freely available from the National Aeronautics and Space Administration (NASA) with 500-m grid resolution on the Earth data gateway customizable service (https://search.earthdata.nasa.gov)

Daily snow products are retrieved using the snow cover detection algorithm, beginning with the MOD10_L2 and MYD10L2 products in the MODIS snow product series (Riggs et al. 2016). The snow cover map of each product was reclassified into three new classes, i.e., 1 (i.e., snow cover conditions), 0 (i.e., snow-free conditions), and 2 (i.e., missing land information conditions). For snow, if the Normalized Difference Snow Index (NDSI) percentage value is greater than 40 and less than or equal to 100, then the land pixel is reclassified as "snow or 1." When the NDSI value is greater than or equal to 0 and less than or equal to 40 as well as inland water, the pixel value is treated as "no-snow or 0." The rest of the pixels were considered "cloud or 2." Here, we have used an NDSI value greater than 40%, as suggested for snow cover mapping (Riggs et al. 2017).

The KH region covers 14 MODIS tiles with numbers h22v05, h22v06, h23v05, h23v06, h24v05, h24v06, h25v05, h25v06, h26v05, h26v06, h27v05, h27v06, h28v05 and h28v06. This study utilized the Terra data from 1 October 2000 to 30 September 2019 and Aqua data from 4 July 2002 to 30 September 2019. A few images were found to be missing in both the products during the study period; therefore, the data gaps were replaced by their corresponding MODIS images (i.e., Terra images were replaced by Aqua or vice versa). We have assumed that the missing images of the non-Aqua period (in Terra) were replaced by 100% cloud-covered images. The spatio-temporal distribution of cloud cover in MODIS products was mapped (Figure 3.2),

illustrating a higher cloud cover percentage in Aqua as compared to Terra of the total geographical area. The cloud cover percentage varied from region to region; the minimum value was observed in CH, and the maximum value was observed in EH.

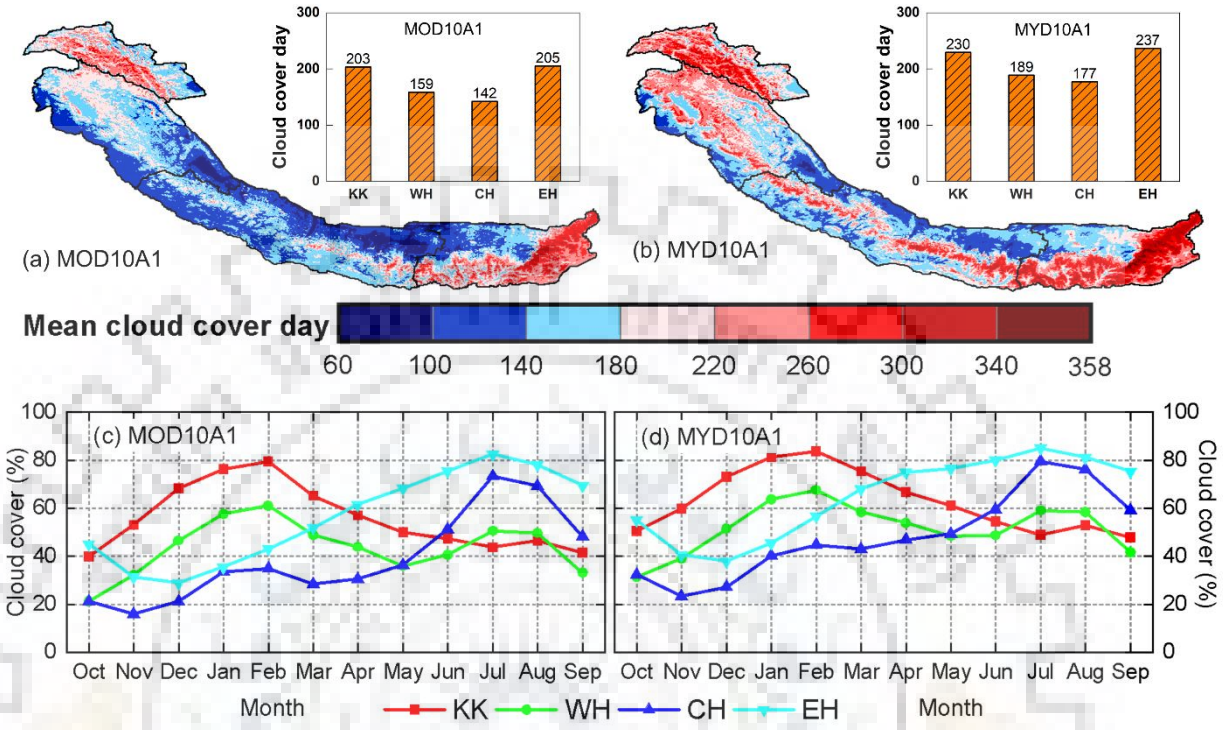

Figure 3.2. Comparison between spatial mean cloud cover day of (a) MOD10A1 (from 1 October 2000 to 30 September 2019) and (b) MYD10A1 (from 1 October 2002 to 30 September 2019) along with temporal mean monthly cloud cover percentage of the total geographical area of (c) MOD10A1 and (d) MYD10A1 products in different sub-regions of the Karakoram and Himalayas (KH). KK: Karakoram; WH: Western Himalayas; CH: Central Himalayas; EH: Eastern Himalayas.

3.5.2. LANDSAT 8-OLI DATA

To assess the reliability of the cloud-gap-filled MODIS snow product, we utilized the Landsat-8 Operational Land Imager (OLI) data between 2015 and 2016. Several researchers have already used the Landsat data to validate the MODIS dataset where the ground observations are rare (Hasson et al. 2014a; Tran et al. 2019). For this, 19 cloud-free images were selected with less than 5% cloud cover from the United States Geological Survey (USGS) EarthExplorer (http://earthexplorer.usgs.gov/) with a spatial and temporal resolution of 30 m and 16 days, respectively (Table 3.1).

Table 3.1. Description of the selected Landsat-8 OLI data for validating the cloud-filled MODIS SCA from 2015 to 2016 over the Karakoram and Himalayan (KH) region.

Region	Row	Path	Date
Karakoram (KK)	149	035	31/10/2015, 02/12/2015, 19/01/2016, 10/05/2016
Western Himalayas (WH)	147	038	01/10/2015, 04/12/2015, 22/02/2016, 26/04/2016, 12/05/2016, 03/10/2016, 19/10/2016
Central Himalayas (CH)	142	040	01/12/2015, 17/12/2015, 03/02/2016, 22/03/2016
Eastern Himalayas (EH)	139	041	28/12/2015, 14/02/2016, 17/03/2016, 21/10/2016

3.5.3. MODIS LAND SURFACE TEMPERATURE (LST) PRODUCTS

The standard monthly LST of MOD11C3 (Terra) and MYD11C3 (Aqua) products level-3 version 6 (V6) were utilized with a spatial resolution of 0.05° × 0.05° during 2000–2019 (19 hydrological years) for assessing the impact of surface temperature (T_S) on SCA variation. The data can be downloaded from https://search.earthdata.nasa.gov. The monthly LST values were retrieved from the average of four LST images (i.e., two images for Terra and two for Aqua, both day and night) of the corresponding month. Wan (2014) found that V6 LST products are much better than the previous V5.

3.5.4. NOAH LAND SURFACE MODEL (LSM) DATA

The NOAH LSM level-4 monthly version 2.1 is a NASA Global Land Data Assimilation System (GLDAS) (Rodell et al. 2004) data product available at a grid resolution of 0.25º × 0.25º from 2000 to the present. It provides a consistent view of surface energy and water balance at the surface level from the past several decades (Rui and Beaudoing 2018). It is forced with a combination of model and observation data (Beaudoing et al. 2020). In this study, data on monthly Relative Humidity (RH), wind speed (u), albedo, sensible heat (H_s), latent heat (H_l), ground heat flux (H_g), net shortwave radiation (SWN), and net longwave radiation (LWN) were acquired between October 2000 and September 2019 to identify the changing pattern of these variables over the KH region. Data were retrieved from https://search.earthdata.nasa.gov.

3.5.5. ERA-5 DATA

ERA5 is a fifth-generation European Centre for Medium-Range Weather Forecasts (ECMWF) re-analysis (ERA5) global climate and weather data, currently available from 1950 onwards and split into two separate periods in Climate Data Store entries, i.e., 1950–1978 and 1979 onwards

at a grid resolution of $0.25^{o} \times 0.25^{o}$ with an hourly and monthly time scale (ECMWF 2019). ERA5 shows many improvements over the ERA-Interim reanalysis (Hoffmann et al. 2019), and it is also better than the other reanalysis products, as demonstrated in a study carried out by Mahto and Mishra (2019) over India. In this study, long-term monthly total precipitation (P_t) and air temperature (T_a) were acquired to quantify the trend of these variables over the KH region in two separate hydrological periods, i.e., 1979–2019 and 2000–2019. The data can be downloaded from https://cds.climate.copernicus.eu/cdsapp#!/dataset/reanalysis-era5-pressure-levels-monthly-means?tab=form.

3.5.6. IN SITU OBSERVATION DATA

Daily climatic variables, i.e., air temperature (maximum and minimum) and snowfall, were used to analyze the relationships between MODIS snow cover and in situ data from 1 January 2013 to 31 December 2016. The data were obtained from the Snow and Avalanche Study Establishment (SASE), Chandigarh, India, Chandigarh, India, at Patsio observatory, located at 3800 m a.s.l. The site is characterized by a dry atmosphere with relatively low precipitation and cold temperature (Sharma and Ganju 2000).

3.5.7. TOPOGRAPHIC DATA

The Global Digital Elevation Model (GDEM) version 3.0 was acquired from the Shuttle Radar Topography Mission (SRTM) at 90-m spatial resolution (Jarvis et al. 2008) to assess the influence of topographical parameters (i.e., elevation, aspect, and slope) on SCA variation. The DEM was resampled at a 500-m resolution using the bilinear interpolation technique (Lopez-Burgos et al. 2013) to match the spatial resolution of MODIS products.

3.6. METHODOLOGY

3.6.1. COMPOSITE METHODOLOGY FOR CLOUD REMOVAL

A composite methodology for cloud-gap-filling in the MODIS snow cover products that incorporates methods with accuracy > 90%, was introduced and applied by numerous authors for cloud block removal (Gafurov and Bárdossy 2009; Parajka et al. 2010; Paudel and Andersen 2011; Hasson et al. 2014a; Wang et al. 2014; Jing et al. 2019; Tran et al. 2019). A five-step sequential non-spectral methodology was applied to mitigate the cloud gap in the MODIS snow products. The significance of using this composite methodology is that it includes all the necessary information about snow cover formation.

The first step includes merging twin satellite (Terra and Aqua) snow cover by assuming no snowfall or snowmelt occurred for a ~3-4 hours time difference at the Equator. Therefore, as long as a satellite captured (treated Terra as a base image) a pixel as snow or no-snow, then the cloud pixel will be replaced by the corresponding cloud-free pixel of the Aqua image. The equation is for this is as follows:

$$if\ \left(M^{T}_{(x,y,t)} = cloud\right) =$$

$$\begin{cases} if\ (M^{A}_{(x,y,t)} = snow\ or\ no-snow);\ then\ M^{CB}_{(x,y,t)} = snow\ or\ no-snow \\ if\ (M^{A}_{(x,y,t)} = cloud);\ \ then\ M^{CB}_{(x,y,t)} = M^{T}_{(x,y,t)} \end{cases} \quad \textbf{Eq. 3.1}$$

Where $M^{T}_{(x,y,t)}$ and $M^{A}_{(x,y,t)}$ are the Terra and Aqua images respectively; $M^{CB}_{(x,y,t)}$ is the combined product (Terra and Aqua) and (x, y, t) represents the spatial location (x, y) of the present (t) image.

In the second step, the present-day cloud pixel was assigned as snow (or no-snow), if the preceding and succeeding two days images were acquired as pixels of snow (or no-snow). The equation for the given method is as follows:

$$if\ \left(M^{CB}_{(x,y,t)} = cloud\right)$$

$$= \begin{cases} if\ (M^{CB}_{(x,y,t+1)}\ and\ M^{CB}_{(x,y,t-1)} = snow\ or\ no-snow);\ then\ M^{AD}_{(x,y,t)} = snow\ or\ no-snow \\ if\ (M^{CB}_{(x,y,t+1)} = snow\ or\ no-snow\ and\ M^{CB}_{(x,y,t-1)} = cloud);\ then\ M^{AD}_{(x,y,t)} = cloud \\ if\ (M^{CB}_{(x,y,t+1)} = cloud\ and\ M^{CB}_{(x,y,t-1)} = snow\ or\ no-snow);\ then\ M^{AD}_{(x,y,t)} = cloud \end{cases}$$

Eq. 3.2

Where $M^{CB}_{(x,y,t+1)}$ and $M^{CB}_{(x,y,t-1)}$ shows the first day forward and backward from the image, respectively and $M^{AD}_{(x,y,t)}$ is an adjacent temporal image. A similar logic was applied for t + 1 and t – 2 as well as t + 2 and t – 1 images.

The third step assigned the cloud grid as snow or no-snow based on the eight nearest neighboring pixels and their topographical information (altitude and aspect) of the surrounding pixel. For this, a 3 × 3 moving window of two sequential iteration processes was considered for spatial filtering. In the first iteration, the cloud pixel is assigned as snow when any of the surrounding eight neighboring pixels were captured as snow by satellite, and their elevation is less than the cloudy pixel with the same aspect. In contrast, if five out of eight cloud neighboring pixels are snow/no-snow and cloud elevation is higher/lower than the elevation of minimum/maximum adjacent

snow/no-snow pixel, then the cloud pixel is assigned as snow/no-snow in the second iteration. The final generated product of this step is defined as $M^{NN}_{(x,y,t)}$.

In the fourth method, the snowline/no-snowline threshold is utilized to classify the cloud pixel correctly. For this, the primary condition was that the present image must have at least 70% cloud-free pixels; otherwise, the method will be skipped. If the elevation of a cloud pixel was higher than the threshold, then the pixel was assigned as snow; otherwise, it was considered no-snow when it was below the threshold of the particular region. The final product of this step is denoted as $M^{SL}_{(x,y,t)}$.

In the last method, the remaining cloud grid pixel was eliminated by multiday backward replacement images. The primary assumption for this method was that there is no snowmelt or snowfall in the present-day image. The current-day cloud pixel was filled with the preceding day's cloud-free pixels, and this continued until all the clouds in the image were removed. When the ground pixel has continuous cloud persistence, the cloud grid was assigned as a cloud, which enhances the uncertainty of that particular pixel. The method is explained by the following equation:

$$If(M^{SL}_{(x,y,t)} = cloud) = \quad if\ (M^{SL}_{(x,y,t-K)} = snow\ or\ no-snow); then\ M^{F}_{(x,y,t)} = snow\ or\ no-snow \qquad \textbf{Eq. 3.3}$$

Where $M^{F}_{(x,y,t)}$ indicates the final product of the applied methodology. K is the multiday previous day image or iteration of the approach (K = 1, 2, 3…). Overall, the sequence and importance of the adopted methodology were explained by Dharpure et al. (2020) over the Chenab basin and validated with direct and indirect methods.

3.6.2. ACCURACY ASSESSMENT AND VALIDATION

The validation of the cloud-gap-filled methodology is commonly carried out using ground truth data; however, this region has limited continuous records and scarce measurement locations and covers a broad geographical area. Therefore, the composite methodology was validated with the high-resolution satellite data and measured climatic data (snowfall and temperature).

In the first method, 19 Landsat-8 images were utilized for area-based comparison with cloud-gap-filled MODIS images between 2015 and 2016. The Landsat obtained snow cover was classified into a binary map based on the information acquired from reflectance bands (band 3 and 6). A NDSI [(band3-band6)/(band3+band6)] threshold of > 40% and near-infrared

(reflectance band 5) > 11% were considered for generating the binary snow cover map. The overlap region in each dataset was extracted and compared based on the relative error ($MODIS_{SCA} - Landsat_{SCA}$) and Mean Absolute Difference (MAD) [$\sum abs(MODIS_{SCA} - Landsat_{SCA})/\text{number of images}$]. For the second approach, the *in situ* measured monthly snowfall and mean air temperature were used to relate the MODIS SCA percentage over the Patsio observatory (western Himalayas) from 1 January 2013 to 31 December 2016. For MODIS SCA estimation, a 5-km buffer zone was generated over the same location.

3.6.3. SNOW COVER INDICES

To understand the interannual variation, the SCD and nine other snow cover timing indices (derived from daily snow cover time series) were estimated during 2000–2019. The time series curve was extracted by plotting the daily SCA from 1 September to 31 August (Figure 3.3), which can be used to characterize snow cover, previously applied by Dariane et al. (2017). In the KH, 19 snow cover time series curves (for each hydrological year) were obtained with a five-day moving average for removing the short-term variation in SCA. A brief description of each index is given below:

- *Snow Accumulation Onset Day (SAOD) and Snow Melt Ending Day (SMED):* The SAOD is the day when the snow accumulation started, and SMED is the day when the pixel is no longer covered by snow. For this, we have estimated a 25th percentile value of daily SCA for each region, i.e., 36.9%, 9.4%, 5.4%, and 5.9% for the KK, WH, CH, and EH region, respectively, during the observational period. If the daily SCA is above the 25th percentile value and remains continuous for the period, that particular date is denoted as SAOD, whereas if the SCA falls below the 25th percentile value for the region, then the date is known as SMED. The changes in SAOD and SMED between years are mainly due to tvariation in precipitation, temperature, and solar radiation. The difference between SAOD and SMED is denoted as the accumulation-ablation period (AAP).
- *Maximum Snow Cover (MSC) and its Day (MSCD):* The maximum snow cover observed in each hydrological year is defined as MSC, and the day on which MSC occurred is denoted the MSCD. These indices are used to quantify the highest snow cover over the study area in a particular year.
- *Snow Accumulation Period (SAP) and Snow Melt Period (SMP):* SAP is a period between the day of snow accumulation onset and maximum snow cover, while the difference between the day of maximum snow cover and the melting end day is considered the SMP.

- *Snow Accumulation Slope (SAS) and Snow Melt Slope (SMS):* The rates of snow cover accumulation and melt are computed as MSC divided by the SAP and SMP during each hydrological year, respectively.

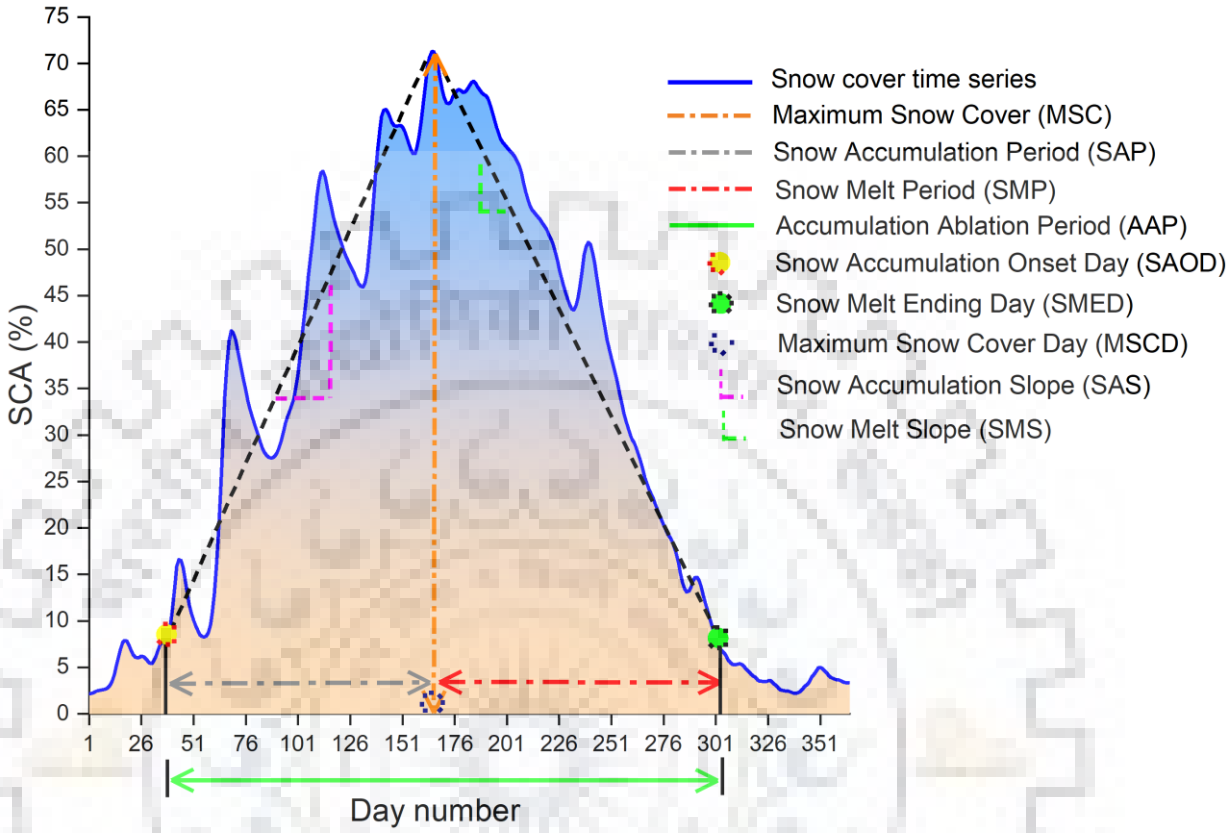

Figure 3.3. Pictorial representation of the snow cover time series and derived snow indices based on daily SCA in the western Himalayas (WH) from 1 September 2001 (Day 1) to 31 August 2002 (Day 366).

3.6.4. STATISTICAL ANALYSIS

The spatio-temporal trends were analyzed using the non-parametric Sen's slope (Sen 1968) and Mann-Kendall (MK) (Mann 1945) trend test for the SCD, snow cover-derived indices, climatic and energy fluxes over seasonal, semi-annual, and annual scales at a 95% confidence interval. Pearson's correlation coefficient (R) was also used to analyze the interrelationships of all variables. Additionally, the performance of estimated cloud-free MODIS SCA relative to Landsat-8 OLI was analyzed based on bias $[(MODIS_{SCA} - Landsat_{SCA}) \times 100/Landsat_{SCA}]$ and Root Mean Square Error (RMSE). The annual Relative Change Ratio (RCR in %) [(slope/mean) × number of years × 100] was estimated based on slope and mean SCA values during the study period (Baniya et al. 2018).

3.6.5. SENSITIVITY ANALYSIS

The sensitivity of SCA to climatic variables and energy fluxes was examined to determine the response of snow cover change with a potential indicator. The choices of these variables were based on the key properties of snowpack related to the snow cover onset timing and the amount of accumulated snow. To analyze the sensitivity of climatic variables (T_a and P_t) and energy fluxes (SWN, LWN, H_s, and H_l) on SCA, we first standardized $\left(\left[\frac{value-mean}{standard\ deviation}\right]\right)$ all the selected variables, and then generated a multivariant linear regression model over the sub-regions of KH.

3.7. RESULTS

3.7.1. VALIDATION OF CLOUD-GAP-FILLED MODIS SNOW PRODUCTS

To test the performance of the composite methodology, we used a two-step approach to validate the cloud-gap-filled SCA against high-resolution satellite data as well as meteorological data. In the first approach, 19 cloud-free Landsat-8 images were selected at different locations of the KH region and used to validate the area-based comparison between Landsat-8 and cloud-free MODIS SCA for the period 2015–2016. The results demonstrated that the MODIS SCA was highly correlated (R = 0.98, $p < 0.001$) with the Landsat-8 under the clear sky condition (Figure 3.4a). The MAD between these two datasets was ~5.5%, while the relative error varied from 0.9 to 20.8. However, MODIS SCA was overestimated compared to Landsat-8.

The second approach was carried out by establishing a relationship between cloud-free SCA and *in-situ* observations (snowfall and air temperature) from 1 January 2013 to 31 December 2016 (Figure 3.4b). The results demonstrate that the mean monthly SCA and snowfall were highly correlated (R = 0.84, $p < 0.001$). The *in situ* measured snowfall was maximum in February and minimum in August. This snowfall pattern may have been caused by the influence of westerlies in the Patsio location (WH), which receives higher snowfall in the winter months (December to April). On the other hand, the observed air temperature shows a significant negative correlation (R = –0.85, $p < 0.001$) with SCA. The lowest temperature was observed in January, while the highest was in July, followed by August over the Patsio location.

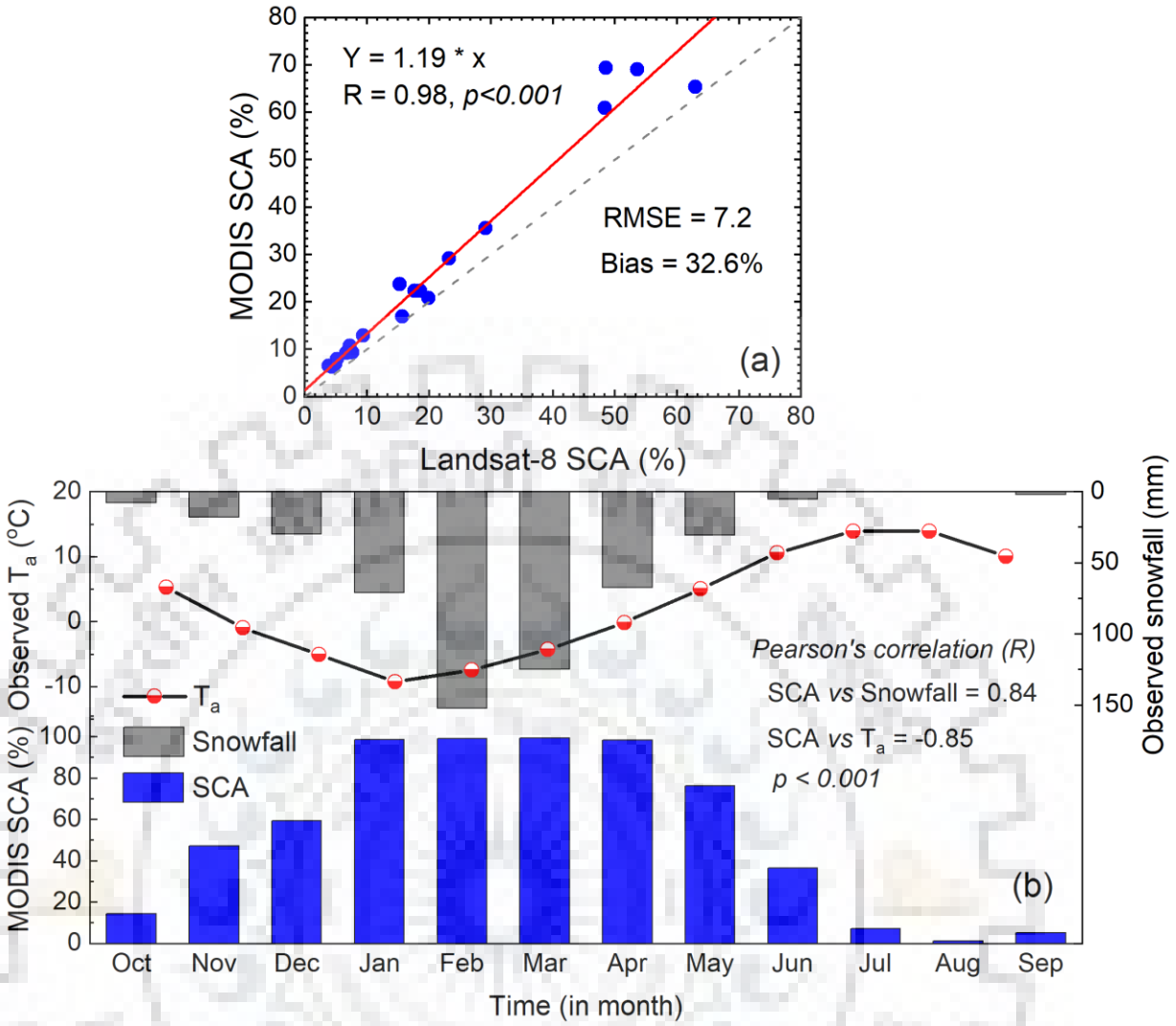

Figure 3.4. (a) Comparison between MODIS SCA and Landsat-8 snow cover and (b) relationship of mean monthly SCA with in situ snowfall and air temperature over the Patsio observatory, western Himalayas.

3.7.2. SNOW COVER VARIABILITY

The accuracy of the composite methodology for cloud-gap-filling was evaluated and suggested that the estimated SCA was well matched with satellite as well as meteorological data. After analyzing the performance of obtained results, we present the snow cover distribution at monthly, seasonal, and annual scales, derived from daily cloud-gap-filled SCA over the KH region from 1 October 2000 to 30 September 2019. The monthly snow cover distribution exhibited a large heterogeneity in temporal scale over the region (Figure 3.5), with higher SCA mainly concentrated in the KK and reduced SCA in the EH. The snow accumulation started from October onwards and reached its maximum in February for the KK, WH, and CH and in March for the EH region. The melting of snow starts from June onwards with the gradual rise in temperature,

and snow cover attained maximum ablation in August. The minimum SCA was observed in August for KK and WH and in July and June for the CH and EH region, respectively. Apart from this, the regions with the earliest snow accumulation onset eventually become the latest areas to melt off. Therefore, there is still scattered snow cover in July and August for the higher mountain areas, particularly the glacier accumulation region of the KH. The results also indicate that the variability of SCA was higher from October to December over the entire region and increased from KK to the EH region with a Coefficient of Variation (CV) varied from 13.3% to 55.6%, respectively.

The mean monthly SCA trend of the KK increased for all months except in December, May, August, and September during the observation period (Figure 3.5a). Similarly, the WH region showed an increasing monthly trend in SCA throughout the months except for December and January (Figure 3.5b), and the CH region experienced an increasing SCA trend in all months except September to November (Figure 3.5c). In the EH region, the mean monthly SCA shows a declining trend for all months, except for a slightly increasing trend from December to March (Figure 3.5d). Overall, the mean monthly SCA shows an increasing trend in the accumulation months (February and March) while decreasing in the ablation months (August and September) in all regions.

The mean annual SCA distribution over the sub-regions of KH was determined, indicating that the KK region shows maximum SCA in 2004/05 and a minimum in 2000/01 (Figure 3.5a). In contrast, the WH received maximum and minimum annual SCA in 2018/19 and 2000/01, respectively (Figure 3.5b). The CH attained maximum mean annual SCA in 2014/15 and minimum in 2015/16 (Figure 3.5c). In the EH region, the minimum and maximum SCA were observed at the start (2000/01) and end (2018/19), respectively (Figure 3.5d) of the observational period. Further, the overall mean annual SCA trend was increasing over the KK, WH, and CH with a rate of 0.05, 0.11, and 0.02 % yr^{-1}, respectively, whereas a decreasing trend (–0.06 % yr^{-1}) was observed in the EH region during the study period; however, none of these trends were significant at $p < 0.05$. Overall, the KK and WH regions follow a similar pattern for SCA over the observational period, whereas the distribution of SCA in the CH region was qualitatively similar to the pattern of the EH region.

To examine the heterogeneity in SCA, we divided the whole hydrological period into two parts, i.e., 2000–2008 and 2008–2018. The year 2018/19 was not considered because it was an exceptional year, according to Randhawa and Gautam (2019). The distribution of SCA and its trend over these two separate periods were evaluated and compared with the whole study period

(2000–2019) (Table 3.2). The mean annual SCA from 2000 to 2019 shows an almost identical increasing trend from 2000 to 2008, except in the EH region. However, a decreasing trend of SCA was observed since 2008/09 in all regions with a maximum in the WH, which is statistically significant at $p < 0.05$, and a minimum in the CH (not significant). Additionally, the RCR shows the highest change in the WH and lowest in the KK region during 2008–2018. The RCR of SCA in the WH was the opposite in 2008–2018 compared to 2000–2008.

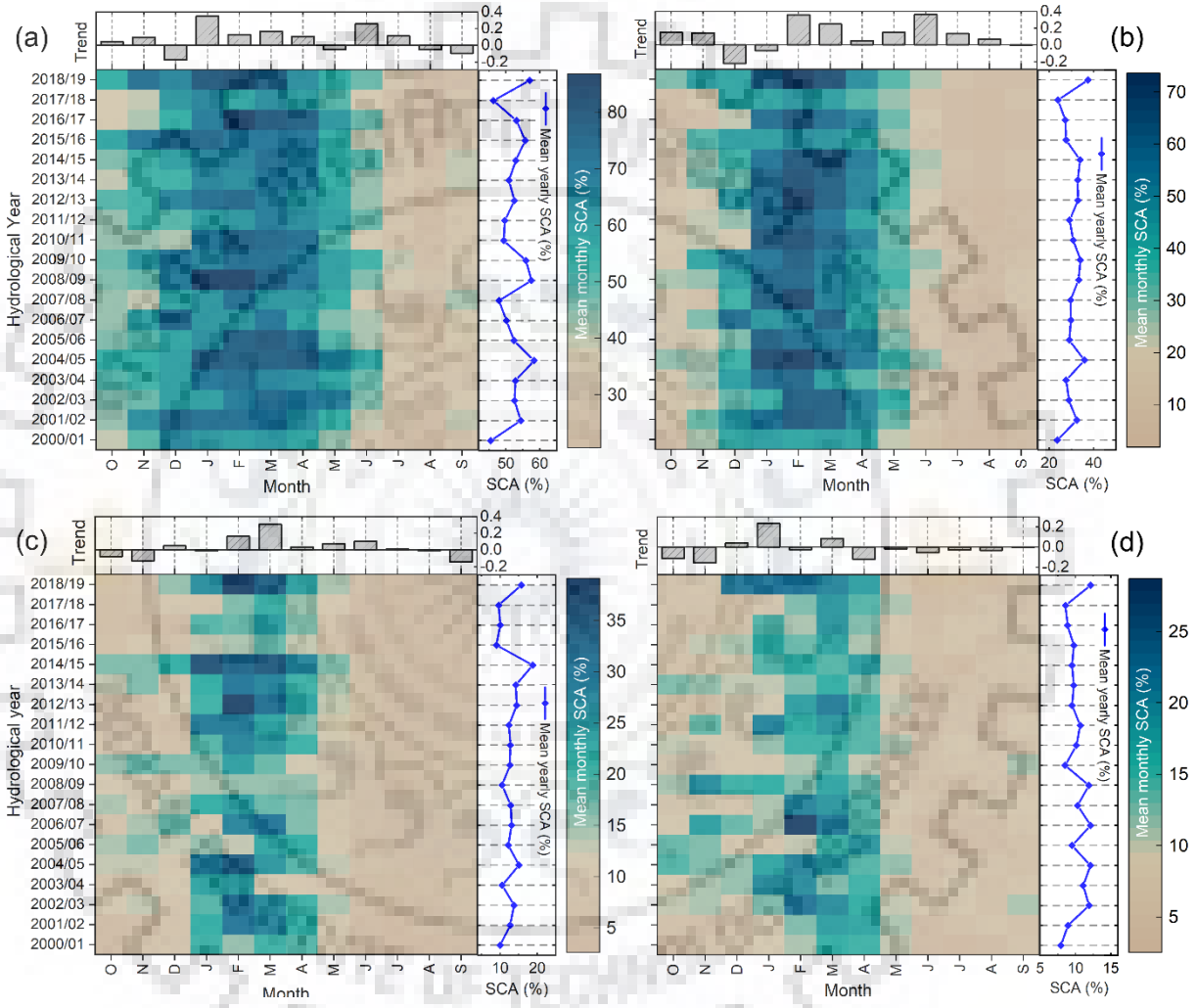

Figure 3.5. Time-series of monthly and yearly SCA in percentage over the a) Karakoram (KK), b) Western Himalayas (WH), c) Central Himalayas (CH), and d) Eastern Himalayas (EH). The bar graph illustrates the mean monthly SCA trends (non-significant at p < 0.05) for the period 2000–2019.

Pixel-wise mean monthly and annual SCD, and their standard deviation (SD), were derived for each hydrological year across the KH region (Figure 3.6). The mean and SD attain minimum and maximum values in June, July, and August (JJA) and December, January, and February (DJF), respectively. The mean monthly spatial distribution of SCD was evaluated over the KH region.

The SD in the interannual variation of SCD displays a heterogeneous pattern similar to the spatially distributed mean, with relatively larger values in the KK and WH. A positive trend of SCD was observed in the KK, WH, and some locations of the CH region, whereas a negative trend was found in the EH region. This increasing trend indicates that the SCD was widened over the observation period for the KK and WH. Our results demonstrate that most of the area has come under no-SCD change, which indicates that SCD neither widened nor shortened for that region.

Table 3.2. Mean annual SCA and non-parametric Sen's slope and Mann-Kendall (MK) trend test with Relative Change Ratio (RCR in %) of SCA in three different hydrological periods over the Karakoram and Himalayan (KH) region and its sub-regions. The bold values indicate a significance level at $p < 0.05$.

	Karakoram (KK)	**Western Himalayas (WH)**	**Central Himalayas (CH)**	**Eastern Himalayas (EH)**	**Karakoram-Himalayas (KH)**
			2000–2019		
Mean	52.4	30.5	12.6	10.2	26.4
Slope	0.05	0.11	0.02	–0.06	–0.00
RCR	1.63	7.16	3.64	–10.72	–0.18
			2000–2008		
Mean	52.4	30.0	12.3	10.6	26.3
Slope	0.11	0.68	0.04	0.33	0.21
RCR	1.93	20.37	3.07	27.79	7.23
			2008–2018		
Mean	52.4	30.6	12.4	9.7	26.3
Slope	–0.44	**-0.80**	–0.13	–0.24	**–0.42**
RCR	–8.37	–26.30	–10.84	–24.32	–16.06

SCD anomalies play a significant role in global-scale atmospheric circulation over seasonal to annual scales. Therefore, we calculated the inter-annual SCD anomalies for each hydrological year from 2000 to 2019, indicating a more positive value in 2018/19 and a negative value in 2017/18 (Figure 3.7). The upper reaches of the CH region experienced higher positive values (> 50 days) in 2014/15 and negative values in 2015/16. Moreover, the year-to-year SCD variation in the KK was almost positive or stable from 2000–2019 except for 2000/01, 2006/08, 2010/12,

and 2017/18. These positive anomalies in the KK suggest that the number of consecutive wet days increased over time.

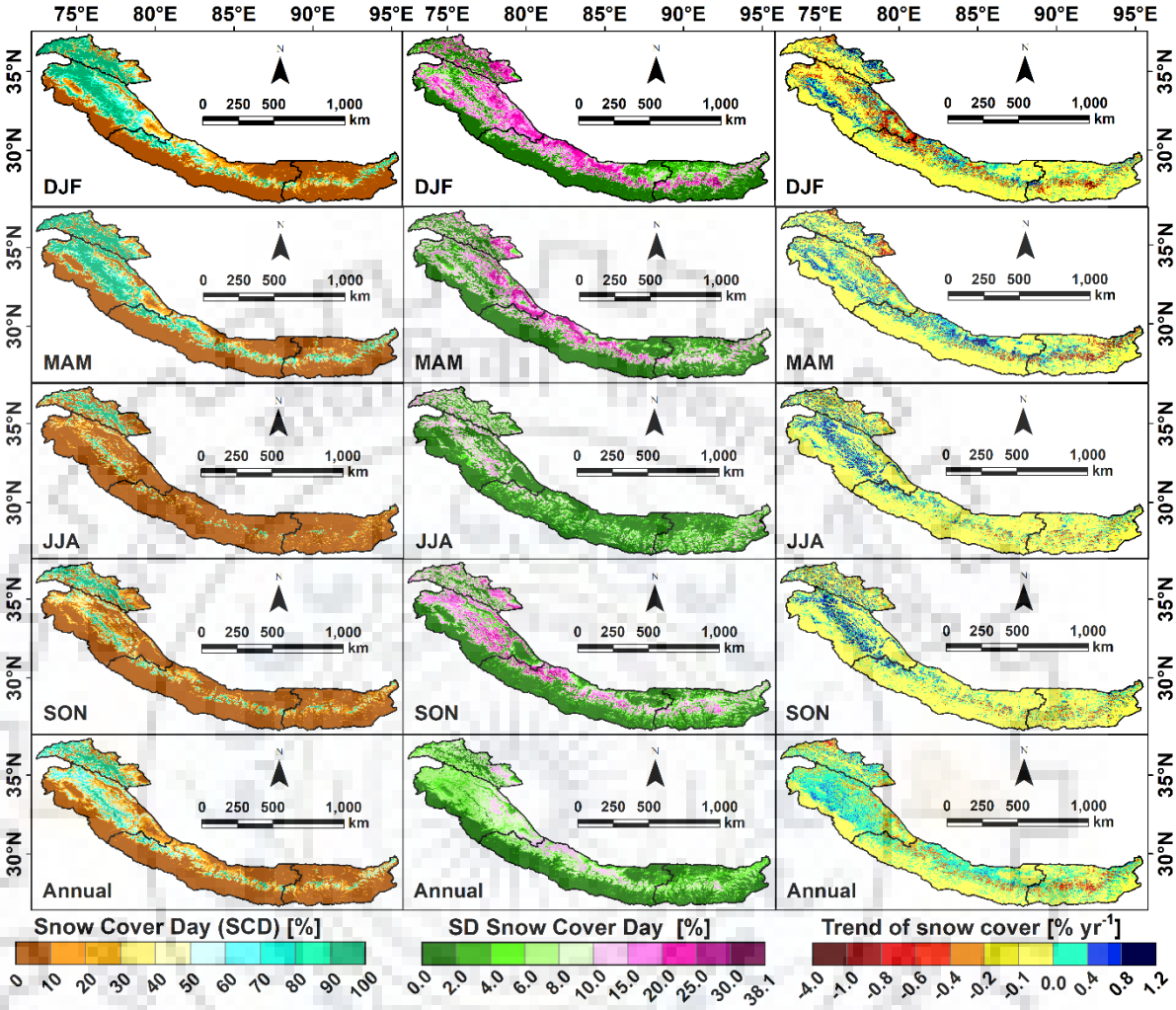

Figure 3.6. Mean seasonal and annual Snow Cover Day (SCD) (left), Standard Deviation (SD) (middle), and SCD trend (right) over the Karakoram and Himalayan (KH) region from 2000 to 2019 hydrological year.

3.7.3. SNOW COVER METRICS

In addition to SCD, the nine other snow cover timing indices were mapped in each hydrological year through a five-day moving average of daily SCA over the sub-regions of KH to comprehend the properties of snow accumulation and melt period (Table 3.3). The results highlighted that the SAOD was shifted later by about one day per year in each region, and the mean onset day was about 4, 6, 12, and 20 October for KK, WH, CH, and EH, respectively during 2000–2019. The MSC shows an increasing trend in all the regions except in the CH, and its mean value decreased from KK to the EH region. The MSCD shifted forward for the KK, WH, and EH at an average rate of one day per year. In comparison, the MSCD moved backward with an approximate trend

of two days per year in the CH. The SAS shows a positive trend over the KK and WH and a negative trend for the CH and EH. The SAP was narrowed for the KK, WH, and EH, while it widened for CH. Furthermore, the SMP increased for KK and WH while it was decreased for the CH and EH region. In contrast, the SMS was also decreased by an amount of -0.003 per year in the WH. The SMED shows a mean snowmelt season end one day prior in each year over the EH, while it was delayed by one day in the other regions. In contrast, the AAP was widened over the KK and WH and shortened for CH and EH.

Table 3.3. Sen's slope and the mean value of snow timing indices in the Karakoram and Himalayas (KH) sub regions during 2000–2019. All trend slopes are not significant at p < 0.05.

Region	**Karakoram**	**Western Himalayas**	**Central Himalayas**	**Easter Himalayas**
Indices		**Trend (Sen's slope)**		
SAOD	0.31	0.64	1.40	0.33
MSC	0.13	0.12	–0.06	0.30
MSCD	–0.32	–0.12	1.67	–0.64
SMED	0.58	0.88	0.80	–0.76
AAP	0.50	0.60	–0.65	–0.90
SAP	–0.63	–0.67	0.45	–0.62
SMP	0.87	1.00	–1.10	–0.25
SAS	0.005	0.005	–0.004	0.002
SMS	–0.011	–0.003	0.001	0.004
		Mean annual		
SAOD	34 (4 October)	36 (6 October)	42 (12 October)	50 (20 October)
MSC	81.6	69.2	35.6	26.6
MSCD	165 (12 February)	164 (11 February)	168 (15 February)	159 (6 February)
SMED	300 (27 June)	304 (1 July)	285 (12 June)	273 (31 May)
AAP	266	269	243	223
SAP	131	129	127	109
SMP	135	140	117	114
SAS	0.78	0.56	0.32	0.28
SMS	0.66	0.50	0.32	0.25

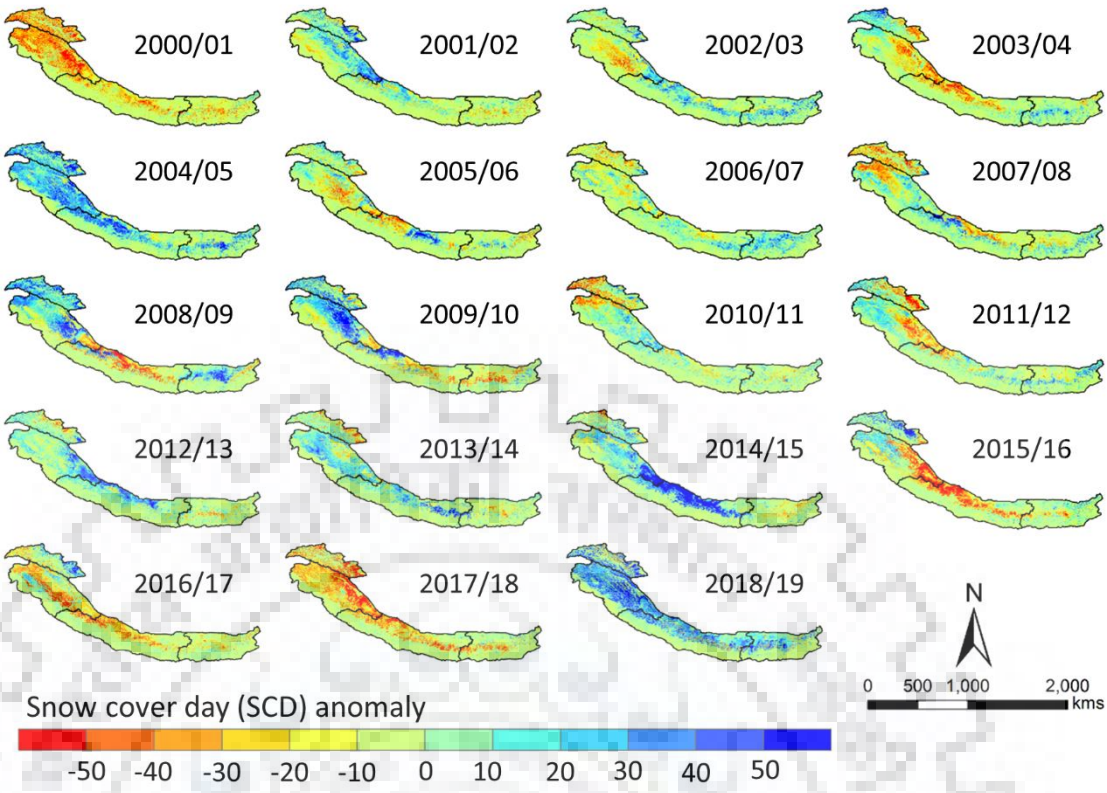

Figure 3.7. Spatial patterns of annual Snow Cover Day (SCD) anomalies during 2000–2019 over the Karakoram and Himalayas (KH) region were obtained by subtracting long-term annual SCD mean from individual hydrological year SCD.

3.7.4. INFLUENCE OF METEOROLOGICAL VARIABLES ON SCA

3.7.4.1. Contribution of climatic variables and energy fluxes

The climatic variables (T_a, T_S, RH, u, albedo, and P_t), as well as energy fluxes (SWN, LWN, H_s, H_l, H_g, and net energy (E_{net}) fluxes) were examined from 2000 to 2019 to determine whether the variables showed any evidence of changes related to snow cover. The mean monthly variation of climatic variables and energy fluxes were assessed over the study area. The climatic variables suggest that the T_a was directly proportional to the T_S and RH, while it was inversely proportional to u and albedo. Other than that, the KK region experienced the highest seasonal variation in energy fluxes and the EH region had the lowest variability throughout the months. The annual temporal and spatial (Figure 3.8) trends of climatic variables and energy fluxes were assessed during 2000–2019. The results show a significant increasing trend of T_a, T_S, P_t, and E_{net} while the other variables show a significantly decreasing trend at any particular location. The distribution of P_t implies an increasing trend on the windward side of the mountain, whereas it decreases on the leeward side of the mountain. Our results also indicate that the albedo and P_t

have a direct relationship with each other; when the albedo increases then P_t also increases, and vice versa. Similarly, a significant decreasing trend of u was observed over the selected region. Also, small pockets of SWN show an increasing trend; on the other hand, at the same location, the LWN was decreasing, which indicates that SWN and LWN have an inverse relationship with each other. Moreover, the E_{net} showed a positive trend in the eastern part of the KK region and a negative trend in the western region, which indicates less energy available for melt on the western side. The RH shows a decreasing trend in most CH and EH regions while increasing in the KK and some parts of CH. However, the higher SCA was mainly concentrated on the upper reaches (snow region) rather than in the lower reaches of KH, indicating the SWN, H_l, and H_g were significantly increasing in the snowy region, which can contribute to SCA change. It was also noted that the variation of P_t and LWN was higher (showing an increasing trend) in the no snow/little snow areas.

3.7.4.2. Relationships between SCA and climatic variables along with energy fluxes

Pearson's correlation test was applied to establish the statistical relationships between mean annual SCA and climatic variables (T_a, T_S, P_t, RH and u) as well as energy fluxes (albedo, SWN, LWN, R_N, H_l, H_S, H_g and E_{net}) over the KH region (Figure 3.9). The results demonstrate that the SCA shows a strong positive correlation with albedo and a negative correlation with T_a and T_S. Among the other climatic and heat flux variables, P_t and RH were positively correlated with SCA over all regions while T_a, T_S, SWN, R_N, H_S, and E_{net} show an inverse relation over the KK, WH, and CH regions. In the EH region, almost all the essential climatic variables and energy fluxes showed an insignificant correlation with each other (except for T_a). Moreover, in the EH region, the T_s was negatively correlated with P_t, RH, u, SWN, and LWN. Similarly, the albedo was negatively correlated with SWN, R_N, H_S, and E_{net} over the selected regions. On the other hand, the positive correlation of H_l with SCA was much stronger in the CH region. Overall, our results indicate that the decreasing pattern of SCA or the prolonged melting period significantly impacted the snow accumulation and decreased surface albedo, which can absorb higher solar radiation on the surface and vice versa. Therefore, the results suggest that the changing pattern of SCA is closely linked with these variables, while SCA characteristics varied from location to location.

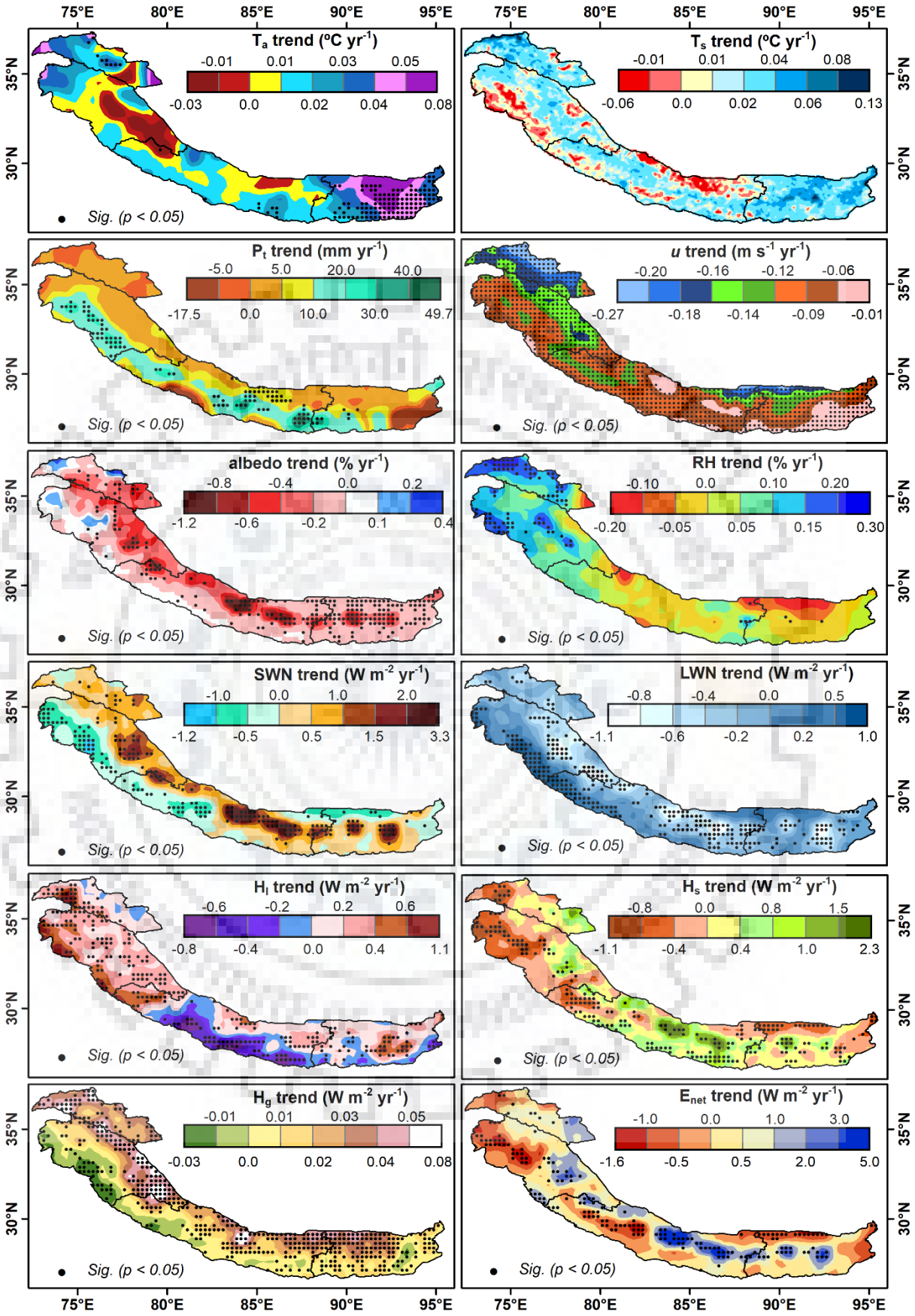

Figure 3.8. Spatial trend of climatic variables and energy fluxes over the Karakoram and

Himalayan (KH) region from 2000 to 2019. The trend indicates Sen's slope value, and black dots represent the significance level at $p < 0.05$.

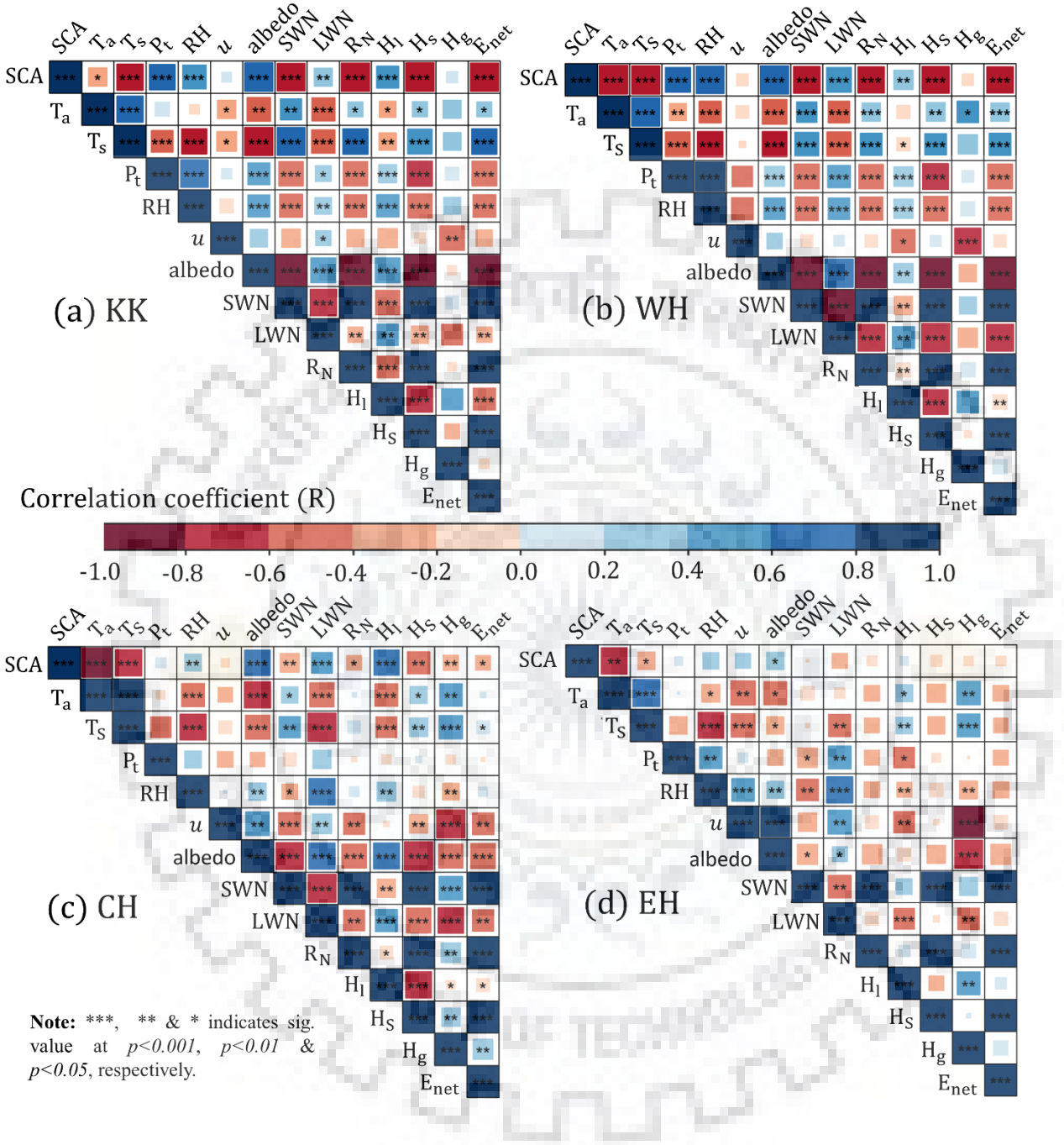

Figure 3.9. Relationships of SCA, climatic variables, and energy fluxes over the a) Karakoram (KK), b) Western Himalayas (WH), c) Central Himalayas (CH), and d) Eastern Himalayas (EH) for the period 2000–2019.

3.7.4.3. Long-term air temperature and precipitation variation (1979–2019)

To examine the long-term climatic variability and its trend over the region, we analyzed T_a and P_t during hydrological years 1979–2019. This long-term analysis will help to determine a relationship between the short-term and long-term responses of the forcing variables. The temporal trend analysis of these variables was performed using linear regression, demonstrating that the P_t slope indicates a declining trend in all regions except CH whereas T_a shows an increasing trend for the whole KH region. Apart from this, the spatial distributions of T_a and P_t and their trends were quantified using Sen's slope and the MK trend test over the region (Figure 3.10).

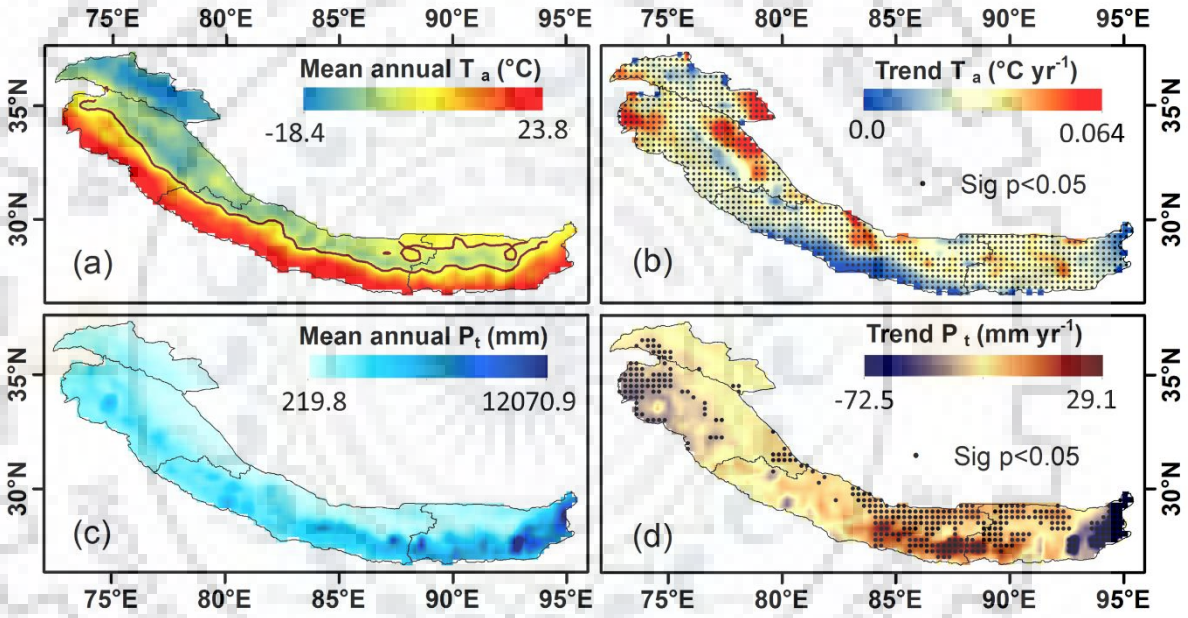

Figure 3.10. Spatio-temporal variation of mean yearly air temperature (T_a) and precipitation (P_t) with their trend (Sen's slope) and trend significance level (black dot) over the Karakoram and Himalayan (KH) region from 1979 to 2019 (Source: https://cds.climate.copernicus.eu/cdsapp#!/dataset/reanalysis-era5-pressure-levels-monthly-means?tab=form).

The mean annual T_a was highlighted by the 0ºC isotherm that separated temperatures above and below 0ºC (Figure 3.10a). The highest P_t was found on the eastern side of the KH region with an overall significant decreasing trend (Figure 3.10c). A hotspot region in the WH was identified that indicates a significant decreasing trend of P_t, whereas an increasing trend was found for T_a. The results also demonstrate that the trend of T_a was significantly increasing over the whole KH region with a higher positive value in the eastern KK and western and northern WH, and a slightly

lower positive value in the lower reaches of CH. Additionally, a small pocket of increasing P_t trend was found over the lower portion of the CH region with a slightly less positive trend in T_a. Overall, this variability of long-term T_a and P_t helps in understanding the homogeneity and heterogeneity of climatic variables on SCA.

3.7.5. SENSITIVITY ANALYSIS OF SCA

For the sensitivity analysis, the selected independent and dependent variables were standardized, and then multivariate linear regression models were generated at an annual time scale during 2000–2019 (Figure 3.11). Our results suggest that the T_a is a more significant climatic contributor than P_t to SCA change for each region except KK. In the radiation components, SWN shows the largest proportion of the variance against LWN except for the EH region. Similarly, the H_s showed higher sensitivity than H_l over KK and CH, whereas in the WH and EH regions, the sensitivity of H_l was higher relative to H_s. After analyzing the strength of all the variables, statistics suggest that the whole KH region experienced higher sensitivity towards SWN, with the maximum in the CH region and the minimum in the EH region.

3.8. DISCUSSION

The spatio-temporal variation of SCA in the KH region is essential to understanding the land-atmosphere interaction and its implications for local water availability. This region is considered one of the more climate-sensitive regions across the world that directly or indirectly influences the livelihoods of millions of people (Choudhury et al. 2021). The monitoring of SCA in the KH region is mainly hindered by the limited availability of continuous in situ records and by cloud obstruction in the optical remote sensing data. The in situ-based constraint was resolved by the use of MODIS snow cover products that provide data at a larger spatial and fine temporal scale. The presence of clouds in the snow cover products was also managed by implementing a five-step composite methodology. Several authors have previously developed and implemented this approach for cloud-gap-filling within the study region (Paudel and Andersen 2011; Hasson et al. 2014a) and its vicinity (Gafurov and Bárdossy 2009; Huang et al. 2017; Li et al. 2019b). Our results on cloud-gap-filling showed higher accuracy with high-resolution satellite data as well as in situ observation. In this Himalayan context, many authors have used satellite and field observations to assess the performance of the cloud removal approach (Jain et al. 2008; Chelamallu et al. 2014; Muhammad and Thapa 2020). In our study, the comparison of MODIS products with Landsat data shows overestimation, consistent with the findings of prior studies (Tang et al. 2012; Hasson et al. 2014b; Muhammad and Thapa 2020).

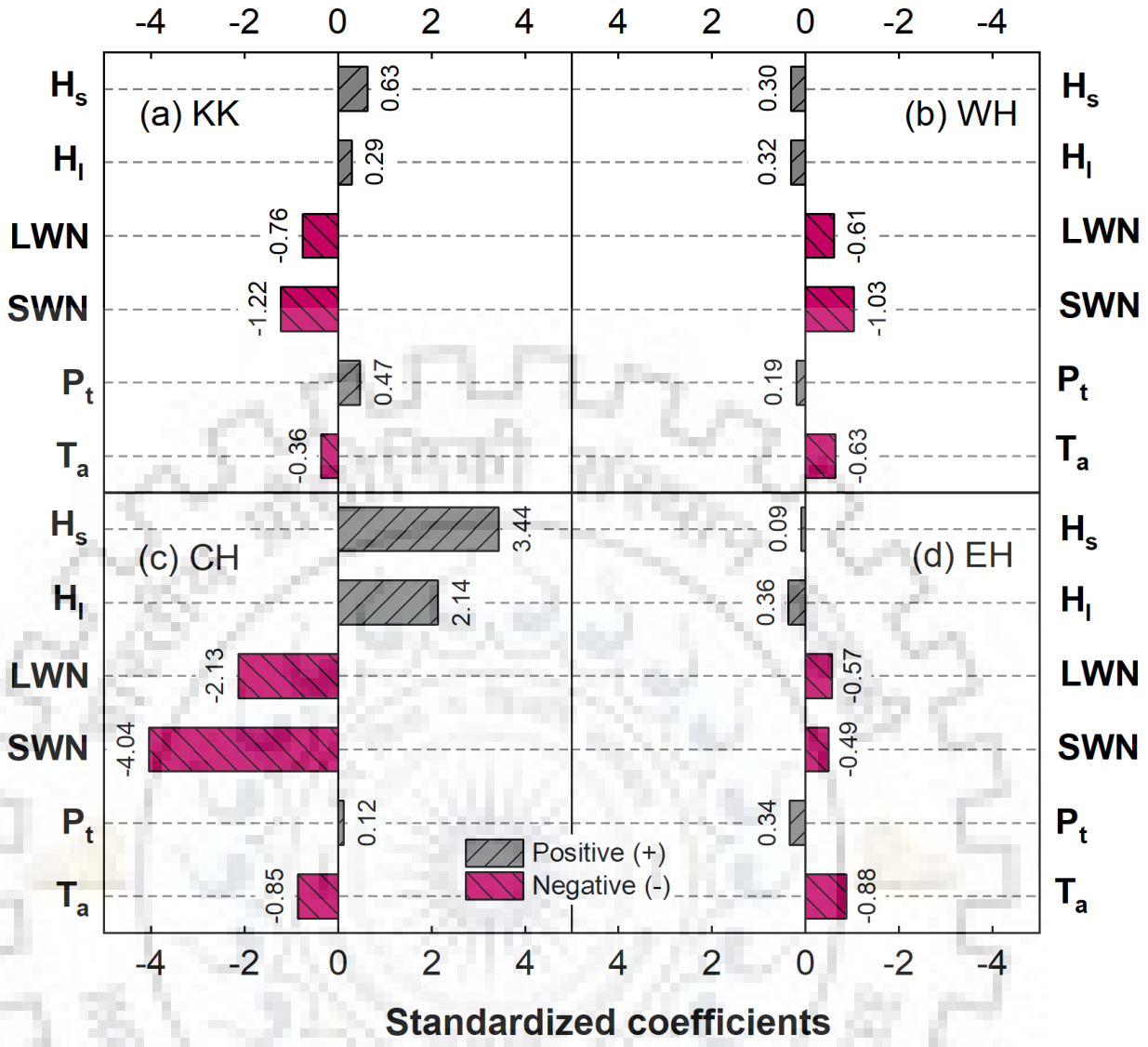

Figure 3.11. Sensitivity analysis of SCA in terms of climatic variables (T_a and P_t) and energy fluxes (SWN, LWN, H_l, and H_s) over the a) Karakoram (KK), b) Western Himalayas (WH), c) Central Himalayas (CH), and d) Eastern Himalayas (EH).

Several inherent uncertainties in MODIS snow cover retrieval mainly occurred due to the larger solar zenith angles, which reduce the accuracy of the snow cover products (Li et al. 2016). On the other hand, the band consideration in Terra (band 6) and Aqua (band 7) for the NDSI calculation show higher accuracy in Terra than Aqua (Hall and Riggs 2007). Therefore, in the first step, the combination of Terra and Aqua can contribute some uncertainties in the cloud-gap-filling. Additionally, uncertainties are linked with the absolute validation of cloud-gap-filling snow cover products that indicate ~ 90% accuracy under clear sky conditions (Klein and Barnett 2003; Hall and Riggs 2007). The correct estimation of snow cover under thick canopies is a major limitation of optical sensors (Simic et al. 2004). Still, this limitation was slightly reduced in the high mountainous region and glacier terrain. In these regions, the errors are likely to be highest

in the transitional period (accumulation and ablation). Therefore, we have considered all-terrain information for reducing uncertainties in the region and enhancing the accuracy of the methodology.

The mean annual SCA trend was increasing for the entire region (KK, WH, and CH) except for the EH, during 2000–2019. Many authors have worked on basin- or local-scale SCA estimation, which shows a similar increasing trend over the KK region (Hasson et al. 2014a; Singh et al. 2014; Tahir et al. 2016; Bilal et al. 2019; Choudhury et al. 2021). This increasing trend of SCA might be the reason for positive mass balance (MB) in the glaciers of the Karakoram region, as illustrated by numerous authors (Gardelle et al. 2012, 2013; Mukhopadhyay and Khan 2014; Mukhopadhyay et al. 2015; Negi et al. 2020). Additionally, Farinotti et al. (2020) revealed that the KK glaciers were experiencing positive mass gain, and their terminus was even advancing due to the surging of the glacier.

Similarly, several authors have investigated the increasing snow cover pattern over the WH region at different spatial scales, i.e., regional (Zhang 2015; Shresth Tayal 2017; Sood et al. 2020; Choudhury et al. 2021), basin (Kulkarni et al. 2010; Snehmani et al. 2016; Dharpure et al. 2020b) and local (Kour et al. 2016b; Shafiq et al. 2018). On the other hand, some studies at a finer scale have documented decreasing SCA in the CH region (Paudel and Andersen 2011; Singh et al. 2014), which is not consistent with our findings; this may be due to the difference in spatial scale. Also, a decreasing SCA trend was observed over the EH, which was previously monitored and explained by several authors (Singh et al. 2014; Barman and Bhattacharjya 2015; Basnett and Kulkarni 2019; Maurer et al. 2019).

Our findings for the KK region not only illustrate the higher SCA but also indicate that the snow accumulation onset was shifted one day later with an increasing snow melting period. This indicates that the amount of snowfall was higher than the rate of melting; therefore, the region depicted mass gain or nearly stable conditions. Farinotti et al. (2020) observed that the KK region experienced an increased snowfall in the accumulation zone with higher surface albedo and even a reduction in net energy available for the melt. Our findings for the WH region highlighted an increasing trend of snow accumulation onset time, whereas the snow melt period was enlarged during the study period. This may have occurred due to the higher snow melting rate under the influence of rising temperature in the WH region (Shekhar et al. 2010). In the CH and EH regions, the snow accumulation onset was shifted forward, whereas the snow accumulation period was positive for CH and negative for EH. In addition, the snow melting period was shortened for both CH and EH regions. Paudel and Andersen (2011) reported a peak snow period delayed by 6.7

days per year and peak snowfall over the Trans-Himalayan region of Nepal (CH) during 2000–2010. Panday et al. (2011) found that the late melt onset of the CH contributed to the shortening of the melt period in 2003 and 2005. They also demonstrated that the EH region in Nepal and Bhutan showed an earlier melt onset than the CH, WH, and KK regions.

Reliable quantification of forcing variables and their mechanisms is needed to understand the interaction of the atmosphere and microclimatic condition with changing SCA. Therefore, we used climatic variables and energy fluxes over the KH region. The climatic variables show that the precipitation followed an increasing trend over the whole region during 2000–2019, with the maximum slope in CH and the minimum in KK, whereas the temperature trend of the KH region was significantly increasing. Our findings are consistent with previous studies over the KH region (Gautam et al. 2013; Sabin et al. 2020). This increasing trend of precipitation causes a significant increase in wet days and an increase in wintertime precipitation which further results in increasing SCA. In contrast, the association of SCA with the radiative forcing variables illustrates that the SWN was the main contributor to the net energy available for melt. The higher SWN was observed in the CH, which is consistent with the findings of Amatya et al. (2015), whereas SWN was slightly lower in the KK region. Bonekamp et al. (2019) found that the melt in KK was controlled by the SWN while LWN dominates the energy balance in the Langtang region (CH). In terms of spatial variability, we found that the significant increasing trends of SWN, H_l, and H_g in the snowy region whereas P_t and LWN increased in the non-snowy region. This pattern was also noticed by some other authors (Amatya et al. 2015; Patel et al. 2021b).

By combining it with the published literature, our results suggest a broad picture of snow cover variability. These records of snow cover change indicate that the majority of the SCA trend was increasing over the KH and its sub-regions (except for the EH region). Also, SCA increased where precipitation increased in the coldest region (KK), whereas it decreased where precipitation decreased in the warmest region (EH). A more detailed investigation in future research will be needed in the KH region, focusing on basin-wide SCA characterization and its modeling for streamflow prediction. This study would be helpful not only for continuous SCA monitoring but also for establishing the relationship of SCA with the direct or indirect dependent variables.

3.9. CONCLUSIONS

This study examined the spatio-temporal snow cover variability using daily MODIS cloud-gap-filled SCA over the KH region during 2000–2019. The results revealed that the maximum SCA

was mainly concentrated on the KK region, while the minimum occurred in the EH region. The annual SCA trend was increasing for each region except for the EH during 2000–2019, but these trends were not significant at $p < 0.05$, whereas it showed a significant declining trend over the entire region and its sub-regions for the period 2008–2018. The mean monthly SCA increased in the accumulation months (February and March) and decreased in the ablation months (August and September) over the region. The results also highlighted that the snow accumulation onset and melt periods were shifted one day later for all regions except the EH. Due to the shrinking of SCA, the flow of rivers originating from the KH region is likely to be reduced during the summer season, which may affect the socio-economic condition at the higher altitudes in terms of vegetation cultivation, tourism, and apple farming.

In relation to this, the annual T_a and P_t trends were evaluated, which indicate an increasing trend of annual P_t during 2000–2019 with a maximum slope in the CH region and a minimum slope in the KK region. The annual T_a shows an increasing trend for the study period, with a higher rate in EH and a lower rate in WH. Our results also indicate that the temperature (T_a and T_s) and P_t from the selected climatic variables and SWN from radiative fluxes were mainly responsible for the changing pattern of SCA over the KH region. Overall, we conclude from this study that the SCA of the KH region is highly variable from location to location. Even the influence of climatic variables and energy fluxes related to SCA change may vary with the snowy or non-snowy region. Therefore, a reliable estimation of SCA and its relationship with these forcing variables will help in providing a better understanding of future water supply and its management in the upstream and downstream regions.

CHAPTER 4

MODELING OF GLACIER ENERGY AND MASS BUDGET OF THE PHUCHE GLACIER, COLD-ARID HIMALAYAN REGION, LADAKH RANGE, INDIA

4.1. INTRODUCTION

Glaciers are retreating in most of the world's mountainous regions and higher latitudes due to global climatic fluctuation (Marzeion et al. 2015; Ebrahimi and Marshall 2016). In response, the reshaping of the freshwater stored glacier may occur, which influences the regional water supply (Radić and Hock 2011) and changes the timing of streamflow around the year (Dadic et al. 2008). On the other hand, the snow and glacier melt in the Himalayan region is a lifeline for the upstream and downstream population. Many studies have reported a mass loss (Banerjee 2017; Murtaza and Romshoo 2017; Bandyopadhyay et al. 2019) and a changing pattern of snow cover or snowfall (Ahmad et al. 2018; Basnett and Kulkarni 2019; Dharpure et al. 2020b) over the Himalayan region. The variation in snow and glacier extents causes a significant influence on the basin, mainly dependent upon meltwater originating from snow and glacier during the summer season.

However, the weather data from high elevations of the Himalayas and trans-Himalaya is seldom available. Given the scarcity of such data sets, the climatic forcing on glacier changes is often studied by extrapolating available low elevation climate data using elevation-dependent or standard relations. Besides, the complex topography of this high-mountain region ensures many topo-climatic zones with varying characteristics (Khan et al. 2017). A significant difference in near-surface temperature lapse rates in different climate regimes of the Himalayas with distinct seasonal variations was reported across the Himalayas (Heynen et al., 2016; Pratap et al., 2019). Therefore, a reliable estimation of glacier mass variation and their response to future climatic change over the Himalayan region is required, which causes a significant impact on regional water availability and also help in understanding the physical processes of the glacier and climate variability (Oerlemans et al. 1998; Oerlemans and Klok 2002).

Earlier, the comprehensive Surface Energy Balance (SEB) was used to quantify the glacier-climate interaction (Hoinkes 1954); though, this method was substantially improved afterward. Then, the improved SEB method was applied by various researchers worldwide (Ayad Ali Faris Beg et al., 2016; Pellicciotti et al., 2005). Previously, many studies were conducted on the glacier

SEB in high mountain Asia (Acharya and Kayastha, 2018; Patel et al., 2021). Glacier SEB studies in the Ladakh range, the Karakoram region, and the eastern Himalayas are unavailable. On the other hand, a study conducted by Wani et al. (2021) over the upper Ganglass catchment uses the meteorological observation collected through Automatic Weather Station (AWS) installed at a lower elevation (4727 m a.s.l.) to quantify the point-based SEB. However, extrapolating low altitude station data does not provide complete insight into the glaciers above the ~5300 m a.s.l. (Schmidt and Nüsser 2017).

Therefore, we analyzed the SEB of Phuche glacier, upper Ganglass basin, Ladakh range to estimate the glacier surface mass balance. The study includes the meteorological observation recorded at 5600 m a.s.l. to substitute the lack of physical-based energy balance measurement over this range. This study also bridges the gap of mass balance study and their interaction with climatic response over the cold and arid region of the Himalayas. The monthly, annual, and seasonal variations of SEB components at point location were analyzed to understand the distribution of each component, their characteristics, and their controlling processes in glacier mass balance estimation.

4.2. RESEARCH QUESTIONS

- **What are the radiative and energy fluxes of the cold-arid region glacier that vary-** How are the radiation and turbulent heat fluxes changed at different temporal scales? Are any significant changes in the fluxes noticed for the selected region?
- **How does the glacier mass balance vary at point-based energy balance measurement-** What are the forcing mechanism that causes perturbations in glacier surface melting and mass balance? Can certain energy balance variables play a direct or indirect role in controlling the seasonal glacier melting of the study region?
- **How are the glacier energy and mass balance variation of the studied glacier related to other glaciers across the catchment?** Is any relation found in the mass variation of cold-arid region glaciers? What is the implication of higher glaciers melting over the region?

4.3. OBJECTIVES

- Analyzing the meteorological observation at 5600 m a.s.l. using physical-based energy balance measurement

- Investigating a long-term field measured Surface Energy Balance components at monthly, annual and seasonal scale
- Assessing the glacier surface melting and mass balance to understand the controlling processes in glacier mass variation

4.4. STUDY AREA

The study site lies in the Ladakh range of the trans-Himalaya at 5600 m a.s.l. elevation (34° 16' 39.40"N, 77° 33' 35.34"E) in the north of the Leh city, Union Territory of Ladakh, India (Figure 4.1).

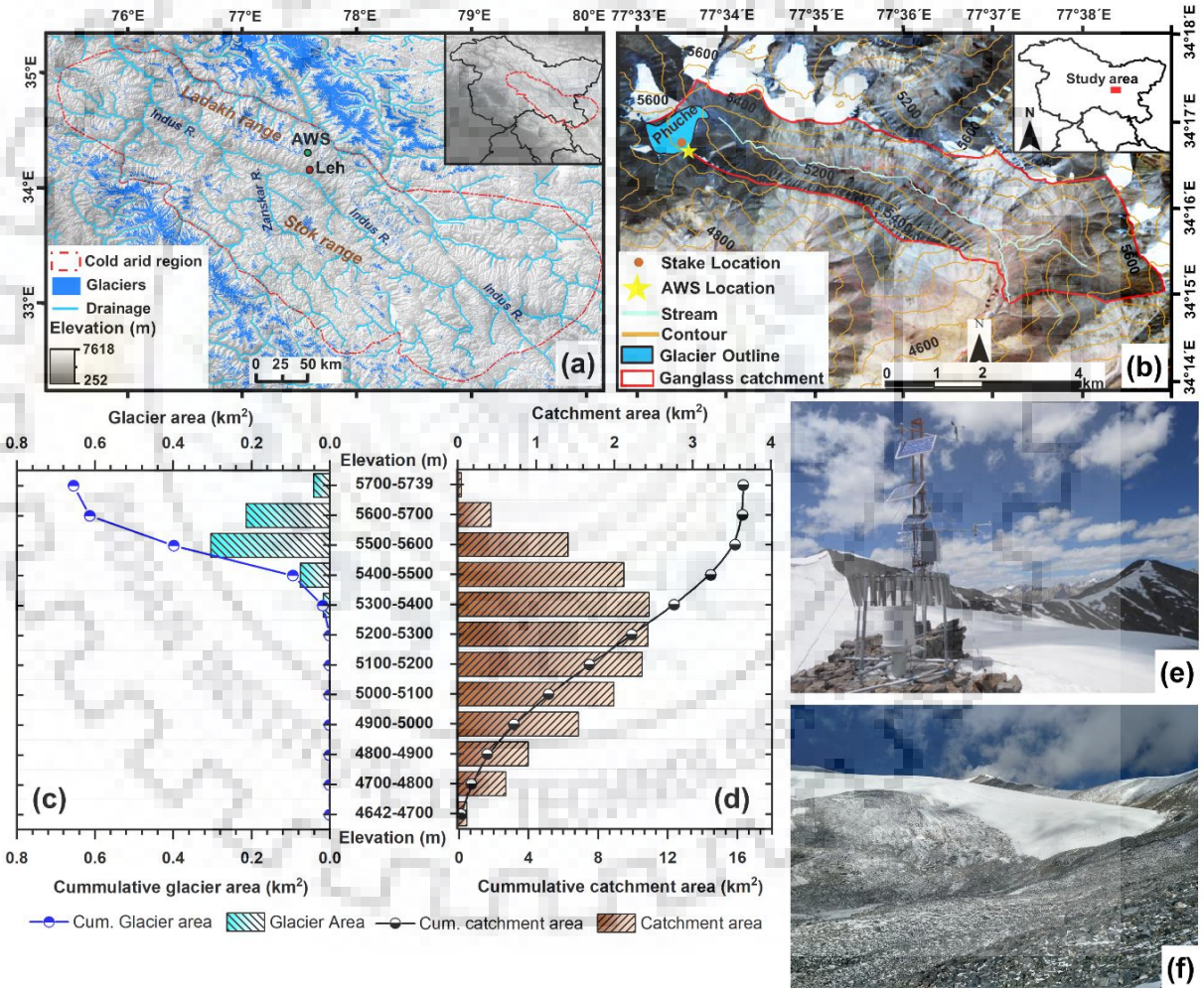

Figure 4.1. Location map of the (a) cold-arid region with glacier boundaries, different ranges, and AWS location and (b) upper Ganglass catchment with the Phuche glacier, AWS, and stake location overlay on a composite satellite image (Source: Landsat-8). (c-d) represent

hypsometry distribution of Phuche glacier and upper Ganglass catchment and (e-f) indicate the AWS location and glacier terminus field photographs.

This region is less influenced by the Indian Summer Monsoon (ISM) precipitation due to the higher ranges of the Himalayas (Wani et al. 2020). 79% of the glaciers located in the Ladakh range are < 0.75 km^2, and approximately 4% of the glacier have > 2 km^2 which mainly occupy the high elevation region above 5300 m a.s.l (Schmidt and Nüsser 2017). Glaciers in the region are experiencing mass loss, and individual glacier cover area has reduced by 17–22% since 1969 (Schmidt and Nüsser 2017). This region's aridity index and temperature range classify the trans-Himalaya as a cold-arid desert.

The cold-arid region of Ladakh experiences a comparatively higher temperature lapse rate ranging from 8 to 10 °C km^{-1} during summer months (AMJJA) as compared to the monsoon-dominated region (3.5 – 5.5 °C km^{-1}), espousing the regional differences in the meteorological forcing on the high elevation cryospheric systems (Thayyen et al. 2013). The region is characterized by strong land-atmosphere interactions, a rarefied atmosphere, and intense incoming solar radiation (Wani et al. 2020). This cold-arid region covers a significant portion of the upper Indus River basin with large snow and glacier extent in the Suru, Zanskar, and Shyok river basins. It contains steep mountain slopes and valley bottom, which were filled with glacio-fluvial deposits (Jowhar 2001; Wani et al. 2020).

The AWS site is located 35 km in north away from Leh city. The base camp to reach this site is established at South Pullu, (4700 m a.s.l.), 25 km from Leh town en route to Khardung-La (Pass). The study site lies within the snow cover area and close to the high elevation margins of the Phuche glacier. The Phuche glacier is a small cirque-type glacier that is 1.3 km long and covers an area of 0.58 km^2. The elevation of the Phuche glacier ranges from 5400 to 5745 m a.s.l. The drastic mass loss of smaller glaciers may create a warm hotspot that can imbalance the ecosystem and affect this region's water supply. The meltwater of this glacier is a part of the headwater zone of Leh stream, which is the primary water source for the Ganglass village and Leh city downstream. These headwater zones are also considered the recharging zone of the groundwater in the Ganglass catchment.

4.5. DATA AND METHODS

4.5.1. METEOROLOGICAL DATA COLLECTION AT 5600 m a.s.l.

A Campbell Scientific CR1000 AWS has been installed at a high altitude (5600 m a.s.l. on the ridge of Phuche glacier) of the cold-arid region in the Ladakh range for weather monitoring. The station is equipped with sensors that record data on a half-hourly interval, including global radiation (Incoming-shortwave (SWI) and outgoing-shortwave radiation (SWO)), albedo (α), net radiation (R_n), air temperature (T_a), barometric pressure (P_{atm}), Relative Humidity (RH), wind speed (u), and direction (WD) from 1 October 2012 to 30 September 2017 (five hydrological years). Detailed descriptions of installed sensors and their specification are listed in Table 4.1. The measurement error in AWS collected data was removed before analyzing the components, if any is available. These errors are associated with the ill-functioning of the sensor and vary with the sensor accordingly. Then, the corrected variables were analyzed on an hourly, daily, and monthly basis.

Table 4.1. Measurement specification of AWS installed near Phuche glacier at 5600 m a.s.l.

Meteorological data	Symbol (unit)	Make	Initial height (m)	Stated accuracy
Air temperature	T_a(°C)	Rotronics-5600-0316-1	2.0	±0.2 ℃
Relative humidity	RH(%)	Rotronics-5600-0316-1	2.0	±1.5 %
Wind speed	u (ms^{-1})	RM Young 05103-45	5 + base*	±0.3 ms^{-1}
Wind direction	WD (°)	RM Young 05103-45	5 + base*	±0.3 °
Solar radiation	R_n(Wm^{-2})	Kipp & Zonen (NRLite)	2.5	
Shortwave/albedo	SWI, SWO (Wm^{-2})	Kipp & Zonen (CMP6)	2.5	
Atmospheric pressure	P_{atm}(hpa)			±0.3 hpa
Precipitation Gauge		Geonor		
Data platform		Campbell CR1000		

*Base height = 1.5m

For winter precipitation, we attempted to measure the precipitation using the Geonor precipitation gauge; however, it failed to achieve good results due to technical snags and harsh weather conditions. Therefore, we have utilized the empirical relationship of snow thickness and density to calculate the accumulated snow water equivalent. These components were measured through a field survey carried out in May. Snow thickness was monitored using the network of

snow-stakes installed over the glacier, and their snow density was estimated by digging the snow pit near the AWS site.

4.5.2. DATA PROCESSING

After eliminating the measurement error, the abrupt spike in the AWS dataset was removed, and then it was filled with linear interpolation. The half-hourly shortwave radiation (SWI, SWO) measured using Kipp & Zonen (CMP6) was carefully processed. The computed R_n and total energy was dominated by the change in shortwave radiation. For this, we have considered a cut-off of 5 W m^{-2} for night-time data of incoming and outgoing solar radiation, which is set to be zero. The collected data indicate that the SWO sometimes shows a higher value than SWI during morning and evening. This occurs because the solar angle at that time was low due to the poor cosine response of the upward-looking sensor (SWI) (Nicholson, Prinz, Mölg, and Kaser, 2013). However, the SWO sensor mostly receives isotropic radiation; therefore, the SWO was relatively less sensitive than SWI towards uncertainties caused due to poor cosine response (van den Broeke et al. 2004). In this study, we have re-analyzed the SWI from raw SWO and with estimated accumulate albedo (α_{acc}), as given by Equation 4.1.

$$\alpha_{acc} = \frac{\sum_{24} SWO\ (raw)}{\sum_{24} SWI\ (raw)} \qquad \textbf{Eq. 4.1}$$

The reflected radiation (SWO) was sometimes higher compared to incoming radiation during the daytime. These higher values may have occurred because the incoming radiation sensor was covered with snow due to heavy snowfall. In this case, the incoming radiation was estimated through reflected radiation which is divided by considering the maximum realistic value of snow albedo (0.9) (Oerlemans and Klok, 2002, Favier et al. 2004). Figure 4.2a and Figure 4.2b show the raw data associated with error values and the corrected values of incoming and outgoing radiations, respectively.

The minimum, maximum, and mean temperature was recorded at a half-hourly interval, further used to generate daily, monthly, and annual temperature (minimum, maximum and mean). Similarly, the half-hourly recorded RH and u were converted into daily, monthly, and annual time scales. Positive Degree Day (PDD) and Freezing Degree Day (FDD) were calculated by measured hourly temperature. PDD and FDD were estimated by averaging the hourly positive and negative temperature by considering base temperature as zero, respectively, expressed by Equations 4.2 and 4.3:

$$PDD = \frac{\sum_{j=1}^{24} T_j}{24}, (T_j \geq 0) \quad \textbf{Eq. 4.2}$$

$$FDD = \frac{\sum_{j=1}^{24} T_j}{24}, (T_j < 0) \quad \textbf{Eq. 4.3}$$

Where T_j is the positive temperature in hour j

The specific humidity was estimated using the T_a and RH measurement as described in Equation 4.4:

$$Specific\ Humidity\ (g\ kg^{-1}) = 1000\ \left[0.622 \frac{e_a}{P_{atm}}\right] \quad \textbf{Eq. 4.4}$$

Where saturated vapor pressure $(e_s) = 6.112 \times exp^{\left(\frac{17.67 \times T_a}{243.5 + T_a}\right)}$ and $(e_a) = (e_s \times RH)/100$.

The surface temperature (T_s) is a significant variable to quantify the turbulent heat fluxes on the glacier surface. The half-hourly observation of solar radiation, T_a, RH and u were used for estimating the T_s, discussed by Fujita and Ageta (2000). The u was measured at 6.5 m height above the surface, it is required to convert at 2 m for energy fluxes caculation. This height (6.5 m) was converted at 2 m using the logarithmic wind profile function, explained by Bastiaanssen et al. (1998).

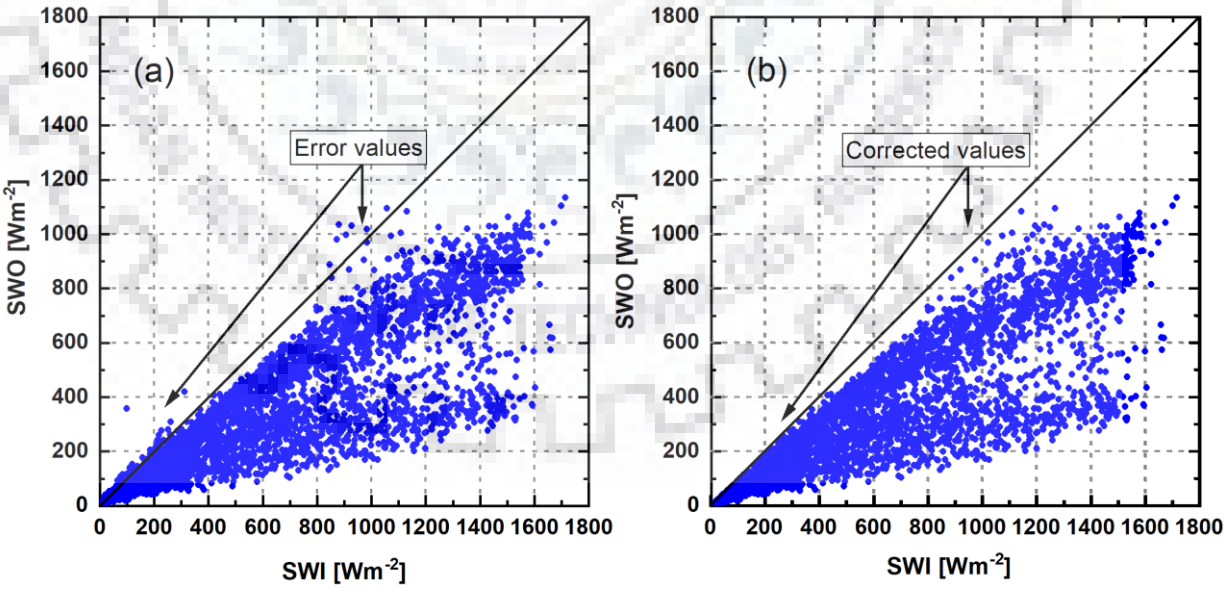

Figure 4.2. A scatter plot of half-hourly values of incoming versus outgoing solar radiation (a)raw data and (b) after error correction data.

4.5.3. SURFACE ENERGY BALANCE (SEB) MODELING

The modelling of SEB components was carried out by the calculation of energy fluxes directed towards the glacier surface that is considered to be positive, and when it goes upward from the surface, then it becomes negative. If we assume that if there is no significant horizontal energy transfer over a unit glacier volume and for a unit of time, then the SEB was calculated at the snow surface, can be expressed by (Equation 4.5) (Oke 1987):

$$F_s = R_n + H_s + H_l + H_g + P \qquad \textbf{Eq. 4.5}$$

Where R_n is the combination of net shortwave and net longwave radiations, H_s and H_l are the sensible and latent energy fluxes, respectively. H_g is the ground heat flux, and P is the supplied heat from precipitation, which is small enough to be neglected. F_s is the total energy available at the glacier surface. The radiation and energy fluxes were measured in W m^{-2}.

Measurement of energy fluxes at the glacier surface has been carried out daily during the summer season between May and September to understand the melting pattern around the selected year. H_s and H_l were carried out by the bulk aerodynamics methods (Oke 1987; Azam et al. 2014), calculated by Equations 4.6 and 4.7:

$$H_l = \rho_a \frac{L_s k^2 u(q-q_s)}{\left(ln\frac{z}{Z_{0m}}\right)\left(ln\frac{z}{Z_{0q}}\right)} (\emptyset_m \emptyset_v)^{-1} \qquad \textbf{Eq. 4.6}$$

$$H_s = \rho_a \frac{C_p k^2 u(T_a-T_s)}{\left(ln\frac{z}{Z_{0m}}\right)\left(ln\frac{z}{Z_{0T}}\right)} (\emptyset_m \emptyset_h)^{-1} \qquad \textbf{Eq. 4.7}$$

Where ρ_a is the air density (in $kg\ m^{-3}$) from the following equation ($\rho_a = \frac{P_{atm}}{R_a T_a}$, where R_a = specific gas constant (for dry air) and P_{atm} = Atmospheric pressure (in hPa) at AWS). L_s is the Latent heat of sublimation ($2.834 \times 10^6\ Jkg^{-1}$), z_{0T}, z_{0q}, and z_{0m} are the surface roughness parameters for temperature, humidity, and momentum, respectively. C_p denoted as specific heat capacity (for air at constant pressure) ($C_p = C_{pd}(1 + 0.84q)$ with $C_{pd} = 1005\ Jkg^{-1}K^{-1}$, the specific heat capacity (for dry air at constant pressure)). k is the von Korman constant (k = 0.4), q and q_s are the mean specific humidity of the air and surface, respectively, calculated based on Equation 4.4**.** The non-dimensional stability functions of momentum ($\emptyset_m$), heat ($\emptyset_h$) and moisture ($\emptyset_v$) is given by R_{ib}. Where R_{ib} is the bulk Richardson number that described the stability of the surface layer, that relates the effects of buoyancy to mechanical forces (Moore, 1983), expressed by Equation 4.8.

$$R_{ib} = \frac{g\,(T_a - T_s)(z - Z_{0m})^2}{T_a u^2 (z - Z_{oT})} \quad \textbf{Eq. 4.8}$$

Where g is the acceleration of gravity ($g = 9.8\, ms^{-2}$). Stability of the Surface Boundary Layer is measured by bulk Richardson number R_{ib}. Sometimes very high and low values of R_{ib} were observed. These high and low values gave rise to a huge fluctuation in H_s and H_l values. Therefore, the lower and upper limits were fixed by calibrating the R_{ib} to remove all the possible outliers (extreme and sudden high or low values of H_s and H_l) in the values, as explained in Equations 4.9 and 4.10. An agreement with $-0.40 < R_{ib} < 0.23$ was achieved and selected for final H_s and H_l calculations (Denby and Smeets, 2000, Favier et al., 2011).

$$if\ R_{ib} > 0\ (stable):\ (\emptyset_m \emptyset_h)^{-1} = (\emptyset_m \emptyset_v)^{-1} = (1 - 5R_{ib})^2 \quad \textbf{Eq. 4.9}$$

$$if\ R_{ib} < 0\ (unstable):\ (\emptyset_m \emptyset_h)^{-1} = (\emptyset_m \emptyset_v)^{-1} = (1 - 16R_{ib})^{0.75} \quad \textbf{Eq. 4.10}$$

4.5.4. CALCULATION OF TOTAL ABLATION (MELT)

An energy balance model based on the physical condition was applied to quantify the surface melt by assessing the radiation and energy fluxes that transfer to and from the glacier surface. When the surface temperature is equal to $0°C$ any surplus energy is assumed to transform the glacier surface layer into the melt. The sublimation/re-sublimation process is another way of glacier mass loss/gain. The melt occurs when the positive surface energy is available, whereas the negative sign indicates the loss of energy at the glacier surface (Hock 2005), as follows (Equation 4.11):

$$\text{Melt (m w. e.)} = \frac{F_s}{L_f \times \rho_w} \quad \textbf{Eq. 4.11}$$

Where ρ_w = $1000\, kgm^{-3}$ (water density) and L_f = latent heat of fusion/melt ($L_f = 3.34 \times 10^5 Jkg^{-1}$). F_s = total energy is available for glacier melt, and it occurs when the surface temperature is at 0°C. Sublimation is derived from the H_l when it is negative (energy going away from the surface), by Equation 4.12 as given below:

$$\text{Sublimation (m w. e.)} = \frac{H_l}{L_s \times \rho_w} \quad \textbf{Eq. 4.12}$$

Where L_s = latent heat of sublimation ($L_s = 2.834 \times 10^6 Jkg^{-1}$) and H_l is the latent heat. To estimate the total ablation, the estimated melt is added with the sublimation and subtracted with the re-sublimation of the study site.

4.6. RESULTS

4.6.1. METEOROLOGICAL VARIABLES

4.6.1.1. Air temperature

The minimum, maximum, and mean T_a were recorded from AWS to capture the seasonal and annual variations during the observational period (2012–2017). Results of mean daily temperature suggested that the prolonged sub-zero mean temperature was noted over the location, varied from September to May (Figure 4.3). During the observational period, the daily mean minimum and maximum T_a were measured as 14.2 and –29.8 °C, respectively, with a mean value of –7.8°C. The inter-annual daily temperature variation was higher in 2016/17 and lower value attained in 2014/15. This finding was consistent with the observation of Soheb et al. (2020) over the Stok Glacier, Ladakh range.

The positive mean temperature was mainly found in two months, i.e., July and August; however, November to April experienced lower temperatures (less than –10 °C) (Figure 4.4). A similar temperature pattern was observed by Soheb et al. (2020) over the Stok glacier and reported by Azam et al. (2014) for the Chhota Shigri glacier, western Himalayas. Our findings also highlighted January as the coldest month (–20.7° C), whereas July was the warmest month (2.4°C). The linear trend of mean monthly T_a was increasing for each month except March and June, while an overall increasing trend of mean annual temperature was observed during the observational period. A similar declining trend of temperature from June to September since 2006 onwards was demonstrated by Koul et al. (2016). This trend thereby results in slow glacier melting and permafrost growth in the upper reaches (Wani et al. 2021). On the other hand, the mean annual temperature was maximum in 2015/16 and minimum in 2012/13 (Figure 4.4). It was also found that the period from 2012 to 2015 experienced lower temperature from the mean, and it increased about 13.0% in 2015/16 followed by 8.1% in 2016/17 relative to the previous period. This increase in temperature was previously illustrated by several authors (Ren et al. 2017; Wester et al. 2019).

The seasonal and annual temperature information was incomplete without estimating PDD and FDD to understand the temperature forcing on the surface melt of the study area (Figure 4.5). Results demonstrated that the region experienced PDD for six months (May–October), with the maximum in July and August (JA). The combined PDD of JA varied from 157 to 225 °C with lower annual PDD in 2014/15 (176.7 °C) and higher in 2015/16 (375.2 °C).

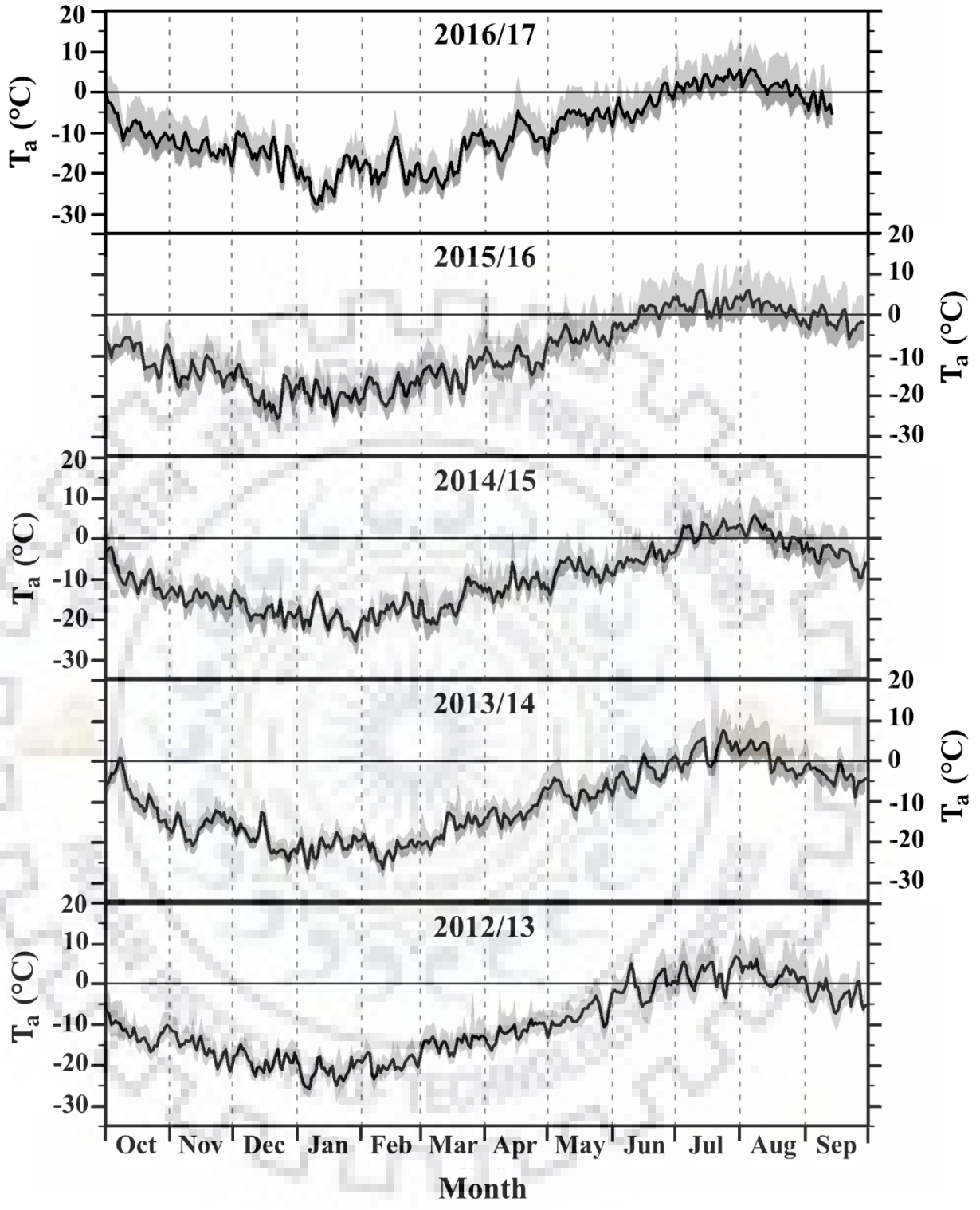

Figure 4.3. Dark black line indicates the daily variation of mean temperature, and the shaded gray color represents the diurnal range of temperature for five hydrological years from 2012 to 2017.

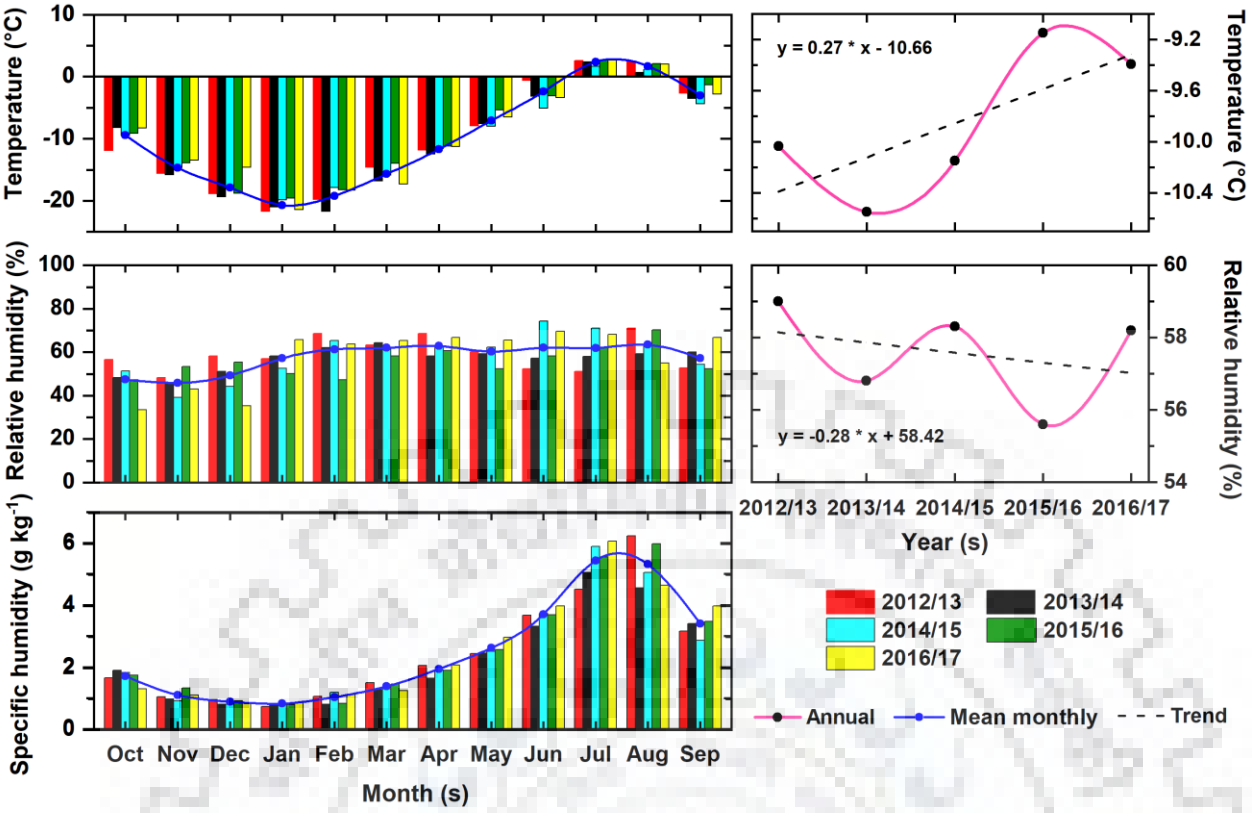

Figure 4.4. Mean monthly and annual distribution of air temperature (T_a), Relative Humidity (RH) and specific humidity for the study period (2012–2017)

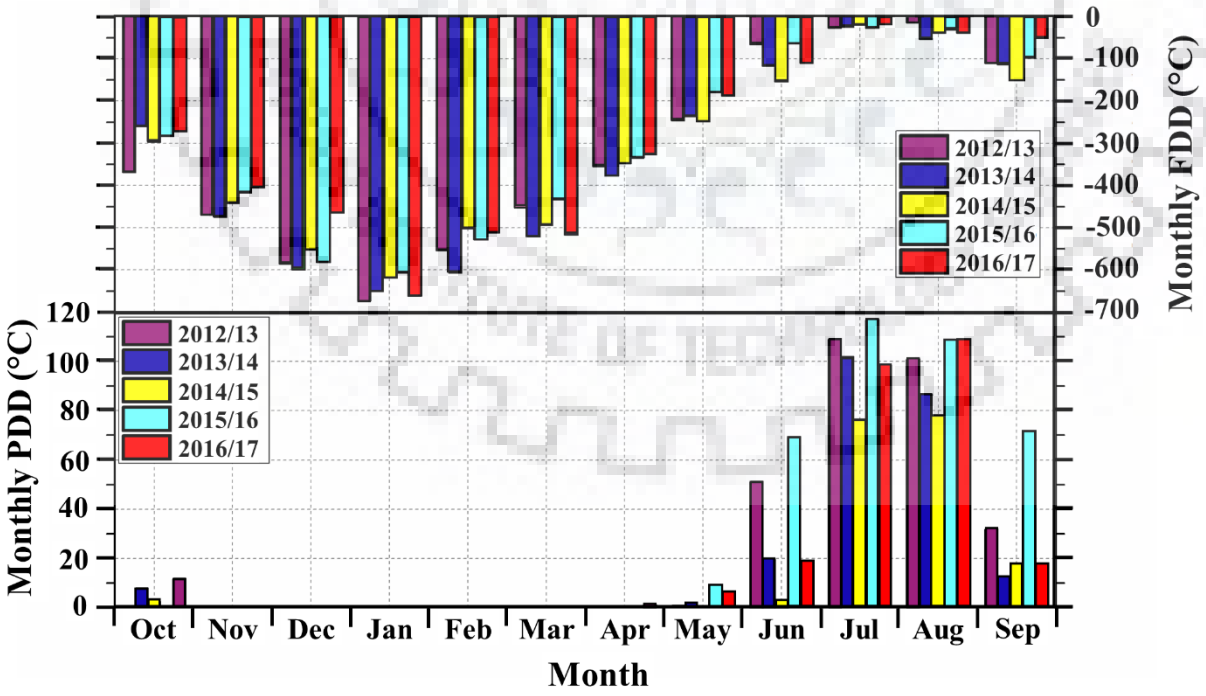

Figure 4.5. Monthly variation of Positive Degree Day (PDD) and Freezing Degree Day (FDD) during 2012–2017.

The mean annual PDD during the observation period was 267.5 °C. Besides, the FDD was extended throughout the year, with the highest value in January and the lowest in July. The annual FDD was ranged from –4036 °C (2013/14) to –3546 °C (2016/17) with a mean of –3789.2 °C. The linear trend of PDD and FDD increased with a rate of 8.4°C and 121.4°C yr^{-1}, respectively. The overall pattern and trend of PDD and FDD indicate an increase in positive temperature with declining in freezing temperature, resulting in a higher amount of melting over the study area.

4.6.1.2. Relative humidity

Other than temperature, RH is one of the influential variables at a higher elevation to determine the arid characteristics of the region. A significant day-to-day variation of RH was observed throughout the year. During the observational period, the RH range 50–80% covers a maximum percentage of days (55%) followed by 35% days in < 50% RH, and only 10% of the days come under > 80% RH (Figure 4.6). The mean monthly value of RH characterized the seasonal variation of RH, showing maximum in August (63.5%) and minimum in November (45.9%) (Figure 4.6). However, a consistent high mean monthly RH was observed from February to August, varying from 60.3 to 63.5%. In the daily analysis, the minimum and maximum value of RH varies from 0.2 to 100%, with a mean value of 57.6%. And, the mean yearly trend obtained from linear regression was declining over the entire observational period. This decreasing trend of RH will further be responsible for the changing rainfall pattern and cloudy conditions (Pratap Singh 2005).

Afterward, the mean monthly pattern of specific humidity was calculated to better understand the total water vapour content in the air (Figure 4.4). Results indicate that July and August have the highest water vapour content in the air, with a specific humidity of 5.4 g kg^{-1} while December and January record the lowest value at 0.8 g kg^{-1}. The seven consecutive months (October to April) received an average water vapour content of 1.3 g kg^{-1}, which was changed to 4.2 g kg^{-1} during May–September. This indicates that the higher moisture influx was concentrated during summer (May – September) compared to the winter season (October – April). However, this region experienced higher precipitation during winter with shallow temperatures in the range of –29 °C. In comparison to this, the western Himalayas (monsoon region) have specific humidity between 10.9 g kg^{-1} during summer months (May – October) and 4.1 g kg^{-1} for winter months (November to March) (Thayyen and Dimri 2018). Combining our results and monsoon region analysis made it clear that this distinct pattern of specific humidity in the summer and winter mainly occurred due to the aridity classification.

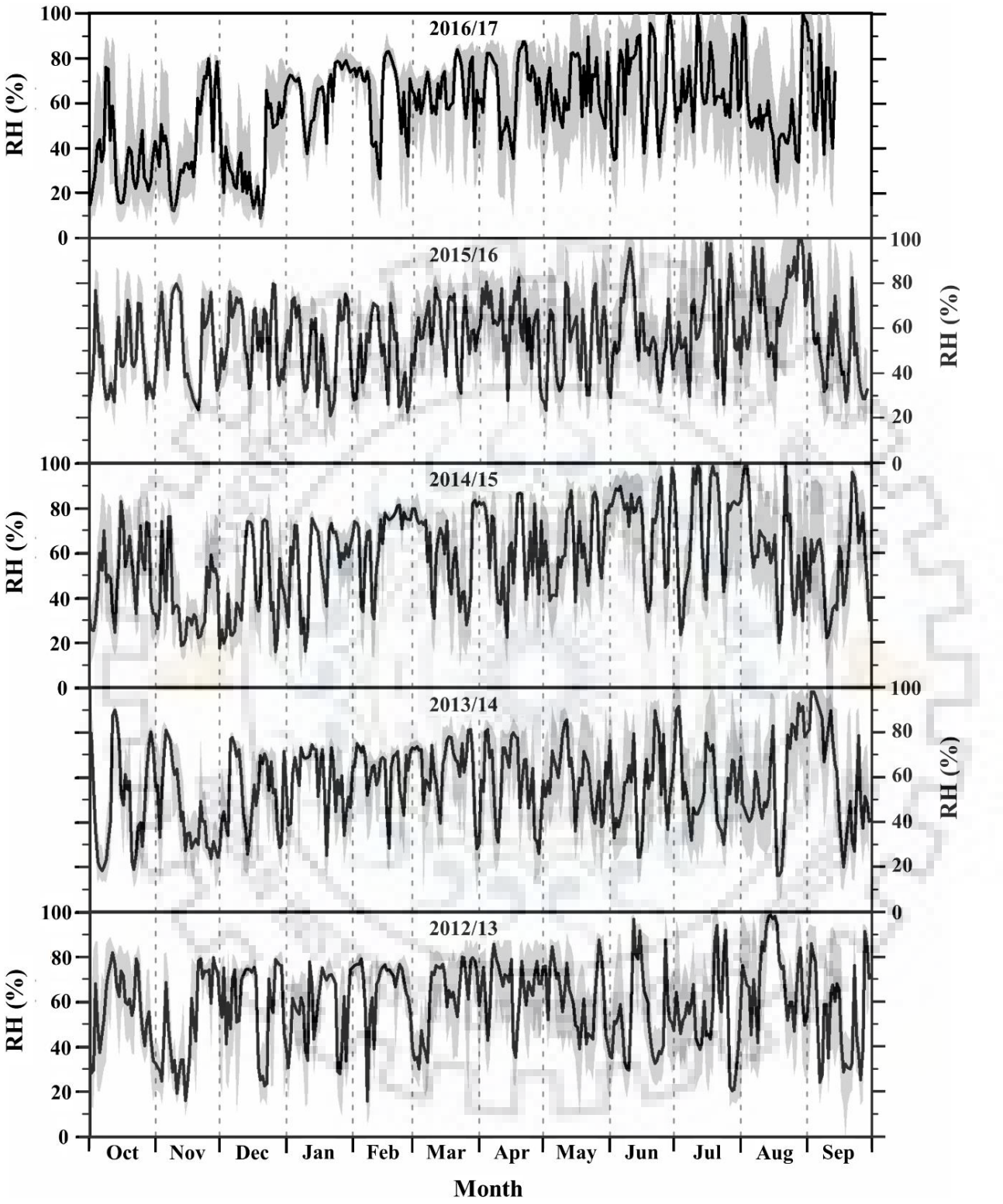

Figure 4.6. Daily variation of mean RH as shown in dark black and shaded gray represents the minimum and maximum range of RH during 2012–2017.

4.6.1.3. Wind speed and direction

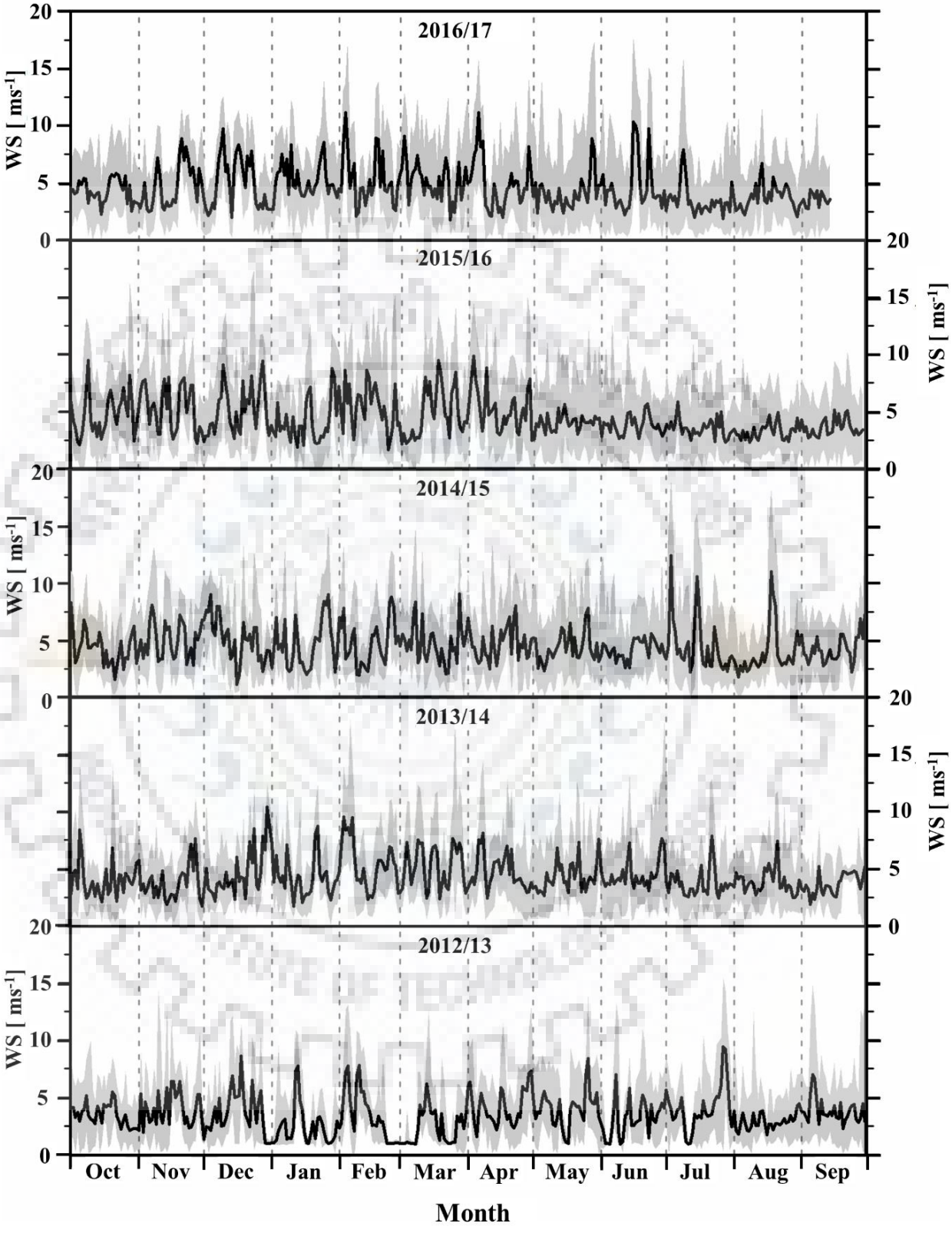

Figure 4.7. Daily variation of mean wind speed shown in dark black and shaded gray color represents the diurnal range of wind speed during 2012–2017.

The half-hourly observation of u and WD was undertaken to understand the wind regimes that regulate moisture transportation, cloud formation, the occurrence of precipitation, and surface energy balance (Figure 4.7). The analysis was performed for both day (07:00–18:00 hours) and night (19:00–06:00 hours) and the summer and winter periods. It was noted that the orographic processes influence wind regime with anabatic flows attaining a higher speed during daytime than night-time. A similar pattern of wind regime and their observation was matched with Singh et al. (2007) over the Gangotri Glacier, central Himalayas.

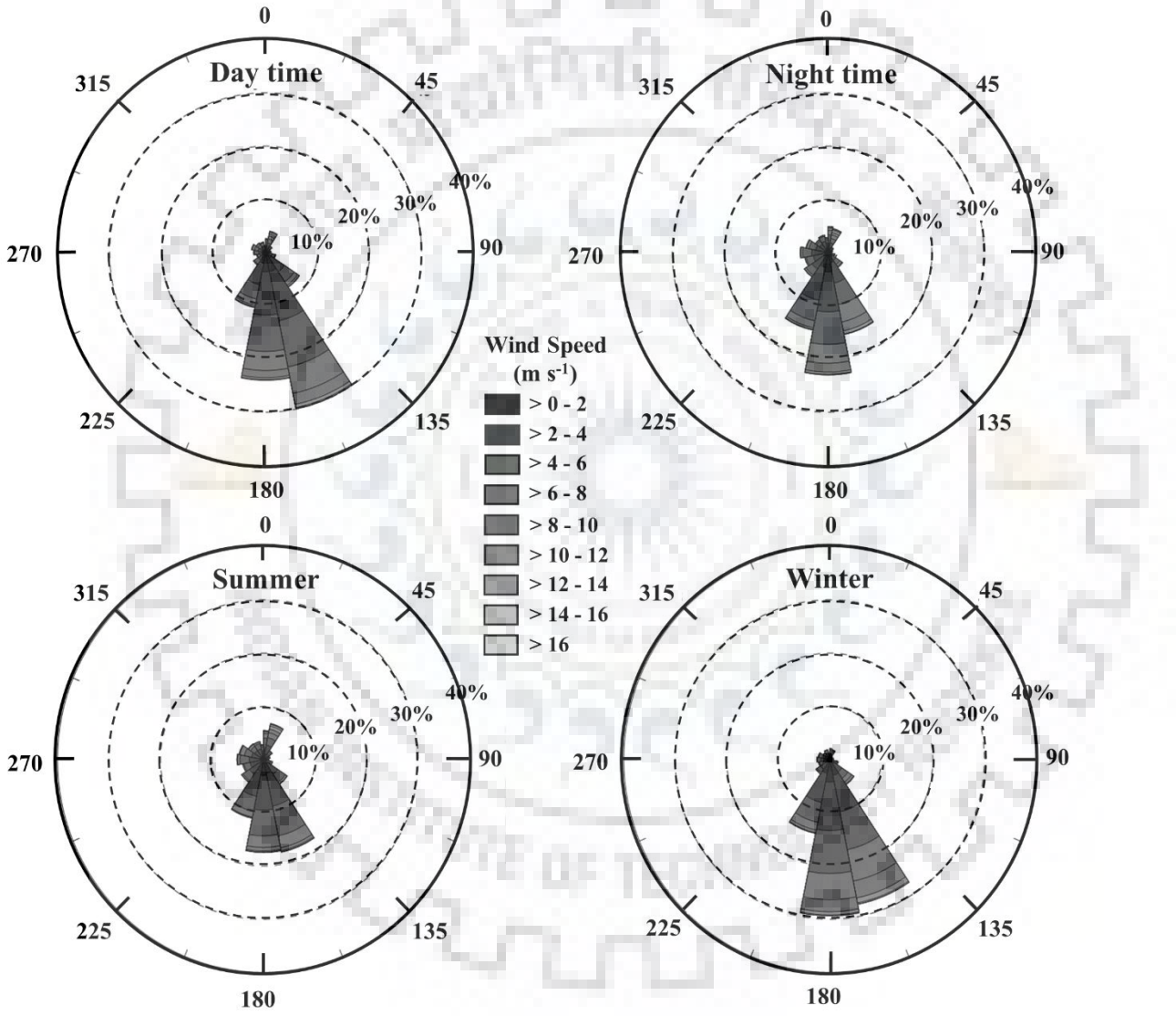

Figure 4.8. Wind direction and speed from half-hourly data for day-time (07:00–18:00 hours) and night-time (19:00–06:00 hours) as well as for summer (April–September) and winter (October–March) seasons.

The daytime wind is dominated by SSE mainly through the local valley (upper Ganglass), and during nighttime southern wind dominates, blowing directly from the main Indus valley (Figure

4.7). The seasonal analysis indicates that the southern winds dominate the study area during summer and winter periods; however, the u was higher in the winter relative to the summer season. This finding was consistent with other authors (Azam et al. 2014; Soheb et al. 2018).

During the five observational periods, the monthly maximum u ranged from 14.3 to 19.2 m s^{-1}, reaching the 'near gale' class in the Beaufort scale. And, the average u was varied from 3.5 to 4.9 m s^{-1}, which is of the 'gentle breeze' category. Apart, 'light breeze', 'Gentle breeze', 'moderate breeze', and fresh breeze conditions prevail for about 26%, 45%, 21%, and 5% of days, respectively, while the calm and light air classes of Beaufort scale do not cover the study site in annual scale. The annual distribution of u indicates an increasing trend at the rate of 0.24 m s^{-1} yr^{-1} for the entire observational period (Figure 4.8). This suggests that the rising pattern of u may cause a significant impact on turbulent heat fluxes (sensible and latent heat) over the region (Acharya and Kayastha 2018).

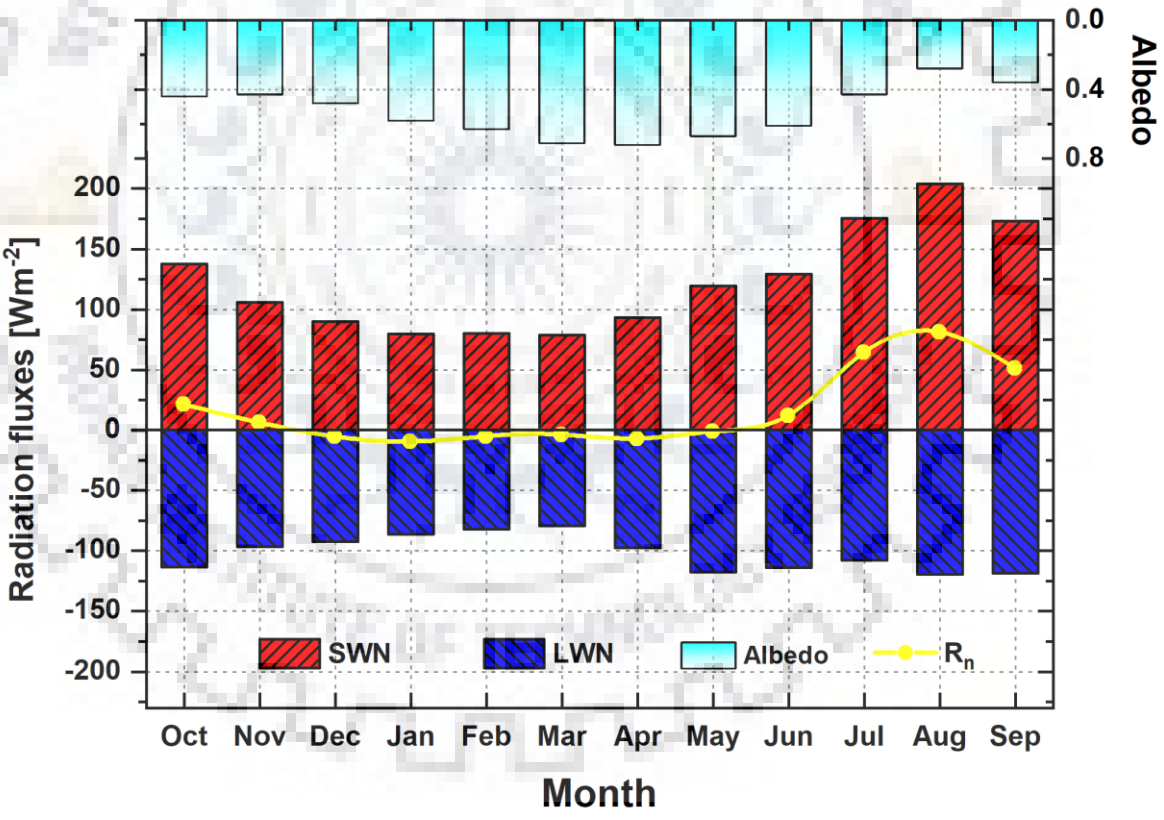

Figure 4.9. Mean monthly variation of SWN, LWN, Albedo and R_n over the period 2012–2017.

4.6.1.4. Shortwave radiation

The monthly, seasonal, and annual distribution of shortwave radiation (SWI and SWO), α, and their net shortwave radiation (SWN: SWI – SWO) were quantified for the observation period to

understand the variation of radiation forces on the glacier surface melt. The daily variation of SWI shows higher variability compared to SWO in all the hydrological years. This higher variability in SWI is mainly influenced by the presence of cloud cover and terrain properties. Apart, the variability in SWO was higher in 2016/17 and lower in 2012/13.

In the monthly analysis, the SWI was peaked in May with a mean value of 356.1 W $m^{-2,}$ and a lower value of 170.0 W m^{-2} was observed in December. The SWO was maximum in May (238.7 W m^{-2}), and a minimum value was recorded in August (76.6 W m^{-2}). This indicates that the higher SWI was trapped in the surface, and less radiation reflects during the summer season. This finding was consistent with other authors (Favier et al. 2011; Patel et al. 2021a). The higher absorption of radiation is mainly owing to the reduced albedo due to snow aging and even exposure of ground surface in some years. Our findings also include that the α was higher in April (0.72) and lower in August (0.28) (Figure 4.9).

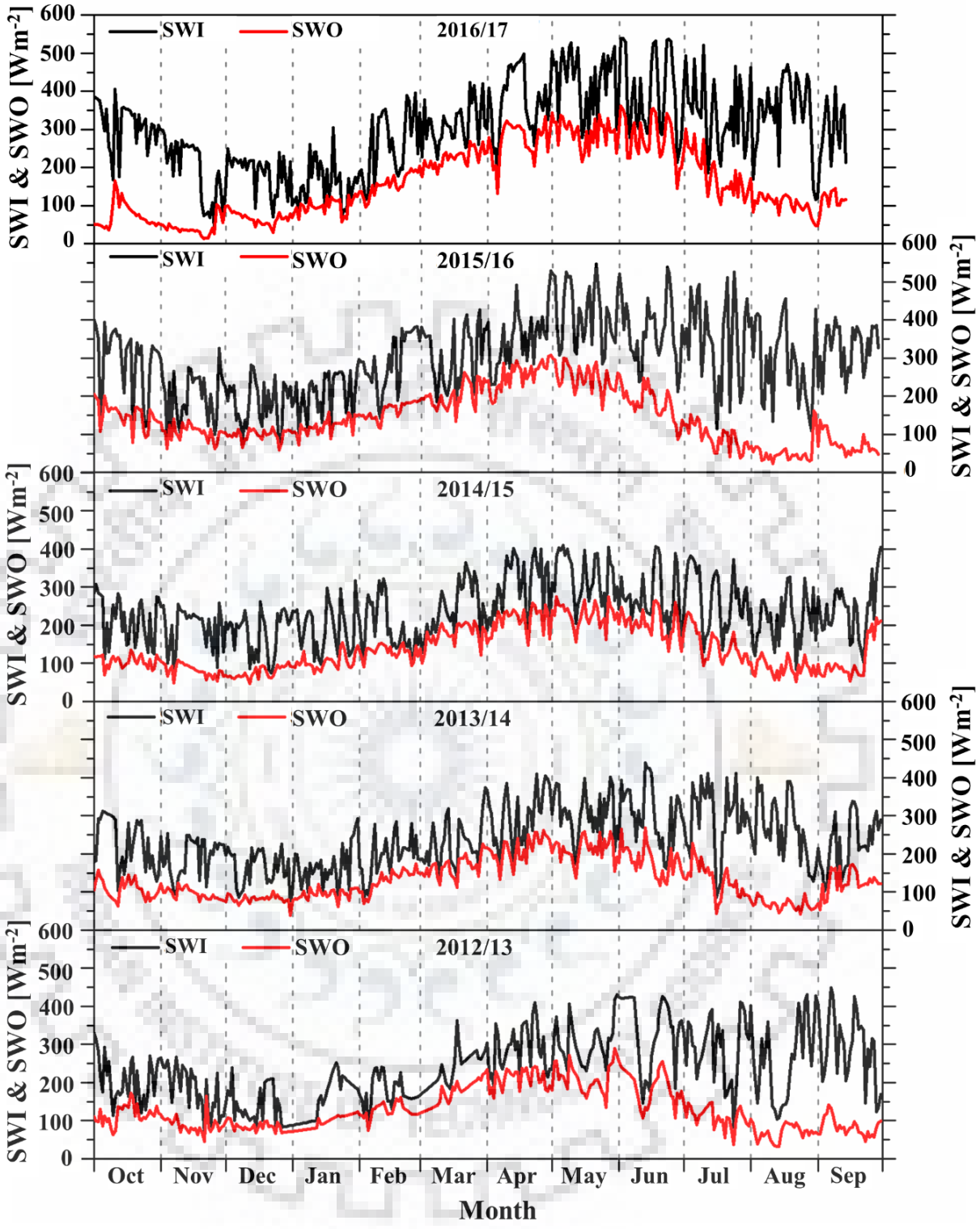

Figure 4.10. Daily mean variation of incoming and outgoing shortwave radiations.

The SWN was calculated from corresponding SWI and SWO, which shows the daily value at the study site ranged from 9.0 to 416.3 W m^{-2} with an average of 122.2 W m^{-2} over the study period. The annual SWN was minimum in 2014/15 (98.6 W m^{-2}) and maximum in 2015/16 (153.9 W m^{-2}) with an average value of 122.2 W m^{-2}. However, the SWI and SWO were highest in 2016/17, whereas the lowest value was attained in 2014/15 and 2012/13, respectively. The linear trend of

SWI, SWO, and SWN increased with a rate of 18.5, 7.0, and 11.0 W m^{-2} $yr^{-1,}$ whereas α shows a declining trend (–0.90 % yr^{-1}) over the whole observation period. This indicates that this region may experience less snow accumulation or snowfall amount during the study period. Our findings suggest that the observation period has two consecutive years in which one attain the highest and the other received the lowest value. By combining T_a, α, and R_n for the period 2015/16, we can conclude that due to an increase in T_a (–9.1 °C) it affects the α (0.49) and causes an adverse effect on R_n (108.0 W m^{-2}). This indicates that this region is highly driven by temperature variation and radiation fluxes. Several authors explained similar observations (Meena et al. 2015; Shafiq et al. 2016; Wani et al. 2021).

4.6.1.5. Atmospheric pressure

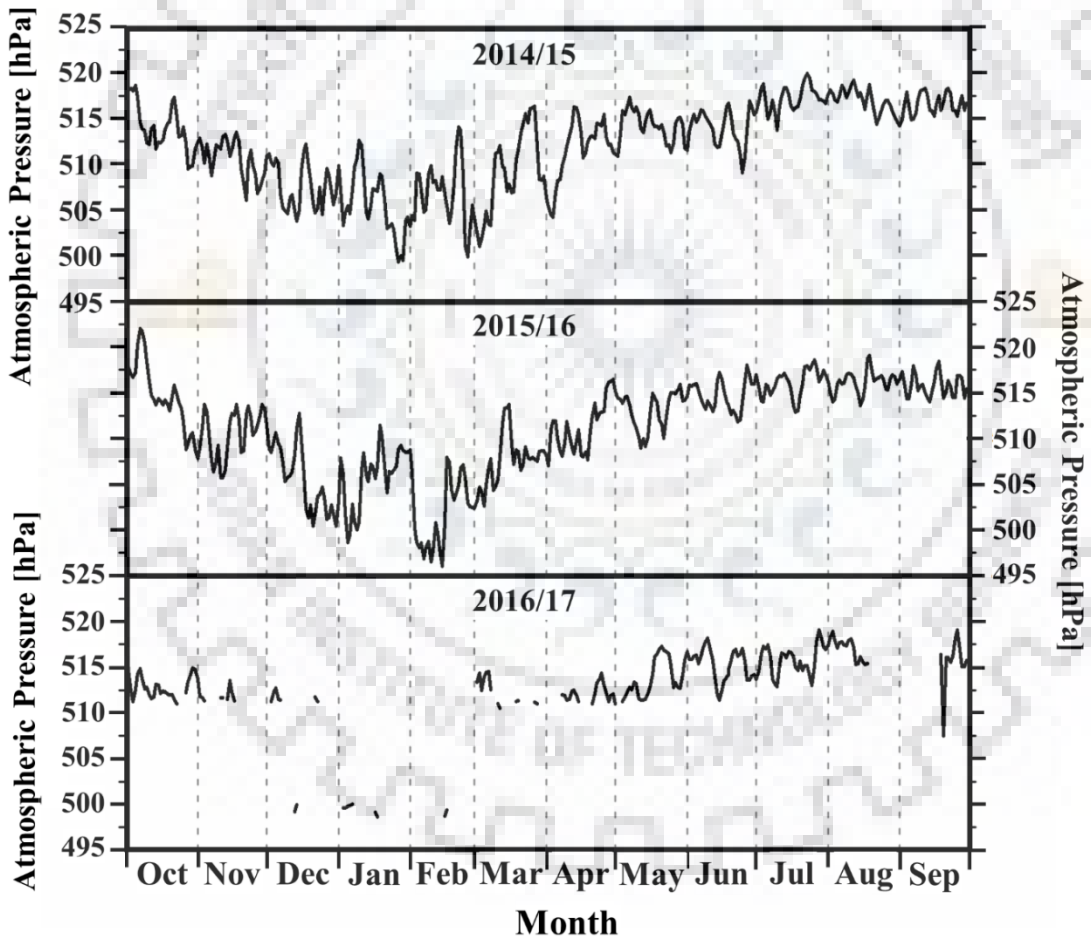

Figure 4.11. Mean monthly variation of atmospheric pressure over the period 2012–2017.

The P_{atm} was recorded by AWS from 1 October 2012 to 30 September 2015, which can be used for H_s and H_l calculation. The mean daily P_{atm} ranged from 496.1 to 521.9 hPa with a mean

value of 512 hPa (Figure 4.11). On a daily variation, the year 2012/13 experienced some data gap over the study site.

The mean monthly analysis indicates that the P_{atm} starts decreasing from October onward and attains minimum value in February (502.6 hPa), then suddenly it starts increasing till September with a maximum value in August (512.7 hPa). Our result also illustrates that the Coefficient of Variation (CV) was highly variable in February (CV = 0.63) followed by January (CV = 0.58) and lower value attained in September (CV = 0.07) followed by August (CV = 0.08). This indicates that the CV was higher in the months where P_{atm} was lower (January and February) than other months.

The lower P_{atm} controlled the u and WD of a region (NCERT 2020). This resultant observation was well-matched with the u of the study site, which was highest in February (4.9 m s^{-1}) and lowest in August (3.5 m s^{-1}). In the yearly analysis, the mean P_{atm} during 2012/13, 2013/14, and 2014/15 were 511.2, 511.1, and 512.0 hPa, respectively. The yearly variation of P_{atm} was not much change relative to monthly variation.

4.6.1.6. Net radiation

After analyzing the variation of radiation fluxes, the R_n was measured over the study site, which indicates that the mean daily R_n ranges from –88.3 to 184.6 W m^{-2} with a mean of 20.1 W m^{-2} over the study period (Figure 4.12). The R_n value starts positive from May onwards, attains its maximum value during August (84.5 W m-2), and further decreases until November. The other remaining months show negative R_n with a maximum in January (–6.5 W m^{-2}) and a minimum in March (–0.5 W m^{-2}) with an average of –3.1 W m^{-2}**.** This positive R_n indicates that these particular months may be able to contribute to surface melt over the region. The mean annual R_n shows an increasing trend with a rate of 2.4 Wm^{-2} yr^{-1} for the study period with maximum value in 2015/16 followed by 2013/14, and the minimum value was received in 2014/15 (Figure 4.13).

Our findings suggest that the observation period has two consecutive years in which one attain the highest and the other received the lowest value. By combining T_a, α, and R_n for the period 2015/16, we can conclude that due to an increase in T_a (–9.1 °C) it affects the α (0.49) and causes an adverse effect on R_n (108.0 W m^{-2}). This indicates that this region is highly driven by temperature variation and radiation fluxes. Several authors explained similar observations (Meena et al. 2015; Shafiq et al. 2016; Wani et al. 2021).

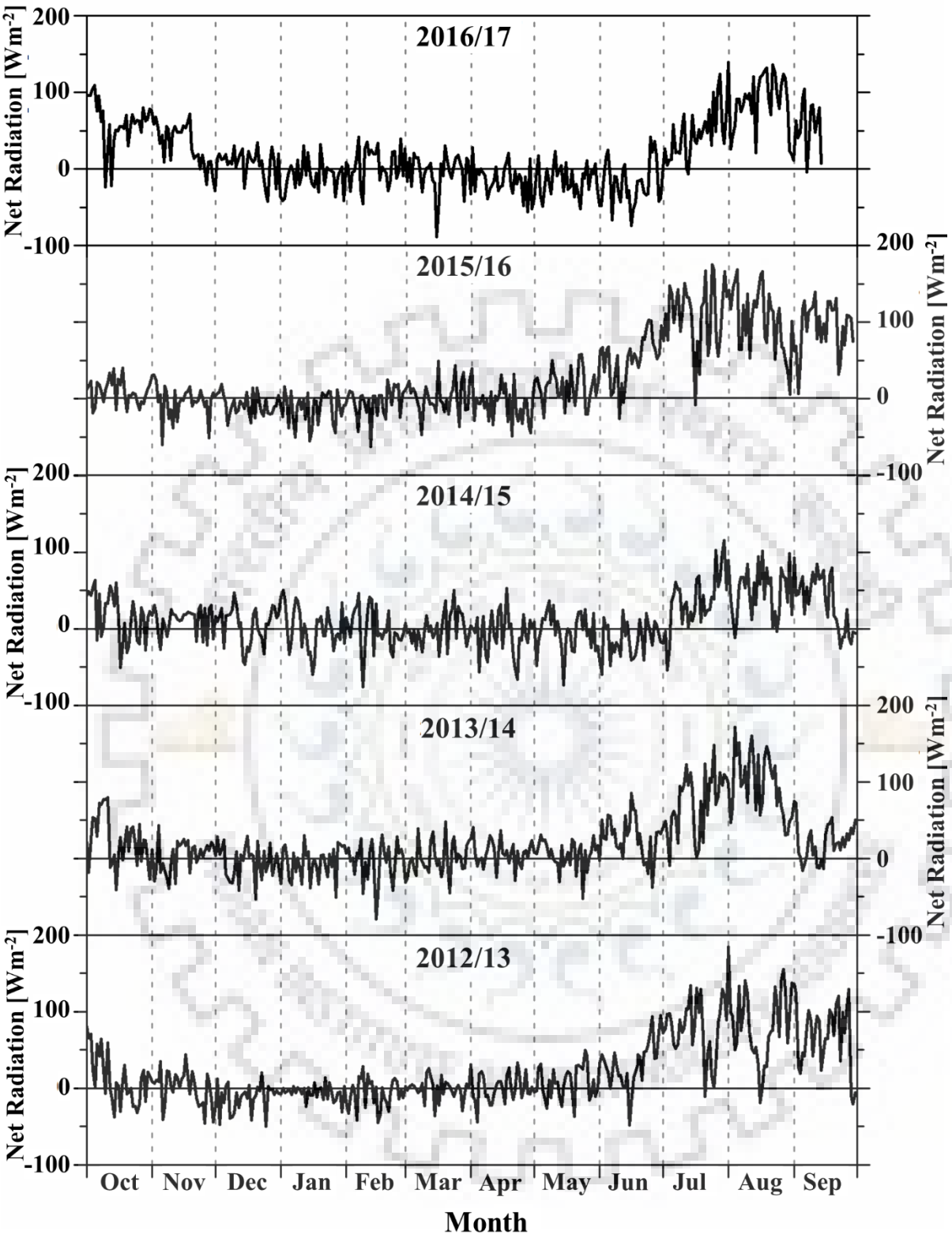

Figure 4.12. Daily mean variation of net radiation of the given hydrological year.

4.6.2. TURBULENT HEAT FLUXES

The turbulent heat fluxes (H_s and H_l) were measured from hourly to monthly and then yearly scales (Figure 4.13). Our finding illustrates that the mean monthly distribution of heat fluxes follows an opposite pattern; however, a higher value attains during May–November.

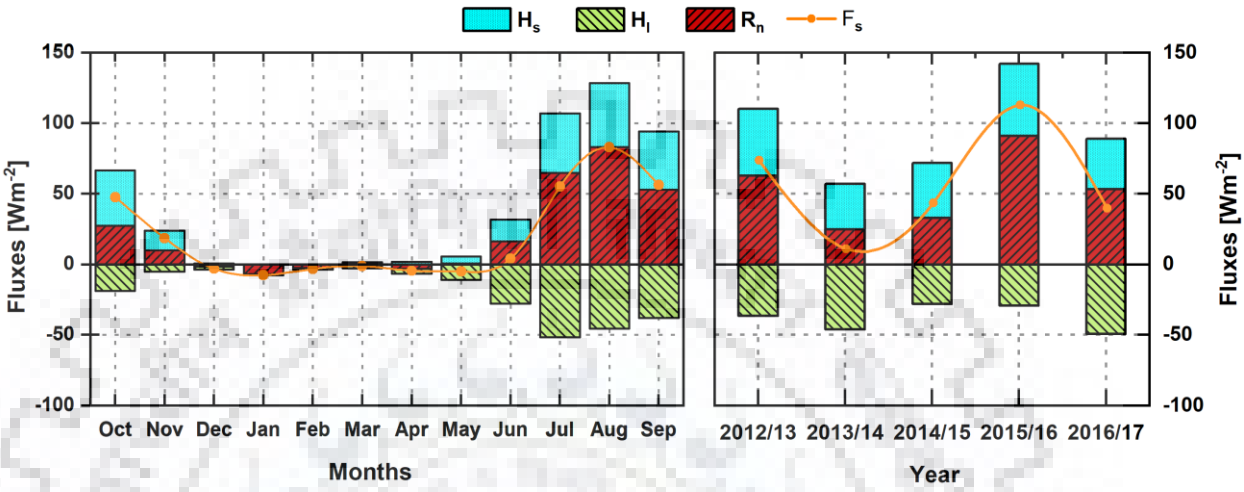

Figure 4.13. Mean monthly and inter-annual distribution of R_n, H_l, H_s and F_s over the study site for the period 2012–2017.

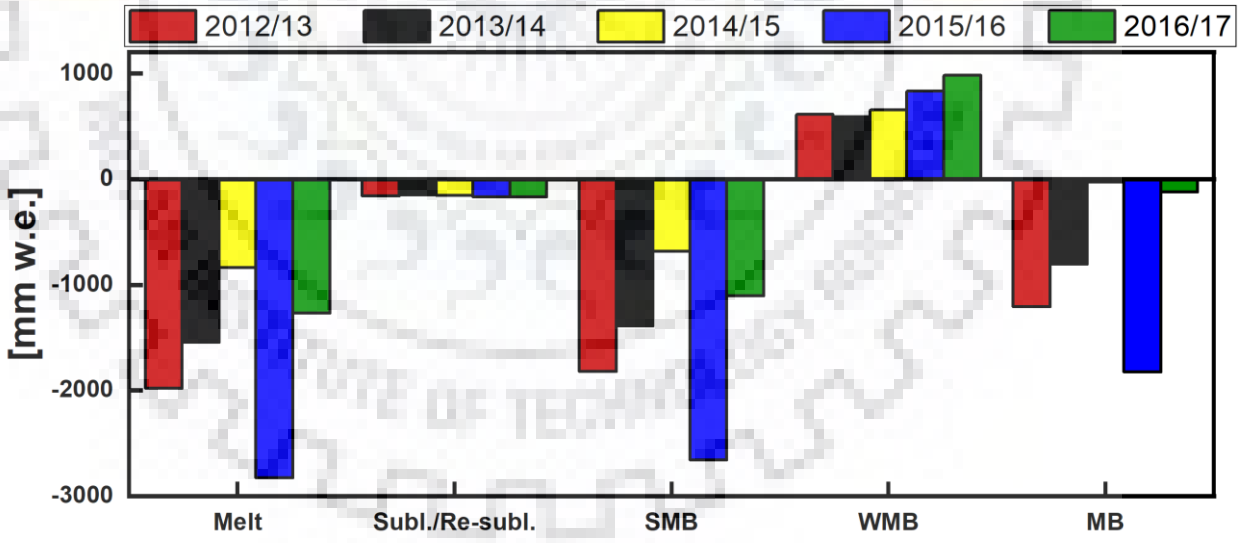

Figure 4.14. The inter-annual variation of melt, sublimation/re-sublimation, SMB, WMB, and overall annual mass balance of the study site during 2012-2017.

The maximum value of H_s was observed in August, and the minimum was attained in January. In contrast, the H_l was highest in January, and the lowest value was observed in July for the entire observational period. The estimated H_s and H_l patterns were matched with the observations of T_a and u of the study site. Our finding revealed that the T_a was higher in July

followed by August, and even u was lower during these months. And, the obtained monthly pattern of H_s and H_l were well matched with the observation of many authors carried out over the Himalayan region (Amatya et al. 2015; Acharya and Kayastha 2018; Patel et al. 2021a). Other than this, the yearly analysis suggests that the H_l shows a declining linear trend with a rate of –0.1 W m^{-2} yr^{-1}, while H_s indicates no change over the study period. This means the turbulent heat flux was not significantly changed as compared to radiation components. The value of H_l was negative or nearly zero throughout the temporal analysis. This means the study site was mainly influenced by the process of sublimation rather than re-sublimation. Wani et al. (2021) have also highlighted a similar observation over the South-Pullu region, Ladakh.

4.6.3. ACCUMULATED WINTER PRECIPITATION

The continuous monitoring of precipitation at this higher elevation is difficult; therefore, the accumulated snow water equivalent-based measurement was performed in May every year from 2012–2017. In the snow water equivalent measurement, the winter snow accumulation was measured through the stake measurement. It was multiplied with snowpack density estimated by digging a snow pit for snow density measurement close to the AWS site. The estimated winter precipitation was minimum (589 mm w.e.) in 2013/14 and maximum (980 mm w.e.) in 2016/17 with a mean value of 734 mm w.e. Our findings also indicated that the winter precipitation shows an increasing trend at the rate of 98.2 mm w.e. yr^{-1}. However, the mean winter precipitation recorded at Leh station was 47.5 mm w.e. (Thayyen et al., 2020). This indicates that the steep precipitation gradient may exist between the valley bottom and mountain ridge, which play a critical role in the region's hydrological and cryospheric system response. Even though this region is devoid of significant monsoon incursions, occasional high-intensity rainfall events in summer were reported by Thayyen et al. (2013). However, there was less evidence suggesting that such extreme events impacted the AWS site at 5600 m a.s.l. High precipitation gradient between these two closely placed valley bottom station and overlooking ridge station at 5600 m a.s.l. suggest that the mountain slope mainly controls the cooler temperature along the mountain ridge. It plays a significant role in assessing the precipitation amount at the higher altitude of the cold-arid region.

4.6.4. NET ENERGY

By the summation of radiations and energy fluxes over the study site, as result, the obtained total surface melt (F_s) was used to quantify the SEB from 2012 to 2017 (Figure 4.14). Only positive melt heat flux was considered, which mainly occurred in the summer period with the prevailing

melting condition all the time. The average F_s was 209.7 W m^{-2} with a maximum (358.8 W m^{-2}) in 2015/16, and a minimum (85.1 W m^{-2}) was observed in 2014/15 (Figure 4.14). In the summer season, the mean value of R_n, H_s and H_l were 43.7, 29.7 and –34.8 W m^{-2}, respectively, which indicate that the R_n and H_s were the main contributor to the total energy available for melt.

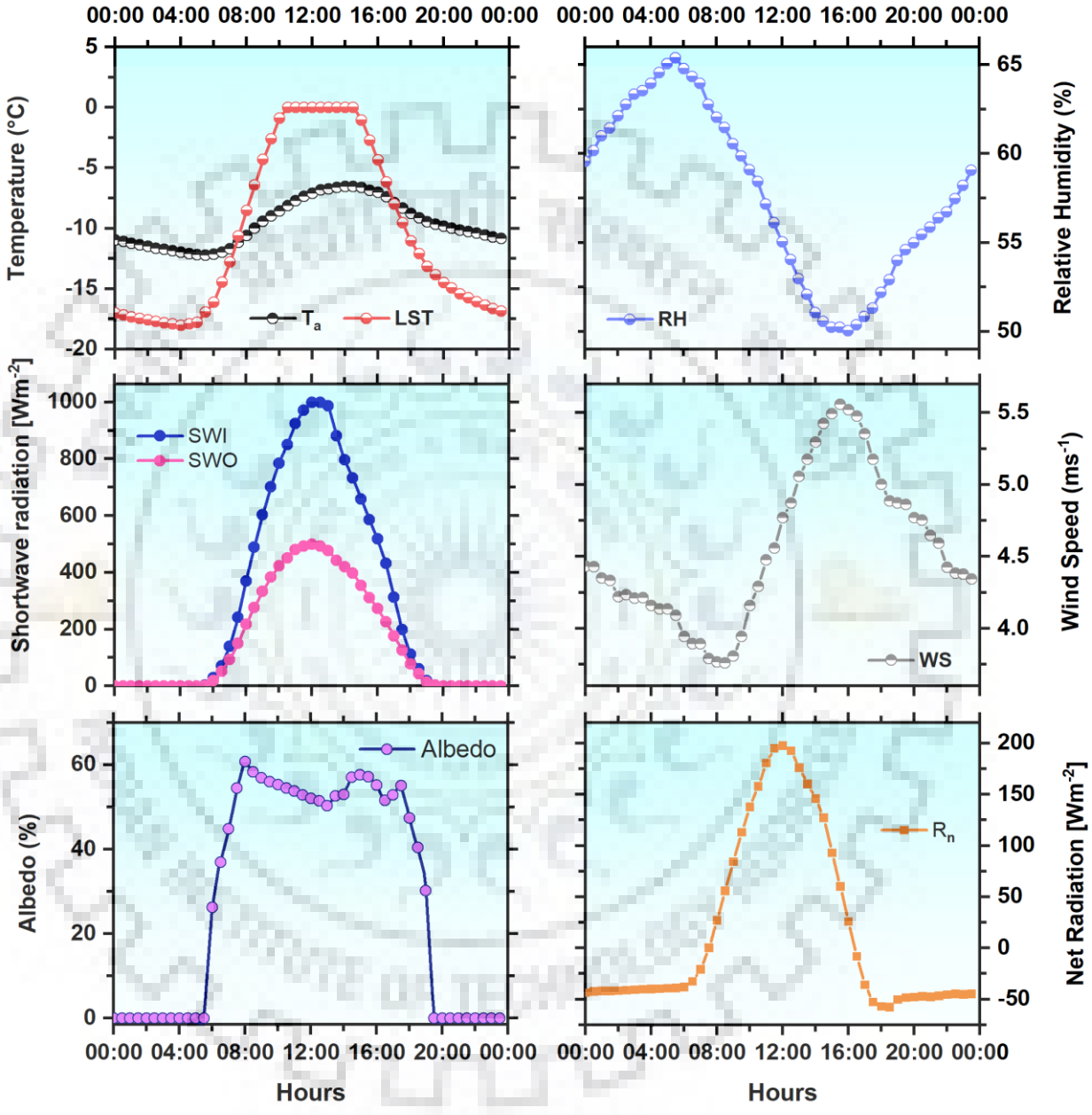

Figure 1.15. Mean diurnal variation of climatic and meteorological variables at 5600 m a.s.l elevation for the period 2012–2017.

The contribution of R_n was higher as compared to other fluxes for the study site. A similar observation was illustrated by many authors (Aizen et al. 2002; Zhang et al. 2013; Sun et al. 2014; Acharya and Kayastha 2018; Soheb et al. 2018). However, the total surface melt and contribution of each variable were changing during the winter season, as the region was

experiencing a low temperature, which resulted in a negative value. The positive melt flux was converted into melt (mm w.e.), indicating that the average melt rate for the observational period was 11.1 mm w.e. d^{-1}.

4.6.5. SUBLIMATION/RE-SUBLIMATION

The sublimation/re-sublimation of the study site was calculated using the daily computed H_l. The positive value of H_l resulted in the re-sublimation process, while sublimation occurred when the H_l was negative. The sublimation process occurred throughout the year, with a higher value observed in summer and a lower was received in the winter. In contrast, the re-sublimation process only occurs in the winter season. This observation shows that the region was highly exposed to radiation and caused a significant loss on the surface (Wani et al. 2021).

During the observational period, the mean surface mass loss was 162.2 mm w.e. through sublimation, while a negligible amount of mass gain (1.3 mm w.e.) was observed through re-sublimation. Both sublimation and re-sublimation were found maximum in 2015/16, while 2013/14 and 2014/15 were experienced the minimum sublimation and re-sublimation, respectively (Figure 4.14). The linear trend of sublimation and re-sublimation were increasing with a rate of 3.32 mm w.e. yr^{-1} and 0.08 mm w.e. $yr^{-1,}$ respectively. This indicates that both the processes witnessed an increasing trend for the selected period; however, the rate of re-sublimation was relatively less increasing than sublimation, which means the glacier loses its mass at a higher rate than mass gain.

4.6.6. DIURNAL VARIABILITY

The mean diurnal variation (half-hourly values) of T_a, RH, u, α, SWI, SWO, and R_n were quantified for the study period, indicating that the distribution of T_a, SWI, SWO, α, and R_n follow a similar pattern (Figure 4.15). Diurnal temperature variation shows that maximum temperature was often observed around 14:00 hour, and the minimum was around 06:00 hour. Results demonstrate that all the radiations intensity increases with the increase in daylight hours, and it reaches a maximum at noon (12:00 hour) then starts decreasing till 19:00 hour. It was also noted that the radiation was negative or nearly zero between 19:00 hour and 06:00 hour. This occurred due to the Earth's rotation, resulting in a change in solar angle with daylight hours. These results were agreed with Al-Hilphy et al. (2014).

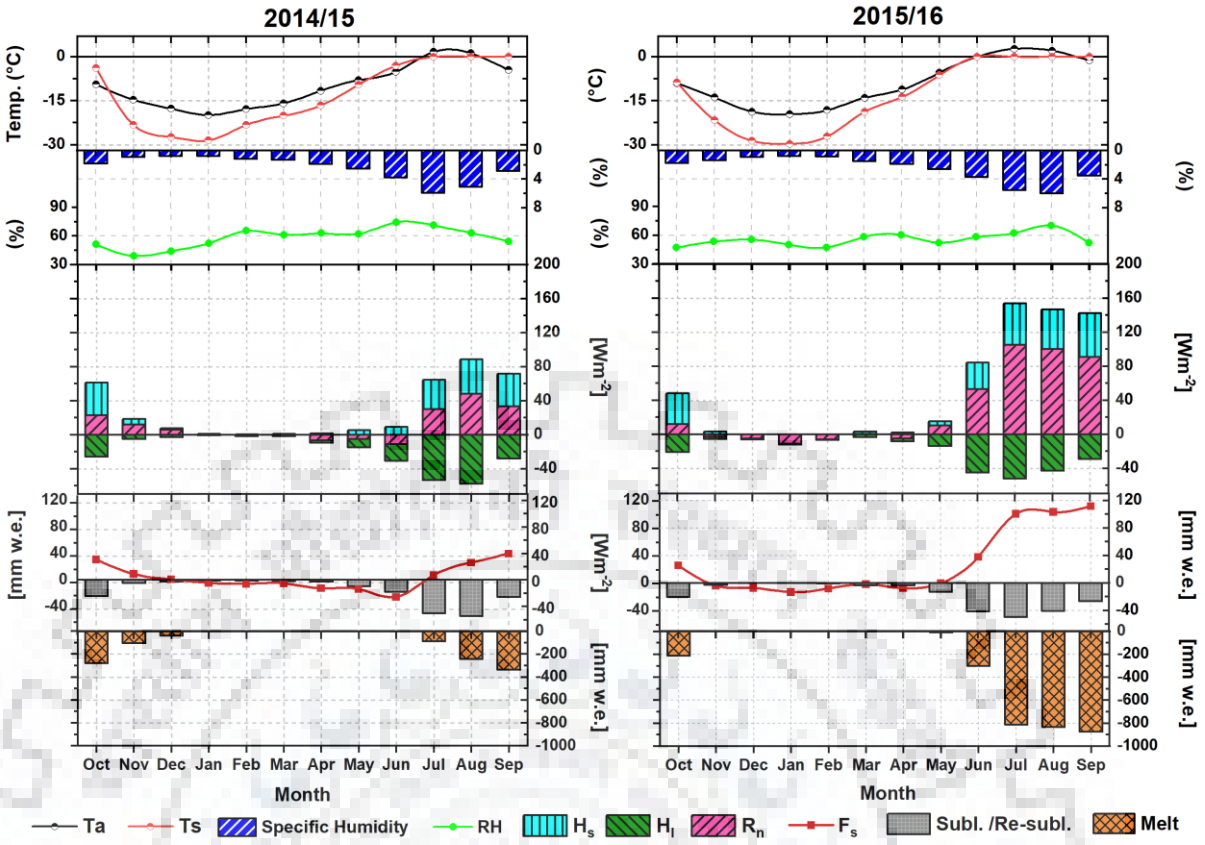

Figure 4.16. Comparison of meteorological, radiation, and energy fluxes components for the two extreme periods, i.e., 2014/15 (minimum mass loss) and 2015/16 (maximum mass loss) during the observational period.

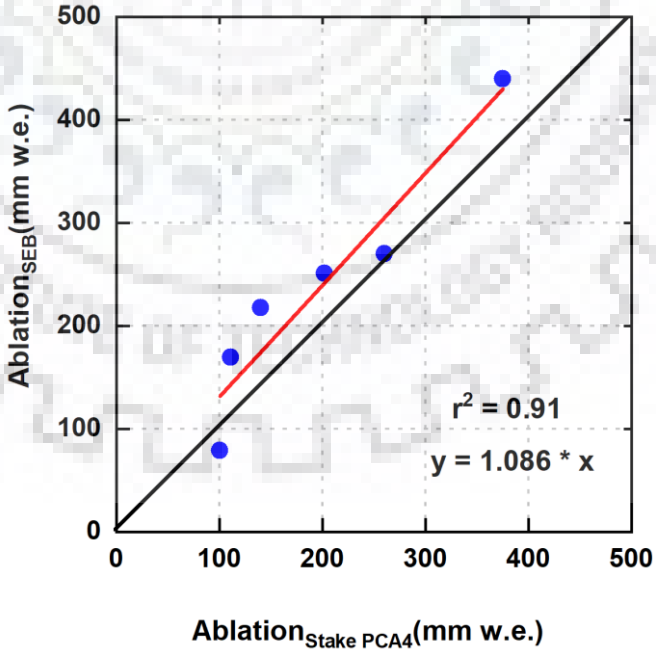

Figure 4.17. Validation of SEB computed ablation and stake no. PCA4 measured surface ablation.

During diurnal analysis, T_a and all radiative fluxes were positive and follow a similar trend; however, radiation attains its peak at noon, two hours before the T_a . This finding was conceded with Azam et al. (2014). The daily variation of SWI, SWO, α, and R_n were also related with the change in cloud cover amount and their formation. A similar observation was illustrated by many authors (Cawkwell and Bamber 2002; Qian et al. 2007). The RH of the study site shows an almost consistent pattern throughout the day, which was similar to Soheb et al. (2017). On the other hand, u was maximum in the afternoon time (16:00 hour), and then it decreased while moving forward. The higher u in the afternoon is a common phenomenon for the valley region, as illustrated by other authors (Klok et al. 2005; Schaefer et al. 2020). As a consequence of an increasing u the T_a of the region was deficit during the mid-afternoon.

4.6.7. MASS BALANCE

The year-wise mass balance was measured by adding the summer mass balance (SMB) and winter mass balance (WMB) of the region (Figure 4.14). Our result reveals that the selected glacier was losing its mass for the entire observational period except for the year 2014/15, which experienced a slightly balanced condition (–0.03 m w.e.). This may have occurred because this year has lower temperatures and higher precipitation as compared to other years. The region experienced a higher mass loss in 2015/16 (–1.83 m w.e.) followed by 2012/13 (–1.21 m w.e.), while the loss was comparatively less (–0.12 m w.e.) during 2016/17. This highest mass loss may have occurred due to higher annual temperatures. Besides, this region receives a higher amount of precipitation during winter but is not able to compensate for the melting caused during the summer season. Our finding was well-matched with the observation highlighted by Soheb et al. (2020) for the Stok glacier. Similarly, the year 2013/14 received comparatively lower winter precipitation (588 mm w.e.) and relatively lower summer temperature, which may change the α and reduces the excessive melting; therefore, the study site witnessed moderate mass loss. Overall, the obtained mass balance result concludes that the precipitation occurred during the winter season and temperature variation in the summer season were the main contributor that influences the glacier surface and regime of the mass loss/gain for the observational period.

4.6.8. COMPARISON BETWEEN 2014/15 AND 2015/16

The maximum (2015/16) and minimum (2014/15) melting years were considered to quantify the driving factors that cause the higher/lower glacier melting over a certain period of time (Figure 4.16). Results demonstrate that the RH and specific humidity almost follow a similar pattern in both the year while T_a and T_s experienced a higher value in 2015/16 relative to 2014/15. The

monthly distribution of RH suggests a higher value in 2014/15 than in 2015/16. Apart, it was also observed that the T_s was consistently zero with higher specific humidity in the summer season for the period 2015/16.

Our findings also indicate that in 2015/16, the Phuche glacier witnessed positive or zero temperatures (T_a and T_s) for a longer period (June to September) than 2014/15 (3 months, i.e., July to September). On the other hand, the R_n and turbulent heat fluxes (H_s and H_l) were higher in 2015/16 in comparison to 2014/15 by a mean difference of 42.17 W m^{-2}, 9.0 Wm^{-2}, and –1.72 Wm^{-2}, respectively. Our findings illustrate that in 2015/16, the melting period was large, starting from May to the end of September and attaining maximum value during July.

The maximum change in these two consecutive years was mainly occurred in R_n component due to a change in α. This variation in α was predominately driven by the change in temperature. The increase in R_n further contribute to the variation of total surface energy available for melt (F_s). The monthly variation of F_s was nearly similar with the R_n while the loss caused by sublimation was almost consistent in both the year. Overall, the comparison of these two extreme years suggests that the maximum melting in 2015/16 was mainly dominated by the change in α cause due to the higher positive temperature for a longer period.

4.6.9. VALIDATION

The observed glacier melting from the SEB components was validated with the total melting measured on stake PCA4. This stake was mounted on the glacier surface, which is near the AWS location. The first observation of snow stake starts from 30 May 2017 to 15 September 2017 with an interval of 10-15 days. Then, the density of accumulated snow was measured on 30th May 2017, which varied from 0.46 to 0.62 g cm^{-3} with a mean value of 0.53 g cm^{-3}. And, the total thickness was melted at a stake of about 219.0 cm during the observation period. The observed total melting at glacier surface using stake measurement was 1188.7 mm w.e. while the SEB measured total melting was 1437.5 mm w.e., showing a difference of 248.8 mm w.e. for the selected period. On the other hand, the sublimation was observed on the snow/ice surface that accounts for 168.1 mm w.e. loss (13.2% of the total melt), and the re-sublimation was observed about 0.9 mm w.e. Result indicates that the sublimation consumes higher latent heat compared to the melting of the glacier; therefore, this higher sublimation used to perverse the glacier surface from high melting. The computed ablation using the SEB model was validated with the stake PCA4 measured ablation, suggesting a higher correlation of 0.91 at $p < 0.01$ for the period (Figure 4.17). This higher correlation between these two ablation rates indicates that the used model was

robustness and their results measured a reliable mass balance across the glacier. The computed ablation (SEB) was overestimated by 8.6% than the measured ablation (Stake-based). Similarly, many authors have reported an overestimation of SEB against the stake measured ablation (Hay and Fitzharris 1988; Acharya and Kayastha 2018; Liang et al. 2018).

4.7. DISCUSSION

4.7.1. COMPARISON BETWEEN THE MEASURED MASS BALANCE AND OTHER STUDIES OF THE SAME REGION

The impact of climatic variables on the glacier mass balance has already been analyzed over the Himalayan glaciers (Mandal et al., 2015; Soheb et al., 2020; Sun et al., 2014) at regional and basinal scale; however, it is still not well understood for cold-arid region glacier (Leh - Ladakh range). A study carried out by Wani et al. (2021) suggested that the temperature and delay in snow occurrence as well as elongated snow cover period in the upper Ganglass catchment, Ladakh are the influential drivers that controlled the SEB of the region. Therefore, we have addressed this topic by analyzing the surface melting through the AWS collected meteorological variables on the Phuche glacier (Ladakh range), and field monitored snow depth variation using the SEB model in detail. On the basis of data availability, an enlarged length of the study period (from 2012 to 2017) was considered to compare the computed surface melting.

By comparing both the results, our finding added a value point in the previous study that the surface melting of this region was related to the summer temperature and changing α. This variation in the analysis may occur because we have taken the AWS data of the glacier area; therefore, it is more efficient to explain the condition of glaciers located in the cold and arid region. Apart from this, a study performed at the Stok glacier lies in the same region (Ladakh) by Soheb et al. (2020) based on the traditional mass balance approach indicated that the glacier witnessed a mass loss for the whole study period from 2014–2019 except in 2018/19. They have also witnessed that the year 2015/16 experience higher mass loss as compared to other years. This observation was well-matched with our findings. It indicates that somehow in 2015/16, any critical variation in a climatic variable may result in higher mass loss during the period. Allen et al. (2016) have also indicated that 2016 was the 37th consecutive year of alpine glacier retreat across the world based on preliminary data.

4.7.2. COMPARISON OF SEB COMPONENTS WITH OTHER GLACIERS IN THE HIMALAYAN REGION

This section compared the observed SEB components and their mass balance with other previously published literature on the glacier mass balance of the Himalayan region. As per the previous studies (Zhang et al. 2013; Azam et al. 2014; Acharya and Kayastha 2018; Patel et al. 2021a), the R_n shows the highest contribution in F_s which was mainly controlled by the α and terrain properties. The present result also illustrates that the R_n and H_s were the main contributor in the total energy in the F_s, whereas the H_l was the greatest energy loss which produces a loss in double through latent heat and by process of sublimation. A similar contribution of H_l was revealed by Mölg and Hardy (2004). Numerous authors have also highlighted that the variation of R_n was highly dominant by the SWN under the clear sky condition during the summer season (Kayastha et al. 1999; Acharya and Kayastha 2018). Our findings also suggested that the obtained SWN shows an inverse relationship with α.

Over the study area, the precipitation during the summer season often occurs in liquid form; therefore, the α value becomes constant or slightly reduced over the time span. However, when the precipitation occurred in solid during the winter season, then the α abruptly changed and control the SWN for melting. Several authors have also experienced similar patterns over the high mountain glaciers (Klok and Oerlemans 2002; Paul and Kotlarski 2010). Our results also included that the region experienced negative H_l throughout the year, further exaggerated the amount of sublimation over the glacier surface. This observation was previously highlighted by Sun et al. (2014) over the Laohugou glacier No.12, western Qilsian mountains. They have indicated that the H_l was negative in the entire summer season (June – September) while slightly positive value exist two days of July (2 and 3) for the year 2011. Similarly, Aizen et al. (2002) and Liu et al. (2010) indicate that the H_l was found negative during their observational period for Xixibangma Glacier, and Keqicar Glacier located in the South-central Tibetan Plateau and Southwest of the Tianshan, respectively. Our result also concluded that the region was predominately influenced by sublimation rather than the re-sublimation process. Similarly, numerous authors have experienced that the High-Mountain Asia glaciers mainly dominate by the process of sublimation (Aizen et al. 2002; Zhang et al. 2013; Sun et al. 2014).

4.7.3. ASSESSING THE IMPLICATION OF MASS BALANCE ON THE SOCIO-ECONOMIC DIMENTION

By gathering all the information related to the mass balance of this catchment and even in the Himalayan region, we can conclude that the glaciers were losing their mass at a significant rate, which varies from location to location. In the broader concept, the study region comes under the Indus basin, predominately driven by summer snow and glacier melt. With this higher mass loss in the glaciers of the Indus basin, the streamflow was mainly influenced, which further generate the probability of an extreme event occurs if any abrupt changes may happen in the precipitation. Many studies were carried out that indicate the higher melting of the glacier can possibly be a reason for the occurrence of extreme events (Bhambri et al. 2018; Sattar et al. 2019). On the other hand, in the long-term aspect, the changing pattern of mass balance over the Himalayan glacier is able to create a water stress-like condition in the near future. This water stress largely impacted the livelihood of upstream and downstream population, tourism of mountainous region as well as the apple farming. Many reports and articles have previously dragged the attention of the research community worldwide over the mass balance of Himalayan glaciers and their implication on billions of population (Bajracharya and Shrestha 2011; Mukherji et al. 2015; Shrestha et al. 2015). Therefore, a necessary preventative measure will be designed by the decision-maker to sustain, restore, and balance the ecosystem.

4.8. CONCLUSIONS

In the cold-arid region of the Ladakh range, a first-ever longest meteorological dataset was recorded at 5600 m a.s.l. from 2012 to 2017. The present study aimed to provide an insight into the SEB components and their computed mass balance. Windy weather with low T_a and RH were found in the winter period while a warm T_a and higher RH with slightly lower u were noticed during the summer season (from June to September). However, the annual T_a and u show an increasing linear trend with a declining RH over the study period.

An energy balance model relay on the physical condition of the region was applied in order to comprehend the melting processes in the Phuche glacier based on their forcing variables (climatic and energy fluxes). The SWN was higher in summer relative to the winter season, and the annual distribution of SWN was minimum in 2014/15 (98.6 W m^{-2}) while maximum in 2015/16 (153.9 W m^{-2}) with an average value of 122.2 W m^{-2}. Similarly, the highest value of R_n was observed in 2015/16 followed by 2013/14 while lowest in 2014/15. On the other hand, the snow depth estimated winter precipitation was minimum (589 mm w.e.) in 2013/14 and maximum (980 mm

w.e.) in 2016/17 with a mean value of 734 mm w.e. Our results conclude that the SWN, R_n and sublimation/re-sublimation shows an increasing trend with varying rates while α and H_l indicate a declining trend, and no trend was observed in H_s. In the summer season, R_n and H_s were the main contributor in the total energy available for melt (F_s).

Our findings suggest that the region witnessed a higher loss in 2015/16 (–1.8 m w.e.) followed by 2012/13 (–1.2 m w.e.), while the loss was comparatively less (–0.1 m w.e.) during 2016/17. Among five consecutive years of observation, this study highlights the importance of summer temperature and winter season precipitation on glacier mass balance. Winter precipitation plays an important role in maintaining the α and compensating for the summer melting. The computed SEB ablation was validated with stake measured total melting, indicating a correlation of 0.91 at $p < 0.01$ between them.

Further, a comparison of estimated SEB with other glaciers of the same catchment and Himalayan region was carried out, suggesting that the SWN is the major energy source that controlled the surface melt. Our results indicated that the region was predominately influenced by sublimation than the re-sublimation process, which was well-matched with the other observations carried out over the High Mountain Asia. The comparison and validation of mass balance suggest that the obtained results are reliable as well as able to predict the future water supply and their management. In the future, a more detailed investigation of glacier mass loss and its implication on socio-economic aspects is needed. Also, a necessary preventative measure and appropriate law will be designed by the decision-maker to sustain and restore the ecosystem.

CHAPTER 5

ESTIMATION OF GLACIOLOGICAL BASED MASS BALANCE AND ITS RELATIONSHIP WITH CLIMATE DRIVERS IN THE PHUCHE AND KHARDUNG GLACIERS, LADAKH RANGE

5.1. INTRODUCTION

The Karakoram and Himalayan (KH) region is an essential freshwater reservoir stored in the form of snow and glaciers (Frey et al. 2014; Azam et al. 2018). The meltwater of Himalayan glaciers provides water for millions of people for their livelihood and agriculture purposes through major and sub-major rivers (Immerzeel and Bierkens 2012). Therefore, the changing pattern of glaciers not only influences the socio-economic aspect but also affect the demographic growth and create mismanagement in the ecosystem. Most KH glaciers have witnessed mass wasting and higher retreat in the past several decades (Bolch et al. 2012b; Kääb et al. 2012; Gardelle et al. 2013; Patel et al. 2021a). This change in glacier mass is mainly attributed by the climate fluctuation; consequently, the river runoff changes and further contributes to global sea-level rise (Richardson and Reynolds 2000; Radić and Hock 2011; Bolch et al. 2012b). In contrast, recent studies on Karakoram glaciers indicate a stable or advancing condition in the past few years (Bhambri et al. 2019; Farinotti et al. 2020b). Based on the importance of Himalayan glaciers and their varying pattern of Mass Balance (MB), a reliable estimation of glacier MB at the local scale is required to understand the water resources response with short-and long-term climate fluctuation.

The continuous monitoring of MB in Himalayan glaciers through in situ observation was rare (Soheb et al. 2020). However, the data collection and glacier change detection using ground observations have increased in recent years over the Himalayan region (Cogley 2011; Mandal et al. 2020). Especially in the Western Himalaya (WH), many glaciers were explored for a short- and long-term glacier characteristics estimation through the glaciological method (Azam et al. 2016; Singh et al. 2018c; Pratap et al. 2019; Mandal et al. 2020; Patel et al. 2021c). However, glaciers are still not well studied in the Ladakh range in terms of glaciological and meteorological observations, limiting scientific research at the glaciological front. In addition, only a few studies were available on the Rulung (Shrivastava et al. 1999) and Stok glaciers (Soheb et al. 2020) of the cold-arid region.

Based on these knowledge gaps over the region, we have selected two different glaciers of the cold-arid region for MB estimation to understand their response to climate change. This region consists of a glacier with a smaller surface area and receives less precipitation than other regions. These small glaciers are vital in maintaining the agricultural activities and socio-economic development of the region (Nüsser et al. 2012). Moreover, in the low precipitation year, the meltwater from snow and glaciers becomes a significant source of water for nearby areas (Thayyen and Gergan 2010).

5.2. RESEARCH QUESTIONS

- **Why is the study of cold-arid region glaciers important?** How is the glacier changed at different temporal scales? Is any significant change in glacier mass balance identified for the selected region? What are the distribution of glacier mass balance and their relation with climate variation?
- **What are the characteristics of the surface mass balance of glaciers in the cold-arid region?** How are the glacier physical and atmospheric processes controlling the mass balance? How does the locale scale glacier mass balance vary?
- **Are traditional glacier mass balance able to simulate the locale scale glacier mass balance evolution**? What is the significant change in glacier mass balance at different time scales? Is the glacier of the cold-arid region losing its mass for the past period? What is the possible implication of negative glacier mass balance on the region?

5.3. OBJECTIVE

- Quantification of glacier mass balance using the traditional technique at different temporal scales over the glaciers of the cold-arid region
- Assessing the glacier area changes, seasonal and annual MB, Accumulation Area Ratio (AAR), and shift in Equilibrium Line Altitude (ELA) with respect to time
- Analyzing the contributing factor that are responsible for contrasting glacier mass balance at same climatic zone

5.4. STUDY AREA

The Phuche and Khardung glaciers are located in the Ladakh range of the trans-Himalayan region (Figure 5.1). The Ladakh range is sandwiched between the Himalayan and Karakoram ranges

with high altitude glaciated region of India. It consists of almost 5000 glaciers, covering an area of 3187 km^2 and a volume of 816 km^3 (Koul et al. 2016). However, the majority of the glaciers (~79%) of this region have a relatively smaller surface area (< 0.75 km^2), and only 4% of glaciers are greater than 2 km^2. Due to the smaller glacier area and scarce precipitation, we have selected these two glaciers to understand the direct response to climate fluctuation. The small size glaciers are a good indicator of climate change (Koul et al. 2016).

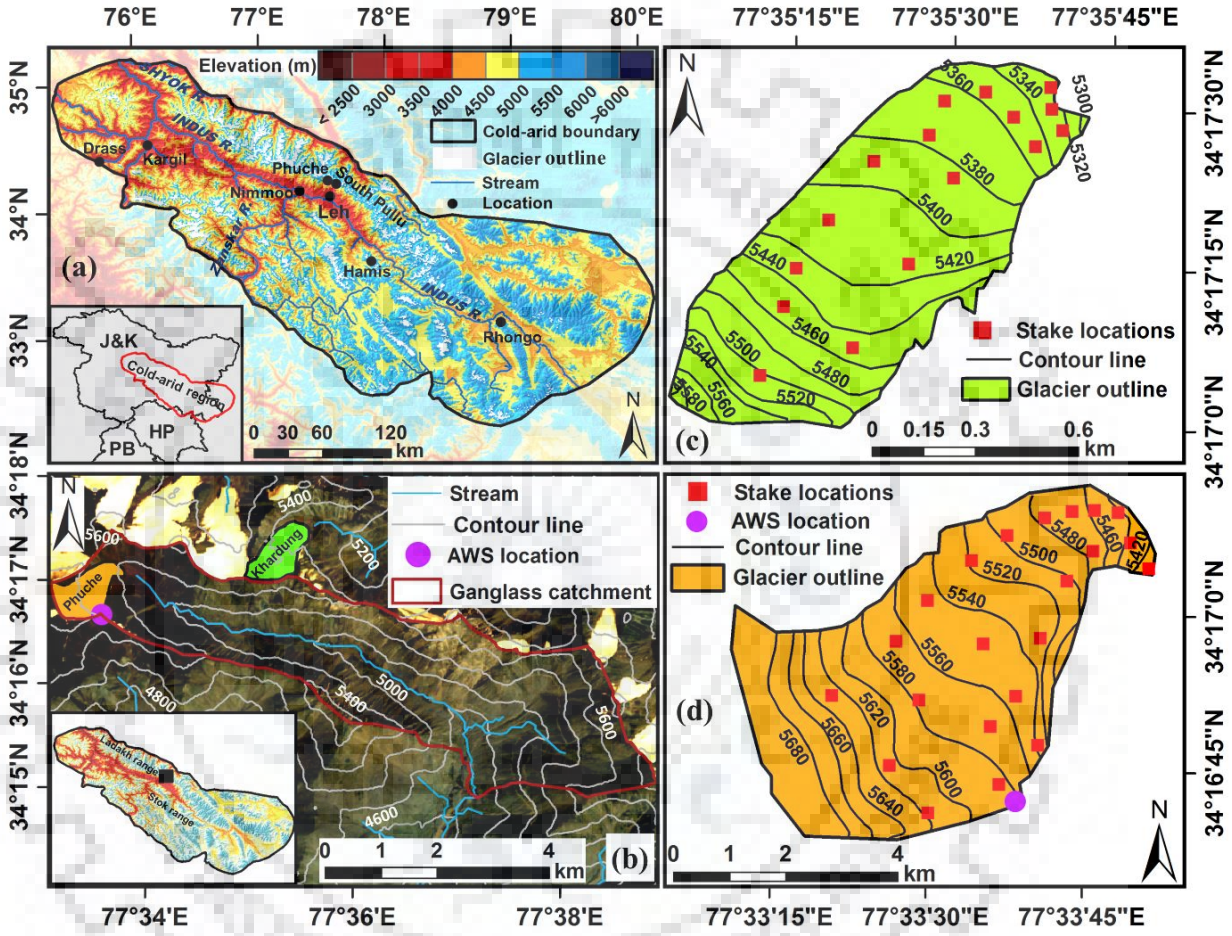

Figure 5.1. (a) Location map of the cold arid region with important locations are indicated over the Shuttle Radar Topography Mission (SRTM) void filled 90-m Digital Elevation Model (DEM) (https://earthexplorer.usgs.gov/), (b) Map of Phuche and Khardung glaciers with AWS location overlay on Landsat-8 composite image of (20 September 2017 with path 147 and row 036), and (c-d) indicate the location of ablation/accumulation stakes in each elevation band of the glaciers.

The Phuche and Khardung are cirque types with 1.3 km and 1.2 km long, covering an area of 0.62 km^2 and 0.56 km^{2,} respectively. These glaciers lie at 34° 17’ 4.5” N and 77° 33’ 48.12”E. The Phuche glacier is extended from 5400 to 5745 m a.s.l. while the Khardung glacier from 5320 to 5580 m a.s.l. with similar Northeast (NE) orientation. The headwater of the Phuche glacier

emerges in the Leh nallah, whereas the headwater of the Khardung glacier falls in the Shyok river basin. The meltwater of the Phuche glacier is the primary source of water for Leh city and the livelihood of nearby villages. To access this glacier, the south Pullu is the base camp around 25 km from Leh town on route to Khardug-La. The Phuche glacier is accessed by a trek of around 7 km through a gently sloped de-glaciated valley, while the Khardung glacier is accessed from the Nubra side after Khardung-La. Moreover, the nearest airport from the selected glacier is at Leh (30 km), and most of the assistance, including medical assistance, can be accessed by Border Road Organization (BRO)/Army Transport Control Post (TCP) at South Pullu.

5.5. DATA AND METHODS

5.5.1. DATA COLLECTION AND PROCESSING

The annual and seasonal (winter (October to April) and summer (May to September)) MB of the Phuche and Khardung glaciers were estimated for three hydrological years (2014–2017) using the glaciological method. For this point-scale analysis, the stakes were emplaced in a vertical hole drilled up to 1-2 meters into the glacier surface using the steam drill machine during the ablation period (generally the end of September). Then, the stake locations were monitored using Global Positioning System (GPS), and next year in ablation month, the same stake locations were measured. The snowpack thickness change (Δh) was calculated by subtracting the stake height of the present year from the previous year. Then, the Δh was multiplied with density to calculate the annual MB (b_a). If the Δh is positive, then the firn density (measured through snow-pit) was multiplied with Δh to calculate the b_a. On the other hand, when the Δh was negative, then we considered the density of ice (900 kg m^{-3}), previously used by many authors (Azam et al. 2012; Wagnon et al. 2013; Soheb et al. 2020). The fresh snow and firn density were measured at the various sites on the glacier surface during the ablation period. Their mean value was used in the MB estimation for a particular year. During the study period, the mean snow and firn densities were 210 and 493 kg m^{-3} for the Phuche and 223 and 520 kg m^{-3} for the Khardung glaciers, respectively.

For seasonal analysis, the winter MB (b_w) was measured by estimating the snowpack thickness and their density during the winter season (generally the end of May). The winter snowpack thickness was estimated for each stake on the glacier surface, and the mean snowpack density was calculated by digging various snow-pits across the glacier. The mean snowpack density was measured about 437 kg m^{-3} for the Phuche and 427 kg m^{-3} for the Khardung glaciers. After estimating the b_w, the measured b_a were used to obtain the summer MB (b_s) at point-scale. The

progressive thinning of the seasonal snowpack and ice melt in each stake was monitored at an interval of 15–20 days during ablation season (May to September) over the Phuche and Khardung glaciers (Figure 5.2 and 5.3). The progressive melting of snowpack indicates that how accumulated snow melted during the ablation months (From May to September). If the winter snowpack is melted early during the ablation period, then the probability of higher mass loss. This early melting of snowpack exposed the glacial ice surface for a longer period, which contributed to the prolonging melting of the glacier (Ryan et al. 2019).

And, this type of condition mainly occurred due to the less snowfall that occurred during the winter period. In this study, we have observed that the snowmelt end date in 2015, 2016, and 2017 was approximately 01 September 2015, 15 July 2016, and 22 August 2017 for the Phuche and 20 August 2015, 14 July 2016, and 8 August 2017 for the Khardung glacier, respectively (Figure 5.2 and 5.3). Our analysis illustrates that, in the year 2016, the snowmelt end date was earlier for both the glaciers, which shows higher melting of ice during 2016 than other years.

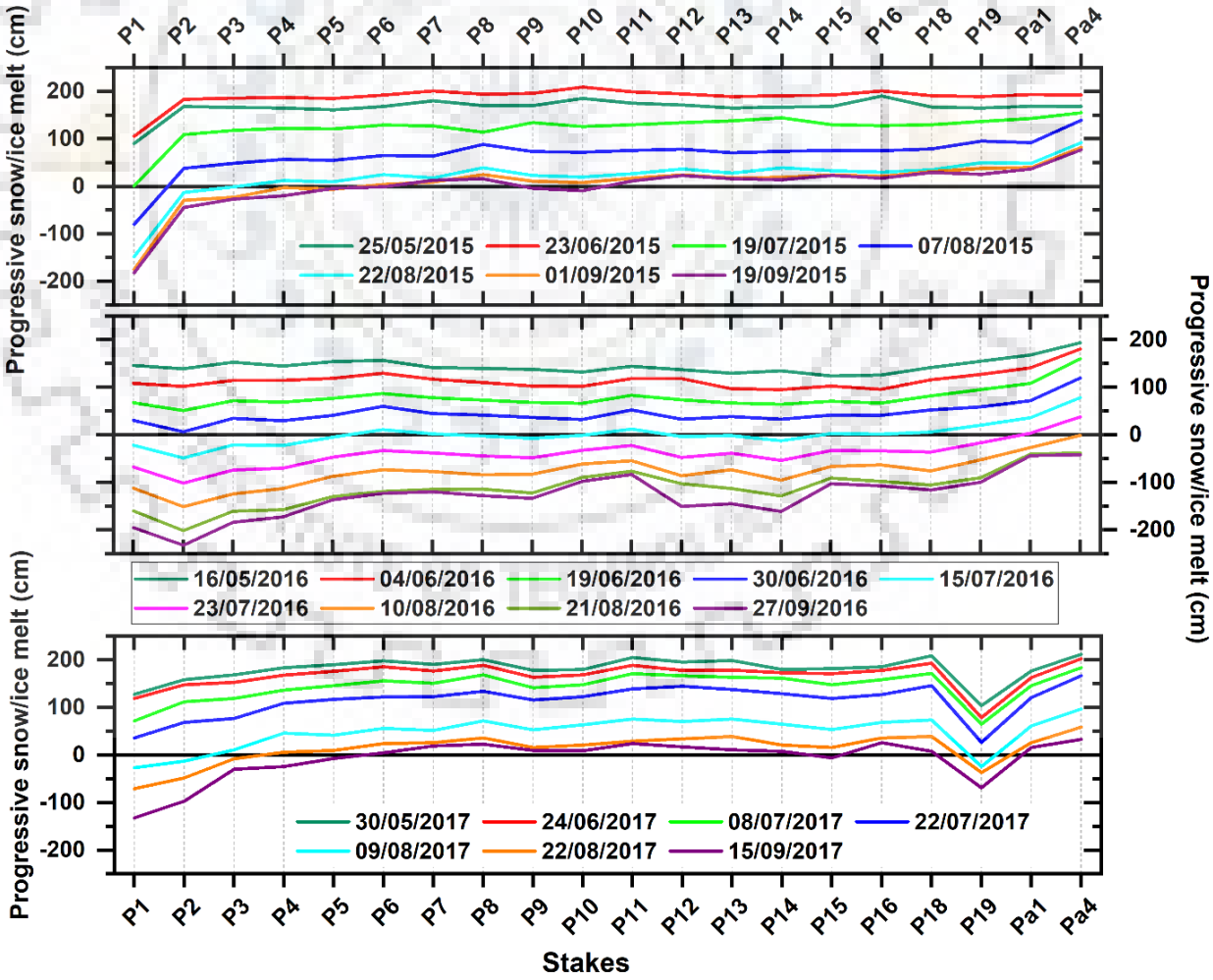

Figure 5.2. Progressive thinning of seasonal snowpack and ice melt in each stake from 2014 to 2017 ablation season (May to September) for the Phuche glaciers.

For glacier-wide MB estimation, the elevation range of the selected glaciers were divided into 20 m intervals. The MB is estimated at each elevation zone by multiplying the mean MB of stakes lies in the particular elevation zone with their corresponding zone area. Then, the summation of measured MB in each elevation zone was then divided by the total glacier area to obtain the glacier-wide MB. It can be expressed by Equation 5.1.

$$B_a = \frac{\int b_a \times dA}{A} \qquad \textbf{Eq. 5.1}$$

Where B_a is the glacier-wide MB balance in m w.e., b_a is the mean specific MB in m w.e., dA is the area of elevation zone in km^2, and A is the total area of the glacier in km^2.

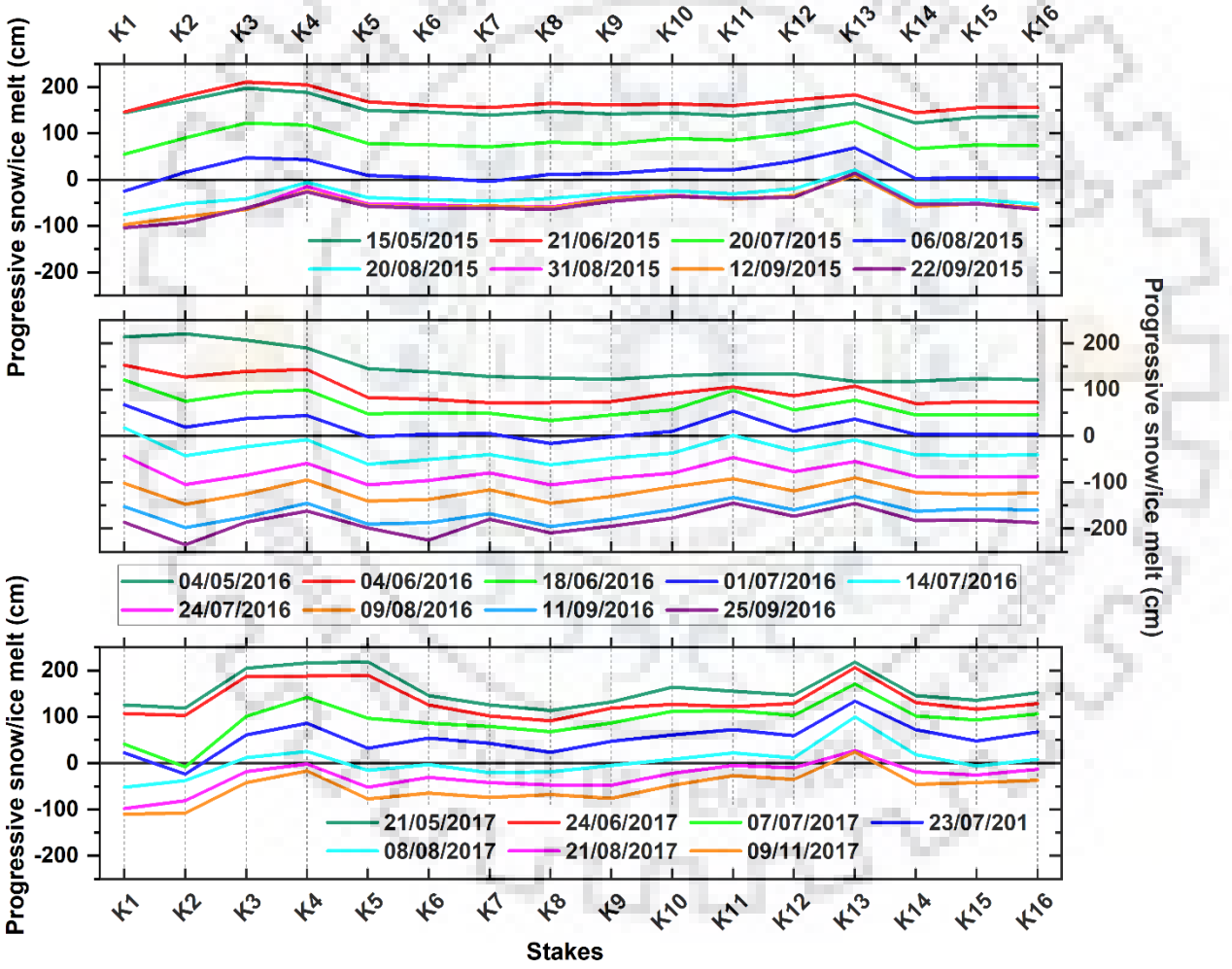

Figure 5.3. Progressive thinning of seasonal snowpack and ice melt in each stake from 2014 to 2017 ablation season (May to September) for the Phuche glaciers.

Further, the year-wise ELA position was mapped by establishing the relationship between annual MB and elevation. When the mass balance value starts moving towards the positive, the mean elevation of a particular elevation zone was considered ELA of that year.

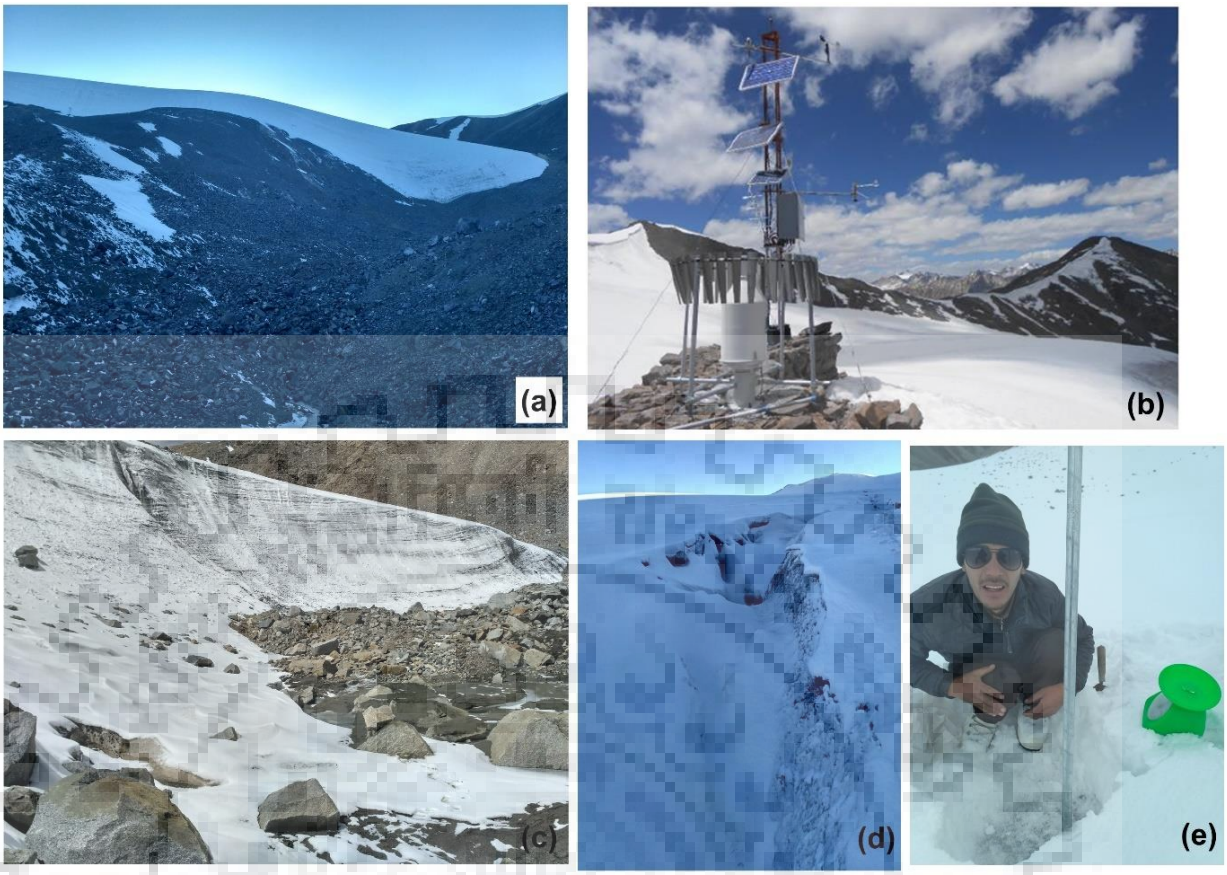

Figure 5.4. Field photographs of (a) Terminus of the Phuche glacier, (b) Location of AWS, (c) Terminus of the Khardung glacier, (d) Supraglacial stream in the Phuche glacier, and e) Measurement of fresh snow thickness and density during 9–15 September 2017.

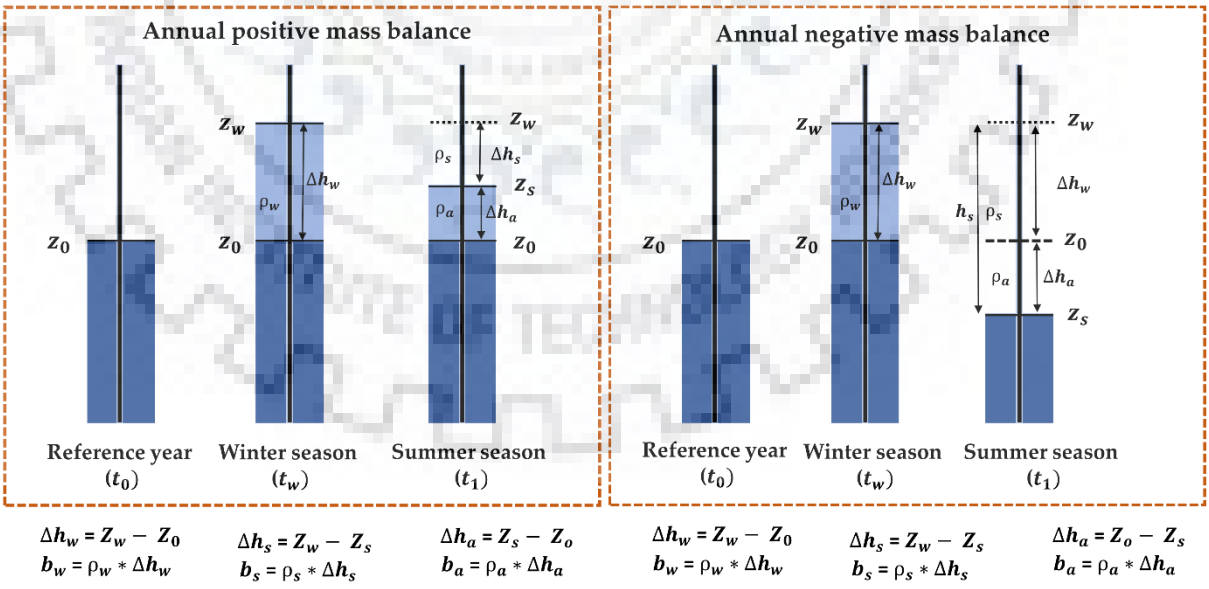

Figure 5.5. Schematic representation of annual positive (left) and negative (right) mass balance and insight processes on a glacier surface.

The shift in ELA helps in understanding the glacier movement and their health for the study period. Even the position of ELA was used to quantify the AAR of a glacier by dividing the area

above ELA (accumulation area) with the total glacier area. Some of the field photographs of the Phuche and Khardung glaciers were taken during 9–15 September 2017, as shown in Figure 5.4.

The pictorial representation of annual positive and negative MB through stake measurement is illustrated in Figure 5.5. Firstly, we understand the insight processes working on the glacier surface when the b_a was positive. Initially, snow stakes were mounted into the glacier surface at the end of the ablation period, used as a reference year (t_0) with a reference height of z_0. Then, in the winter season, the snow is accumulated, and it reaches till z_w at t_w. The amount of snow gained over the glacier surface (h_w) is measured by subtracting the z_o from z_w, which is positive. The height change (Δh_w) is multiplied with mean snow density (ρ_w) measured through snowpits to calculate b_w. The b_w illustrate the amount of snow water equivalent accumulated between t_0 and t_w. While, in the summer season, the snow surface is melted and the height of the stake reached at z_s at t_1. The difference between the stake height of the winter (Δh_w) and the summer (Δh_s) seasons provide the net height (Δh_a) for the b_a. If the winter accumulation is higher with lower summer melting, then the b_a was positive because the snow accumulation can able to compensate for the snow melting during the summer season for a particular year. On the other hand, if the summer melting was higher than the winter accumulation and not able to compensate for the mass loss caused in the summer season, then the b_a becomes negative for the glacier.

5.5.2. SATELLITE DATA

We have acquired Landsat-8 Operational Land Imager (OLI) Collection 2 Level 2 products for the ablation month of the year (15 September 2015, 17 September 2016, and 20 September 2017) during the study period. This data is downloaded free of cost from the United States Geological Survey (USGS) EarthExplorer (https://earthexplorer.usgs.gov/). A detailed description of the product can be found in Data Format Control Book (DFCB) (Engebretson 2020). The cloud-free Land Surface Temperature (LST) band 10 product was utilized over the study region of path 147 and row 36. The standard LST product is provided in Digital Number (DN) stored in a 16-bit unsigned integer format. It is converted into degree centigrade (°C) using the scaling factor provided by the USGS (https://www.usgs.gov/landsat-missions/landsat-collection-2-level-2-science-products), given by Equation 5.2.

$$\text{LST (°C)} = (0.00341802 \times \text{LST\_band10} + 149.0) - 273.15 \qquad \textbf{Eq 5.1}$$

5.5.3. METEOROLOGICAL VARIABLES

The meteorological variable, i.e., air temperature (T_a) was obtained (2m height from the surface) from the Automatic Weather Station (AWS) of data platform Cambell CR1000 installed at a high altitude (5600 m a.s.l.) of the Phuche glacier. The AWS was placed on the ridges of the Phuche glacier and equipped with various sensors, which recorded data on a half-hourly basis. However, we have considered the data acquired from Phuche AWS, as there was no AWS functional at the Khardung glacier, and both glaciers are close to each other with an aerial distance of ~2.5 km. A similar consideration of station data based on aerial distance was used by numerous authors (Azam et al., 2014; Soheb et al., 2020) in order to assess the changing pattern and their response to glacier MB change. The half-hourly interval data of the meteorological variables were converted into monthly and annually Positive Degree Day (PDD) and Freezing Degree Day (FDD) from 2014 to 2017.

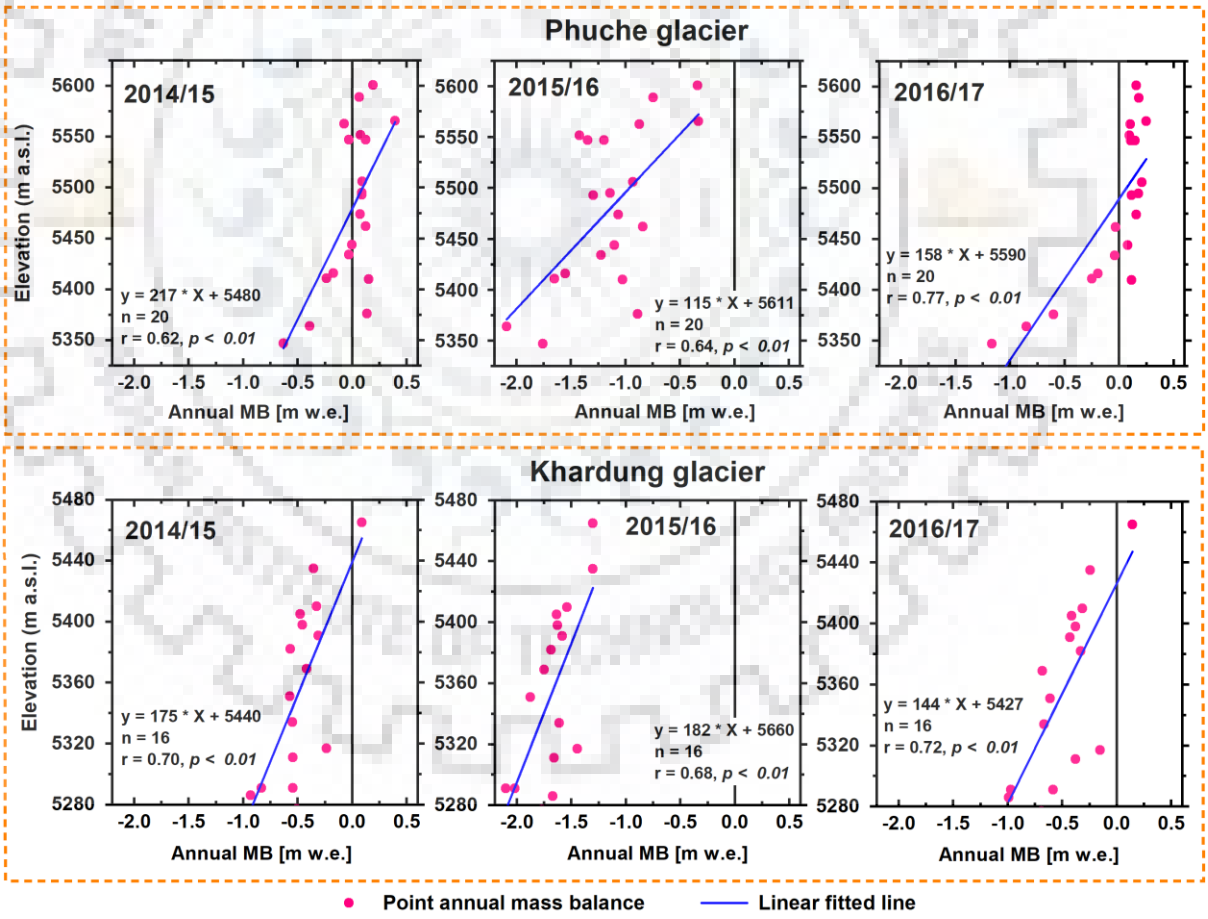

Figure 5.6. Point-wise annual glacier mass balance of the Phuche and Khardung glaciers for the period 2014–2017.

5.6. RESULTS

5.6.1 POINT-WISE GLACIER MASS BALANCE

The point-wise annual MB (b_a) measurement was mapped at different glacier altitudes for the observational period. The glacier MB shows higher melting at the lower altitude for the Phuche (< 5400 m a.s.l.) and Khardung (< 5320 m a.s.l.) glaciers. In contrast, the b_a was nearly equal in the upper reaches, i.e., > 5500 m a.s.l. and > 5400 m a.s.l. for the Phuche and Khardung glacier, respectively. The mean b_a for the Phuche glacier varied from –0.09 (2016/17) to –0.98 (2015/16) m w.e. with an average of –0.39 m w.e. (Table 5.1).

However, the higher (–0.11 m w.e.) and lower (–1.40 m w.e.) MB was observed in 2016/17 and 2015/16, respectively, with a mean value of –0.56 m w.e. for the Khardung glacier (Table 5.1). The relationship between b_a and altitude shows a significant positive correlation ($p < 0.01$) for the entire study period over the selected glaciers (Figure 5.6). This means that the MB is increasing while moving from lower elevation to higher elevation. During the 2015/16 periods, all stakes show a negative MB for both the glaciers and a comparatively higher mass loss was found in the Khardung than the Phuche glacier. Also, the maximum mass loss was observed in the lower elevation range, i.e., 5300–5400 and 5280–5320 m a.s.l. for the Phuche and Khardung glaciers, respectively. The steep slope was observed in 2014/15 for the Phuche and 2015/16 for the Khardung glacier; however, both years show a positive and negative MB for the selected glaciers, respectively. This indicates that the steep slope may have been responsible for less variability in the glacier MB change.

Annual vertical mass balance gradients (db_a/dz) were calculated in each hydrological year using all available stakes of the selected glaciers. The minimum db_a/dz was found in 2014/15 (0.18 m w.e. (100 m)$^{-1}$) for the Phuche (Table 5.1**)** and 2015/16 (0.26 m w.e. (100 m) $^{-1}$) for the Khardung glacier **(**Table 5.1). However, the maximum db_a/dz was witnessed during 2016/17 in both the glaciers. The mean vertical MB for the Phuche and Khardung glaciers over the entire study period was found to be 0.31 and 0.30 m w.e. (100 m) $^{-1}$, respectively.

The understanding of vertical MB gradient is an essential factor for analyzing the climate setting of a glacier (Oerlemans 2001), which is controlled by the change in air temperature at a different elevation. The observed mean gradient was lower than the other glacier of the same ranges (Stok glacier (0.61 m w.e. (100 m) $^{-1}$) (Soheb et al. 2020). A study over the Chhota Shigri glacier suggests a vertical mass balance gradient of 0.68 m w.e. (100 m)$^{-1}$ (Mandal et al. 2020). Also,

the vertical gradient of the Mera glacier, Nepal Himalayas was 0.46 m w.e. (100 m)$^{-1}$ calculated by Sherpa et al. (2017), which is nearly equal to the Khardung and Phuche glaciers. On the other hand, many other Nepal Himalayan glaciers, i.e., Pokalde (1.16 m w.e. (100 m)$^{-1}$), West Changri Nup (1.49 m w.e. (100 m)$^{-1}$), Rikha Smba Dhaulagiri (1.48 m w.e. (100 m)$^{-1}$) and Yala glacier (1.04 m w.e. (100 m)$^{-1}$) were reported a higher vertical gradient (Stumm et al. 2020; Wagnon et al. 2021) than the Mera glacier (0.46 m w.e. (100 m)$^{-1}$) and this studied glaciers. Similarly, the vertical gradient of the Patsio glacier was 0.47 m w.e. (100 m)$^{-1}$ (Angchuk 2021), which is close to the studied glaciers as well as the Mera glacier. A lower vertical gradient at the Khardung and Phuche glaciers could be occurred due to continuous snow accumulation on the glacier surface during the summer season, which significantly influences the ablation (Sherpa et al. 2017).

Table 5.2. Annual and seasonal point-scale and glacier-wide mass balance (m w.e.), dba/dz (m w.e. (100)-1), ELA (m a.s.l.), AAR (%) and density (kg m-3) for the Phuche and Khargung glaciers during 2014–2017.

	Phuche glacier				**Khardung glacier**			
	2014/15	**2015/16**	**2016/17**	**Mean**	**2014/15**	**2015/16**	**2016/17**	**Mean**
ba (m w.e.)	–0.09	–0.98	–0.09	–0.39	–0.17	–1.40	–0.11	–0.56
bw (m w.e.)	0.66	0.67	0.97	0.77	0.72	0.72	0.85	0.76
bs (m w.e.)	–0.75	–1.65	–1.06	–1.16	–0.89	–2.12	–0.95	–1.32
db/dz	0.18	0.36	0.38	0.31	0.28	0.26	0.36	0.30
Ba (m w.e.)	0.15	–0.79	0.13	–0.17	–0.22	–1.46	–0.20	–0.63
Bw (m w.e.)	0.67	0.67	1.03	0.79	0.71	0.68	0.77	0.72
Bs (m w.e.)	–0.52	–1.47	–0.90	–0.96	–0.93	–2.14	–0.97	–1.35
ELA (m a.s.l.)	5470	No ELA	5490	–	5510	No ELA	5490	–
AAR (%)	93.8	0.0	89.2	–	9.8	0.0	15.1	–
	Mean density measurement ablation month (September) (in kg m-3)							
Fresh snow	200	100	330	210	200	200	270	223
Firn	500	440	540	493	500	–	540	520
Ice	900	900	900	900	900	900	900	900
	Mean snowpack density during winter month (May) (in kg m-3)							
Snowpack	390	430	490	437	390	430	460	427

5.6.2. GLACIER-WIDE SEASONAL MASS BALANCE

During the study period, the glacier-wide seasonal MB was measured over the Phuche and Khardung glaciers to analyze the MB distribution at the seasonal scale and their contribution to annual MB change. Results demonstrated that the glacier-wide winter MB (B_w) of the Phuche glacier was almost similar (0.67 m w.e.) for 2014/15 and 2015/16 with a maximum value (1.03 m w.e.) attained in 2016/17 (Table 5.1). While, in the Khardung glacier, the B_w was minimum (0.68 m w.e.) in 2015/16, and the maximum value (0.77 m w.e.) was observed in 2016/17 (Table 5.1). The mean B_w of the Phuche and Khardung glaciers were 0.79 and 0.72 m w.e., respectively. It was noted that the winter precipitation over this range was comparatively lower than the other regions of the western Himalayas. Similarly, Soheb et al. (2020) have witnessed the mean winter MB was 0.71 m w.e. during 2011–2019 for the Stok glacier. On the other hand, the Chhota-Shigri glacier of the western Himalayas observed a mean winter MB of 1.11 m w.e. for the same observational period (2014–2017), demonstrated by Mandal et al. (2020). The glacier-wide summer MB B_s of both the glacier attain a higher negative value in 2015/16, whereas it was lowered in 2014/15 for the observational period. The mean annual B_s was –0.96 m w.e. for the Phuche and –1.35 m w.e. for the Khardung glacier from 2014 to 2017. On the other hand, Angchuk (2021) has revealed a mean summer MB of –1.49 m w.e. for the Patsio glacier, western Himalayas, during the same observational period. Similarly, Mandal et al. (2020) have demonstrated that the mean summer MB was –1.54 m w.e. for the Chhota-Shigri glacier of the western Himalayas during 2014–2017. Also, a study conducted by Soheb et al. (2020) over the same region glacier (Stok glacier) suggested that the average MB in the summer season was –1.17 m w.e. between 2011 and 2019.

The glacier-wide annual MB (B_a) distribution was maximum in 2015/16 and nearly equal for the rest of the years (2014/15 and 2016/17) for both the glaciers. Our findings revealed that the winter accumulation in 2015/16 was less than other years, and the summer period mass loss attained higher value for both the glacier, which means the lower winter accumulation is not able to compensate for the amount of melting caused in the summer season. Apart, the summer mass loss in the Phuche glacier was higher in 2016/17 (–0.90 m w.e.) than in 2014/15 (–0.52 m w.e.), on the other hand, the B_a of the same period was slightly higher in 2016/17 (–0.15 m w.e.) compared to 2014/15 (–0.13 m w.e.). This B_a variation occurred due to the winter precipitation, which was higher in 2016/17, easily compensating for the summer mass loss and stabilizing the glacier condition. Therefore, we can conclude that the B_a of both the glaciers were highly

dependent upon the winter accumulation and summer mass loss, which was mainly dominated by the change in temperature for a particular year.

5.6.3. GLACIER-WIDE ANNUAL MASS BALANCE

The B_a is one of the ways to understand the changing pattern of a glacier with respect to time which provides insight into the glacier-climate interaction. Therefore, this study includes annual MB measurement using the traditional stakes and snow pits-based observations for the Phuche and Khardung glaciers during 2014–2017 (Figure 5.6). For measurement, the start and end of the season in every year were demarcated as the day when the MB was maximum (end of winter) and minimum (end of the summer) to quantify the winter and summer MB from the time series data **(**Figure 5.7**)**.

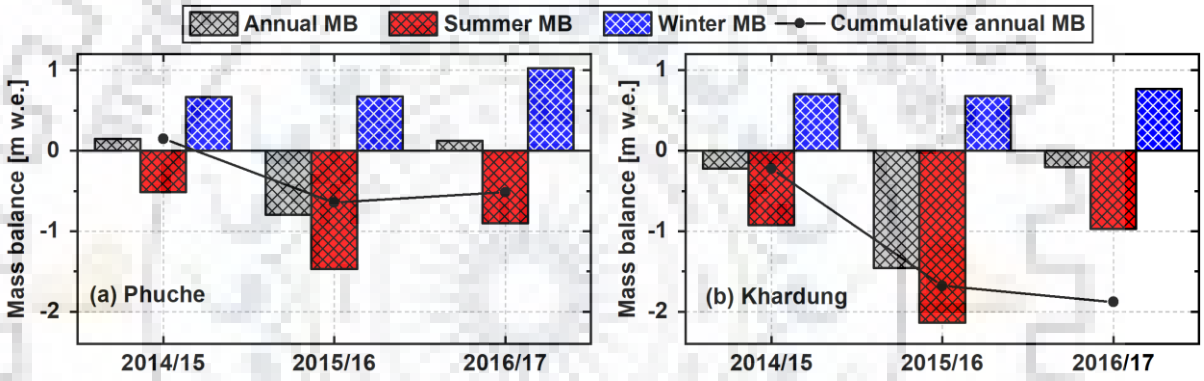

Figure 5.7. Seasonal, annual, and yearly cumulative mass balance of (a) Phuche glacier and (b) Khardung glacier for the period 2014/15–2016/17.

The measured annual MB of the Phuche glacier was ranged from –0.79 to 0.15 m w.e. with a mean of –0.17 m w.e. for the whole observational period. A slightly positive or balanced condition of annual MB was observed for 2014/15 and 2016/17 (Table 5.1). A similar positive MB of 2014/15 was observed by Angchuk (2021) over the Patsio glacier, western Himalayas. In contrast, the yearly MB of the Khardung glacier was varied from –1.46 to –0.20 m w.e. with an average of –0.63 m w.e. (Table 5.1). However, a relatively less negative MB was found in 2016/17 for the Khardung glacier. Angchuk (2021) has revealed a positive or stable MB was observed during 2016/17. Both glaciers witnessed high inter-annual variability with maximum mass loss in 2015/16, and the minimum was observed in 2016/17. A similar higher mass loss was illustrated by Soheb et al. (2020) over the Stok glacier using the glaciological method. Also, Angchuk (2021) has reported a higher negative MB in 2015/16 over the Patsio glacier, western Himalayas. Numerous authors have worked on the MB of the western Himalayan glaciers suggesting a higher mass loss during 2015/16 (Soheb et al. 2020; Mandal et al. 2020). The inter-

annual mass variation of the Khardung glacier was relatively more mass loss (3.7 times) than the Phuche glacier.

On the other hand, the Khardung glacier was experienced negative MB throughout the observational period whereas, in the Phuche glacier, only 2015/16 attained negative MB, and the other years (2014/15 and 2016/17) experienced positive at the glacier surface. A similar slightly positive MB of the Patsio glacier during 2014/15 was illustrated by Angchuk (2021). On the other hand, both the glaciers follow a declining pattern with a higher cumulative mass loss was observed in the Khardung (–1.88 m w.e. yr^{-1}) relative to the Phuche glacier (–0.52 m w.e. yr^{-1}) during the observational period (Figure 5.7).

5.6.4. ELA AND AAR

The annual MB were utilized to measure the year-wise ELA and AAR to understand the glacier response with climate variation in term of glacier areal changes (Figure 5.8). The yearly distribution of ELA suggests that in 2014/15, the ELA was shifted towards the accumulation and attained the maximum elevation in 2016/17(~5590 m a.s.l.) for the Phuche glacier. While the ELA was relatively less shifted in 2014/15 (5500 m a.s.l.) to 2016/17 (~5480 m a.s.l.) for the Khardung glacier. However, both the glaciers witnessed no ELA in 2015/16 because of the higher mass loss in each elevation zone. Soheb et al. (2020) have revealed that 2015/16 experienced a higher value of ELA, whereas it was lowest in 2014/15 over the Stok glacier, western Himalayas. Similarly, Angchuk (2021) has demonstrated that the ELA was maximum in 2012/13 (5366 m a.s.l.) followed by 2015/16 (5354 m a.s.l.) for the Patsio glacier from 2010 to 2017.

The AAR measurement of both the glacier highlighted that the Phuche glacier witnessed a higher Accumulation zone (AAR > 50%) for the entire observational period except for 2015/16. While, in the Khardung glacier, the AAR was less than 20% for the whole observation period with zero AAR in 2015/16. Overall, a larger accumulation zone was demarcated in the Phuche glacier rather than the Khardung glacier. This suggests that the Khardung glacier experienced a higher variability in terms of MB, ELA, and AAR, which means this higher interannual variability in the glaciers may be attributed to the effect of climate variation and anthropogenic activities. A combined effect of climate change and anthropogenic activities was highlighted by Bhutiyani (2014) over the north-western Himalayas.

5.6.5. INFLUENCE OF TOPOGRAPHICAL PARAMETERS ON MASS BALANCE

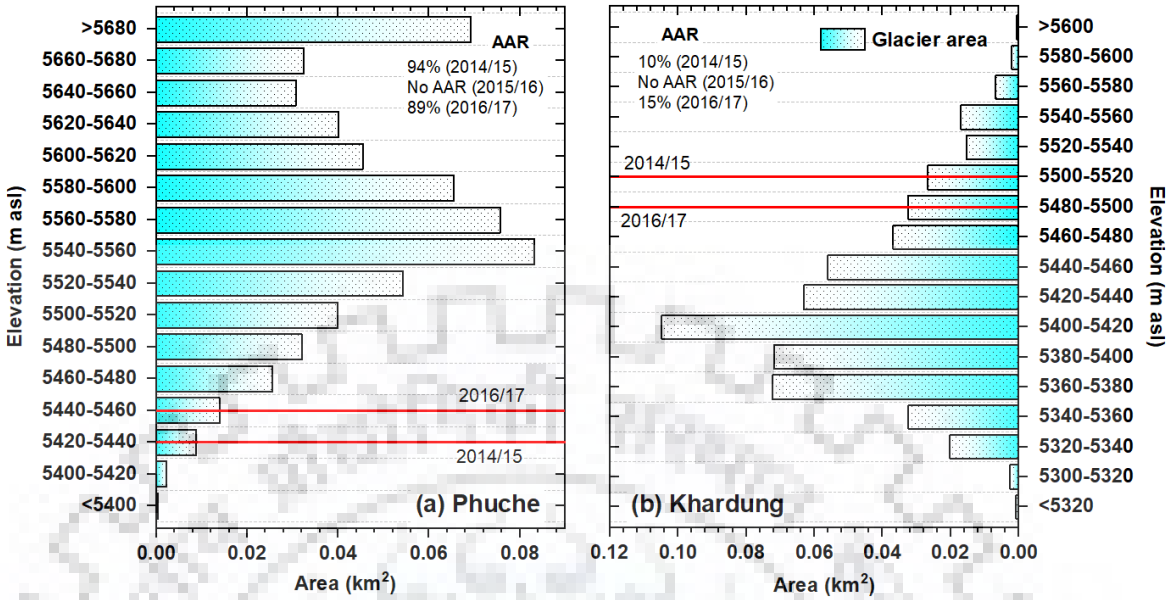

Figure 5.8. Elevation-wise glacier area distribution with its year-wise Equilibrium Line Altitude (ELA) and Accumulation Area Ratio (AAR) for the (a) Phuche and (b) Khardung glaciers during 2014/15–2016/17.

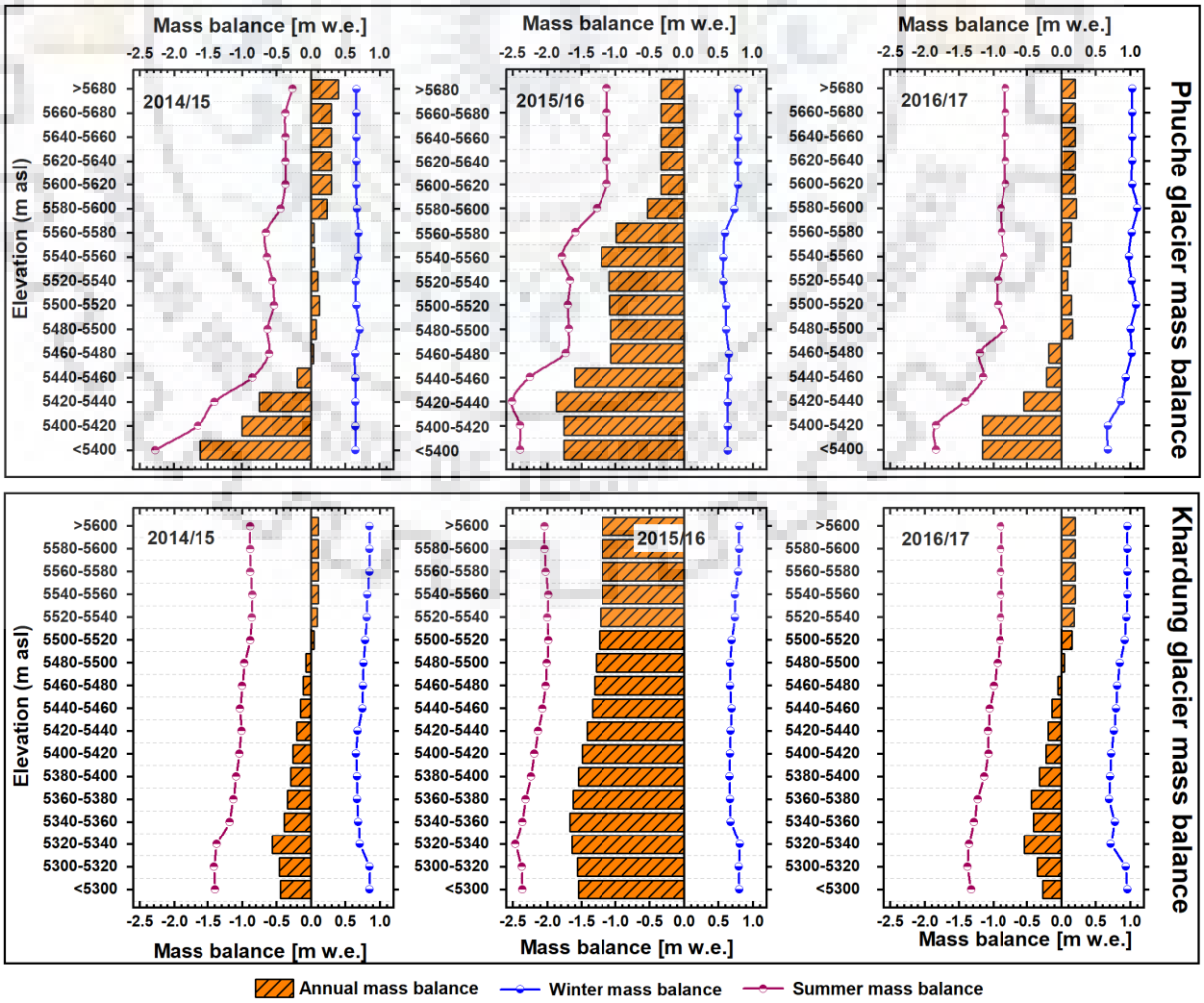

Figure 5.9. Elevation-wise glacier summer, winter, and annual mass balance variation in the Phuche and Khardung glaciers for the period 2014/15–2016/17.

The MB was measured at 20 m a.s.l. altitude interval from 2014 to 2017 over both the glaciers. Results demonstrate that the average annual MB was initially negative in the snout, then started increasing while moving towards the higher elevation and experienced nearly zero MB at the elevation range of 5580–5600 m a.s.l. for the Phuche glacier (Figure 5.9). On the other hand, the Khardung glacier has witnessed a negative value in the terminus and attained the highest negative value at 5320–5340 m a.s.l. (Figure 5.8). Then, the mean annual MB starts following a similar increasing pattern till 5520–5540 m a.s.l. and attain an almost uniform pattern in the accumulation zone of the glaciers.

Also, the mean annual MB distribution of the Khardung glacier shows a negative value in each elevation zone over the selected period. This throughout negative MB in the mean annual pattern may be occurred due to the exceptional mass loss in 2015/16. A similar higher melting of snow and glaciers in 2015/16 was illustrated by several authors (Randhawa et al. 2016; Blunden and Arndt 2017). This means the glacier experienced higher glacier mass loss which was not compensated with the winter accumulation; therefore, this glacier witnessed negative mass throughout the surface. A similar effect of summer MB on annual MB measurement was noticed by Soheb et al. (2020) over the Stok glacier, Ladakh range.

In the Phuche glaciers, the mean annual distribution shows positive MB above 5580 m a.s.l. and if we remove the outlier year (2015/16), then the mean annual MB of the Khardung glacier start positive from 5480 onwards. It was noticed that in the Phuche glacier, the aspect above the mentioned elevation was mostly the south quadrant (South, Southeast, and Southwest), while the Khardung glacier was mainly dominated by the North quadrant aspect (North, Northeast, and Northwest). Therefore, it was observed that the higher mass loss in the Khardung may predominately be driven by the aspect, as the south quadrant responds in less glacier melting than in the North quadrant. Numerous researchers have previously explained the theory of aspect-wise glacier melting (Das and Sharma 2019; Hugonnet et al. 2021; Wan et al. 2021).

On the other hand, the coefficient of variation for both the glaciers was quantified at each elevation interval during the observation period. Our findings suggest that the coefficient of variation value was higher at 5580–5600 m a.s.l. for the Phuche glacier, while in the Khardung glacier, it attained in the upper reaches of the glacier (from 5540 to 5620 m a.s.l.). The obtained observation pattern was well-matched with the finding of McGrath et al. (2018). Which slightly

increases across the glaciers during the summer season. Our finding also illustrates that the lower elevation of the Phuche glacier experienced higher melting than the Khardung glacier for the summer season. While the winter season receives mass accumulation across each elevation with higher heterogeneity in Khardung relative to Phuche glacier.On the other hand, the coefficient of variation for both the glaciers was quantified at each elevation interval during the observation period. Our findings suggest that the coefficient of variation value was higher at 5580–5600 m a.s.l. for the Phuche glacier, while in the Khardung glacier, it attained in the upper reaches of the glacier (from 5540 to 5620 m a.s.l.). The obtained observation pattern was well-matched with the finding of McGrath et al. (2018). Which slightly increases across the glaciers during the summer season. Our finding also illustrates that the lower elevation of the Phuche glacier experienced higher melting than the Khardung glacier for the summer season. While the winter season receives mass accumulation across each elevation with higher heterogeneity in Khardung relative to Phuche glacier.

5.7. DISCUSSION

5.7.1. ESTABLISHING RELATIONSHIP BETWEEN MB AND DEGREE DAYS

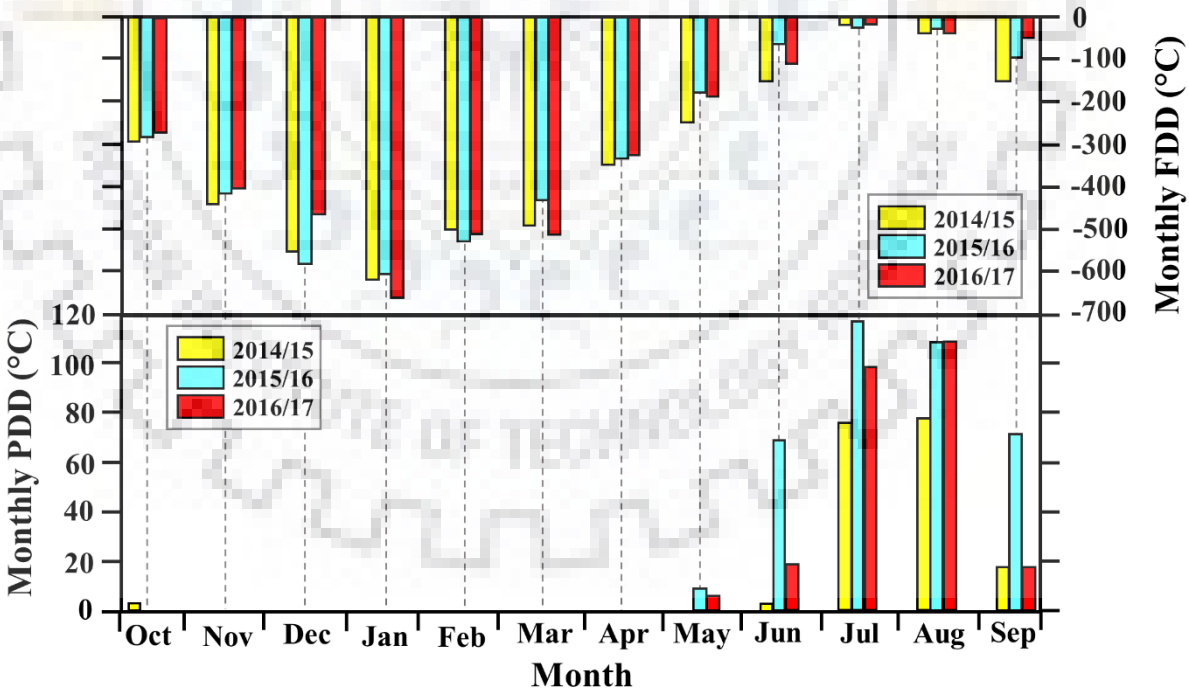

Figure 5.10. Month-wise Positive Degree Day (PDD) and Freezing Degree Day (FDD) over the Phuche glacier from 2014 to 2017.

The inter-annual PDD and FDD were plotted monthly to quantify the temperature forcing on the surface melt for the selected study area. The PDD and FDD were measured over the Phuche

glacier during the study period (Figure 5.10). The region experienced PDD for six months (May–October), with the maximum in July and August (JA). A similar PDD was observed by (Kayastha et al. 2003; Wiltshire 2014) over the Hindu Kush, Karakoram, and Himalayan regions. The combined PDD of JA varied from 157 to 225 °C with lower annual PDD in 2014/15 (176.7 °C) and higher in 2015/16 (375.2 °C). It was also noted that the slight increase in temperature might result in substantially higher PDDs and then potentially affect the melt of the region (Jury et al. 2019). The higher PDD indicates that, the higher negative glacier MB was closely related to the PDD pattern over the selected region. The glacier melt is directly proportional to the PDDs, which means this higher mass loss during 2015/16 may be induced due to higher PDDs during the period. While lower PDDs in 2014/15 may be responsible for the positive mass balance of the Phuche glacier.

On the other hand, the FDD was extended throughout the year, with the highest value in January, and the lowest was experienced in July. The maximum FDD was found in 2014/15 (–3860.9 °C), whereas the minimum value was observed during 2016/17 (–3546.5 °C) followed by 2015/16 (–3578.1 °C). The value of FDD was closely related in 2015/16 and 2016/17; however, the MB was found positive in 2016/17 for the Phuche glaciers. The FDD and PDD result also illustrates that the year 2016/17 has a lower PDD and higher FDD value than 2015/16, which may be responsible for positive mass balance. Overall, the monthly and inter-annual variation of PDD and FDD was closely linked with the mass balance change during the observational period. Therefore, we can conclude that the changes in the Phuche glacier mass balance may be attributed by the change in temperature that causes a direct implication on freezing and melting of the glacier surface.

5.7.2. OTHER FACTORS INFLUENCING THE MB

The MB of the selected glaciers shows a contrasting pattern during the period except 2015/16. This contrasting behavior of MB may be attributed to the location of the glaciers, elevation variation, and human intervention. The geographical location of the Khardung glacier was close (distance from road) to Khardung-la road, which is the gateway of Shyok and Nubra valleys, and a large number of heightened vehicle activity has taken place in this region. An increase in the number of vehicles and tourists over the Khardung la pass may be responsible for the higher mass loss of the Khardung glacier than the Phuche glacier. However, these two glaciers were close to each other with an aerial distance of ~2.5 km; therefore, the climatic condition may be similar at both glaciers.

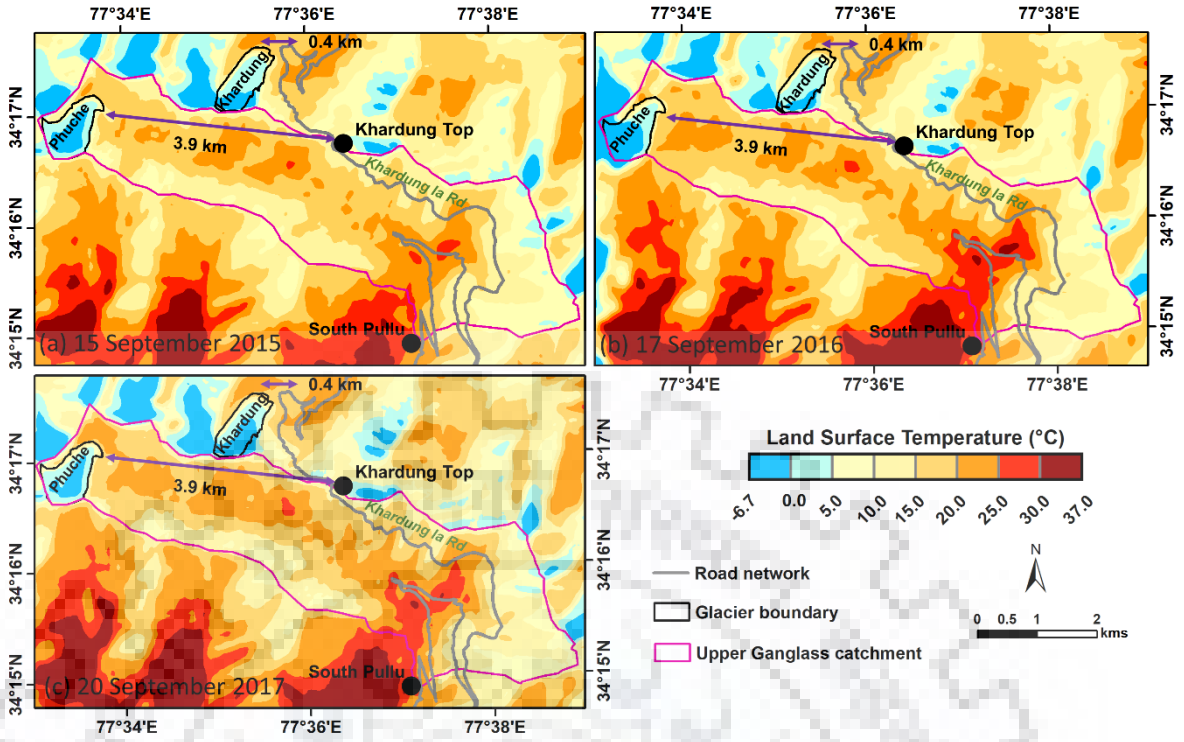

Figure 5.11. Spatial distribution of Land Surface Temperature (LST) acquired from Landsat-8 OLI for (a) 15 September 2015 (b) 17 September 2016, and (c) 20 September 2017 over the study region.

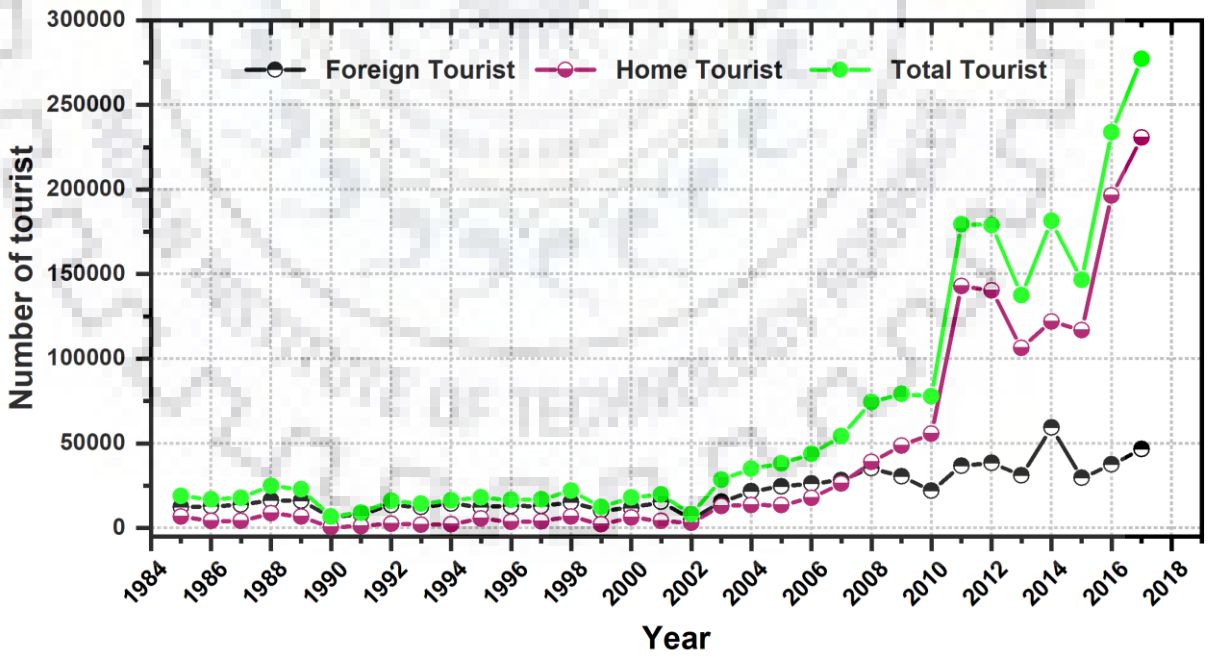

Figure 5.12. Annual foreign and home tourists of the Leh city, collected by the government of Ladakh from 1985 to 2017 (Source: https://leh.nic.in/tourism/).

To better understand human interaction and vehicle movement, the LST of Landsat 8-OLI were acquired to quantify the spatial temperature variation over the road (a buffer of 20m drawn) from

South Pullu to the snout of the Khardung glacier (Figure 5.11). Result demonstrates that the mean LST value across the road buffer was increasing from 2014/15 (17.3 °C) to 2016/17 (18.7 °C). Results also demonstrate that the LST was slightly lower in 2015/16 (18.4 °C) than 2016/17. This means the LST of the road buffer was relatively higher during 2015/16, which may become a contributing variable for glacier MB change. And, this LST variation might occur due to increased transport movement or the change in climatic variables. A similar pattern of glacier mass loss in the high transport region was demonstrated by Dhungel et al. (2018).

The higher value of LST over the road buffer may be attributed to the presence of a large number of vehicles which causes emission and is then responsible for higher glacier melting. A similar higher glacier melting impact by anthropogenic activities was illustrated by Marzeion et al. (2014). Apart from this, the number of tourists in Ladakh was increased over the past few decades, monitored by the Government of Ladakh. The observation of total tourists (Foreign+ home) indicates that the number of tourists started increasing from 2003 (above 30,000) and attained maximum value in 2017 during 1985–2017 (Figure 5.12). The pattern suggests that the number of foreign tourists consistently increased over the observational period while home tourists suddenly increased from 2010 onwards. Therefore, the total number of tourists shows an increasing trend from 1985 to 2017. Overall, the surface temperature variation and increase in tourism indicate that this might be another reason for the glacier mass loss after winter precipitation and rise in summer temperature. A necessary preventative measure is needed to develop for regulating the vehicle movement in the Khardung-la pass in order to maintain the ecosystem and environmental balance.

In addition, the elevation ranges of the Khardung glacier were lower than the Phuche glacier. Also, the Khardung glacier mainly lies in the North quadrant aspect (North, Northeast, and Northwest), whereas the Phuche glacier comes under the south quadrant. It was noticed that the North quadrant-based aspect glacier melted faster than the south quadrant glacier (Wan et al. 2021). Similarly, numerous researchers have previously explained the theory of aspect-wise glacier melting (Das and Sharma, 2019; Hugonnet et al., 2021).

5.7.3. COMPARISON OF MB WITH OTHER STUDIES

In this section, we have tried to compare the glacier MB pattern of the selected glaciers with other glaciers lies in the same catchment or the similar Himalayan zone (western Himalayas). The MB of the western Himalayan glacier was well explored with various MB estimation methods, including traditional, geodetic, and remote sensing-based approaches. In the Ladakh

range, two major studies based on glaciological methods were conducted by Soheb et al. (2020) and Shrivastava et al. (1999) over the Stok and Rulung glaciers during 1978–2019 and 1980/81 respectively. Authors have found that the glaciers were experiencing mass loss except in 2018/19; in that year, the MB witnessed a balance condition for the Stok glacier. However, they have also revealed a higher glacier mass loss in 2015/16 which was consistent with our observation for the Phuche and Khardung glaciers.

On the other hand, many other glaciers have experienced a similar mass loss during 2015/16 using the traditional MB method in the vicinity of western Himalayas (Mandal et al. 2016; Angchuk 2021). Other than the traditional method, numerous other glacier MB methods also witnessed similar glacier loss for the period 2015/16 (Tawde et al. 2017; Kumar et al. 2018, 2019; Negi et al. 2020; Patel et al. 2021a). This higher mass loss during 2015/16 was mainly attributed to the summer air temperature and winter precipitation. Many authors have demonstrated that the year 2015/16 received less snowfall and experienced less snow cover area for the period (Randhawa et al. 2016; Dharpure et al. 2020b). Also, Blunden and Arndt (2017) have noticed that 2016 was the 37th consecutive year of alpine glacier retreat across the world based on preliminary data.

Therefore, it was clear that the selected glaciers of the cold-arid region have witnessed a similar influence of climatic drivers on glacier MB, which means that the rise in temperature can influence the glacier MB in the future. For this, a detailed investigation of small/large glacier MB is required to understand the changing pattern and their influence on river runoff. Also, a necessary preventative measure will be designed and applied by the stakeholder to manage the water resource and reduce the water stress in the near future.

5.8. CONCLUSIONS

In the cold-arid region of the Ladakh range, this is the first study to analyze glacier MB using the glaciological method over the Phuche and Khardung glaciers for three hydrological years (2014 to 2017). The present study aimed to provide an insight into the stake-based glacier MB estimation and also analyze the influence of climate drivers on glacier MB. Results demonstrate that the annual MB of the Phuche glacier was ranged from –0.79 (2015/16) to 0.13 m w.e. (2016/17) with a mean of –0.17 m w.e. for the study period. While the yearly MB of the Khardung glacier was varied from –1.46 (2015/16) to –0.20 m w.e. (2016/17) with an average of –0.63 m w.e. Our finding also revealed that the glacier MB of the Khardung glacier was 3.7 times more mass loss than the Phuche glacier.

Other than this, the seasonal glacier MB was assessed for both the glacier between 2014 and 2017. The observation of seasonal MB suggested that the winter MB of the Phuche glacier was almost similar (0.67 m w.e.) for 2014/15 and 2015/16 with a maximum value (1.03 m w.e.) attained in 2016/17. While, in the Khardung glacier, the winter MB was minimum (0.68 m w.e.) in 2015/16, and the maximum value (0.77 m w.e.) was observed in 2016/17. It was also noted that the winter accumulation in 2015/16 was less than in other years; however, the mass loss was higher in summer, which indicates that the lower winter accumulation is not able to compensate for the amount of melting caused in the summer season. Apart, the ELA of the Phuche glacier was maximum shifted (~5490 m a.s.l.) towards the accumulation with low AAR (89%) during 2016/17. While, in the Khardung glacier, the maximum ELA shift was measured during 2014/15 at 5510 m a.s.l. with lower AAR (10%) for the entire period. It was also found that the year 2015/16 had no ELA for both the glacier due to higher summer mass loss.

After analyzing the seasonal, annual MB, the influence of air temperature (PDD and FDD) and other factors on MB variation were quantified to better understand the forcing variables in MB change. The result indicates that the maximum PDD was mainly concentrated in JA, and their combined values varied from 157 to 225 °C. The PDD was lower in 2014/15 (176.7 °C) and higher in 2015/16 (375.2 °C). While, the FDD was carried out throughout the year with maximum value in January, and the minimum was experienced in July. By combining the PDD and FDD, we can conclude that the changes in the Phuche glacier mass balance may be attributed by the air temperature variation, which directly or indirectly influences the glacier MB change.

On the other hand, the other contributing variables and their relation with glacier MB change were identified using the LST over the road buffer and by the number of tourists who visited Ladakh over the past period. Results demonstrate that these variables were also interconnected with glacier MB variation. And, these variables might be the reason for the contrasting behavior of the Khardung and Phuche glaciers MB for the studied period.

Overall, this study concludes that the selected glaciers of the cold-arid region have witnessed the influence of climatic drivers on glacier MB, which means that the temperature rise can impact the glacier MB in the future. A more detailed investigation of glacier MB and its implication on socio-economic aspects is required. Even a locale scale vehicle movement and their influence on glacier MB need to be studied in the future for designing the rules and regulations for the vehicles in Khardung-la pass. Also, a necessary preventative measure and appropriate law will be designed and applied by the decision-maker stakeholder to manage the water resource and reduce water stress in the near future.

CHAPTER 6

QUANTIFY THE COMBINED EFFECT OF HYDROCLIMATIC AND ANTHROPOGENIC FACTORS ON GROUNDWATER RECHARGE OVER THE GANGA RIVER BASIN

6.1. INTRODUCTION

The Ganga River basin sustains one of the densest global populations (~10% of the global population), the basin has serious water stress and quality problems from the past few years (Mukherjee et al. 2018). It has a serious problem with water stress and quality (IITs 2015). About 77% of the population is concentrated on the plain that supports extensive irrigated agriculture land, as ~85% of the rainfall accounts for 3–4 months of monsoon period (June to September) (Chaturvedi and Srivastava 1979). In addition, irrigation is being practiced using surface and groundwater during the dry months over the region, which led to a decrease in groundwater level. Moreover, the Ganga river is considered as a perennial river that sustains by groundwater discharge (as base flow) during the dry and non-monsoon periods (IITs 2015; Mukherjee et al. 2015; MacDonald et al. 2016) with its maximum flows in the monsoon season that contributes for an increase in overland flow (> 70% from rainfall) (Eriksson et al. 2009). Therefore, it is a major challenge to quantify the Groundwater Recharge (GR) and discharge over the densely populated region.

Various studies were carried out over different parts of India to estimate GR (Sakthivadivel 2007; Shah 2008; Mukherjee et al. 2015; CGWB 2017; Prasad and Rao 2018; Senthilkumar et al. 2019; Bhanja et al. 2019). For example, Mukherjee et al. (2015) suggested that GR rates show a higher unevenness in the diverse regions of India. They indicated that the overall GR shows a higher variability in the parts of India. Moreover, a rapid change in GR was reported in the GRB (Anand et al., 2018; Bons, 2018; Chaturvedi and Srivastava, 1979; IIT, 2015; World Bank, 2011) and its sub-basins (Kumar and Seethapathi 2002; Rajmohan and Prathapar 2013). Also, Vat et al. (2019) have highlighted that the ecological health of the GRB had deteriorated significantly due to high pollution, river modifications, flow regime changes, high levels of water abstraction, and hydropower generation. Therefore, an accurate estimation of the GR rate is essential for efficient and sustainable groundwater resource practices.

Quantification of GR is estimated using various approaches (de Vries and Simmers, 2002; Petheram et al., 2002; Scanlon and Cook, 2002), i.e., direct measurement, water-balance methods, Darcian approaches, tracer techniques, and empirical methods. The problem

encountered in each method was addressed by several authors (Gee and Hillel 1988; Allison et al. 1994; Stephens 1994; Kumar 1997). Additionally, Petheram et al. (2002) provide a review of various recharge estimation techniques applied in Australia. Also, Sophocleous (1991) discussed the soil water balance (SWB) approach and water table fluctuation (WTF) method to estimate the water recharge and its major uncertainties. The SWB method for recharge estimation has large data demands, and their reliability depends on how accurately the values of the variables are measured. For measuring the groundwater storage changes, the in situ measurement is expensive and not continuously available at a large spatial scale. Therefore, remote sensing data acquired from the Gravity Recovery and Climate Experiment (GRACE) satellite enable the estimation of groundwater storage at a large and continuous scale all around the world (Rodell et al. 2007). Recently, a few attempts have been made to estimate regional-scale GR rates using GRACE data (Henry et al. 2011; Gonçalvès et al. 2013; Ahmed and Abdelmohsen 2018; Wu et al. 2019). The obtained groundwater storage (GWS) changes can be used for average GR estimation based on an empirical approach of the WTF method (Henry et al. 2011). Nevertheless, GR is also often quite challenging or is difficult to be accurately estimated; therefore, more than one method should be used to verify the results (Sumioka and Bauer 2003).

6.2. RESEARCH QUESTIONS

- **How does the total water storage behave in response to change in surface or sub-surface water?** Is the groundwater recharge of Indian major river basins increasing or decreasing? What are the contributing variables responsible for the groundwater recharge change?
- **Which model of groundwater recharge estimation is best?** Do the gravimetric observation able to quantify the recharge accurately? Is the measured recharge well matched with the field observations?
- **How the mapping of groundwater recharge at a varying spatial scale behaves with the contributing variables?** Is groundwater recharge affected by changing climatic variables? Does the human intervention also impact the change in groundwater recharge?

6.3. OBJECTIVES

- Analyzing the spatio-temporal distribution of GRACE derived Groundwater Storage Anomaly (GWSA) and its trend at a seasonal and annual scale
- Quantification of groundwater recharge using a remote sensing-based, water balance approach and empirical equation-based approach

- Establishing linkage between estimated GR and water fluxes components (P, ET, runoff, and SM)

6.4. STUDY AREA

The Ganga basin is one of the most populous (about 440 million people) river systems in the World (Anand et al. 2018). The basin is situated in the northern part of the country and lies between latitude 21º 32' 8.6" – 31º 27' 36.2" N and longitude 73º 14' 33.4" – 90º 53' 18.9" E, over an area of 10,86,000 km^2 (Figure 6.1).

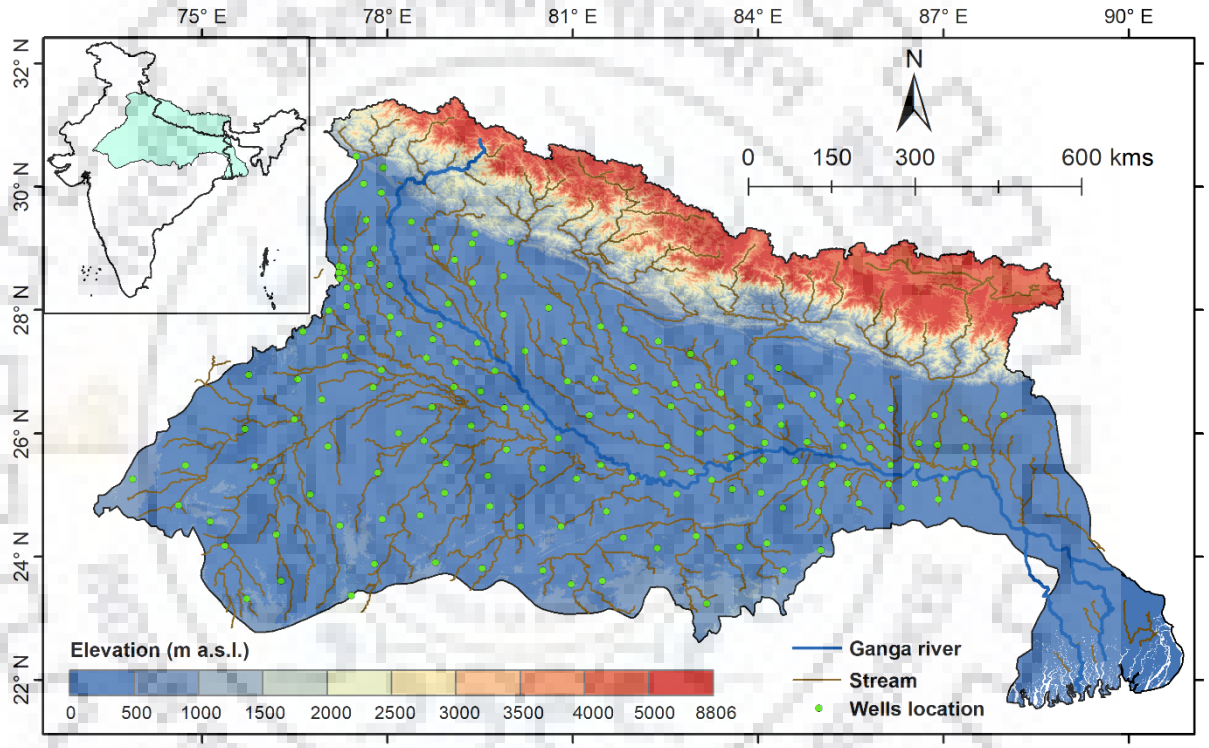

Figure 6.1. Location map of the Ganga river basin and its tributaries along with varying elevation. The point location shows the spatial distribution of observational wells collected from the Central Ground Water Board.

The basin outspreads in four countries, i.e., India (79%), Nepal (14%), Bangladesh (4%), and China (3%). In India, it covers an area of 8,61,452 km^2, which is nearly 26% of the total geographic area of the country (India-WRIS 2012). The Ganga basin originates in the Himalayan Mountains at the snout of the Gangotri glacier at an elevation of ~7000 m a.s.l. The confluence of the Bhagirathi River and Alaknanda Rivers joins in the town of Devprayag, then officially called the Ganga River. The main tributaries of the Ganga River are the Yamuna, the Ramganga, the Gomti, the Ghaghra, the Sone, the Gandak, the Kosi, and the Mahananda. And, it flows for about 2,510 km, generally southeastward, through a vast plain to the Bay of Bengal.

The main source of water in the Ganga River is a surface runoff generated by precipitation (~66%), base flow (~14%), glacier melt (~11.5%), and snowmelt (~8.5%). The basin received 84% of total rainfall during the monsoon season (June to October). Though, the monsoon season accounts for 75% of the rain in the upper basin and 85% of the rain in the lower basin (Shrestha et al. 2015). The elevation range varies from sea level to the highest mountain peak (~8850 m a.s.l) in the world.

6.5. DATA USED

6.5.1. GRACE TERRESTRIAL WATER STORAGE ANOMALY

In this study, 168 monthly solutions of GRACE Terrestrial Water Storage Anomaly (TWSA) data (level-3 RL-05, special harmonics) with 1° × 1° grid resolution were obtained from three research agencies, i.e., Center for Space Research (CSR), NASA Jet Propulsion Laboratory (JPL), and the German Research Centre for Geosciences (GFZ). Seventeen months of images were missing in the datasets that were replaced by the mean value of sequent months (before and after) (Long et al. 2015; Yang et al. 2017). Further, an average TWSA of the three data centre's solutions (JPL, GFZ, and CSR) were used to reduce the gravity field noise (Sakumura et al. 2014; Xiao et al. 2015). This data was used for GWSA and GR estimation over the GRB between January 2003 and December 2016 (14 years). The TWSA comprises the GWSA, Soil Moisture Storage Anomaly (SMSA), Canopy Water Storage Anomaly (CWSA), Snow Water Equivalent Anomaly (SWEA), and Surface Water Storage Anomaly (SWSA) (Thomas et al. 2017) is expressed by Equation 6.1.

$$GRACE_{TWSA} = GWSA + SMSA + CWA + SWEA + SWSA \quad \textbf{Eq. 6.1}$$

6.5.2. GLDAS LSM OBSERVATION DATA

The Global Land Data Assimilation System (GLDAS) data integrates the hydrological components obtained from the ground and satellite-based observation with fine spatial and temporal resolution (Rodell et al. 2004). This data comprises four Land Surface models (LSM) data, i.e., the Community Land Model (CLM2.0) (Dai et al. 2003), Variable Infiltration Capacity (VIC) (Liang et al. 1994), Noah (Chen et al. 1996; Ek et al. 2003), and Mosaic (Koster and Suarez 1996) at 1°x1° grid resolution. In this study, a Total Water Storage (TWS) was estimated for each LSM by the summation of SMS, SWE, and CWS at a monthly scale. And, the average of four TWS datasets was used to estimate the monthly $GLDAS_{TWS}$ with minimum bias (Feng et al. 2013; Yang et al. 2017). None of these LSMs dataset includes GWS and SWS (Dai et al. 2003; Rodell

et al. 2004). Nevertheless, there might be a contribution of other sources of SWS (reservoirs, canal, tank, ponds, etc.) in groundwater recharge, which can be ignored, accounting for a relatively small proportion of TWS changes (Rodell et al. 2009). Many studies neglected the SWS changes for GWS estimation (Moiwo et al., 2009; Rodell et al., 2009, 2007; Strassberg et al., 2007; Tiwari et al., 2009). The estimated $GLDAS_{TWS}$ was converted into anomalies ($GLDAS_{TWSA}$) with the same consideration of GRACE data (baseline period of January 2004 to December 2009). The monthly GWSA was obtained by subtracting the $GLDAS_{TWSA}$ with $GRACE_{TWSA}$ through rearranging the Equation 6.1. GLDAS has been used in many studies to isolate the GWSA from the GRACE derived TWSA in different regions of the world (Leblanc et al., 2009; Rodell et al., 2009, 2007; Tiwari et al., 2009).

6.5.3. ERA-5 REANALYSIS DATA

The European Centre for Medium-Range Weather Forecasts ReAnalysis version 5 (ERA-5) Land is a monthly global reanalysis data (1981–present) available at 9 km spatial resolution and free to download from the Climate Data Store (https://doi.org/10.24381/cds.68d2bb30). In this study, we have acquired monthly P, ET, runoff and T_a for understanding the hydroclimatic variability as well as GR estimation over the GRB from 2003 to 2016. The performance of ERA-5 datasets (P, ET, SM, runoff, and T_a) was evaluated against the observed gridded datasets from the India Meteorological Department by Mahto and Mishra (2019). They have reported that the ERA-5 performed better than other reanalysis products, and it can be used for hydrological modeling in India. Likewise, Albergel et al. (2018) also revealed that ERA-5 has a consistent improvement over ERA-Interim products.

6.5.4. GROUNDWATER LEVEL MEASUREMENTS

The groundwater level (GWL) data were acquired from the Central Ground Water Board (CGWB, India) from January 2003 to December 2016. CGWB records the GWL data four times in a year, such as a winter (January), pre-monsoon (April/May), monsoon (August), and post-monsoon (November) (CGWB 2017). In this study, we have used a total number of 167 wells over the GRB for validating the estimated GR from six different methods.

6.6. METHODOLOGY

6.6.1. ESTIMATION OF GR

6.6.1.1. Henry and Wu methods

In this study, we have used GRACE-derived GR estimation methods discussed by Henry et al. (2011) and Wu et al. (2019). The conceptual diagram of these two methods is shown in Figure 6.2. The GR from the Henry (R_{Henry}) method was estimated by subtracting the trough (S_B) of GWSA from peak (S_P) value in each year. In contrast, the GR from the Wu (R_{Wu}) was assessed by the summation of net recharge (R_S) and the recharge that balances discharge (R_D). Generally, the R_{Wu} of each year was calculated through the antecedent recession curve. It is the difference between the peak (S_P) of GWSA and the extrapolated value from antecedent recession curve to the time of the peak (S_L). The estimated R_{Wu} from Wu method can be represented by the following Equation 6.2:

$$R_{Wu} = \frac{\Delta GWSA}{\Delta t} = \frac{S_P - S_L}{\Delta t} = R_S + R_D \qquad \textbf{Eq. 6.2}$$

The primary assumption of the Henry method was that the unrealized recession is negligible, while the Wu method estimates and corrects for it episode by episode (Nimmo et al. 2015).

6.6.1.2. Soil water balance (SWB) approach

The Soil Water Balance (SWB) approach has been widely used for GR estimation (Rushton and Ward 1979; Sophocleous 1991; Dripps and Bradbury 2007; Demlie 2015). This method is to estimate the temporal and spatial distribution of GR (R_{SWB}) in the GRB for the period 2003-2016. The month-wise R_{SWB} is estimated using the following Equation 6.3:

$$R_{SWB}(t) = P(t) - ET(t) - Runoff(t) - \Delta S(t) \qquad \textbf{Eq. 6.3}$$

Where t is the specific time, P is the precipitation, Runoff is the total surface and sub-surface drainage, ET is evapotranspiration, and ΔS is the change in soil water storage in the unsaturated zone. The R_{SWB}^{N} is estimated for the monsoon season by considering the assumption, i.e., if the P > ET, then residual water (P-ET-R) that enters the soil reservoir will cause an increase or decrease in the water level. Although, if the residual water is higher than the positive change of soil water (assume that GWL will not change if ΔS is negative), then we subtract ΔS from residual water, and the remaining water considered as a R_{SWB}.

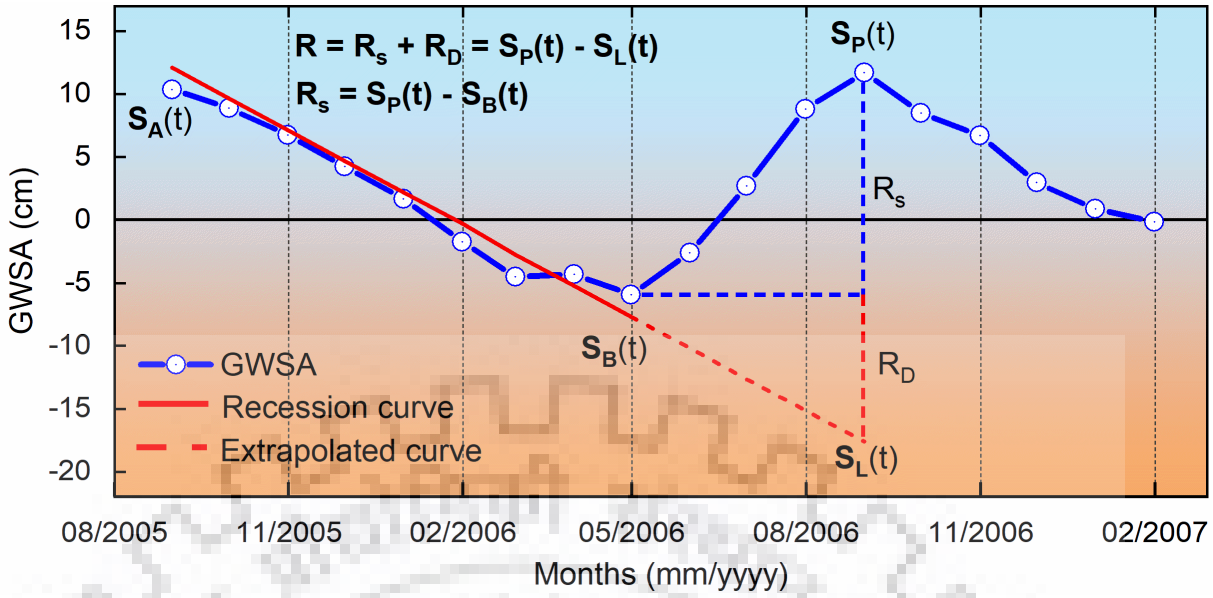

Figure 6.2. The conceptual diagram of Henry and Wu methods to show the GWSA from 08/2005 to 01/2007 for estimating GR. (Note: S_A is the peak in the previous year (2005), S_B is the trough of decline and S_P is the peak of the rise in the next year (2006). The solid line is the antecedent recession curve that indicate the best-fit of GWSA as a function of time between A and B. Furthermore, S_L is the GWSA extrapolated from antecedent recession curve to the time of the peak. The dashed line is the unrealized recession from S_B to S_L.

6.6.1.3. Groundwater storage change (GWSC) approach

The GR from GRACE derived GWSA (R_{GWSC}) were acquired by assuming that the total water storage change (TWSC) is equal to the incoming and outgoing water fluxes. Also, Syed et al. (2008) have demonstrated that the difference between the incoming (P) and outgoing (ET and Runoff) water fluxes, i.e., residual water content is equal to satellite estimated TWSC. It can be represented by the following Equation 6.4.

$$GRACE_{TWSC}(t) = P(t) - ET(t) - Runoff(t) \quad \textbf{Eq. 6.4}$$

For TWSC estimation, $GRACE_{TWSC}(t) = GRACE_{TWSA}(t) - GRACE_{TWSA}(t-1)$

The R_{GWSC} obtained by combining the equations 6.3 and 6.5 (discussed in next section 6.6.1.2), expressed by Equation 6.4**.**

$$GRACE_{TWSC}(t) = P(t) - ET(t) - Runoff(t) = GR_{SWB}(t) + \Delta S(t) \quad \textbf{Eq. 6.5}$$

Where, GR_{SWB} is corresponding to R_{GWSC} and ΔS is equal to the change in GLDAS TWSA ($GLDAS_{TWSC}(t) = GLDAS_{TWSA}(t) - GLDAS_{TWSA}(t-1)$). The R_{GWSC} can be calculated by rearranging the Equation 6.5, expressed by Equation 6.6.

$$R_{GWSC}(t) = GRACE_{TWSC}(t) - GLDAS_{TWSC}(t) = GWSA(t) - GWSA(t-1) \quad \textbf{Eq. 6.6}$$

Where R_{GWSC} can be either positive or negative. The summation of positive R_{GWSC} were considered for recharge estimation during the monsoon period (June to September).

6.6.1.4. Kumar and Seethapathi method

An empirical relationship between GR and P was developed by Kumar and Seethapathi (2002) for the upper Ganga canal system. It was derived by fitting the estimated values of GR and the corresponding values of P in the monsoon season through the non-linear regression technique, expressed by Equation 6.7:

$$R_{Kumar} = 0.63(P - 15.28)^{0.76} \quad \textbf{Eq. 6.7}$$

Where, R_{Kumar} is the GR from precipitation (inch), and P is the mean precipitation in monsoon season (inch). In this study, we have used this empirical relationship for R_{Kumar} estimation over the GRB from 2003 to 2016.

6.6.1.5. Rainfall infiltration factor (RIF) method

The rain-fed GR was estimated using the Rainfall Infiltration Factor (RIF) (CGWB 2017) for the monsoon period over the GRB. It states that the GR (R_{RIF}) is a product of rainfall infiltration factor (f) and P, which can be expressed by Equation 6.8:

$$R_{RIF} = f \times P \quad \textbf{Eq. 6.8}$$

The value of f ranged from 0.08 to 0.25, with a mean value of 0.165 (for the unconsolidated formation of alluvium soil). The major portion of the GRB comes under the Alluvium soil (CGWB 2017); therefore, the mean value (0.165) of f is adopted for R_{RIF} estimation during 2003-2016.

6.6.2. RECHARGE ESTIMATION USING GROUNDWATER LEVEL DATA

The WTF method is generally used for groundwater storage or recharge estimation based on groundwater levels data (Sophocleous 1991; Healy and Cook 2002; Heppner and Nimmo 2005).

The GR (R_{GWL}) can be calculated by multiplying the water-table rise (Δh) (assume that the rainfall is the key parameter for recharging the aquifer) over a specified period of time (Δt) with the specific yield (S_y) by following Equation 6.9:

$$R_{GWL} = S_y \times \frac{\Delta h}{\Delta t} \quad \textbf{Eq. 6.9}$$

When Δh is equal to the difference between the peaks of the rise and low point of the extrapolated antecedent recession curve at the time of the peak (extrapolation method), then the WTF method produces the total recharge. When Δh is the difference in heads between two points in time, the WTF method produces a value for net recharge (no extrapolation) (Healy and Cook 2002). In this study, we have estimated the R_{GWL} based on pre-monsoon and monsoon GWL data (used for Δh estimation). Also, a constant 0.044 value of S_y was used over the entire GRB for R_{GWL} estimation, reported by Bhanja et al. (2016). Many studies have been used as a constant S_y for the entire region (Rodell et al. 2009; Panda and Wahr 2016; Mukherjee et al. 2018).

6.6.3. STATISTICAL ANALYSIS

To identify the trend in the GR and hydroclimatic variables, a nonparametric Mann-Kendall (MK) (Mann 1945) and Sen's slope (Sen 1968) methods were applied to the annual and seasonal data during 2003-2016. The Pearson's correlation coefficient (R) was also used for analyzing the dependency of each parameters. In addition, standard anomalies were calculated for the GR and hydroclimatic variables by using the following Equation 6.10:

$$z = \frac{x-\mu}{\sigma} \quad \textbf{Eq. 6.10}$$

Where z is the standard anomaly, x is the annual variable, μ is the mean of the variable during the study period, and σ is the standard deviation. Additionally, the performance of GR acquired from different methods was analyzed with R_{GWL} based on bias [(estimated - observed) ×100/observed], Root Mean Square Error (RMSE), and an overall score. The score (out of 10) is assigned for each method based on the following Equation 6.11, suggested by Graham et al. (2019).

$$Score = \left[R + \left\{1 - \frac{abs(bias)}{RANGE}\right\} + \left\{1 - \frac{RMSE}{RANGE}\right\}\right] \times \frac{10}{3} \quad \textbf{Eq. 6.11}$$

Where RANGE is the maximum range (difference between the maximum and minimum values) of the estimated R_{GWL} during the study period.

6.7. RESULTS AND DISCUSSIONS

6.7.1. GRACE-DERIVED GROUNDWATER STORAGE ANOMALY

The monthly comparison of various GRACE TWSA products (Figure 6.2a) and GLDAS models (Figure 6.3b) was extracted over the GRB from 2003 to 2016; the overall results were consistent (Figure 6.3a,b). Besides, the estimated mean water storage components were used to understand the seasonal and annual patterns of the datasets. It indicates that the seasonality between $GRACE_{TWSA}$ and $GLDAS_{TWSA}$, generally, increases from May to September and start decreasing during the rest of the year. Despite that, a shift in peak and trough months were observed in 2013 (2-months) and 2016 (1-month). This shift may be occurred due to the poor timing of simulated soil-water storage changes (Grippa et al. 2011; Henry et al. 2011; Ndehedehe et al. 2016; Wu et al. 2019). Moreover, the time-series of spatial mean monthly GWSA were derived based on the difference between $GRACE_{TWSA}$ and $GLDAS_{TWSA}$ (Figure 6.3c). The GWSA pattern was similar to the $GRACE_{TWSA}$ and $GLDAS_{TWSA}$, with a maximum in September and a minimum in May. However, the seasonality in GWSA was apparently weaker than that of the $GRACE_{TWSA}$. Observed pattern agreed with the reported literature in all around the world (Rodell and Famiglietti 2001; Lettenmaier and Famiglietti 2006; Swenson and Wahr 2006; Strassberg et al. 2007; Wu et al. 2019).

The trend of $GRACE_{TWSA}$, $GLDAS_{TWSA}$, and GWSA were estimated over the GRB at annual, monsoonal, and non-monsoonal periods (Figure 6.4). $GRACE_{TWSA}$ shows a significantly decreasing trend at the rate of 1.68 ($p < 0.001$) for monsoon and 1.65 cm yr^{-1} ($p < 0.01$) for the annual period (Figure 6.4a).The annual trend of $GLDAS_{TWSA}$ was declining with time at the rate of 0.18 cm yr^{-1}, but statistically insignificant (Figure 6.4b). The mean annual GWSA showed a decreasing trend, with a rate of 1.39 cm yr^{-1} ($p < 0.001$) (Figure 6.4c), which is concurred with estimates from previous studies (MacDonald et al. 2016; Mukherjee et al. 2018; Bhanja et al. 2020). For example, Bhanja et al. (2020) have revealed that the GWS diminishing (at rates of > 0.4 km^3 yr^{-1}) in the Ganges-Brahmaputra river basin based on in situ observations for the period 2003–2014. The overall GWSA shows a significant decreasing trend, besides; it shows an increasing trend (1.25 cm yr^{-1}) in recent years (2013–2015) for the monsoon period. The similar patterns of GWSA were reported by Panda and Wahr (2016b), Bhanja et al. (2017), and Bhanja et al. (2018) through in situ measurement. In addition, the correlation coefficient between the mean annual $GRACE_{TWSA}$ with $GLDAS_{TWSA}$ and estimated GWSA were 0.53 and 0.97, respectively, at $p < 0.05$.

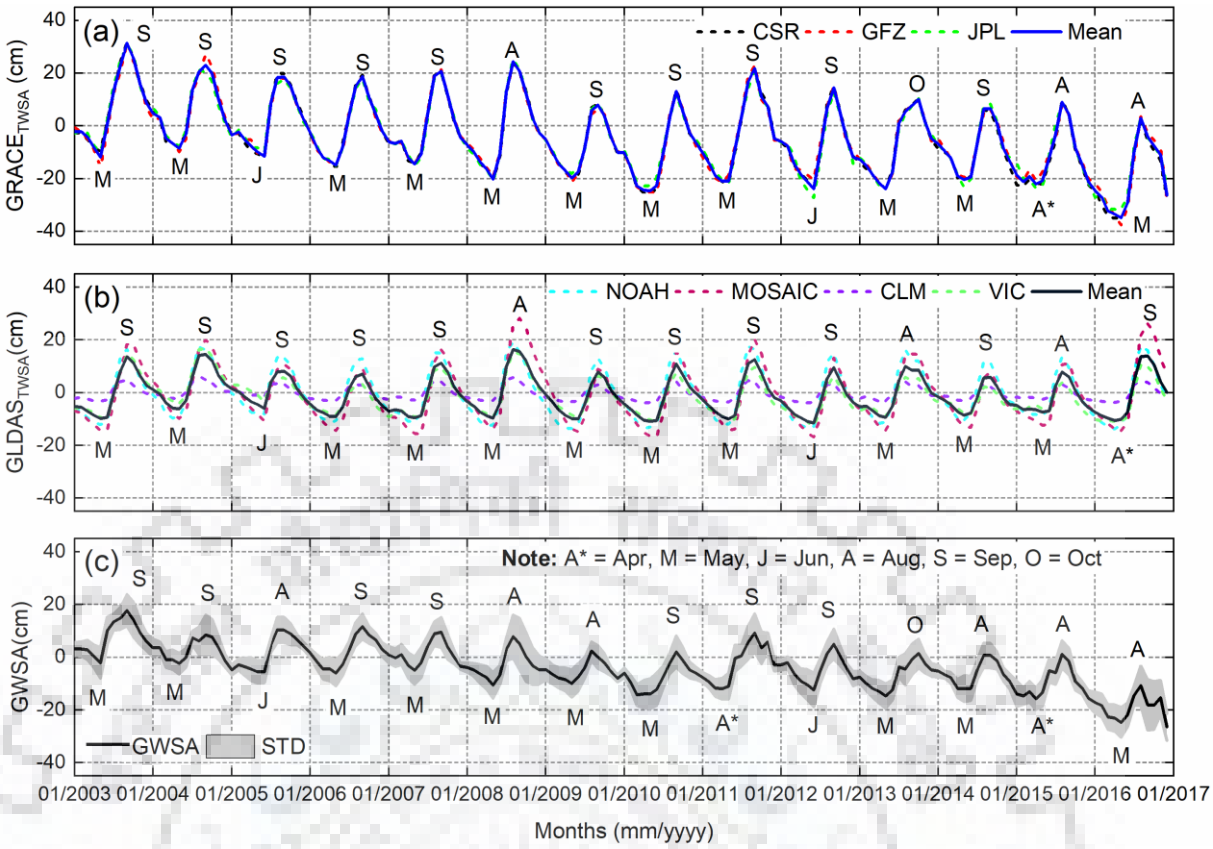

Figure 6.3. Monthly time-series of a) GRACE TWSA products with their combined mean; b) GLDAS TWSA of LSM datasets with their combined mean, and c) estimated GWSA and its standard deviation (gray shadows).

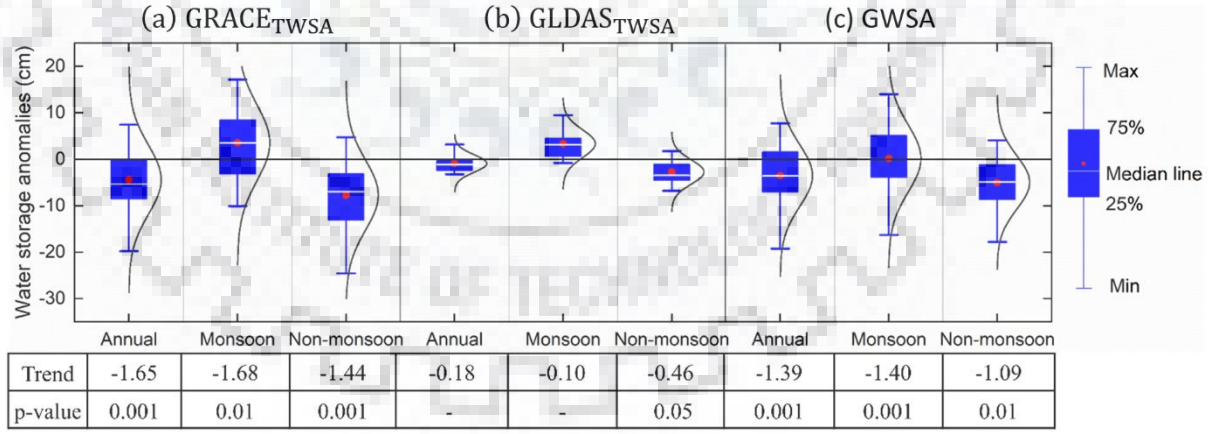

Trend	-1.65	-1.68	-1.44	-0.18	-0.10	-0.46	-1.39	-1.40	-1.09
p-value	0.001	0.01	0.001	-	-	0.05	0.001	0.001	0.01

Figure 6.4. Boxplot of the mean annual and seasonal of a) GRACE TWSA, b) GLDAS TWSA, and c) GWSA with its trend over the Ganga river basin from 2003 to 2016.

6.7.2. ESTIMATION OF GR

6.7.2.1. Basin-wide spatial GR rates

The basin-wide spatial distribution of estimated GR was demonstrated over the GRB for the period 2003-2016. For this, the GR obtained from Henry, SWB, GWSC, Kumar, RIF methods along with in situ based GR (R_{GWL}) were used to assess the changing pattern of recharge during the observation period (Figure 6.5). Result indicates that the higher value of mean annual R_{Henry} was identical with the R_{GWSC} over the southeastern part of GRB. While the R_{Kumar} and R_{RIF} shows similar pattern over the northern part of the basin. Similarly, the higher value of GR has obtained in the upper part of the Ganga basin lies in the Indian territory (Bhanja et al. 2019). The R_{SWB} was not capturing the similar distribution as of other methods. The spatial trend of the R_{RIF} shows a similar decreasing pattern with the R_{GWL} over the central part of the GRB. Therefore, this region comes under the semi-critical to over exploited classes based on groundwater stress categorization presented by CGWB (2017). In the western region of the basin, the majority of observations wells location shows a positive trend over the study period which was comparable with the R_{Kumar} and R_{SWB}. Similar spatial trend of GR have been reported by Bhanja et al. (2018a) over India by in situ measurement.

6.7.2.2. Basin-wide mean GR rates

The GR was estimated using six different approaches, i.e., Wu, Henry, SWB, GWSC, Kumar, and RIF methods over the GRB in each year from 2003 to 2016. All the methods estimate net recharge for the monsoon period (June to September) except the Wu method that determines total recharge for the annual scale. The annual R_{Wu} was estimated (discussed in section 6.6.1.2) over the GRB in each subsequent year from 2003 to 2016. For this, the monthly time-series of GWSA were used to draw a fitted linear line from S_P(t-1) of the previous year to the trough $S_B(t)$ of the current year. Then, the linear line of the recession curve was extrapolated upto the S_P(t) of the current year.

Afterward, the R_{Wu} was estimated by subtracting the extrapolated low value $S_L(t)$ of the recession curve from the S_P(t) value of GWSA in the current year (Figure 6.6a). In Table 6.1, σ_{GR} represents the standard deviation of monthly GWSA that is used for annual GR estimation, and N is the number of sampling points used to fit the antecedent recession curve. The number of measurements in each recession curve was ranged from 7 to 9, with an average of 8 during the observation period, except in 2003 (5-observations) (Table 6.1).

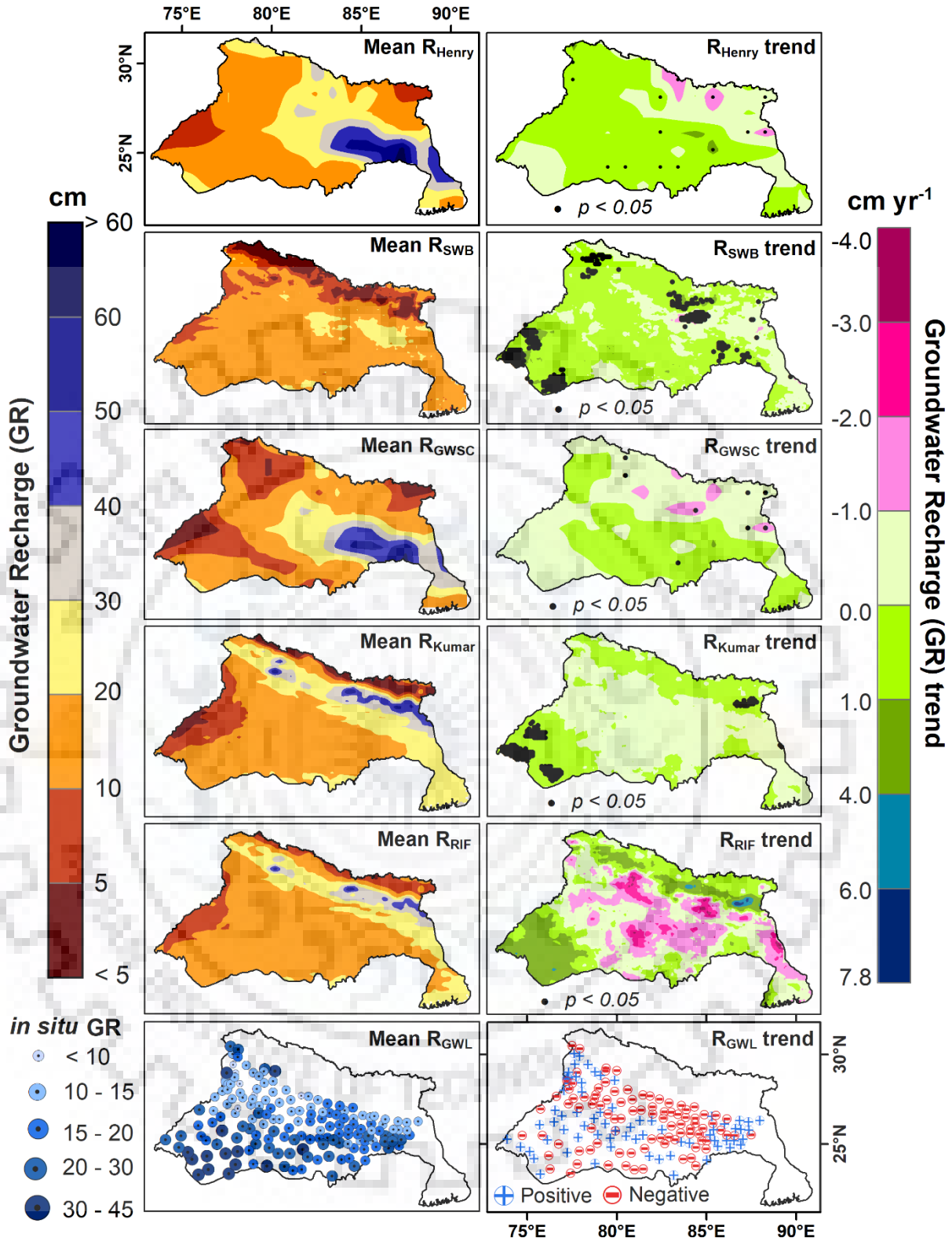

Figure 6.5. The mean annual GR and its trend of Henry, SWB, GWSC, Kumar, RIF methods along with in situ GR over the Ganga river basin from 2003 to 2016.

In 2003, we considered data from January onwards for recharge calculation. The R^2 ranged from 0.80 to 0.98, with an average of 0.92 (Table 6.1; $p < 0.01$) (number of measurements in each recession curve), which indicates the best fitting curve of the data. The 14-year average of the

R_{Wu} was estimated at 24.4 ± 3.5 cm yr^{-1}, which ranged from 18.6 to 32.3 cm yr^{-1}. It indicates that the inter-annual variation of R_{Wu} with an insignificant increasing trend (0.03 cm yr^{-1}). Nevertheless, a consistent decreasing trend of GWSA (1.39 cm yr^{-1}) was observed during the observation period, which is much smaller than the maximum (7.8 cm) and larger value relative to the minimum (–19.2 cm) mean annual amplitude of GWSA. Therefore, it will be unable to mask the seasonal changes in GWSA (Wu et al. 2019). Besides, the R_{Wu} estimated from the difference between the peak and the extrapolated recession at the time of peak, thus, the decreasing trend of GWSA does not affect the difference between $S_P(t)$ and $S_L(t)$. The R_{Henry} rate was estimated based on the difference between S_P(t) and S_B(t) value of GWSA in each year for the period 2003-2016 (Table 6.1). A 14-year average of R_{Henry} was 16.1 ± 2.9 cm yr^{-1} that varied from 10.9 to 21.2 cm yr^{-1}. A declining trend of R_{Henry} was observed at the rate of -0.09 cm yr^{-1} with insignificant.

Table 6.1. The variables used in estimating the GR from GWSA over the GRB from 2003 to 2016.

Year	S_P (cm)	S_B (cm)	S_L (cm)	R_{Henry} ($cm\ year^{-1}$)	R_{Wu} ($cm\ year^{-1}$)	σ_{GR} ($cm\ year^{-1}$)	N	R^2
2003	17.8	-2.1	-6.6	19.9	24.4	7.1	5	0.83
2004	8.5	-2.4	-14.2	10.9	22.8	5.0	8	0.94
2005	10.4	-5.5	-12.8	15.9	23.1	6.2	9	0.80
2006	11.7	-5.9	-16.1	17.6	27.8	6.0	8	0.98
2007	9.5	-5.0	-12.8	14.5	22.3	4.9	8	0.94
2008	7.9	-10.6	-17.7	18.5	25.6	5.7	8	0.91
2009	2.4	-9.9	-17.0	12.3	19.4	4.6	9	0.90
2010	2.1	-14.3	-23.3	16.4	25.4	5.5	9	0.94
2011	9.3	-11.9	-23.1	21.2	32.3	6.9	7	0.96
2012	5.0	-12.3	-19.7	17.4	24.7	6.0	9	0.93
2013	1.5	-14.6	-20.7	16.1	22.2	5.4	8	0.92
2014	0.8	-11.8	-17.8	12.6	18.6	4.3	7	0.95
2015	1.1	-15.7	-26.9	16.8	28.0	6.1	8	0.91
2016	-10.7	-26.4	-35.6	15.7	25.0	6.8	9	0.94
Mean				**16.1**	**24.4**		**8.0**	**0.92**

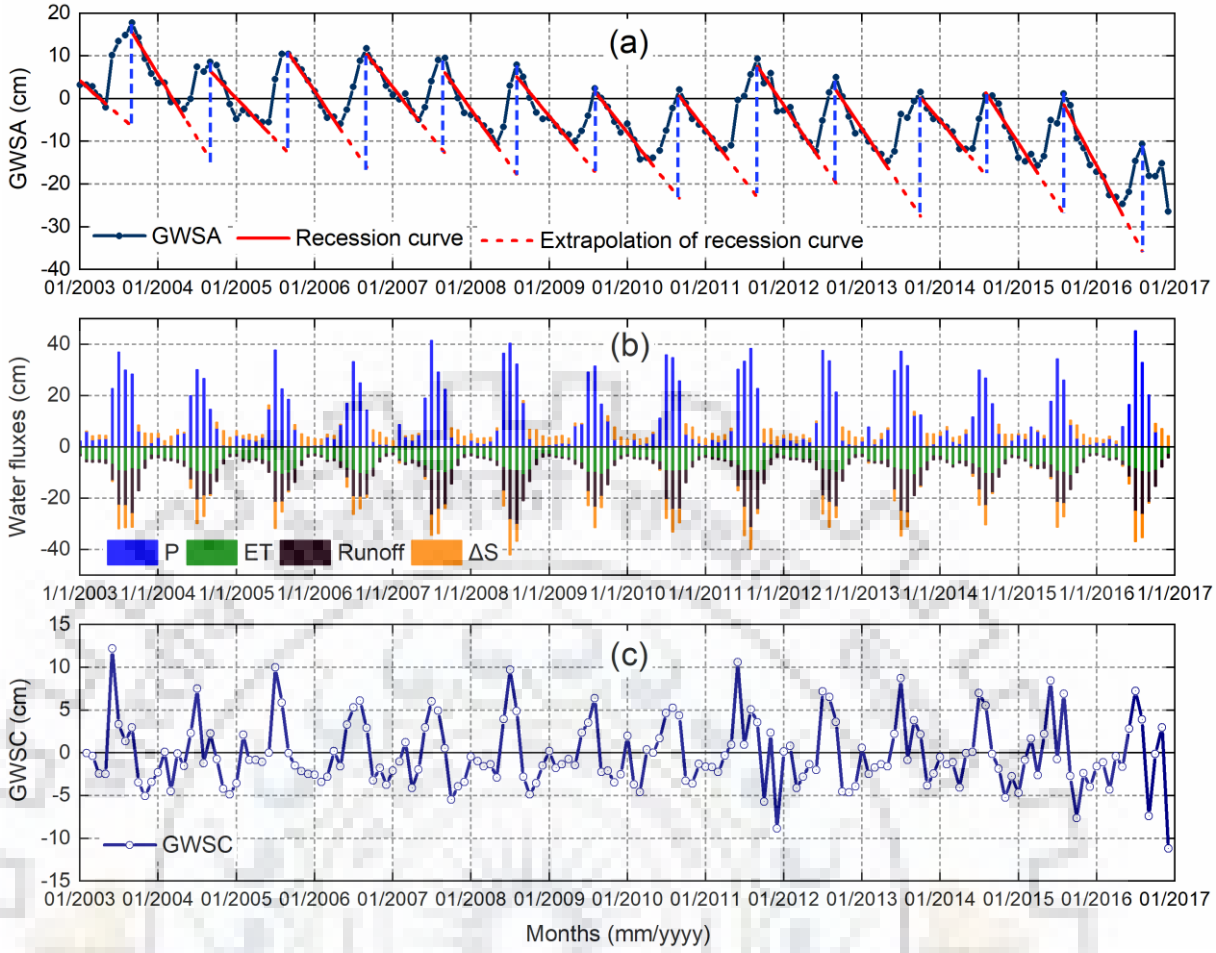

Figure 6.6. The monthly time series of a) GWSA and its antecedent recession curve, b) water flux components, and c) GWSC used for GR estimation over the Ganga river basin between January 2003 and December 2016.

The R_{SWB} rate was calculated at a monthly scale by applying the SWB approach from 2003 to 2016 (Figure 6.6b). The mean monthly P, ET, runoff, and ΔS were analyzed for monsoon period (June to September) recharge estimation. P shows the incoming water flux towards the ground represented by positive, whereas other outgoing water fluxes (ET, runoff, and ΔS) shown as negative. The R_{SWB} rates varied from 4.5 to 15.1 cm yr^{-1}, with a mean value of 11.7 $\pm$ 3.1 cm yr^{-1}. The R_{SWB} shows a decreasing trend at the rate of 0.10 cm yr^{-1} with statistically insignificant.

Moreover, the monthly time series of GWSC was examined using equation 6.4, which indicates that the positive values are recharge of water towards the ground, while negative values as the deficit of water or discharge (Figure 6.6c**)**. Overall, the maximum R_{GWSC} (~96%) was observed from June to August, with the highest value in July. The mean annual R_{GWSC} varied from 12.1 (2004) to 20.2 cm yr^{-1} (2011), with a mean value of 15.8 $\pm$ 2.7 cm yr^{-1}, which indicates that

the interannual variation in net recharge. There was no significant trend observed during the study period, however, R_{GWSC} shows a decreasing trend with a rate of 0.25 cm yr^{-1}.

The R_{Kumar} rate was estimated using the Kumar method, established by the empirical relationship between P and GR for the monsoon period. The annual R_{Kumar} ranged from 14.7 (2014) to 23.7 (2008), with an average of 18.7 ± 3.2 cm yr^{-1}. Furthermore, RIF method was also used to estimate annual R_{RIF} explained by CGWB (2017). This method primarily considered the monsoonal precipitation and infiltration factor. It indicates that the R_{RIF} varied from 14.1 to 20.9, with an average of 17.1 ± 2.4 cm yr^{-1}. The R_{Kumar} and R_{RIF} were experienced a decreasing trend over the time with a rate of 0.06 and 0.04 cm yr^{-1}, respectively.

Overall, all the adopted methods demonstrated a decreasing trend of GR in the GRB during the study period, except in the Wu method. The inter-annual variation of GR was analyzed for each method over the study area for the 14-years (2003–2016). The mean annual GR were 24.4, 16.1, 11.7, 15.8, 18.7, and 17.1 cm yr^{-1} or 23.5, 15.5, 11.3, 15.2, 18.0, and 16.5% of monsoonal averaged precipitation (~103.9 cm) assessed by Wu, Henry, SWB, GWSC, Kumar, and RIF methods, respectively. The observations were consistent with Bhanja et al. (2018a), who also found a rapid decline in recharge rates over the GRB. The results suggested that the SWB estimated GR was less than the other recharge estimation methods due to the preferential flow path recharge mechanism, which was not captured by the SWB method (Demlie 2015). In contrast, the estimated GR from the Wu method was higher than the mean recharge of other methods. This may be occurred because of the R_{Wu} considered the annual recharge in term of net recharge and recharge that compensate the discharge while the other methods accounts the monsoon net recharge as annual GR. Though, each method has its own consideration, procedure, and uncertainties for the GR estimation using different datasets.

6.7.3. VALIDATION OF ESTIMATED GR WITH IN SITU MEASUREMENT

The R_{GWL} were estimated over the 167 locations lies under the GRB. The estimated R_{GWL} were used to assess the grid-wise performance of six selected methods for the period 2003-2016. Observed mean R_{GWL} varied between 15.3 and 21.7 cm yr^{-1}, with an average of 18.1 cm yr^{-1}. The R_{GWL} shows a decreasing trend at the rate of 0.02 cm yr^{-1} during the study period. In Table 6.2, we have found that Wu, Henry, SWB, GWSC, Kumar, and RIF methods show all the GRB bias of 34.5%, 8.6%, –21.1%, 6.6%, –16.3%, and –20.6%, respectively for the observation period. We observed that the precipitation dependent methods show underestimation with the R_{GWL} while the GRACE based methods were experiencing an overestimation. The maximum

over and under estimation were found in Wu and SWB methods, respectively. While all the methods were highly correlated ($p < 0.05$) with the R_{GWL}, varied from 0.64 (SWB method) to 0.77 (Kumar and RIF methods), except for Wu method, i.e., 0.30. Based on the overall score, the result indicates that the Kumar method outperformed the other selected methods for the GRB (Table 6.2). The better performance of the Kumar method is to simulate the GR can be attributed to the improved precipitation product taken from ERA-5. The significant improvement in the horizontal and vertical resolution of precipitation can result in a better estimation of GR from other methods. A previous study revealed that the ERA-5 precipitation was found under- and over-estimation in different parts of India (Mahto and Mishra 2019). Also, the GRACE based Henry and GWSC methods presented a good overall score of 7.14 and 7.26, respectively, with a significant positive correlation. Henry et al. (2011) found the average annual net recharge using the GRACE based WTF method was very similar to the recharge estimated from historical wells observations. Similar to the R_{GWL}, in GRB, all the methods shows a consistent decreasing trend except for SWB during the observation period. The observed R_{SWB} shows a relatively less increasing trend (0.03 cm yr^{-1}) with statistically insignificant. Overall, the result concluded that the rainfall dependent method, i.e., Kumar was well performed than other methods in terms of R and overall score. Although, the GRACE based Henry method outperformed than the GWSC and Wu methods based on R, bias and overall score.

Table 6.2. Statistical results of the correlation coefficient, bias, root mean square error (RMSE), overall score, and p-value of the six selected GR estimation methods against in situ based estimated recharge.

Methods	R	Bias	RMSE	Score	*p*-value
Wu	0.30	34.5	8.25	3.18	0.306
Henry	**0.68**	8.6	3.38	7.14	0.007
SWB	**0.64**	-21.1	4.17	6.54	0.013
GWSC	**0.67**	6.6	3.10	7.26	0.008
Kumar	**0.77**	-16.3	3.22	7.48	0.001
RIF	**0.77**	-20.6	3.43	7.35	0.001

6.7.4. IMPACT OF CLIMATIC VARIABLES ON GR

The GR is mainly influenced by how precipitation enters and is retained in the soil layer. High-intensity precipitation alters the soil structure as well as soil porosity, which further reduces the infiltration capacity of the soil layer. Consequently, it reduces the GR and increases the surface

water runoff; therefore, it is essential to understand the changing pattern of these variables that influence the GR (Owuor et al. 2016). However, it is difficult to comprehend the hydro-physical properties of soil, i.e., soil structure, grain size, porosity, etc. Therefore, we quantify the variability of P, runoff, ET, and SM content relative to the GR for the period of 2003-2016. The GRB is subjected to differential precipitation rates and patterns in Spatio-temporal variation for the study period. The mean annual P varies from 111.9 to 147.4cm, with an average of 129.1 $\pm$ 13.8cm from 2003 to 2016. The GRB received the highest P rate (~81%) during the monsoon (June to September) while the smallest (1.7%) in the post-monsoon (November to December) season. The minimum and maximum mean monthly P were observed in December (1.1cm) and July (36.0cm) during the study period. The annual P rate is unevenly distributed in all across the basin, with its trend ranging from 8.33 to –5.5 cm yr^{-1}, with a mean value of –1.34 cm yr^{-1}. A study carried out by Bhanja et al. (2020) reported that the Ganga and Brahmaputra river basins experienced a long-term decreasing trend from 1961 to 2014 using rain gauge measured precipitation. The spatial distribution of P and runoff shows a higher value in the northeastern part of the basin; on the other hand, this region attains a significant declining trend. However, the lower value of these variables was observed in the western region of the GRB with a significant increasing trend (Figure 6.7).

Figure 6.7 shows that the amount of P, runoff, and $GLDAS_{TWSA}$ increases with time in the northeastern part of the basin; however, the groundwater storage decreases. This may occur due to the high anthropogenic activities as well as climate change (Abeysingha et al. 2016). Also, the precipitation intensity increased over the region (Shrestha et al. 2015), which may influence the soil hydro-physical properties (Owuor et al. 2016) and further lead to high surface runoff with low GR rate. Anand et al. (2018) suggested that the maximum flow in the GRB generated by the precipitation. Besides, many studies demonstrated that the GRB experiencing a groundwater withdrawal through intensive pumping of groundwater for irrigation and other purposes (Famiglietti et al. 2011; Feng et al. 2013; Abeysingha et al. 2016; Asoka et al. 2017; Anand et al. 2018; Bons 2018). Similarly, the annual mean T_a ranged from 20.4 (2013) to 21.8 °C (2010), with an average of 21.0 $\pm$ 0.43 °C. However, the mean annual ET for the observation period was 74.9 $\pm$ 2.7 cm, which varied from 70.9 (2012) to 80.4 cm (2015). The mean annual T_a and ET trends were increasing at the rate of 0.006 $\pm$ 0.02 °C and 0.08 $\pm$ 0.37 cm, respectively. Likewise, the spatial trend of both variables (T_a and ET) illustrated an increase in the northeastern while decrease in the western region of the GRB. Mean monthly T_a range from 11.9°C (January) to 27.4°C (May), while the ET varied from 3.0cm (January) to 10.0cm (September).

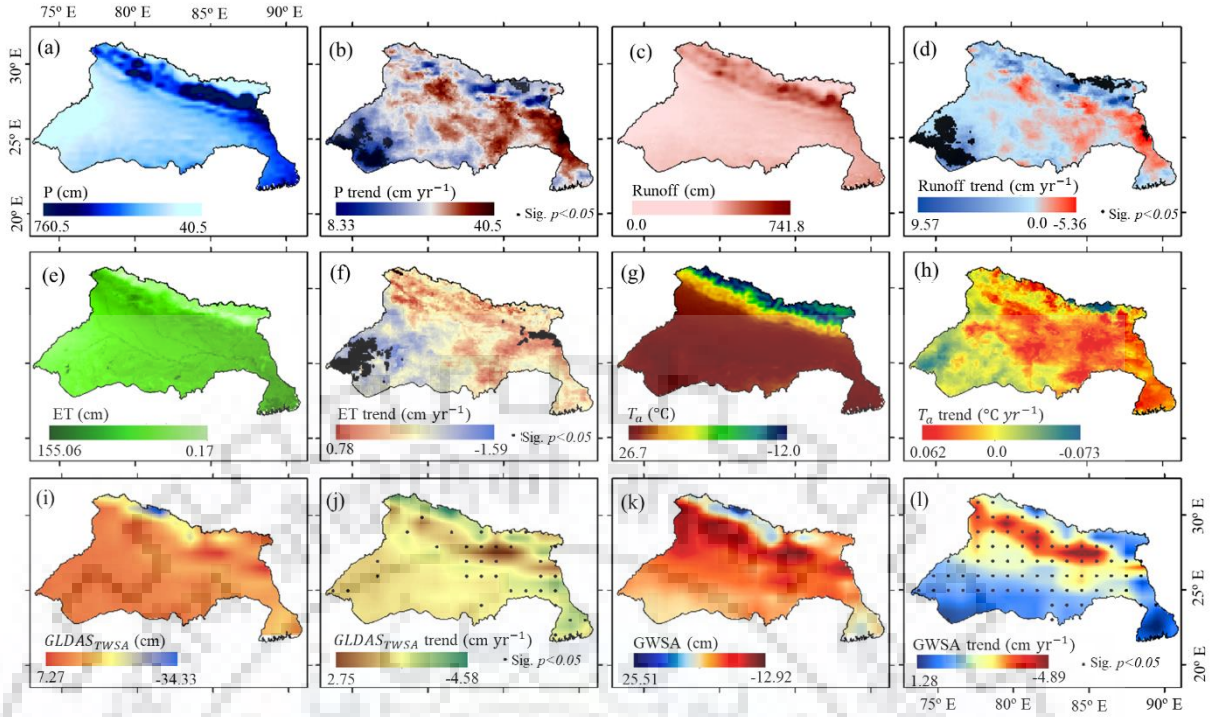

Figure 6.7. Mean annual and its trend of precipitation (a, b), runoff (c, d), evapotranspiration (e, f), air temperature (g, h), $GLDAS_{TWSA}$ (i, j), and GWSA (k, l) over the Ganga river basin.

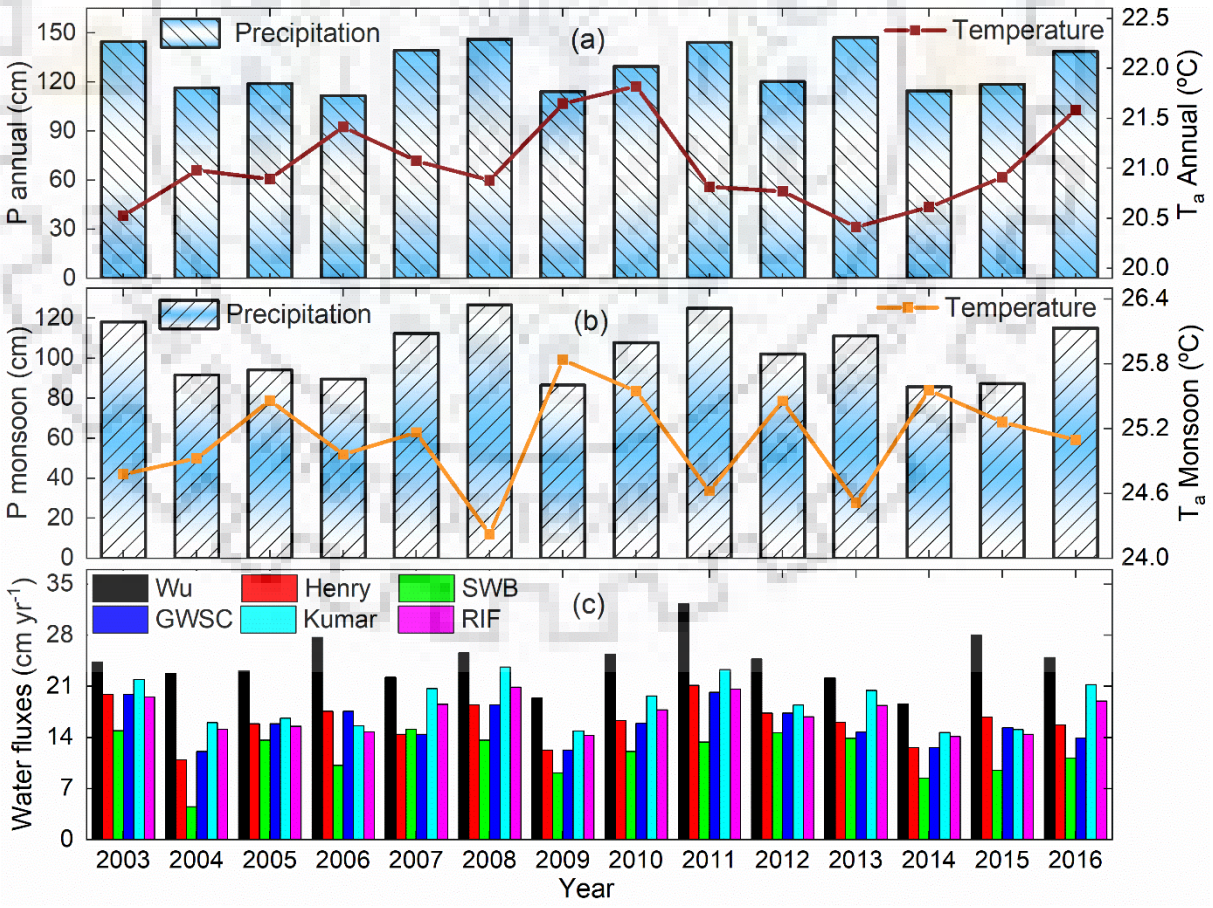

Figure 6.8. Inter- annual (a) -monsoonal (b) variation of precipitation and air temperature; c) annual GR rates estimated through Wu, Henry, SWB, GWSC, Kumar, and RIF methods.

Furthermore, there are no significant long-term trends observed in the GR for the period 2003-2016. The inter-annual and monsoonal variation of P along with T_a were examined by their linear relationship with GR (Figure 6.8a, b). The results demonstrated that the mean annual P was experiencing a similar pattern of monsoonal P with a minimum in 2014 and a maximum in 2008. This pattern mainly occurred because the Ganga basin received ~81% of P in the monsoon period. A similar distribution of precipitation has been observed by Shrestha et al. (2015) over the Ganga basin. Conversely, the observed T_a in annual and monsoonal scale shows a varying distribution with minimum in 2013 and 2008, respectively. While the maximum T_a was observed in 2010 for annual and 2009 for monsoonal period. The statistical analysis indicates that the monsoonal P play a significant role in annual GR over the basin while the T_a was significantly changing throughout the year that losses the water flux in the form of ET. Many similar studies have also reported the dominance of recharge by precipitation (Sheffer et al. 2010; Min et al. 2015; Turkeltaub et al. 2015).

The standardized anomalies for each of the water flux components and estimated GR were generated for the period 2003–2016 to reduce the spatial bias and random fluctuation in data (Figure 6.9). These indicators help in comparing the hydrometeorological variables with GR. After the bias correction through the standardized anomaly, the estimated GR methods were highly correlated with the water fluxes (Figure 6.8). The results indicate that 2003, 2008, 2011, and 2013 were identified as extremely wet years, while 2004, 2006, 2009, 2014, and 2015 were relatively dry years. Observed results are consistent with the findings by several authors (Chen et al. 2014; Goldin 2016; Nandargi and Shelar 2018; Bhanja et al. 2019; Dharpure et al. 2020a). However, the negative anomalies of ET progressively increase from 2013 to 2015, with a maximum in 2015.

Pearson's correlation test was applied between the hydroclimatic variables (P, ET, runoff, SM, and T_a) and estimated GR (through different methods) for monsoonal and annual scales to indicate the degree of linear association between them (Figure 6.10). Accordingly, almost all the hydrometeorological variables were found to be significantly correlated with the estimated GR, except in ET (all the methods) and ΔS (except for R_{RIF} and R_{Kumar}) over the monsoon period. The low correlation between estimated GR and ET may occur due to these methods only constituting precipitation components in the recharge calculation. However, each method was highly correlated with the other at $p < 0.01$.

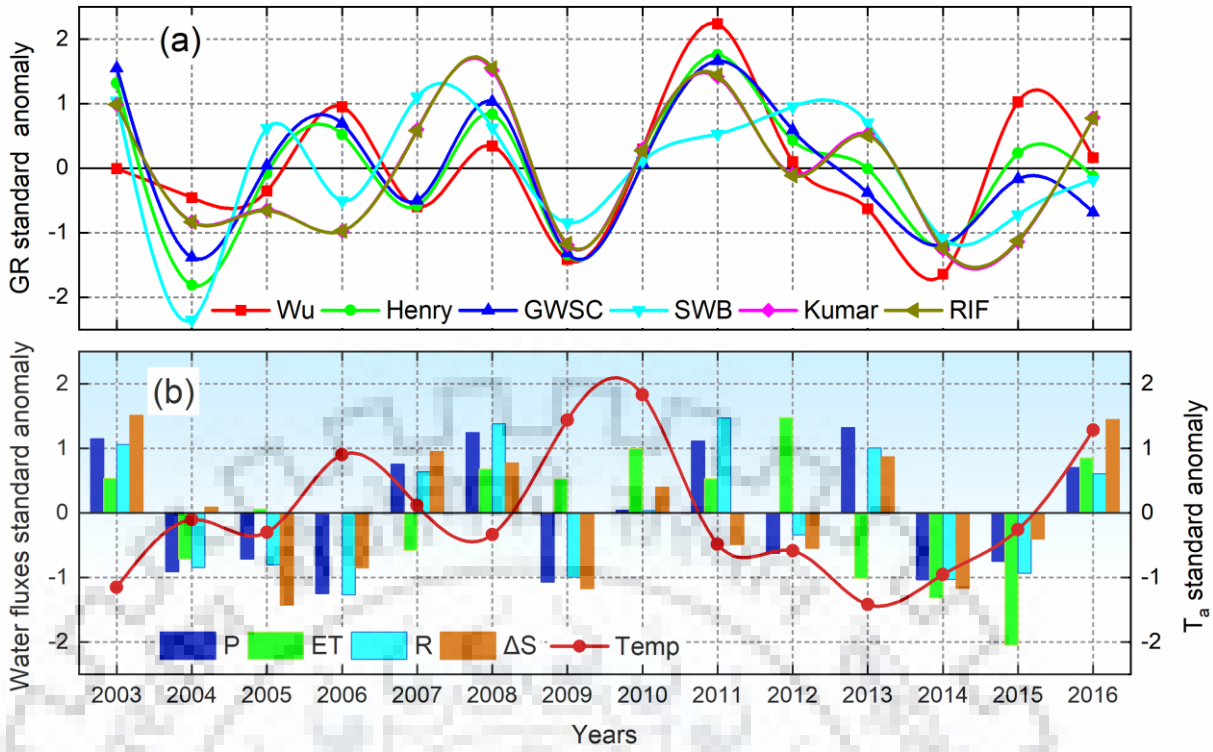

Figure 6.9. Standardized anomalies of annual a) estimated GR using different methods and b) water fluxes with air temperature over the GRB from 2003 to 2016.

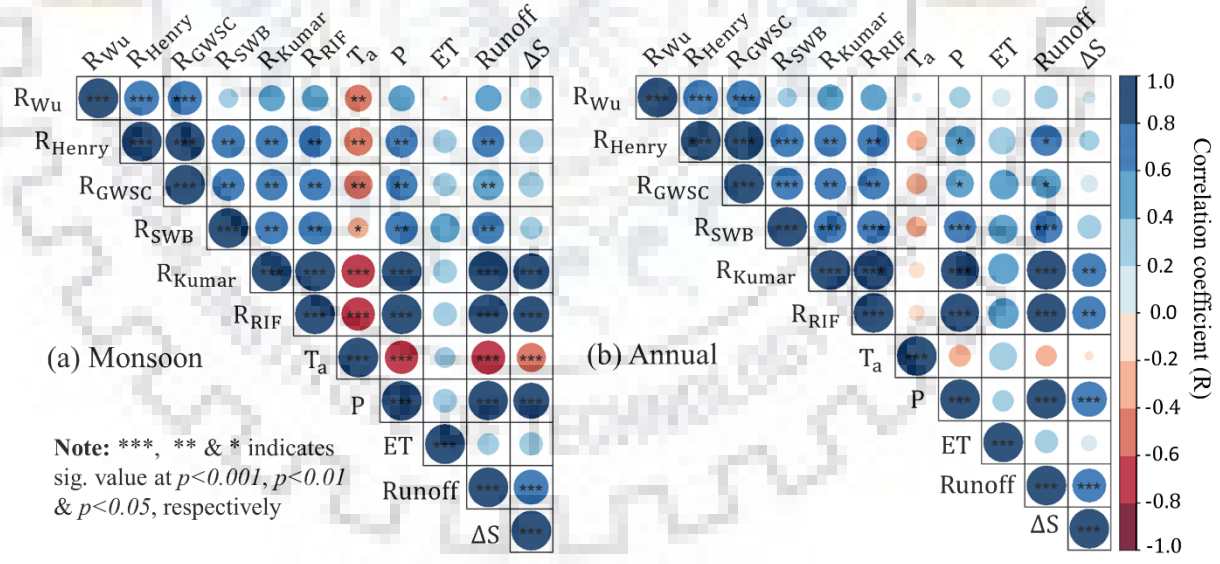

Figure 6.10. Correlation coefficient of estimated GR with hydroclimatic variables for a) monsoon and b) annual period over the Ganga river basin.

The highest positive correlation was obtained with P and runoff for all the methods except the Wu method over the annual period. This positive correlation is found to be a natural principle in many hydrogeological studies (Zomlot et al. 2015).

The observed T_a showed a negative correlation with each GR calculation method, while, ET was positively correlated with GR methods. This result suggested that the high ET might contradict with the maximum GR of the aquifer, while the low value will cause an increase in GR. A similar finding have been reported previously (Richard et al. 2015; Rukundo and Doğan 2019). Syed et al. (2008) have also reported a positive correlation with P (incoming water flux) and a negative relationship with ET and runoff (outgoing water fluxes) against GR. The selected hydroclimatic variables (P, ET, Runoff, and ΔS) found to be directly proportional with each other except for T_a. Similar, positive correlation of P, ET and SM have been demonstrated by the Wang et al. (2018). They have also revealed that these three variables attain strong correlation with R = 0.897 between SM and ET, R = 0.894 between ET and P, and R = 0.795 between SM and P. However, these relationships will help to identify the aquifer factors that can control the spatial and temporal distribution of recharge. Therefore, a further study is recommended to determine the exact processes, which may contribute to an increase in recharge across the basin.

6.7.5. IMPACT OF OTHER FACTORS ON GR

As earlier, we have noticed that the precipitation-dependent methods found well correlated with the observation wells along with higher inter-annual variability were observed over the GRB. The GRB attains highly fertile sedimentary formations that facilitate both direct and indirect recharge (Bhanja et al. 2019). The higher agricultural-based groundwater withdrawal in the GRB may lead to a decrease in water storage. The decreasing water storage resulted in increased recharge by generating more recharge space. However, the unconsolidated formation of the basin leads to a non-homogenous recharge rate throughout the basin. Therefore, in this study, we have quantified the other factors that influencing the groundwater variability.

The spatial distribution of total withdrawal, irrigation-based groundwater abstraction along with population density (domestic factor), and overall water stress against GR were analyzed over the GRB (Figure 6.11). Results demonstrated that the major portion of the GRB lies under Indian territory was experiencing the higher groundwater abstraction through irrigation. According to the World Resource Institute (WRI), the northwestern part of the GRB comes under extreme water stress. This stress may be created because of the higher withdrawal of irrigation along with domestic factors (for population livelihood). Cao and Roy (2018) have highlighted that the total area under wells and tube-well irrigation enlarged from 14.5 million ha to 16.3 million ha between 2004 and 2014 in Uttar Pradesh, India. Shamsudduha et al. (2012) have demonstrated that the extensive abstraction of groundwater for irrigation of rice crops in South Asia may lead to lowering of groundwater table in the shallow aquifers of the Ganges-Brahmaputra Basin.

Besides, the widespread evidence of groundwater withdrawal for a growing population has been shown by CGWB (2011) over the metropolitan area of India, such as Ahmedabad, New Delhi, and Lucknow. Moreover, the high intensity of rainfall will be responsible for increased runoff that leads to a decrease in GR (Patel et al. 2020), much of which can attribute to the higher proportion of impermeable surfaces associated with urbanization.

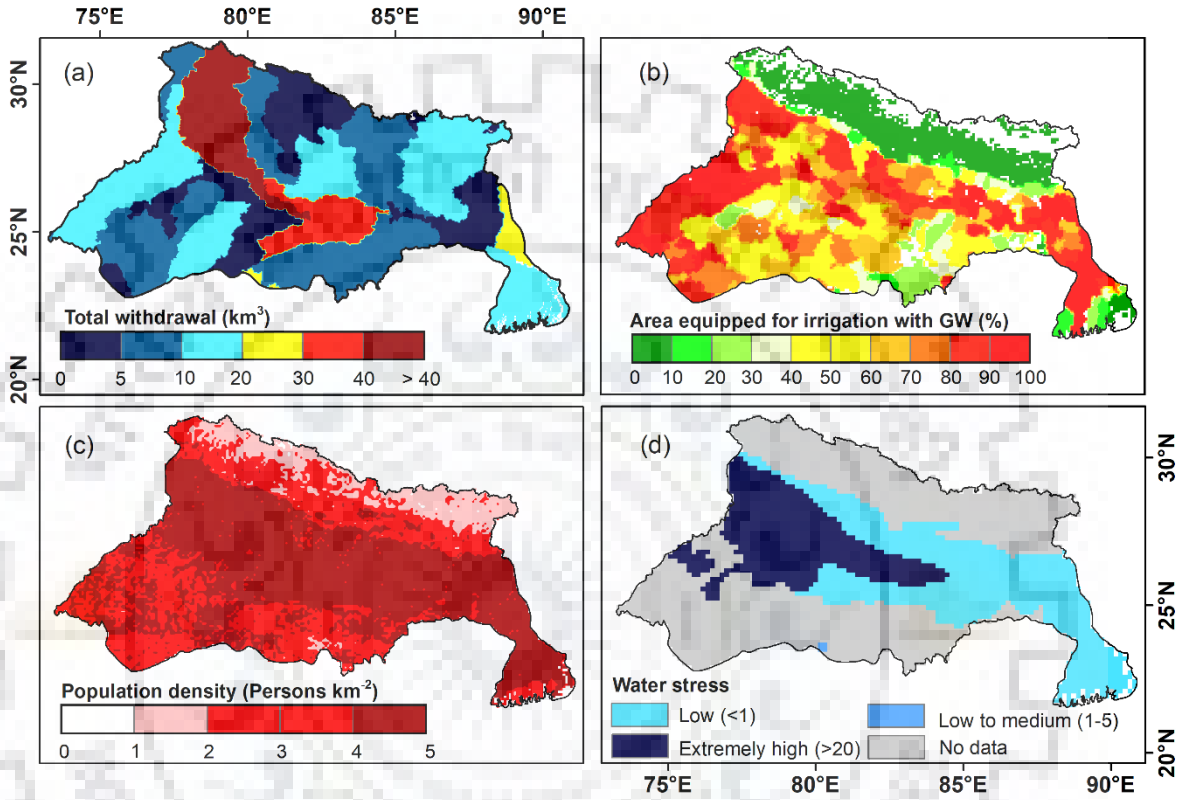

Figure 6.11. (a) Total withdrawal (Source: Gassert et al., 2014), (b) Percentage of area equipped for irrigation with groundwater (Source: Siebert et al., 2010), (c) Population density (Source: Dobson et al., 2000) and Water stress (Source: Gassert et al., 2014) over the Ganga river basin.

6.7.6. ASSOCIATED UNCERTAINTY AND SENSITIVITY ANALYSIS

A number of uncertainties in GR estimation were demonstrated for the adopted methods, which will help in understanding the sources of errors and level of accuracy. Firstly, the major uncertainty in satellite-based GR (R_{GWSC}, R_{Henry}, andR_{Wu}) estimation comes under the consideration from input variables (GRACE TWSA and GLDAS models) used. The GRACE-derived GWSA is associated with the uncertainties related to the simulation of GLDAS soil moisture (CLM, MOSAIC, NOAH, and VIC) and GRACE signal-processing techniques (Shamsudduha et al. 2012). In addition, the uncertainty associated with not considering a surface-

water-storage change that presenting a source of error in GWSA. Secondly, the GWL offered a high accuracy for GR estimation, however, a reliable estimation of S_y (determined from long-term pumping test data) required to reduce the associated uncertainties. In this study, we have used a constant S_y (0.044) for the GRB because of unavailability of pumping test data. On the other hand, S_y is not constant for the entire region but varies as a function of depth to the water table (Childs 1960); therefore, this will account for uncertainty. Lastly, the other methods, i.e., R_{RIF}, R_{Kumar}, and R_{SWB} have empirical relationship between GR, P and other driving components (Bonsor et al. 2017). Therefore, the highly accurate P and other water fluxes (ET, runoff, and SM) data are required for GR modeling. On the other hand, the accurate measurement of the infiltration factor is needed to reduce the possible uncertainty in the RIF method (CGWB 2017). Additionally, a major limitation of R_{Kumar} is that the mean annual P above 38.84 cm must be considered for GR estimation.

The sensitivity of GR to change in P, ET, runoff, and SM were conducted using the SWB equation from 2003 to 2016. All the variables were altered by ± 2 cm to identify the possible changes in GR. When P is increased by 2 cm, the value of GR increases by 66% from the reference GR. With an increment of ET by 2 cm, the decreased in GR value by 37%. A similar decrease in GR (value by 37%) is observed with an increase of 2 cm in runoff and SM. Overall, it was found that the GR is more sensitive to P as compared to ET, runoff, and SM. Many studies highlighted similar results in different region (Mechal et al. 2015; Condon and Maxwell 2019).

6.8. CONCLUSION

The Ganga river basin is a major river system of India, which irrigates large tracts and supports livelihood. This basin depends on the perennial river system and groundwater; therefore, different methods were used to estimate the GR. The analysis of GR with remote sensing-based SWB approach along with empirical relation (between P and GR) were used over the GRB for the period 2003-2016.

The result of this study suggested that the GWSA shows a significant decreasing trend with a rate of 1.39 cm yr^{-1} for the study period. The overall estimated GR were 24.4, 16.1, 11.7, 15.8, 18.7, and 17.1 cm yr^{-1} or 23.5, 15.5, 11.3, 15.2, 18.0, and 16.5% of monsoonal averaged precipitation (~103.9 cm) assessed by Wu, Henry, SWB, GWSC, Kumar, and RIF methods, respectively. Also, the basin-wide spatial distribution of GR indicates that the higher value of mean annual R_{Henry} was identical with the R_{GWSC} over the southeastern part of GRB. Additionally, the estimated GR was validated with in situ GWL data, which showed a high

correlation and varied from 0.64 (SWB method) to 0.77 (Kumar and RIF methods), except for the Wu method, i.e., 0.30. The result also concluded that the rainfall-dependent method (Kumar method) was well performed than other methods in terms of R and overall score. Although, the GRACE-based Henry method outperformed the GWSC and Wu methods based on R, bias, and overall score.

The study also assessed the impact of water fluxes change on the GR, which indicates that a decreasing trend of P and runoff with a progressively increasing trend of ET and T_a in the northeastern part of the basin. Moreover, the impact of other influencing factors was also assessed, which characterized that the GRB lies under low to extreme water stress regions. The observed result established that the GR is affected by both climate change and anthropogenic activities in the GRB for the observational period. Likewise, a Pearson's correlation test was applied between the water balance components (P, ET, runoff, SM and T_a) and estimated GR (through different methods), which suggested that almost all the hydrometeorological variables were found to be significantly correlated with the estimated GR, except in ET (all the methods) and ΔS (except for R_{RIF} and R_{Kumar}) over the monsoon period. The uncertainty of the different methods and sensitivity of water fluxes were analyzed to identify the level of accuracy in the GR methods. The sensitivity analysis reveals that the GR is more sensitive to P rather than ET, runoff, and SM. Overall, this study concluded that the higher impact of climatic variability and anthropogenic activities in the form of irrigation and urbanization might alter the GR.

CHAPTER 7

DROUGHT CHARACTERIZATION USING THE COMBINE TERRESTRIAL EVAPOTRANSPIRATION INDEX IN THE INDUS, GANGA, AND BRAHMAPUTRA RIVER BASINS

7.1. INTRODUCTION

Drought is one natural disaster that brings long and short-term socioeconomic losses to millions of people worldwide compared to any other form of natural disaster (i.e., floods, tropical cyclones, tornados, earthquakes, etc.) (Hagman 1984; Wilhite 2000; Sinha et al. 2019). All across the world, drought-related calamities have intensified with varying severities due to the impact of climate change over the past few decades (Allen et al. 2011). The occurrence of drought is interconnected with the scarcity of water that often aggravates the severity of each other. It can also trigger major hindrances for the population from scarcity to migration and displacement. According to United Nations, water scarcity alone could affect some of the regions up to 6% of their GDP by 2050 due to mass migration and dismissing of resources. As per the United Nations/World Bank High-Level Panel on Water 2018, 40% of the world's population is affected by water scarcity, with almost 700 million people at risk of being displaced due to drought by 2030. A single drought year can destabilize the several years of social-economic development particularly in terms of vulnerability to livelihoods. In India, the climatology of drought events over 130 years (1875–2004) of meteorological time series data shows that the frequency of drought occurrence has increased after 1965 (Shewale and Kumar 2005). Drought in the Indian region can be monitored from the progress of onset and withdrawal of southwest monsoon (NRAA 2009). Several studies have shown that precipitation is the main variable determining the onset, duration, intensity, and end of droughts (Chang and Kleopa 1991; Heim Jr. 2002). Some of the studies have been linked the droughts in the Indian continent with El Niño Southern Oscillation (ENSO) (Gadgil et al. 2003; Ashok et al. 2004; Kumar et al. 2006; Mishra et al. 2012). Therefore, comprehensive policies and innovative approaches at a global, national and local scale need to be developed to make water management more disaster-resilient.

Due to the complex phenomena of drought and their involvement with various hydrological and climatological processes, various indices evolved over time for drought monitoring (Heim Jr. 2002). Numerous specialized drought indices have been developed recently, such as Standardized Precipitation Evapotranspiration Index (SPEI: Vicente-Serrano et al., 2009), Vegetation Drought Response Index (VegDRI: Brown et al., 2008), Total Storage Deficit Index

(TSDI: Yirdaw et al., 2008), Streamflow Drought Index (SDI: Nalbantis and Tsakiris, 2009), Multi-variate Standardized Drought Index (MSDI: Hao and AghaKouchak, 2013), Standardized Groundwater level Index (SGI: Bloomfield and Marchant, 2013), Catchment Land Surface Model (CLSM) based Groundwater Drought Index (GWI) (Li and Rodell 2015), GRACE derived Drought Severity Index (DSI: Zhao et al., 2017), GRACE derived GRACE Groundwater Drought Index (GGDI: Thomas et al., 2017), GRACE derived Water storage deficit index (WSDI: Sun et al., 2018) and Combined Climatologic Deviation Index (CCDI: Sinha et al., 2019). Among the wide list of drought indices, the Palmer Drought Severity Index established by (PDSI: Palmer, 1965), Standardized Precipitation Index (SPI: McKee et al., 1993), and Standardized Runoff Index (SRI: Shukla and Wood, 2008) are widely used for drought characterization over the past few decades (Hayes et al., 2011). Drought–prone areas can be identified based on moisture index which is computed using the data of annual precipitation and water need (PET: Potential Evapotranspiration) (Thornthwaite and Mather 1955). Reconnaissance Drought Index (RDI) was also proposed to incorporate cumulative precipitation and evapotranspiration (Tsakiris and Vangelis 2005; Tsakiris et al. 2007).

While most of the indices modeled the drought based on model simulations or land Surface states and fluxes observations, only a few are depend on remote sensing techniques. Indeed, until the launch of Gravity Recovery and Climate Experiment (GRACE) satellites in 2002 (Tapley et al., 2004), the drought monitoring was only restricted to agricultural droughts based on the vegetation indices using remote sensing techniques (Bhuiyan et al., 2006; Kogan, 1997; Singh et al., 2003). However, recently the direct Terrestrial Water Storage (TWS) observation from GRACE (Yirdaw et al. 2008; Agboma et al. 2009; Long et al. 2013; Girotto et al. 2017) or its deviation from the climatologic mean (Thomas et al. 2014; Zhao et al. 2017a, b) have been used for drought identification and characterization. Several preexisting drought indices were available, but still, considerable debate on the performance and effectiveness of each index in terms of drought events monitoring and its applicability for practical purposes exists. Therefore, it is necessary to formulate a holistic drought index that incorporates all meteorological, agricultural, and hydrologic droughts over large regions with varied climatic conditions. This will further contribute to the drought event identification, monitoring, characterization, and its severity assessment, improving the preparedness and preventive measure of resource management on the local scale.

In India, a majority of the earlier studies mainly concentrate on drought characterization (Bhalme and Mooley 1980) others were case studies of particular drought years, i.e., 1987, 2002, 2004, and 2009 (Krishnamurti et al. 1989; Gadgil et al. 2003; Sikka 2003; Francis and Gadgil 2010).

Further, these studies were predominantly based on rainfall data only (Guhathakurta 2003; Pai et al. 2011) and revealed less information about the state of land water storage. Furthermore, the drought assessment in India mostly concentrated on quantifying the agricultural and economic losses. Therefore, the spatio-temporal drought characterization is not assessed at a basinal scale using a holistic representation of drought (DACFW 2016). In India, the drought management system majorly focused on the relief-based approach rather than preparedness and prevention by evaluating the water stress conditions. Thus, holistic development of indices for drought monitoring would be needed over a large scale.

7.2. RESEARCH QUESTIONS

- **What are the factors that cause drought-like conditions over the study region?** How can the monitoring of drought occurrence be done using the remote sensing approach? Is any model available that can easily identify meteorological and hydrological droughts?
- **What is the major requirement for the development of new drought measurement indices?** What are the advantage and limitations of a new index? Do the index outcomes match with the published literature or field observation?
- **How are the drought indices related to the hydro-climatological condition of a basin?** Any significant relationship was established between them?

7.3. OBJECTIVES

- Development of a new drought index using the gravimetric and satellite observation over the three major river basins (Indus, Ganga, and Brahmaputra)
- Identification of drought events, their patterns, and trends using derived index (Combined Terrestrial Evapotranspiration Index)
- Comparing between new drought index and other recently used drought indices like WSDI, GGDI, CCDI, and SPEI
- Assessing the influence of climatic variables on the drought occurrence in order to understand the physical condition for drought event

7.4. STUDY AREA

7.4.1. GEOGRAPHICAL AREA

The drought characterization is assessed of the three major river basins, originating from the Hindu-Kush Himalayan (HKH) region, i.e., the Indus, the Ganga, and the Brahmaputra river (IGB) basins (Figure 7.1). The geographical area of IGB basins lies between Latitude 21º and 37º N and Longitude 66º and 97º E with a total area of about 26.45×10^5 km^2, covering an area of 33.3 % of the HKH (Bajracharya and Shrestha 2011). A detailed description of each basin is given in Table 7.1**.** The study area comprises a diverse geographical landscape.

The Himalayan Mountain range varies from the north to the northeastern part of India. It includes the highest mountain peak in the world, i.e., Mount Everest, K2 (also known as Mount Godwin-Austen), and Kangchenjunga, the first, second, and third Mountain peaks, respectively. The Great Northern Plains (i.e., Indo-Gangetic plains) is situated south of the Himalayas, which is one of the most fluvial systems in the world (Banerjee and Kumar 2018). These river basins encompass the part of five countries, i.e., India, Nepal, Pakistan, Bhutan, and Bangladesh. The Indus River merges into the Arabian Sea, whereas the Ganga and Brahmaputra River fall into the Bay of Bengal.

Table 7.1. A detailed description of the Indus, Ganga, and the Brahmaputra river basins.

Basin	**Area**	**Area in HKH**	**Number of glaciers**	**Population in 2015** *(Million)*	**Total irrigated area in 2005** *(Million ha.)*
Indus	1,116,086	555,450	18,495	268.42	25.29
Ganga	1,001,019	244,806	7,963	580.09	29.58
Brahmaputra	528,079	432,480	11,497	68.07	2.03
Total	**2,645,184**	**1,232,736**	**37,955**	**916.58**	**56.90**

7.4.2. CLIMATE

The climate of the IGB basins is mainly dominated by the East Asian and Indian monsoon systems and the Westerlies. The East Asian and Indian Summer Monsoon system mainly influences the eastern part of the Himalayas. In these regions (Eastern part of the Himalayas), most precipitation occurs during the monsoon period of June to September, and orographic effects intensify the north-south gradient in precipitation (Galewsky 2009). However, in the

western part of the Himalayas, the westerlies precipitation has become increasingly important. In the Hindu Kush and Karakoram, precipitation is more equally divided over the year due to the influence of both the westerlies in the winter and the Indian monsoon systems in the summer (Bookhagen and Burbank 2010). In the Karakoram and at the western margins of the upper Indus basin, most precipitation occurs during the winter period (Wijngaard et al. 2017). The complex topography of the Himalayan region introduces the altitude-dependent climatic variability ranging from semi-tropical to semi-arctic (Bahadur 1993). Many studies have documented that the temperature has increased in the upper part of the Ganges basin (Nepal) (Shrestha et al. 2000) and Brahmaputra basin (Bongartz et al. 2007), whereas in the Indus Basin, both increasing and decreasing temperature trends were observed since the 1960s (Archer and Fowler 2006). Wijngaard et al. (2017) investigated the influence of climate variability on extreme hydrological events. Furthermore, the climatic extremes were projected to increase in magnitude towards the end of the 21st century in the IGB basins.

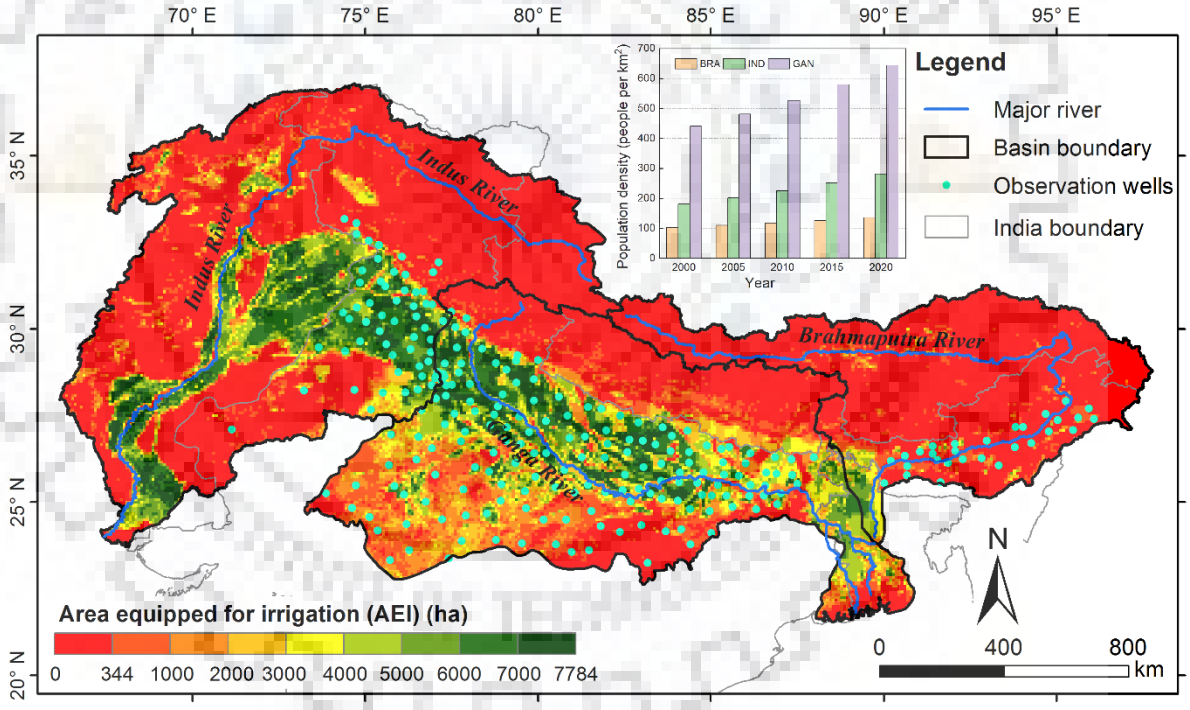

Figure 7.1. Location map of the study area, which includes area equipped for irrigation (AEI) of 2005 (data: http://www.fao.org/nr/water/aquastat/irrigationmap/index.stm) and observation wells (CGWB 2016) over the Indus, Ganga, and Brahmaputra river basins. The bar graph represents the population density map from 2000 to 2020 with five years of the time interval in each river basin (https://sedac.ciesin.columbia.edu/data/set/gpw-v4-population-density-rev11/data-download).

7.5. DATASETS UTILIZED

7.5.1. GRACE TERRESTRIAL WATER STORAGE ANOMALIES (TWSA)

GRACE is a twin satellite launched on 17 March 2002 in collaboration with the US-German space agencies (NASA-GFZ), continuously monitors variation in the Earth's gravity field (changes in mass) on monthly time scales with unprecedented accuracy (Tapley et al. 2004a; Famiglietti and Rodell 2013). The GRACE data provides a solution for eliminating atmospheric inundations and oceanic influences (Flechtner et al. 2007). The processed GRACE monthly mass grids land data is freely available and provided by the GRCTellus (source: https://grace.jpl.nasa.gov/data/get-data/monthly-mass-grids-land/).

We utilized 151 monthly solutions of GRACE data (level-3 RL-05, special harmonics) with 1° × 1° spatial resolution obtained from three research agencies, i.e., Center for Space Research (CSR) at the University of Austin/Texas, NASA Jet Propulsion Laboratory (JPL) and the German Research Centre for Geosciences (GFZ) for TWSA change between January 2003 and December 2016 (14 years). To enhance the accuracy of GRACE data, various filters were applied, such as de-striping filter, Gaussian filter, and special harmonics filter (Landerer and Swenson 2012). The 17 months of datasets were missing during the study period; the missing images of a particular month were replaced by the mean values of sequent months (before and after) (Long et al. 2015; Yang et al. 2017).

The mean TWSA was used by averaging the three data centre's solutions (JPL, GFZ, and CSR) for reducing the noise in the gravity field (Sakumura et al. 2014; Xiao et al. 2015) (Figure 7.2). The anomalies in the GRACE TWSA were computed using the baseline period (January 2004 to December 2009) because no missing datasets were found during this period. The total GRACE errors (measurement and leakage errors) are calculated over the Indus, Ganga, and Brahmaputra river basins to be 7.47, 7.07, and 7.02 cm, respectively (Wahr et al. 2006; Wiese et al. 2016). The TWSA includes the Groundwater Storage (GWSA), Soil Moisture Storage (SMSA), Surface Water Storage (SWSA), Snow Water Equivalent Anomaly (SWEA) (Thomas et al. 2017) is given in Equation 7.1.

$$TWSA_t = SMA_t + SWA_t + SWEA_t + GWA_t \quad \textbf{Eq. 7.1}$$

7.5.2. GLDAS OBSERVATION

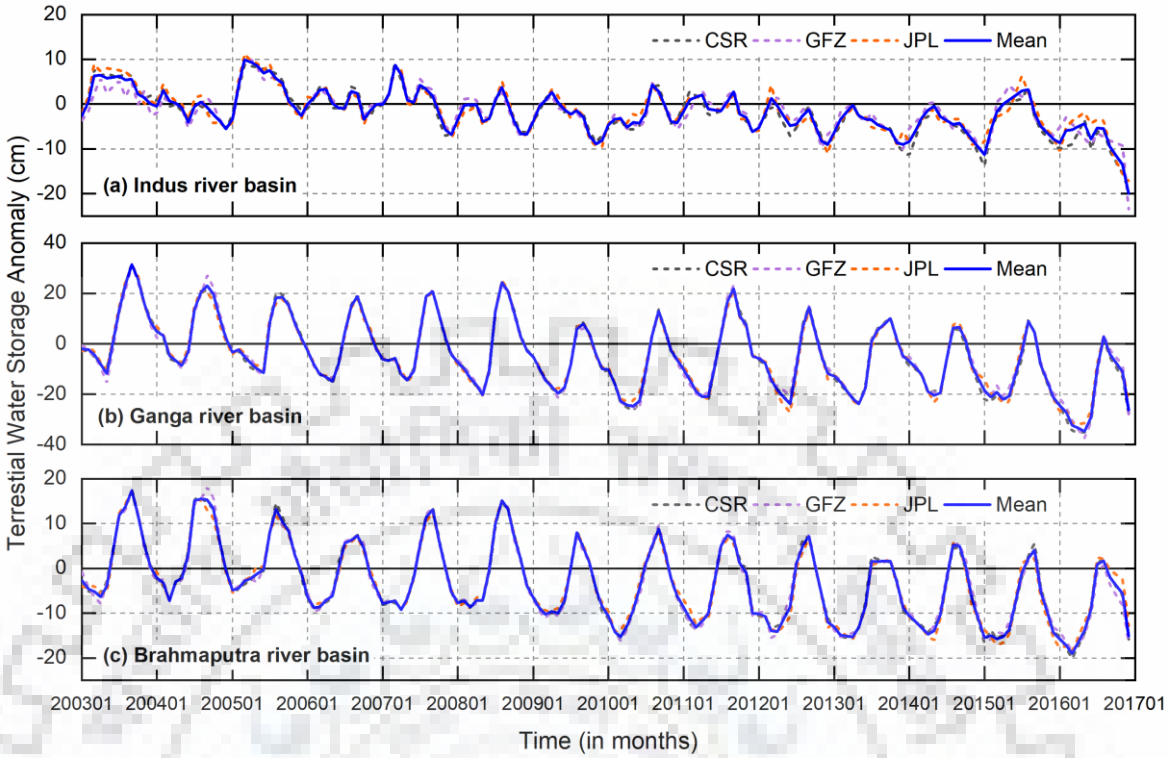

Figure 7.2. Mean monthly comparison of each GRACE TWSA product (CSR, GFZ, and JPL) and its combined mean over the a) Indus, b) Ganga, and c) Brahmaputra river basins.

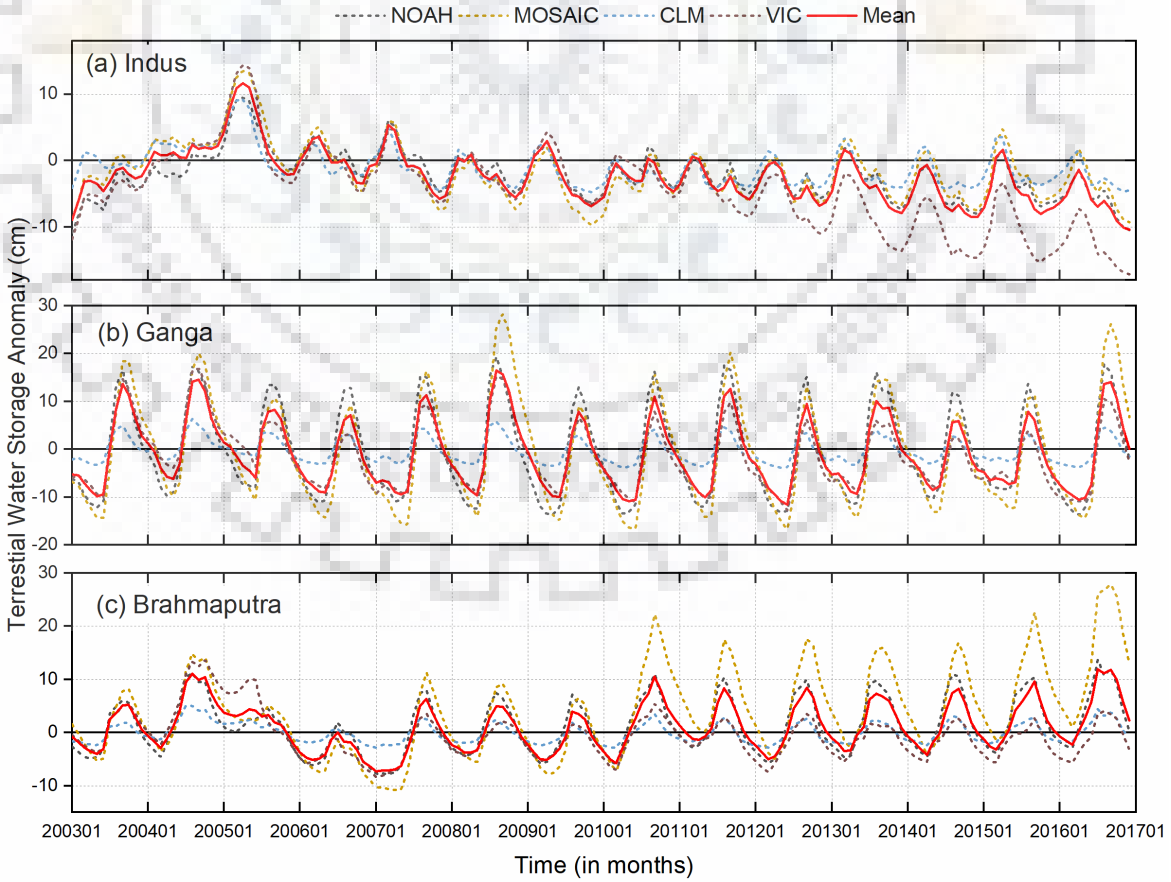

Figure 7.3. Comparison of GLDAS TWSA models (NOAH, MOSAIC, CLM, and VIC) and estimated mean measured by averaging the four products.

GLDAS is a joint project designed by NASA, the National Oceanic and Atmospheric Administration (NOAA), and the National Centers Environmental Prediction (NCEP) by integrating the hydrological components obtained from the ground and satellite-based observations with fine spatial and temporal resolutions (Rodell et al. 2004). The details of the data products are described by Rui and Beaudoing (2018). The GLDAS data comprises four Land Surface models (LSM) data, i.e., the Community Land Model (CLM2.0) (Dai et al. 2003), Variable Infiltration Capacity (VIC) (Liang et al. 1994), NOAH (Chen et al. 1996; Ek et al. 2003), and Mosaic (Koster and Suarez 1996).

For monthly TWS data through GLDAS, a summation of monthly Soil Moisture (SM) layer, Snow Water Equivalent (SWE), and the Canopy Water Storage (CWS) from four LSM datasets were used from 2003 to 2016. A comparison between each LSM model was established, as shown in Figure 7.3. The average of four LSM datasets was used to estimate the monthly TWS with minimum bias (Yang et al. 2017). A similar approach was adopted by other authors (Huang et al. 2015; Xiao et al. 2015; Ahmed and Abdelmohsen 2018; Wu et al. 2019). None of these LSMs datasets includes groundwater storage (Dai et al. 2003; Rodell et al. 2004). We neglect Surface Water Storage (SWS) in surface reservoirs such as rivers, lakes, dams, etc., which is not modeled in GLDAS, and assume it is likely a minor component in this region. Numerous studies are neglected the surface water storage changes for GWS estimation (Yeh et al. 2006; Rodell et al. 2007, 2009; Strassberg et al. 2007; Moiwo et al. 2009; Tiwari et al. 2009). The GLDAS TWS was converted into anomalies with the same consideration of GRACE data (baseline period of January 2004 to December 2009). The GWSA is obtained by subtracting the model-based $TWSA_{GLDAS}$ anomalies from the GRACE obtained $TWSA_{GRACE}$ (Sun et al. 2019) using equation 7.1. GLDAS has been used in numerous studies to isolate the GWSA from the GRACE derived TWSA in different regions of the world (Andersen et al. 2005; Leblanc et al. 2009; Matthew Rodell et al. 2007; Matthew Rodell,Velicogna, and Famiglietti 2009; Tiwari, Wahr, and Swenson 2009).

7.5.3. TROPICAL RAINFALL MEASURING MISSION (TRMM)

The Tropical Rainfall Measuring Mission (TRMM) 3B42 daily research Version 7 (TRMM-3B42-V7) precipitation data at 0.25º × 0.25º spatial resolution were used over the IGB river basins during 2003–2016 (Huffman et al. 2018). This product is designed for global precipitation analysis, and its algorithm combines several instruments (Huffman et al. 2007). Several authors have compared the TRMM data with observational data and reported good accuracy worldwide (Jia et al. 2011; Yang et al. 2017; Khan et al. 2018).

7.5.4. POTENTIAL EVAPOTRANSPIRATION (PET)

The daily global Potential Evapotranspiration (PET) with a spatial resolution of 1° × 1° datasets were used from 2003 to 2016. This data is generated from climate parameters, i.e., extracted from Global Data Assimilation System (GDAS) analysis fields. The National Oceanic and Atmospheric Administration (NOAA) generates the GDAS data every 6 hours and provides it freely on the USGS website https://earlywarning.usgs.gov/fews/product/81. The daily PET is calculated on a spatial basis using the Penman-Monteith equation (Shuttlewor 1992; Allen et al. 2006). The monthly and yearly PET was obtained using the accumulation of daily data.

7.5.5. STANDARDIZED PRECIPITATION-EVAPOTRANSPIRATION INDEX (SPEI)

Table 7.2. Detailed descriptions of each dataset used in this study from 2003 to 2016.

Data used	Variables	Agencies/Model (version)	Spatio-temporal resolution
GRACE	TWSA (CSR, GFZ, JPL)	CSR (RL05)	1º × 1º, Monthly
		GFZ (RL05)	1º × 1º, Monthly
		JPL (RL05)	1º × 1º, Monthly
GLDAS	TWSA (Mosaic, NOAH, VIC, CLM)	MOSAIC (V001)	1º × 1º, Monthly
		NOAH (V001)	1º × 1º, Monthly
		VIC (V001)	1º × 1º, Monthly
		CLM (V001)	1º × 1º, Monthly
TRMM	Precipitation	3B42v7	0.25º × 0.25º, Daily
SPEI	SPEI	SPEIbase v2.4	1º × 1º, Monthly
GDAS	Potential Evapotranspiration	SPEIbase v2.4	1º × 1º, Daily
MODIS	LST	MOD11C3 v6	0.05º × 0.05º, Monthly
	LST	MYD11C3 v6	0.05º × 0.05º, Monthly

The SPEI is the global drought monitor gridded datasets, provided by the Spanish National Research Council (CSIC) at time scales between 1 and 48 months with a 1° × 1° spatial resolution. The calibration period for the SPEI is from January 1950 to December 2010 (http://sac.csic.es/spei/). Currently, the SPEI is based on the Thortnthwaite equation for estimating potential evapotranspiration. This study used the one-month time-scale of SPEI data with an updated version (SPEIbase v2.4).

7.5.6. MODIS LAND SURFACE TEMPERATURE (LST)

The monthly MODIS LST products (MOD11C3 and MYD11C3) version 6 (day & night) have been used during 2003–2016. The LST products are freely available and downloaded from the EARTHDATA website (https://search.earthdata.nasa.gov/). The LST values in the products are derived by averaging the values from the corresponding month of daily (LST) images. The spatial resolution of products is $0.05° \times 0.05°$ with contaminated less cloud cover. The accuracy of data was validated using in situ measurements across the world (Wan 2014; Duan et al. 2019). The combination of day and night products was used to estimate the mean monthly LST of a corresponding month. The LST was reconstructed below the cloud cover pixel by averaging a 3-by-3 filter. A detailed description of all the datasets used in this study is shown in Table 7.2.

7.5.7. GROUND WATER LEVEL DATA

The groundwater levels of the IGB river basins (India part only) were acquired from Central Ground Water Board (CGWB 2016). The water levels of the observed well were analyzed from 2003 to 2016. The CGWB records the data during January (Post Rabi), April/May (Pre-monsoon), August (Monsoon), and November (Post Kharif) over the country. The groundwater level (GWL) monitoring by the State governments and archived by CGWB for assessment of groundwater resources. However, most of the GWL data is incomplete for each well in the database (block-wise data in a district) during the study period. The number of observational wells varies from district to district in the state. Therefore, we have analyzed the district-wise mean GWL data (i.e., all available wells in a district).

Total 253 observations GWL were used for in situ groundwater storage anomaly. In this study, a fixed mean specific yield (S_y) values were used over the IGB river basins (Indian part: Indus Basin = 0.095; Ganges Basin = 0.044; Brahmaputra Basin = 0.087) for groundwater storage (GWS) estimations (Bhanja et al., 2016). Since this S_y value of each basin is not based on field methods in the study area, it should be regarded as a source of uncertainty (Henry et al. 2011). Some studies have used a uniform specific yield value (0.12) in the whole study region to change groundwater levels to groundwater storage (Rodell et al. 2009; Panda and Wahr 2016). The specific yields were generated using long-term pumping test data conducted over the years (GEC 2017). The GWS has been observed by multiplying S_y and groundwater head (Δh) at all the well locations (Thomas et al. 2017). The Δh was calculated as per the procedure given by Bhanja et al. (2016). The GWS anomaly was calculated after subtracting mean GWS values (2004 to 2009) for comparing GRACE TWSA from all the individual observation data. The in situ groundwater

drought index (IGDI) was calculated using the in situ GWS anomaly, suggested by Thomas et al. (2017).

7.6. METHODOLOGY

7.6.1. COMPUTATION OF COMBINED TERRESTRIAL EVAPOTRANSPIRATION INDEX (CTEI)

In this study, a novel index was developed, i.e., Combined Terrestrial Evapotranspiration Index (CTEI), to accurately characterize drought occurrences by integrating the contribution of precipitation and PET anomalies as well as the TWSA over the three major river basins of the Himalayas. In contrast, several GRACE based indices were developed to describe the characteristics of water storage change in multi-temporal scales, e.g., the GRACE Groundwater Drought Index (GGDI) (Thomas et al. 2017), Water Storage Deficit Index (WSDI) (Sun et al. 2018) and the Combined Climatologic Deviation Index (CCDI) (Sinha et al. 2019). The GRACE-derived TWSA comprises the total water storage change within the vertically integrated water storage columns. It comprises surface, sub-surface, and groundwater storage variations.

The recently developed CCDI includes all the aspects of meteorological, agricultural, hydrologic, and human-induced drought occurrences. However, the main limitation of the CCDI is that its calculation is based only on precipitation and TWSA data. It does not consider the other drought-influencing variables, i.e., temperature, evapotranspiration, wind speed, and soil water holding capacity. Therefore, the motivation of developed indices is to integrate the contribution of hydrologic flux, i.e., precipitation, PET, and the hydrological storage conditions (the Terrestrial Water storage Anomalies) for assessing the drought conditions and identification of occurrences.

For the PET calculation, the Penman-Monteith (PM) equation (Allen et al. 2006) and the Thornthwaite equation (Thornthwaite and Mather 1955) are two representative methods which is based on physical principles (changes in available energy, humidity, and wind speed) and air temperature respectively. In this study, the PET was calculated using the PM based equations that is adopted by the International Commission on Irrigation and Drainage (ICID), the Food and Agriculture Organization of the United Nations (FAO), and the American Society of Civil Engineers (ASCE) as the standard procedure for computing PET. With a value for PET, the difference between the precipitation P and PET for the month i is calculated using Equation 7.2 (Vicente-Serrano et al. 2010).

$$D_i = P_i - PET_i \quad \textbf{Eq. 7.2}$$

Where D is the differences between the P and PET of each month. The differences anomaly (DA) was calculated using the following Equation 7.3 (Sinha et al. 2019):

$$DA_i = D_i - D_\mu \quad \textbf{Eq. 7.3}$$

A monthly differences anomaly (DA_i) time series is computed as the deviation of monthly D_i values from its mean D_μ (e.g., an average of January 2004 to December 2009) and TWSA is acquired directly from GRACE satellite solutions. The climatology of DA and TWSA are computed based on the GRACE deficit approach, discussed by Thomas et al. (2014). The climatology of 168 months (January 2003 to December 2016) was computed for the DA and TWSA time series in the study region by averaging the DA and TWSA values respectively of each month (e.g., all January in the 14 year record are averaged) (Thomas et al. 2017; Sinha et al. 2019). In this study, the monthly climatology was used to remove the influence of seasonality in DA and TWSA (Zhang et al. 2014). The monthly climatology of DA and TWSA were subtracted from each month of DA and TWSA respectively to obtain the residual in DA and TWSA time series. Both the residual were added to obtain the Combined Water Storage Anomalies (CWSA), which represents the net deviation in the volume of water storage based on seasonal variability. Finally, we normalize the CWSA by removing the mean CWSA_μ and dividing by the standard deviation CWSA_σ, expressed by Equation 7.4 where

$$CTEI = \frac{CWSA_i - CWSA_\mu}{CWSA_\sigma} \quad \textbf{Eq. 7.4}$$

CTEI represents the normalized net deviation in water storage volumes. The combined observed water storage anomalies and deficits over the IGB river basins as shown in Figure 7.4.

The severity of the drought events is calculated as a product of mean negative values (deficits) of CTEI and the duration (number of months) of a particular drought event persists (Yevjevich 1969; Thomas et al. 2014; Sinha et al. 2016, 2019). The drought severity is a dimensionless value because CTEI does not have any unit. Once the onset and termination of a drought event are identified, the severity for an event is calculated using the following Equation 7.5. (Thomas et al. 2014):

$$S(t) = \bar{M}(t) \times T(t) \quad \textbf{Eq. 7.5}$$

Where S is the severity, $\bar{M}$ represents the mean negative values of CTEI, T total duration of the drought events, and t denotes the occurrence of the specific drought events.

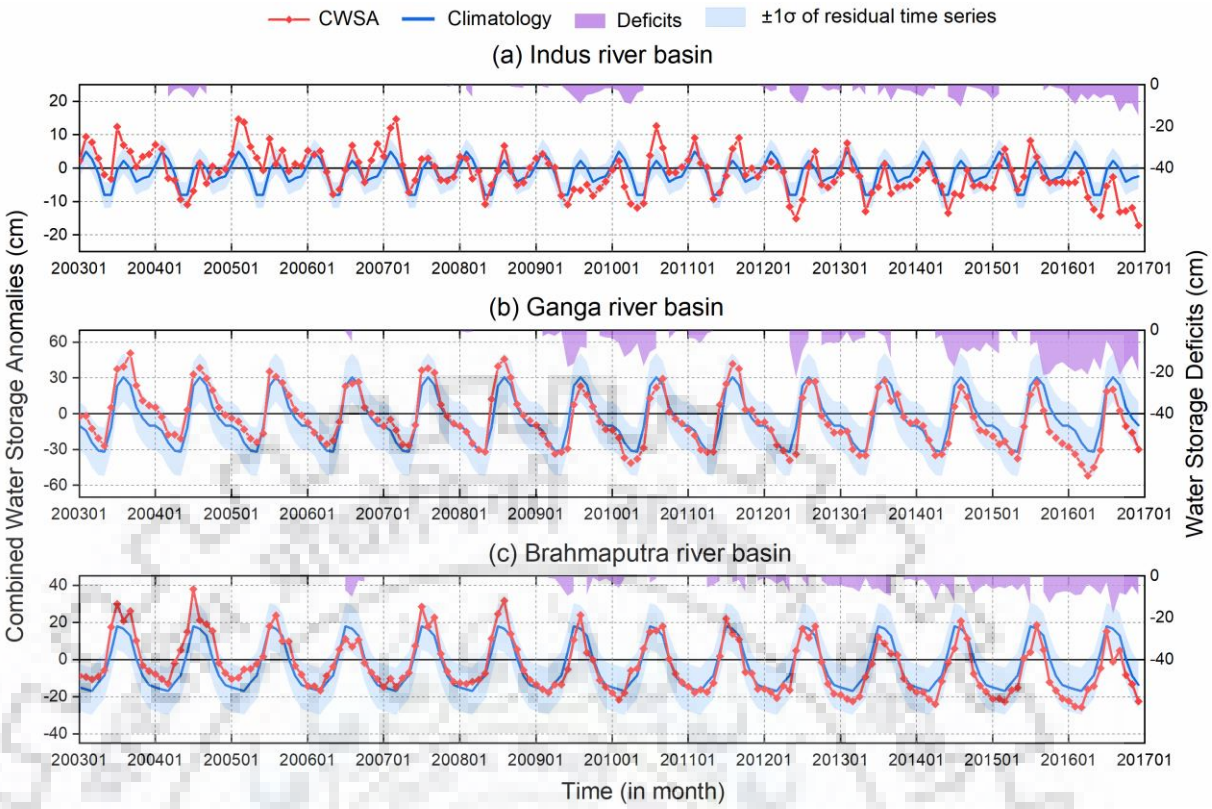

Figure 7.4. Combined observed water storage anomalies and deficits over the a) Indus; b) Ganga and Brahmaputra river basins. Red lines indicate the mean monthly CWSA; blue lines show the monthly climatology; purple-shaded area shows the water storage deficits (differences between the total anomalies and climatology of each month), and the blue-shaded area represents the $\pm 1\sigma$ of residual time series.

7.6.2. TREND ANALYSIS

Mann-Kendall (MK) (Mann 1945) and Sen's slope (Sen 1968) trend test non-parametric (i.e., distribution-free) methods were used to assess the monotonic trend (linear or non-linear) significance and their magnitude at defined confidence interval. These methods were widely used in hydro-meteorological time series data (Hamed 2008; Li et al. 2015; Deng et al. 2018a, b). Sen's slope test was used to detect the trend on CTEI, temperature, precipitation, and PET on monthly and annual time series data. The calculated MK Z-statistics value indicates an increasing (Positive Z-value), decreasing (negative Z-value), or no trend (zero z-value) in the time series data. In this study, the null hypothesis is rejected if $|Z| > 2.576$ at the 1% significance level, if $|Z| > 1.96$ at the 5% significance level and if $|Z| > 1.645$ at the 10% significance level were used.

7.7. RESULTS

To characterize the drought event, the potential of CTEI was developed based on the statistics obtained from GRACE TWSA, P, and PET over the IGB basins during 2003–2016. Results derived from CTEI mainly focus on assessing drought events and their severity in the major river basin. The performance and effectiveness of the methodology were validated with groundwater observation wells to monitor drought events accurately. Estimated CTEI drought events were compared with the existing drought indices for the same study period. Moreover, the correlation between CTEI and other derived drought indices was mapped to understand the best-fitted method for drought event identification. Furthermore, the spatio-temporal and the graphical interrelationship between CTEI and climatic variables (e.g., precipitation, PET, and LST) were analyzed to assess the changing variable pattern and their influence on drought events.

7.7.1. ASSESSMENT OF CTEI

The integration of precipitation, PET, and GRACE TWSA was used to develop a new index called CTEI. The IGB basins have diverse in terms of their area, topography, climate, culture, and livelihood. The basins are one of the most densely populated regions of the world, and the groundwater extraction rate is greater than 85%, mainly used for irrigation purposes (Mukherjee et al. 2015). A monthly scale of CTEI was mapped to characterize the drought events that occure from 2003 to 2016. A detailed analysis of CTEI was assessed to estimate the drought events, duration, peak month of the drought, severity, and total deficit (Table 7.4). The drought periods were identified if the CTEI value was negative continuous for three or more months. Figure 7.5 demonstrates the surplus (positive) and deficit (negative) water on monthly (left) and 3-month (right) moving average value of CTEI from 2003 to 2016. The monthly values of CTEI show a high frequency of fluctuations in time series data. Therefore, the centered 3-month simple moving-average technique was used for smoothing the data. The impact of drought on a particular month is influenced by water availability in the previous and next months of the year. Therefore, these three monthly average CTEI shows fewer identified drought events than one-month CTEI value (Figure 7.5).

The Indus river basin was identified ten drought periods based on monthly CTEI (Figure 7.5a). Two severe drought events were monitored in the Indus basin, i.e., May 2009 – August 2010 (14 months) and October 2015 – December 2016 (14 months), with the severity of –8.82 and –11.55, respectively. The highest peak month was observed in December 2016, with a magnitude of –1.90. The total water deficit of drought events in 2004, 2009, 2012, 2013, 2014, 2015, and 2016

were –23.46, –59.48, –21.43, –33.84, –41.10, and –94.72 cm with a duration of 8, 14, 4, 8, 9 and 14 months, respectively (Table 7.4)**.** The water deficit in 2004 was almost the same as in 2012, while the duration of the drought month was double in 2004, showing the severity of the drought was higher in 2012; however, the drought in 2004 was prolonged. These results are consistent with the reported results by several authors in the region (NRAA 2009; Rathore et al. 2013; PMD 2015; Torres 2015; Kothawale and Rajeevan 2016; Young et al. 2019). The drought events and total water storage deficit was increased during the study period. The time series of CTEI show a significantly decreasing monthly trend with a value of –0.006 month^{-1}.

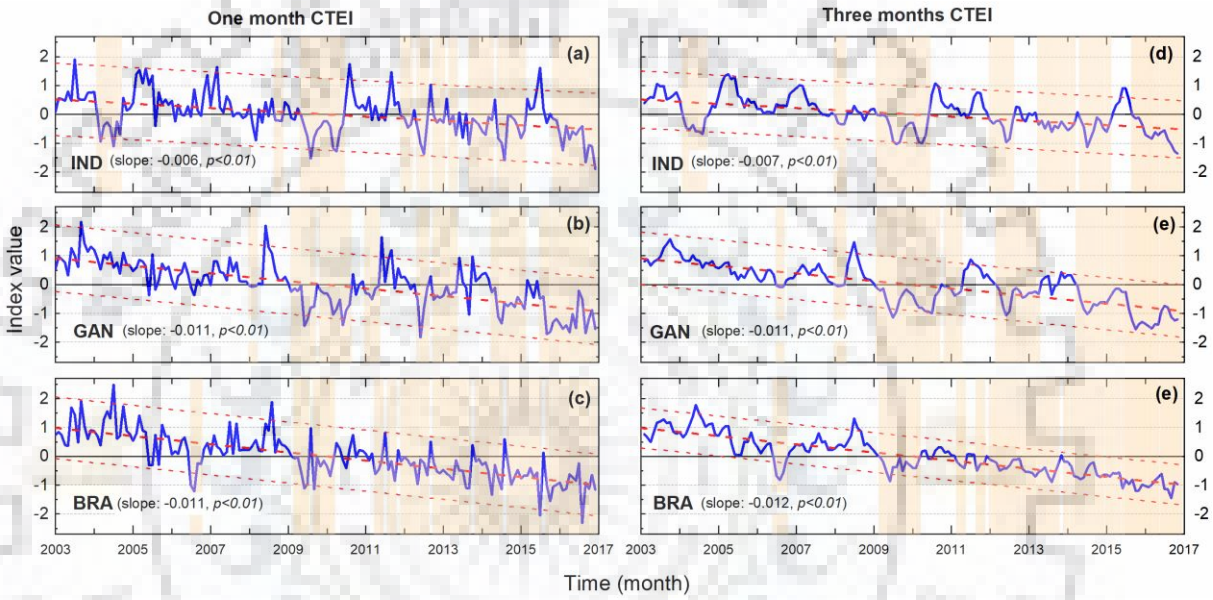

Figure 7.5. Monthly (left: a, b, c) and an average of three-month CTEI (right: d, e, f) over the three major river basins, i.e., Indus, Ganga, and the Brahmaputra. Blue lines: CTEI; Thick red dash lines: trend line; Red dash lines: 95% prediction band of CTEI; Orange bands: major drought events that exhibit negative CTEI for periods of three or more months.

The Ganga River basin has experienced eight drought events during the study period, illustrated by CTEI in Figure 7.5b. One was observed as the longest hydrological drought event for 18 months (July 2015 – December 2016), while the second and third were around 11 (April 2014 – February 2015) and 10 (October 2009 – May 2010) months, respectively. The highest severity occurred in September 2016, with a CTEI of –1.71. The total water storage deficit was about –278.64 cm (Table 7.4). The results are consistent with several studies over the region (NRAA 2009; Rathore et al. 2013; Torres 2015; Kothawale and Rajeevan 2016; Young et al. 2019). Apart, the total water storage deficit was higher (~ –43.30 cm) with a shorter duration (May 2012 – August 2012). The mean monthly trend of CTEI shows a decreasing trend (–0.011 month^{-1}) with statistically significant at $p < 0.05$.

In the Brahmaputra river basin, three out of ten drought events were observed the most prolonged drought about 16 months (September 2015 – December 2016), for 12 months (October 2012 – September 2013), and for 11 months (September 2014 – July 2015), respectively. It was observed that one month of surplus water storage interrupted the long drought events from May 2011 to August 2015 (a total of about six months of surplus water during the period). The largest peak severity was observed in August 2016, with a magnitude of –2.31. Kothawale and Rajeevan (2016) reported that the year 2003, 2005, 2006, 2009, 2010, 2011, 2013, 2014, and 2016 were the deficit year over North-East India based on summer monsoon (June to September). The monthly time series of CTEI represents a significant decreasing trend with a value of –0.011 $month^{-1}$.

Table 7.4. Summary of identified drought events using monthly CTEI values over the IGB river basins.

Time period	Duration (months)	Peak CTEI	Peak month	Severity	Total deficit (cm)
Indus river basin					
2004.02 – 2004.09	8	-1.10	Jul 2004	-4.16	-23.46
2008.09 – 2008.11	3	-0.23	Oct 2008	-0.64	-3.01
2009.05 – 2010.06	14	-1.53	Aug 2010	-8.82	-59.48
2011.12 – 2012.03	4	-0.47	Feb 2012	-1.02	-6.47
2012.04 – 2012.08	4	-1.37	Jul 2012	-3.08	-21.43
2012.10 – 2013.01	4	-0.30	Jan 2013	-0.77	-8.04
2013.03 – 2013.05	3	-0.73	May 2013	-1.07	-8.80
2013.09 – 2014.04	8	-1.05	Sep 2013	-3.38	-33.84
2014.06 – 2015.02	9	-1.59	Aug 2014	-4.96	-41.10
2015.11 – 2016.12	14	-1.90	Dec 2016	-11.55	-94.72
Ganga river basin					
2008.01 – 2008.03	3	-0.08	Feb 2008	-0.18	-1.77
2009.02 – 2009.09	8	-1.44	May 2009	-4.87	-56.53
2009.11 – 2010.08	10	-1.41	May 2010	-6.70	-80.43
2011.01 – 2011.05	5	-0.52	Mar 2011	-1.33	-14.90
2012.05 – 2012.08	4	-1.84	May 2012	-3.30	-43.30
2012.10 – 2013.05	8	-0.53	Oct 2012	-2.76	-37.41
2014.04 – 2015.02	11	-1.35	Jul 2014	-7.53	-98.87
2015.07 – 2016.12	18	-1.71	Sep 2016	-21.23	-278.64

Brahmaputra river basin					
2006.07 – 2006.10	4	-1.21	Aug 2006	-2.73	-21.05
2009.03 – 2009.07	5	-1.12	Jun 2009	-2.70	-23.74
2009.09 – 2010.03	7	-1.14	Sep 2009	-2.90	-22.65
2011.04 – 2011.06	3	-0.62	Apr 2011	-1.24	-11.57
2011.08 – 2011.10	3	-0.85	Oct 2011	-1.49	-11.96
2011.12 – 2012.08	9	-0.97	May 2012	-2.85	-24.17
2012.10 – 2013.09	12	-1.12	Sep 2013	-7.25	-63.62
2013.11 – 2014.07	9	-1.34	Apr 2014	-4.82	-44.01
2014.09 – 2015.07	11	-2.05	Jul 2014	-8.26	-63.83
2015.09 – 2016.12	16	-2.31	Aug 2016	-16.39	-129.74

7.7.2. COMPARISON BETWEEN CTEI AND OTHER EXISTING DROUGHT INDICES

A well-defined preexisting drought indexes were derived over the subjected basins, and outcomes were compared with the CTEI index for the study period (Figure 7.6). Three drought indexes (WSDI, GGDI, and CCDI) were derived using GRACE satellite data, while the SPEI were used precipitation and evapotranspiration. The monthly value of WSDI, GGDI, CCDI, and SPEI is demonstrated through a dashed line, and the CTEI is represented through a solid line (Figure 7.6). The observed result of CTEI and its response to the climatic anomalies reasonably agrees with preexisting indices. SPEI is the most important indices used for drought characterization as it is more sensitive to precipitation and evapotranspiration rates; consequently, high-frequency variations are observed in their time series. It is also important to recognize that the CCDI and CTEI demonstrated an almost similar pattern in their magnitude. However, the CCDI incorporated the impact of precipitation, whereas the CTEI uses the climatic water balance (differences between the Precipitation and PET) (Thornthwaite 1948) along with total water storage.

The spatial correlation was observed between CTEI and the other four drought indices over the three basins from 2003 to 2016 (Figure 7.7). The mean correlation between CTEI and GGDI varies from 0.99 to –0.18, with a mean value of 0.55 (Figure 7.7a). The spatial pattern illustrates a very heterogamous pattern in the region. A significantly higher correlation was observed in the Ganga (R = 0.92, $p < 0.01$) followed by the Indus (R = 0.86, $p < 0.01$) and the Brahmaputra (R = 0.85, $p < 0.01$) basins (Table 7.5). The correlation was measured slightly lower than the other GRACE-derived drought index, which may be the GGDI uses groundwater storage, computed using GLDAS data (Thomas et al. 2017). The correlation was measured between CTEI and

WSDI, varying from 0.99 to 0.18, with a mean value of 0.90 (Figure 7.7b). Similarly, the estimated correlation between CTEI and CCDI ranged from 0.99 to –0.17, with a mean value of 0.96. The correlation of CTEI with CCDI and WSDI was higher than other indexes, which may be these indexes were computed from the GRACE TWSA data (Sun et al. 2018). Further, the correlation of CTEI with SPEI varies from 0.87 to –0.57, with a mean value of 0.39. The SPEI indicates a significant correlation over the Indus (R = 0.07, $p < 0.01$), and no significant correlation was found in the Ganga and Brahmaputra basins (Table 7.5).

Table 7.5. Mean annual Pearson's correlation coefficient (Bold format represents the significant value at p < 0.01) matrix of drought indices for the IGB river basins.

	CTEI	GGDI	WSDI	CCDI	SPEI	IGDI
Indus river basin						
CTEI	1.00					
GGDI	**0.86**	1.00				
WSDI	**0.95**	**0.96**	1.00			
CCDI	**0.97**	**0.88**	**0.96**	1.00		
SPEI	**0.70**	0.44	0.60	**0.69**	1.00	
IGDI	**0.77**	**0.90**	**0.88**	**0.73**	0.48	1.00
Ganga river basin						
CTEI	1.00					
GGDI	**0.92**	1.00				
WSDI	**0.98**	**0.96**	1.00			
CCDI	**0.98**	**0.93**	**0.99**	1.00		
SPEI	0.42	0.34	0.35	0.44	1.00	
IGDI	0.57	0.45	0.57	0.60	0.60	1.00
Brahmaputra river basin						
CTEI	1.00					
GGDI	**0.85**	1.00				
WSDI	**0.97**	**0.90**	1.00			
CCDI	**0.98**	**0.87**	**0.98**	1.00		
SPEI	0.34	-0.09	0.25	0.32	1.00	
IGDI	0.49	0.30	0.43	0.49	0.28	1.00

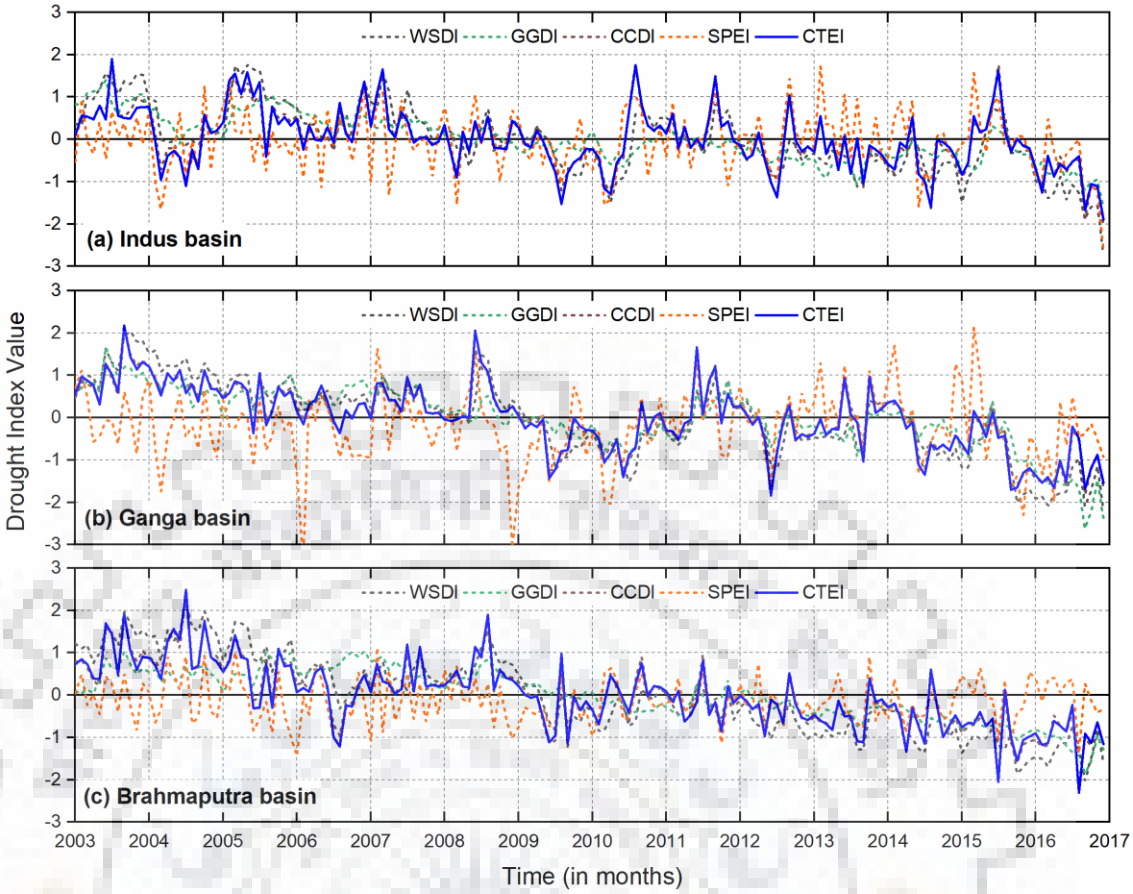

Figure 7.6. Comparisons between monthly CTEI and four other drought indices (WSDI, GGDI, CCDI, and SPEI) over the a) Indus, b) Ganga and, c) Brahmaputra river basins.

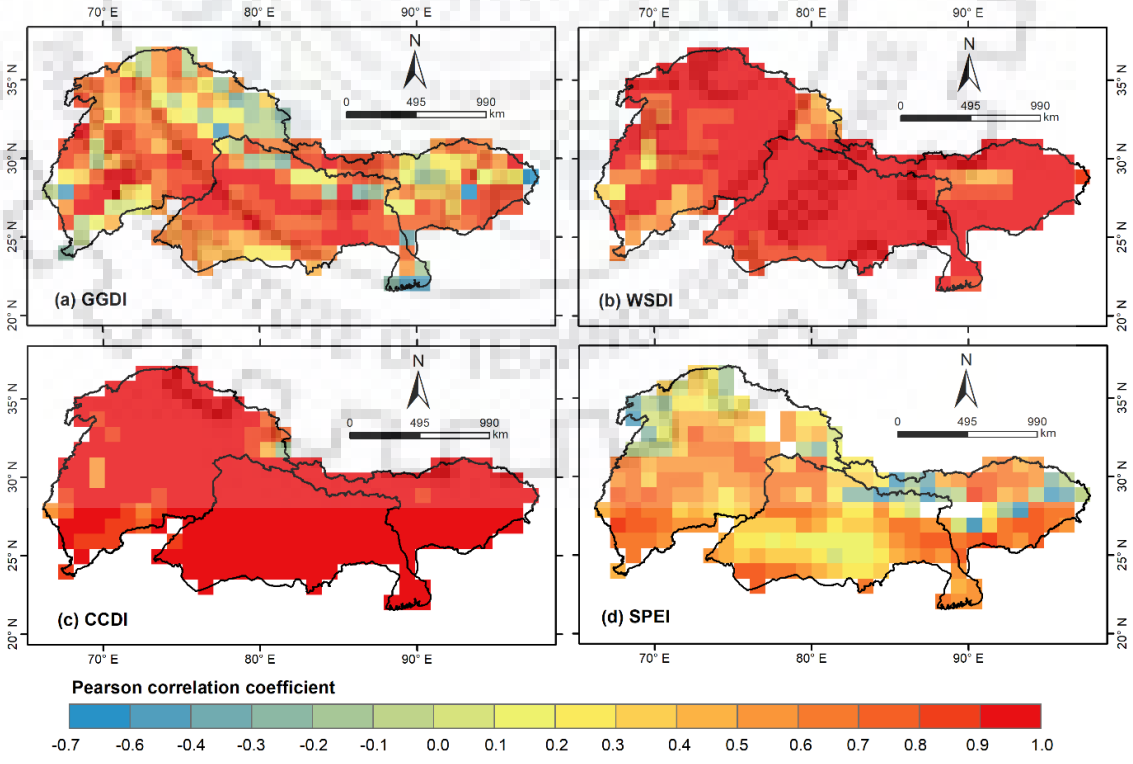

Figure 7.7. Pearson's correlation of mean annual CTEI with a) GGDI, b) WSDI, c) CCDI, and d) SPEI indices over the IGB river basins.

The estimated correlation of SPEI was lower because it may not include the total water storage and depends only on the climatic water balance (Vicente-Serrano et al. 2009). The relationship was also estimated between the CTEI and IGDI over the IGB basins from 2003 to 2016 (Table 7.5). A significant correlation was observed between CTEI and IGDI about 0.77 at $p < 0.01$ in the Indus basin, whereas it was insignificant in the Ganga (R = 0.57) and Brahmaputra (R = 0.49) basins. A similar relationship was observed between GRACE-based and in situ GWS anomalies in the northwest India aquifer (Long et al. 2016), the Indian state of Punjab (Panda and Wahr 2016), and the entire India (Bhanja et al. 2016).

7.7.3. COMPARISON OF CTEI WITH GROUND OBSERVATION DATA

The validation between remote sensing-derived results and in situ observation is essential to improve the effectiveness of algorithms or indices associated with the data retrieval (Bhanja et al. 2016). The proposed CTEI was compared with generated IGDI over the Indian part of the IGB river basins. The IGDI was computed using the dense networks of in situ observation wells. The performance of CTEI shows a good correlation with in situ data on a basinal scale. The mean annual trend of CTEI shows a significant decreasing trend in the Indus (–0.093, $p < 0.01$), Ganga (–0.139, $p < 0.01$), and Brahmaputra (–0.142, $p < 0.01$) river basins. Similarly, the IGDI shows a significant decreasing trend in the Indus (–0.056, $p < 0.01$) while an insignificant decreasing trend in the Ganga (–0.019) and Brahmaputra (–0.049) basins (Figure 7.8). The relationship between GRACE-derived GWSA and observational wells data was demonstrated by Bhanja et al. (2016) over India. Several studies show that the GRACE-based and ground-based observations found good agreement over different parts of the world (Long et al., 2016; Panda and Wahr, 2016; Matthew Rodell et al., 2007; Scanlon et al., 2012; Shamsudduha et al., 2012; Strassberg et al., 2007; Swenson et al., 2006). Our results show that both the indices (CTEI and IGDI) exhibit well match in the three river basins.

7.7.4. INFLUENCE OF CLIMATIC VARIABLES

Precipitation and temperature are the most influential climatic variables responsible for generating the condition of natural drought on a global scale. The increasing human-induced activities are accountable for declining the groundwater and changing the climatic parameters. The mean annual trend of rainfall shows decreasing in the Ganga (–0.13 cm yr^{-1}) and Brahmaputra (–1.14 cm yr^{-1})) basins whereas an increasing trend in the Indus (0.87 cm yr^{-1}) basin. The southwest monsoon rainfall in northeast India has decreased significantly since 1950, reported by Guhathakurta et al. (2015). However, the PET was increasing in the Ganga (1.01 cm

yr^{-1}, $p < 0.05$) and Brahmaputra (0.66 cm yr^{-1}) basin but decreasing in the Indus (–0.05 cm yr^{-1}, $p < 0.05$) basin. Similarly, the LST was insignificantly increasing with a rate of 0.07, 0.02, and 0.02 °C yr^{-1} for the Indus, Ganga, and Brahmaputra basins, respectively. Panda and Wahr (2016) reported groundwater storage depletion, which constitutes almost 90% of the TWS loss, is mainly influenced by the rise in temperatures since 2008.

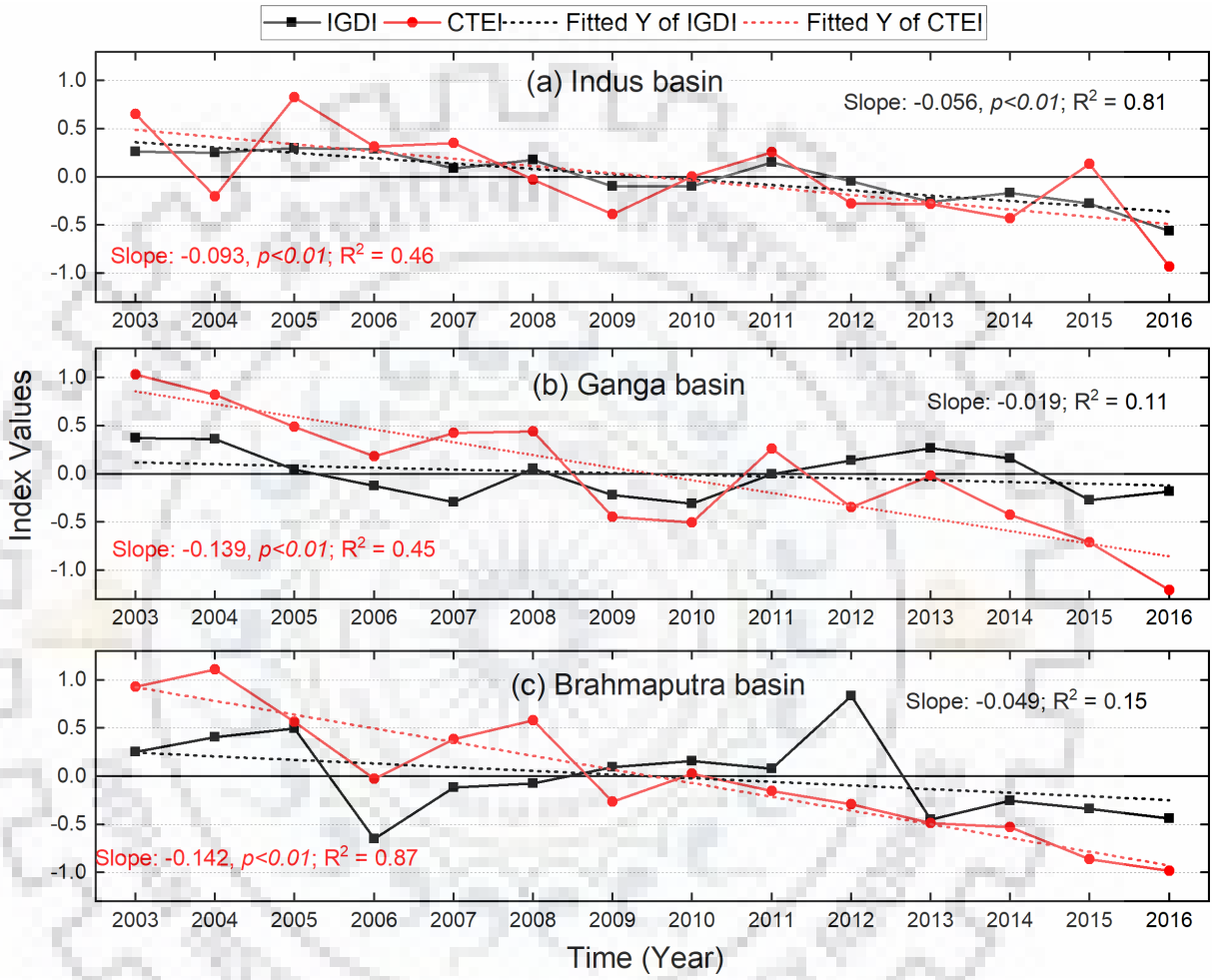

Figure 7.8. Comparison between the GRACE-derived CTEI and in situ based IGDI averaged over the (a) Indus (b) Ganga (c) Brahmaputra river basins from 2003 to 2016.

The relationship was established between annual CTEI and the estimated anomaly of LST, precipitation, and PET in each river basin during the study period (Figure 7.9). The anomaly was generated by subtracting the mean value (from 2004 to 2009) from each year to match the GRACE-derived CTEI value. A qualitative assessment of the drought/non-drought distribution indicates the interrelationship of these three crucial climatic parameters with CTEI. The interconnection of CTEI with climatic variables is more noticeable in the Brahmaputra, followed by the Ganga and the Indus basins. A negative precipitation anomaly was associated with positive LST and PET in 2004, 2009, and 2016 over the Indus basin, which CTEI successfully recorded

(Figure 7.9a). Similar climatic conditions were observed in the Ganga basin for drought years 2006, 2009, 2010, 2012, 2014, and 2015 (Figure 7.9b). In the Brahmaputra basin, the drought years 2006, 2009, 2011, and 2013 to 2016 were strongly associated with the CTEI and climatic variables (Figure 7.9c). The low precipitation with high PET and LST have strongly supported the observed drought years.

India has experienced four major droughts in 2004, 2009, 2014, and 2015 (NRAA 2009; Rathore et al. 2013; Kothawale and Rajeevan 2016). These droughts were severely affecting the various sectors and overall economic development of the country. Similar drought years were observed by Panda and Wahr (2016) in the Ganges basin that occurred due to anthropogenic groundwater withdrawals that sustain rice and wheat cultivation. Preethi et al. (2011) have reported the severity of drought events in 2009 due to the Indian summer monsoon deficit and link with the El Nino condition. Similar observation by the Indian Central Ground Water Board (CGWB 2011), the groundwater table declined in the northwest and north India from 2006 to 2008. The GWS depleted (derived from GRACE data) at the rate of 1.25 and 2.1 cm yr^{-1} has been observed in the Ganga basin and Punjab state (Indus basin) from January 2003 to May 2014 (Panda and Wahr 2016).

The interrelationship of the CTEI with PET and LST shows a significant negative correlation in the IGB basins (Table 7.6). A maximum negative correlation was observed in the Ganga, followed by Brahmaputra river basins. Similarly, a significant positive correlation was observed between the CTEI and precipitation over the Brahmaputra basin, and no significant correlation was observed in the Indus and Ganga basins. The interrelation between climatic variables was also observed. Precipitation shows a significant negative correlation with PET and LST in the Ganga basin. In the Brahmaputra basin, a significant negative correlation was observed between precipitation and PET and an insignificant with LST.

Table 7.6. Mean annual correlation coefficient (bold format shows the significant value at p<0.05) matrix of CTEI with climatic parameters over the IGB river basins.

	Indus River basin				Ganga River basin				Brahmaputra River basin			
	P	PET	LST	CTEI	P	PET	LST	CTEI	P	PET	LST	CTEI
TRMM	1.00				1.00				1.00			
PET	-0.49	1.00			**-0.58**	1.00			**-0.67**	1.00		
LST	-0.13	0.50	1.00		**-0.62**	0.45	1.00		-0.51	0.39	1.00	
CTEI	0.27	**-0.67**	**-0.54**	1.00	0.40	**-0.80**	**-0.63**	1.00	**0.56**	**-0.72**	**-0.63**	1.00

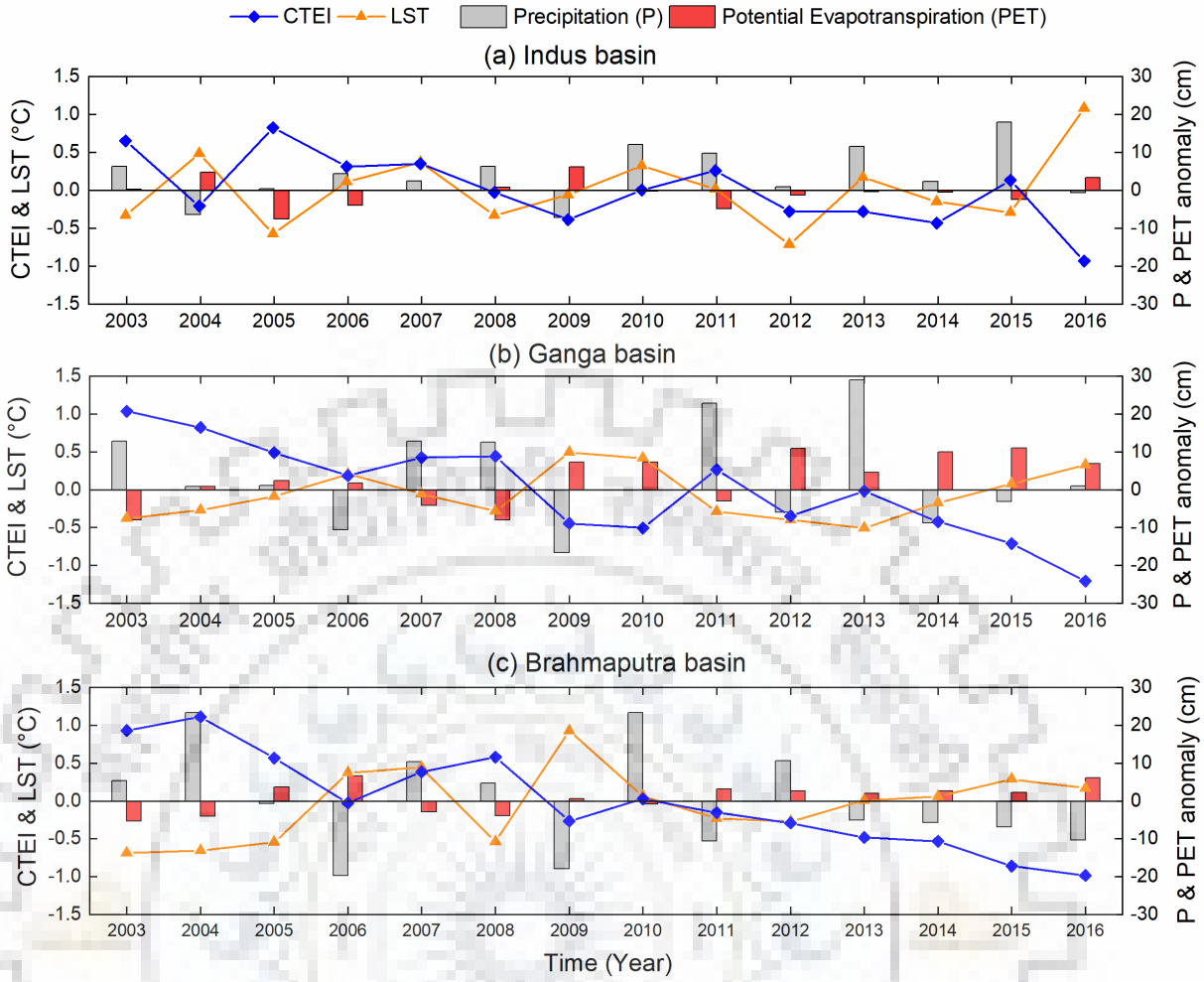

Figure 7.9. Mean annual anomalies of CTEI and other climatic variables (LST, precipitation, and PET) over the a) Indus, b) Ganga and, c) Brahmaputra river basins.

7.8. DISCUSSIONS AND CONCLUSION

The new CTEI index combines GRACE TWSA and the deviation of precipitation and PET from normal climatological conditions. To establish the efficiency and applicability of the index, the three major river basins (Indus, Ganga, and Brahmaputra) were selected over the Himalayan region. The selected basins are most important in terms of socioeconomic regions among the world's productive ecosystems. Further, the drought severity events are closely linked with food production and livelihood. The CTEI has the capability to correctly identify the drought events over the river basins through a comprehensive concept based on the hydrological and climatological conditions. Results comprise the temporal drought variability and intensity in the IGB basins with its implication for better understanding the actual drought condition and severity level. The estimated drought events correspond well matched with the historical reported events in the basins from 2003 to 2016. Besides, a few more drought events were characterized by CTEI, which was not yet reported due to capturing the multi-dimensionality of droughts, requiring

exhaustive measures. As drought event recognized by the CTEI endorsed as the low precipitation and high PET conditions for the study area. This condition further corroborates the hydro-climatological supported occurrence of drought.

A comparison of CTEI and other commonly used drought indices in spatial and temporal scales was used to highlight their fundamental difference. Result demonstrates that CTEI were highly correlated with the CCDI and WSDI over the basin. However, the difference between these two indices would be more prominent when analyzed over a small region with diverse hydro-climatological conditions and the contribution of precipitation easily identified. Because the precipitation shows a non-uniform and heterogeneous pattern that varies from location to location. The reason for the relatively low correlation of CTEI with other indices is that the new indices represent both the natural and human-induced drought occurrences. In contrast, other indices manifest meteorological conditions and other climatological conditions.

Furthermore, CTEI, a GRACE-based index, accounts for the surface and subsurface water column anomalies, which help to understand the availability of groundwater. The computation of SPEI allows a basic water balance calculation to scale the intensity of the drought. The SPEI uses monthly precipitation and PET data to identify and monitor the drought conditions and their associated impacts (Vicente-Serrano et al. 2009; Gautam and Bana 2014). Hence, SPEI can be considered to be somewhat similar to CTEI. However, it does not incorporate the contribution from the storage components in their computation, which is critical while assessing the drought events. Instead, CCDI is computed using precipitation and the number of water balance parameters. Therefore, it also explains why CTEI is highly correlated with CCDI compared to other indices. Consequently, it is suggested that the new CTEI could serve as a potential and complementary metric for drought identification and characterization.

The requirement of a new index is mainly related to a question of its efficiency over the other existing indices. About this, we need to acknowledge the parameter required to understand the drought's intensity, behavior, severity, and occurrence. In this regard, previously existing GRACE-derived drought indices incorporated the precipitation and the vertical land water column information to characterize drought. However, drought occurrence is mainly driven by natural and human-induced driving factors. Existing indices would be able to quantify the natural drought associated with precipitation and global warming. However, the formulation of CTEI with a holistic consideration of water balance components, precipitation, and PET has been considered to improve the accuracy of drought identification. The main objective of developing this index is to incorporate the climatological and hydro-meteorological responsible factors for

holistic drought monitoring over a large spatial and temporal scale. The selection of drought index by stakeholders mainly depends upon the geographical coverage, climatic conditions, and objective associated with the drought index. However, the CTEI will be particularly beneficial for drought assessment on a larger scale. Nonetheless, at the small scale, the choice of drought index may vary with the stakeholder as this index may not work for the smaller area (limitation of GRACE data < 2, 50,000 km^2).

CTEI has several advantages over the existing drought indices. It is a simplistic computation index, which reduces intensive numerical modeling & simulation and calibration & parameterization. The major contribution is to determine the intensification of drought by virtue of a reduction in precipitation and increase in PET, probably due to climate change and the growing demand for freshwater, which increases the stress on the groundwater resources. As the GRACE, observation is highly efficient for representing column land water storage variation in monthly time scale. Hence, the utilization of GRACE observation in CTEI can implicitly account for the natural and human-induced effect on drought assessment.

Overall, the CTEI is an innovative, effective index and observes potential results. Furthermore, the ease of computation and availability of datasets utilized in the public domain communicates the universal applicability of the proposed index. The result demonstrates the proposed index's ability to illuminate extreme climatic events and their comprehensive monitoring over local-regional-global scales. The study area has diverse climatic conditions and heterogeneous rainfall patterns; it is essential to employ the CTEI to quantify climatological and hydro-meteorological drought related to its integral deviation. This methodology presented here is expected to improve the drought characterization and monitoring for disaster management programs.

CHAPTER 8

PREDICTION OF DAILY DISCHARGE USING LONG SHORT-TERM MEMORY (LSTM) NEURAL NETWORKS, SUTLEJ RIVER BASIN (WESTERN HIMALAYA)

8.1. INTRODUCTION

Forecasting river discharge is a significant driver linked with the planning and operation of the water resource systems (Alizadeh et al. 2017; Chang and Guo 2020). The changing river discharge pattern not only impacted agriculture but also affected the livelihood of millions of populations. Therefore, a reliable prediction model needs to be developed for short-term and long-term streamflow events monitoring. The Long Short-Term Memory (LSTM) deep neural network model has been widely used for time series forecasting in several fields, such as runoff simulation (Callegari et al. 2015; Kan et al. 2017; Kratzert et al. 2018, 2019a; Le et al. 2019; Fan et al. 2020; Liu et al. 2020; Thapa et al. 2020), wind speed forecasting (Altan et al. 2021), drought prediction (Zhang et al. 2020; Dikshit et al. 2021), sea surface temperature (Zhang et al. 2017), weather forecasting (Hewage et al. 2020), water breakthrough prediction (Bai and Tahmasebi 2021), and stock prediction (Liu and Wang 2018; Lu et al. 2020; Rasheed et al. 2020). For example, Kratzert et al. (2019b) have found that the LSTM achieved better results of regional rainfall-runoff modelling against the multiple locally and regionally existing benchmark hydrological models. Also, Fan et al. (2020) investigated the runoff simulation using LSTM, Artificial Neural Network (ANN), and Soil & Water Assessment Tool (SWAT) model using meteorological variables. The performance of the LSTM model scored best in comparison to ANN and SWAT. Similarly, Thapa et al. (2020) have compared the result of the LSTM model with Nonlinear Autoregressive Exogenous (NARX), Support Vector Regressor (SVR), and Gaussian Process Regression (GPR) models over the Langtang basin in the Himalayas. They have also suggested that the LSTM outperformed other snowmelt-driven streamflow prediction models.

Numerous deep neural network-based prediction models exist; however, selecting a best-suited model for the study area is needed. Many studies have proven that the LSTM networks can predict reliable hydrological processes (Gauch et al. 2020; Zhang et al. 2020). Different environmental processes require hydrological components and discharge information at various time scales (Gauch et al. 2020). For example, hydropower generation projects may require discharge information daily or weekly (as input) into their reservoir. At the same time, we

consider the flood forecasting model that needed data at hourly or daily scale. Several studies have predicted the discharge using the deep learning approach at a daily scale in a different location (Hussain et al. 2020; Liu et al. 2020; Ajayi et al. 2021; Yao 2021).

In the Indian Himalayas, the application of deep neural networks on a basinal scale is less studied due to the scarce discharge locations and rugged terrain of the Himalayan region. However, the many regions of the Himalayas experienced several extreme events that affected the lives of millions of populations and infrastructure (Dale et al. 2017; Zhang et al. 2020). Therefore, a high-performance streamflow/river discharge prediction model is required at high temporal resolution in order to measure the implication on the ecosystem and even have the capability to fill the inconsistency in time series data. On the other hand, a comparison between different architectures of LSTM was established, and the best suitable model was selected in different regions (Althelaya et al. 2018; Cao et al. 2018; Wang et al. 2019; Rasheed et al. 2020). A similar approach of best model selection over the Himalayan region needs to be studied; therefore, five different LSTM architectures were applied, and their accuracy is being tested over the study region. Before selecting the best model for discharge prediction, a significant step is to select multiple sets of forcing variables that directly or indirectly contribute to river discharge change. Chollet and Allaire (2018) have also pointed out that picking the correct network architecture is more an art than science. Ideally, all the models should be able to process all forcing variables together to combine and correlate information across products and obtain better estimates of the true meteorological conditions (Kratzert et al. 2021).

8.2. RESEARCH QUESTIONS

- **Is it possible to forecast discharge using the machine learning model, and if so, to what extent?** Does the prediction model have the capability to incorporate all the necessary physical conditions into the model? Is the performance of the prediction model satisfactory?
- **What type of deep learning and machine learning model are suitable for prediction.** What is the performance of different LSTM forecasting models? Which kind of machine learning model is best suited for discharge prediction?
- **Does the use of PCA-based prediction improve the model performance?** Does the machine learning-based models outperform PCA-based? Is the best-suited model able to predict the short and long-term discharge over the region?

8.3. OBJECTIVES

- Quantification of contributing variables and selection of best-suited variable combination for discharge prediction
- Implementation of different LSTM architecture and identification of best-suited model for the study area
- Comparison between the best selected LSTM model and PCA generated prediction to analyze the suitable forecasting model and their reliability with time

8.4. STUDY AREA

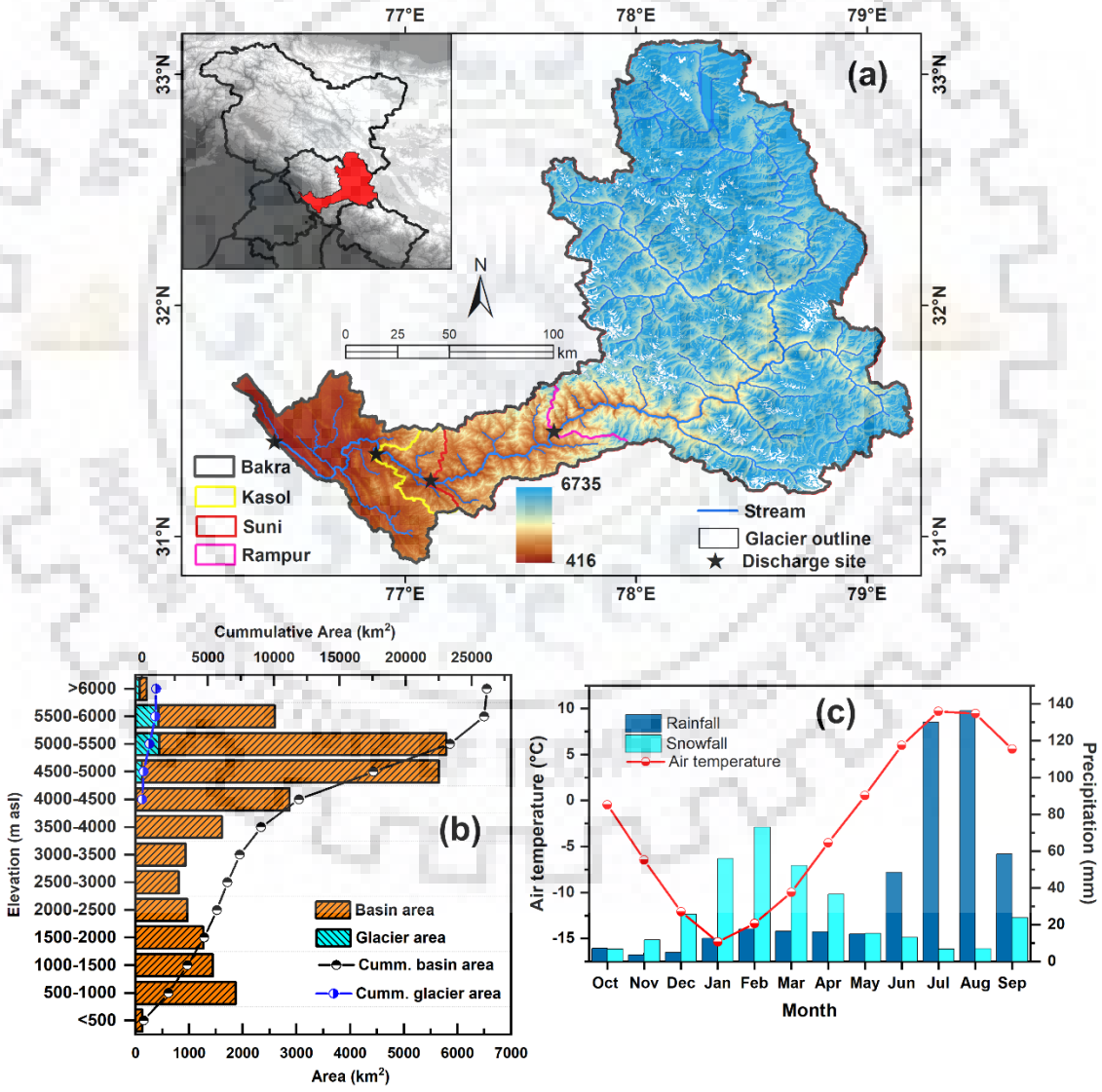

Figure 8.1. (a) Location map of the Sutlej River basin in India and its altitude variation using Shuttle Radar Topography Mission (SRTM) Digital Elevation Model Version 3.0 (DEM V3.0)

(~90-m spatial resolution). The basin boundary includes discharge sites, streams, glacier boundaries, and sub-basins represented up to the discharge sites (Bhakra, Kasol, Suni, and Rampur). (b) Hypsometry of the basin along with glacier areas, and (c) mean monthly distribution of rainfall and snowfall as well as air temperature measured through ERA-5-Land reanalysis data.

The Sutlej River originates from the Mansarovar-Rakastal lakes of the Tibetan plateau at an elevation above 4500 m a.s.l. and flows in the west and southwest direction while entering Himachal Pradesh, India (Singh et al. 2014). The study area of the basin is considered up to Bhakra dam with an outlet point of 76° 26'N and 31° 25'E (Figure 8.1a). The basin area lies between 76° 15′ – 79° 12′E and 30° 53′ – 33° 09′ N, covering an area of 26,158 km^2 and 21,845 km^2 area under Indian territory and lies between 76° 15′ – 79° 08′E and 30° 53′ – 33° 09′N. It covers parts of Simala, Kullu, Mandi, Bilaspur, and Solan districts of Himachal Pradesh. The basin has an elevation range from 415 to 6735 m a.s.l. based on SRTM DEM Version 3.0 (DEM V3.0) (~90-m spatial resolution). The majority of basin area (~66%) come under the elevation zone (above 4000 m a.s.l.), and even ~1084 km^2 glacier area estimated from Randolph Glacier Inventory (RGI 6.0) (RGI Consortium 2017) also exist in the same elevation zone. Therefore, the area above 4000 m a.s.l. is crucial for discharge prediction, as it contributes to melting in the summer season and feeds the basin population. (Figure 8.1b). This region is also characterized by a steep slope, dissected topography with high relief features.

The basin experiences a diverse climate variation ranging from tropical and warm temperate (in the lower part of the basin) to very cold (in the upper part of the basin). In the uppermost of the basin, the climate is characterized by the frozen area similar to the Polar regions (Mir et al. 2015). This uppermost region is predominantly nourished by western disturbances originating from the Mediterranean Sea (Dimri and Mohanty 2007). However, the lower portion of the basin receives rain, while the middle part of the basin is influenced by liquid and solid precipitation (Mir et al. 2015). The higher value of snowfall occurs between December and April, whereas the rainfall is mainly received from June to September. Apart from this, this region attains both types of precipitation throughout the year (Figure 8.1C).

Apart from the geography and climate of the basin, this region contains the second-highest gravity dam of Asia, which is constructed at Bhakra in Himachal Pradesh which is the terminus of the river (Mir et al. 2015). The other hydropower projects are the Sunni Dam Project of 1080 Mega Watt (MW), Rampur Hydro-electric Power Project (RHEP) of 412 MW, and Nathpa Jhakari Hydro-Electric Power Project (NJHEP) of 1500 MW. This basin identified hydropower

potential as 9,22,675 MW (Singh et al. 2014). Therefore, the meltwater of snow and glacier during the summer season is essential not only for hydropower generation but also for sustaining the ecosystem.

8.5. DATA USED

8.5.1. MODIS SNOW COVER PRODUCTS

In this study, the MODIS daily snow cover products version 6 (V6) of Terra (MOD10A1) and Aqua (MYD10A1) were utilized over the study area from 1 October 2000 to 30 September 2019. The datasets are freely available at the National Aeronautics and Space Administration (NASA) Earth data gateway customize service (https://search.earthdata.nasa.gov) with 500 m grid resolution and sinusoidal map projection. The Sutlej basin is covered in MODIS single tile with tile number h24v05 (i.e., horizontal 24 and vertical 5). A total of 6873 out of 6939 (66 images missing) images of Terra and 6374 out of 6390 (16 images missing) of Aqua were utilized during the observation period. While a total of 66 and 16 images of Terra and Aqua were missing for the entire period, respectively. All the missing images in each product were filled with the corresponding product. However, in the non-Aqua period, missing images were considered 100% cloud cover during the day. A detailed description of snow cover products generation could be found in Riggs et al. (2016).

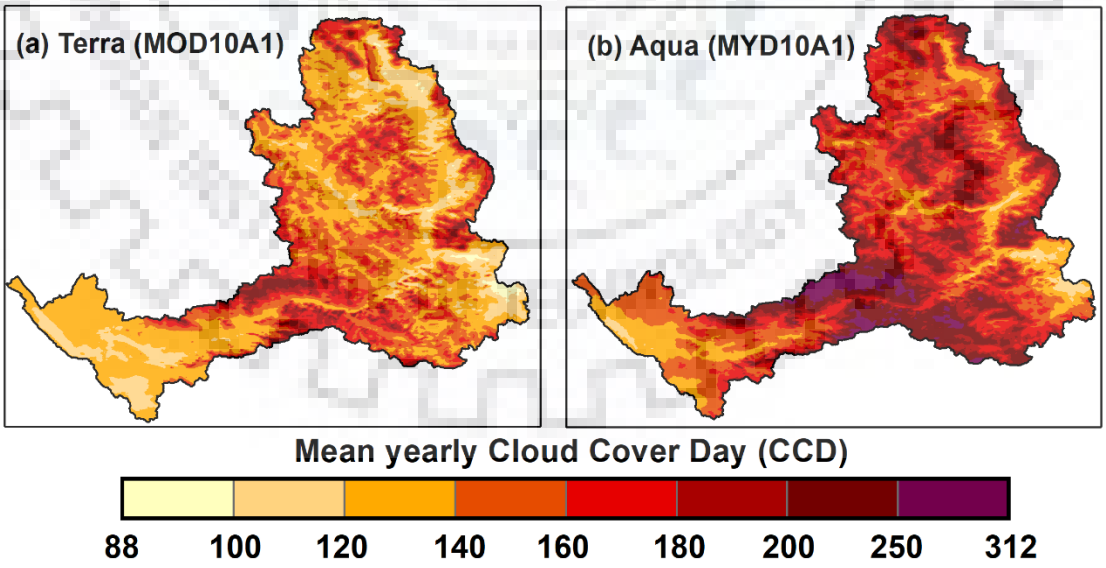

Figure 8.2. Mean yearly Cloud Cover Day (CCD) of the (a) Terra (MOD10A1) and (b) Aqua (MYD10A1) snow cover products, estimated over the Sutlej River basin from 2000 to 2019.

The datasets were stored in Hierarchical Data Format (HDF) with seven different parameters

(Normalized Difference Snow Index [NDSI] snow cover, raw NDSI, basic QA, algorithm flags QA, snow albedo, orbit pointer, and granule pointer). For this study, the NDSI snow cover parameter was used for both the snow products for SCA analysis. For this, we have used the global value of the NDSI threshold 0.4, as suggested (Riggs et al. 2016, 2017). The new images were generated from 9-standard MODIS classes (NDSI snow cover, Missing data, No decision, Night, Inland water, Ocean, Cloud, Detector saturated, and Fill), then reclassified into three new classes, i.e., no-snow, snow, and cloud. The mean Cloud Cover Day (CCD) of Terra and Aqua was 143 and 175, respectively, which is 18% higher in Aqua than the Terra images of the total geographical area (Figure 8.2).

8.5.2. ERA5-LAND REANALYSIS DATA

ERA5-Land is a global reanalysis dataset with a series of improvements that enhances the accuracy of the datasets and their applicability for all types of land cover monitoring. It is available from 1981 to the present on a regular latitude/longitude grid of 0.1° × 0.1° (~9 km) with an hourly and monthly time scale. ERA5-Land provides a single simulation with a consistent view of the water and energy cycles at a surface level (C3S 2019). Many authors have already used the ERA-5 over the Himalayan region (Bandyopadhyay et al. 2019; Yi et al. 2020; Patel et al. 2021a). In this study, we have utilized hourly data of snowfall, total precipitation, air temperature (T_a) and dew point temperature (T_d) at 2m, surface temperature (T_s), and wind speed (u_{10}) at 10-m (assessed from U and V components). The derived variables such as rainfall (total precipitation – snowfall) and relative humidity (RH: estimated from T_a and T_d) variables were also used to develop a discharge prediction model over the Sutlej River basin.

The hourly data of selected variables were obtained from 1 October 2000 to 30 September 2019 (19 hydrological years), available at Coordinated Universal Time (UTC) zone, which is 05:30 hours lag from the Indian Standard Time (IST) zone. Therefore, we marked 00:00 hour (UTC) as 05:30 hour (IST) and then converted the entire data into the IST zone. After converting UTC into IST, we have generated a daily time scale data from 00:30 hour to 23.30 hour (IST) for daily analysis. The hourly accumulated total precipitation and snowfall were taken from ERA5-Land between 1 October 2000 and 30 September 2019 (Table 8.1). These data are produced by accumulating the value from the beginning (01:00 hour UTC) to the end (00:00 hour UTC) of the forecast.

For this study, we have first converted the hourly accumulated value into hourly (next – previous hour) to analyze the variation in the IST zone. We have accumulated the hourly data to generate

the daily total precipitation and snowfall by considering the above criteria for UTC to IST conversion. The convention for accumulations used in ERA5-Land differs from ERA5, and a detailed description is available at https://confluence.ecmwf.int/pages/viewpage.action?pageId=197702790. Further, all hydrometeorological variables were interpolated into 500-m grid resolution to match the resolution of MODIS snow products using the bilinear interpolation technique.

8.5.3. FIELD MEASURED DISCHARGE DATA

A long-term daily discharge observation (1964 – 2012) over the Sutlej River basin was collected and supplied by Bhakra Beas Management Board (BBMB). The data was measured at four gauging stations, i.e., Bhakra, Kasol, Suni, and Rampur. The discharge observations were taken from the National Institute of Hydrology (NIH), Roorkee. The data is available for a period of 12 years (from 2000 to 2012) at Kasol, Sunni, and Rampur and for six years (2000 – 2006) at Bhakra (Table 8.1). This daily time step data was utilized for training and testing the model.

Table 8.1. A detailed description of the dataset used in this study for developing a time series forecasting model.

Dataset	Variables/location	Spatial resolution	Temporal resolution	Period	Source
MODIS	MOD10A1	500 m	Daily	2000–2019	National Snow and Ice Data Center
	MYD10A1	500 m	Daily	2002–2019	
ERA5-Land	Snowfall (P_s), Total precipitation (P_t), Air temperature (T_a), Dew point temperature (T_d), Surface temperature (T_s), U and V components of wind speed at 10 m	9 km	Hourly	2000–2019	Copernicus Climate Data Store
Discharge	Bhakra	--	Daily	2000–2006	Bhakra Beas Management Board (BBMB)
	Kasol, Sunni, and Rampur	--	Daily	2000–2012	

8.6. METHODOLOGY

This section comprises a detailed methodology to develop a discharge prediction model over the Sutlej River basin. The study includes remote sensing and reanalysis data to quantify the forcing climatic variables and their influence on discharge prediction. For this, a hierarchical methodology was developed, including cloud-gap filling in snow products, selecting contributing variables, analysing the sensitivity of hyperparameters, implementing different LSTM model architectures, and then finally predicting the river discharge for the study site. Also, we have predicted the time series daily discharge from 2012 to 2019 over the basin. All the selected datasets were split into training and testing. The first 80% of the data were used for the model generation, and the remaining 20% were used for validation purposes. A detailed description of the methodology is given below:

8.6.1. CLOUD REMOVAL METHODOLOGY

The presence of cloud cover hindered the daily MODIS snow products as a limitation of optical sensors. Many sequential composite methods were used to estimate snow under the cloud pixel (Gafurov and Bárdossy 2009; Parajka et al. 2010; Paudel and Andersen 2011; Hasson et al. 2014; Wang et al. 2014; Tran et al. 2019). In the present study, we have applied five steps sequential composite methodology for cloud removal. These are 1) combination of Terra and Aqua snow products, 2) short term temporal filter (2-days), 3) 8-nearest neighbourhood spatial filter, 4) regional snowline filter, and 5) multiday backward temporal filter. The selection of the methods and their sequence is based on the accuracy and its consideration, described in (Dharpure et al. 2020, 2021). Several studies have utilized the Snow Cover Area (SCA) as one of the main input variables for snowmelt-driven discharge hydrology (Kumar et al. 2013; Callegari et al. 2015; Thapa et al. 2020). The topographical information (elevation, slope, and aspect) was utilized in the nearest neighbour and regional snowline filters, extracted from Shuttle Radar Topography Mission (SRTM) Digital Elevation Model Version 3.0 (DEM V3.0) (~90-m spatial resolution) (Jarvis et al. 2008). The DEM was resampled at the MODIS grid resolution (500-m) using the bilinear interpolation technique (Lopez-Burgos et al. 2013).

8.6.2. SELECTION OF INPUT VARIABLES FOR MODEL GENERATION

All the essential climatic variables were selected for the discharge prediction over the study area. To quantify the best suitable variables, different approaches were applied, which will improve the performance of the model and to understand the association between input and output variables. For this, we have used correlation and Recursive Feature Elimination (RFE) techniques

for selecting the variables.

8.6.2.1. Correlation

A cross-correlation between all independent (T_a, T_s, u, RH, snowfall, rainfall, and SCA) and dependent (discharge) variables were measured at a daily time scale to assess the best-suited variables for the discharge prediction over the selected gauging discharge sites (Figure 8.3).

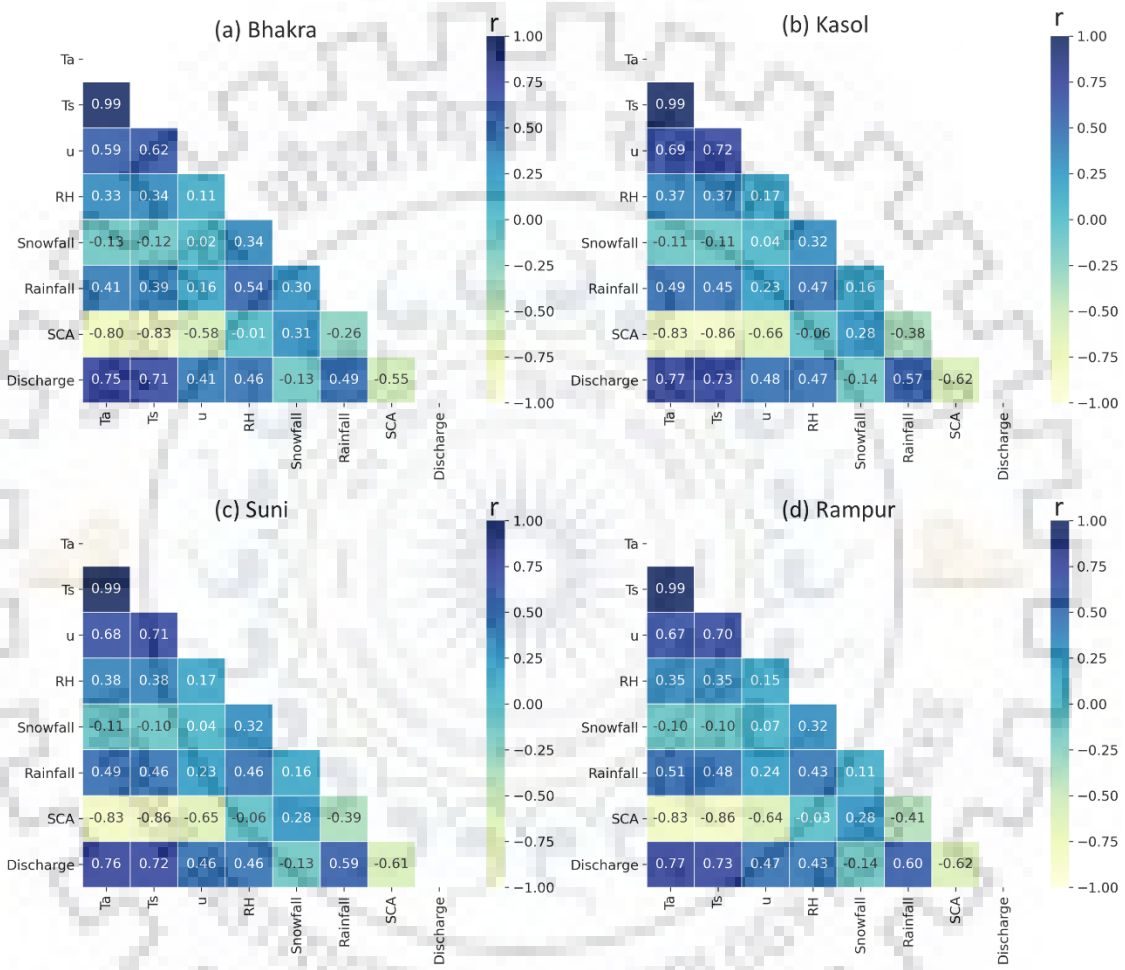

Figure 8.3. Correlation map depicts the interrelation between daily climatic (air and surface temperature: T_a and T_s, wind speed: u, relative humidity: RH, snowfall, and rainfall), SCA with discharge in the (a) Bhakra, (b) Kasol, (c) Suni, and (d) Rampur discharge sites during 2000–2012.

Result demonstrates that the T_a, T_s, u, RH and rainfall were directly correlated with discharge, whereas snowfall and SCA follow a negative correlation. Many authors illustrated a similar discharge relation with these variables over the Himalayan region (Banerjee et al. 2021; Thapa et al. 2021). The temperature (T_a and T_s) was highly correlated with discharge, while snowfall was less correlated relative to other variables. It indicates that any significant change in

temperature causes a direct impact on discharge. However, the less correlation of snowfall with discharge may have occurred because snowfall is an event that appears to have a dampening effect on discharge for about 5-7 days (Larsen 2017). The obtained result illustrates that the T_a and T_s were strongly correlated with each other. Gómez et al. (2021) have suggested that if any variable shows a higher correlation to each other, then any variable can be taken for further consideration. Therefore, we have selected T_a, RH, u, rainfall, and SCA for further model development.

8.6.2.2. Recursive Feature Elimination

After correlation-based feature selection, an RFE technique was used to rank all the variables and then select the best-suited variables with less Mean Absolute Error (MAE). This method can be applicable for categorical and regression data, used by many authors (Chen and Jeong 2007; Mathew 2019). In this study, we have a time series regression data of different variables (T_a, RH, u, rainfall, and SCA) from 2000 to 2012. For this, selecting the best subset of features (1 to N where N is the number of features) was done using RFE for different supplied estimators (Gradient Boosting and Random Forest). The selection of N features from the model was performed by fitting the time series data. The robust features were selected from each model by determining it either coefficient or feature essential attribute of the fitted model. For estimating the MAE of each selected model, the cross-validation technique was performed over the whole time series data by splitting (6 splits) it into the training and testing in a forward-chaining fashion, as described by Arize and Nogueira Rios (2019).

Table 8.2. Five generated models (based on the selection of features) and their mean MAE (standard deviation) using gradient bossing and random forest repressors applied on Recursive Feature Elimination (RFE) and cross-validation techniques.

Model	No. of selected variables	Gradient Boosting	Random Forest
Model-1	T_a	89.9 (14.4)	104.9 (14.9)
Model-2	T_a and RH	85.5 (15.9)	91.6 (15.2)
Model-3	T_a, RH, and SCA	85.5 (15.5)	89.4 (13.9)
Model-4	T_a, RH, rainfall, and SCA	85.2 (14.8)	88.3 (13.5)
Model-5	T_a, RH, u, rainfall, and SCA	84.9 (15.5)	87.4 (13.7)

Initially, we start cross-validation with a training set that includes the minimum number of observations needed to fit the model. Afterward, we progressively changed our train and test set

with each iteration and then measured the MAE of the model. When we increase (1 to N) the number of optimal features, the mean MAE starts increasing (at one) and becomes constant or no significant change after four selected features, as given in Table 8.2. If the MAE of the eliminated feature is flat or does not change significantly, their influence in the model is less. Based on MAE, the u was eliminated and T_a, RH, rainfall, and SCA were considered for further discharge prediction. And the model-4 and model-5 data were used for developing the prediction model.

8.6.3. BASIC LONG SHORT-TERM MEMORY (LSTM) ARCHITECTURE

LSTM neural network is an upgraded version of Recurrent Neural Network (RNN) and is more efficient than the standard version of RNN. LSTM can solve long-range dependencies by a sequence of input and output pairs introduced by Hochreiter and Schmidhuber (1997). The main advantage of LSTM has improved the problem of exploding or vanishing gradients in the back-propagation step (Kratzert et al. 2019b). A typical architecture of the LSTM neural network is shown in Figure 8.4. It comprises three types of gates, i.e., forget gate, input gate, an output gate, and one cell state or memory cell for controlling the flow of information. The data can be added or modified in the memory cell via this specific structure of gates. However, the basic LSTM network was enhanced by storing or neglecting the cell information via forget gate, introduced by Gers et al. (2000).

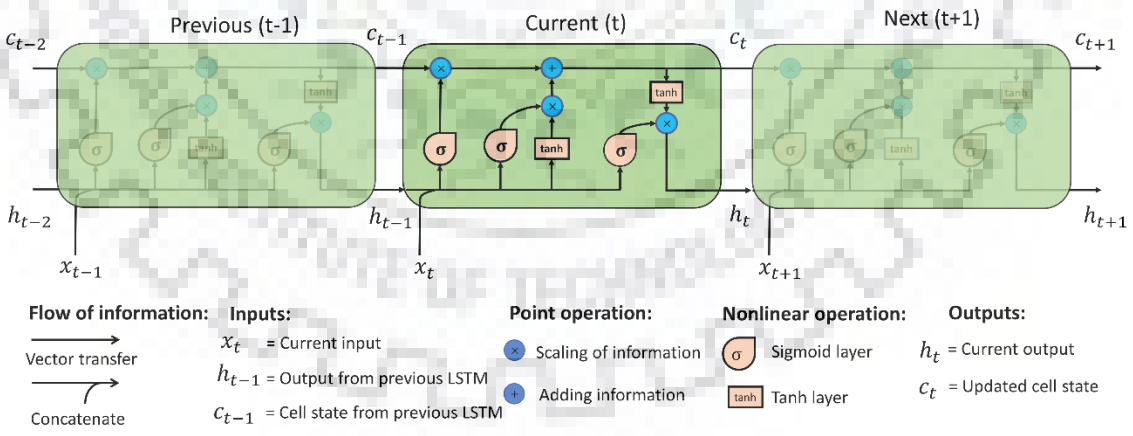

Figure 8.4. Repeating module of standard Long Short-Term Memory (LSTM) neural network.

The forget gate includes the previous LSTM output (h_{t-1}) and the current input (x_t) with bias (b_f), which passes through a nonlinear sigmoid activation function. The value of forget gate output (f_t) produces a binary vector, indicating one as new information that keeps in the cell state while a zero is completely forgotten. The f_t can be achieved by following Equation 8.1.

$$f_t = \sigma(W_f[h_{t-1}, x_t] + b_f \quad \textbf{Eq. 8.1}$$

Then, updating or omitting the new information in the cell state was performed by passing the previous (h_{t-1}) and current (x_t) input information from the two nonlinear functions, i.e., sigmoid and hyperbolic tangent function (tanh). The sigmoid layer (i_t) decides which new information will be ignored or updated in the cell state based on 0 and 1 while the tanh layer used for providing the weights based on the level of importance (-1 to 1) called g_t cell state. It can be expressed by Equations 8.2 and 8.3**.**

$$i_t = \sigma(W_i[h_{t-1}, x_t] + b_i \quad \textbf{Eq. 8.2}$$

$$g_t = tanh(W_n[h_{t-1}, x_t] + b_n \quad \textbf{Eq. 8.3}$$

To update the current cell state (c_t), the output of sigmoid (i_t) and tanh (g_t) vector was multiplied element-wise and then added with the multiplicative output of f_t and previous cell state (c_{t-1}), expressed by Equations 8.4.

$$c_t = c_{t-1} \odot f_t + g_t \odot i_t \quad \textbf{Eq. 8.4}$$

To estimate the current output (o_t), the previous (h_{t-1}) and current (x_t) input information was passed through the sigmoid function to decide which parts of the cell state make it to the output, expressed by Equation 8.5.

$$o_t = \sigma(W_o[h_{t-1}, x_t] + b_o \quad \textbf{Eq. 8.5}$$

The updated current cell state (c_t) was passed from the tanh function, and the obtained vector was element-wise multiplied ($\odot$) with current output (o_t), which produce current hidden output (h_t), expressed by Equation 8.6.

$$h_t = o_t \odot tanh(c_t) \quad \textbf{Eq. 8.6}$$

Where W is the adjustable weight metrics and b is the adjustable bias vector for the forget, input, and output gates. $\odot$ indicates the element-wise multiplication. $\sigma(\cdot)$ and $tanh(\cdot)$ are the logistic sigmoid and hyperbolic tangent functions, respectively. The final output of the layer of the LSTM is obtained through Equation 8.7.

$$y = W_d h_n + b_d \quad \textbf{Eq. 8.7}$$

Where y is the final discharge, h_n is the output of the last LSTM network obtained from **e**quation 8.6, W_d and b_d are the weight matrix and bias vector of the dense layer, respectively.

8.6.4. DESCRIPTION OF DIFFERENT LSTM MODEL ARCHITECTURE

LSTM model includes different structures to forecast the spatial and temporal time series data, for example, single layer (Vanilla), multilayer (stacked), and bidirectional LSTM (BLSTM). The major difference between these models is the varying hidden layer, i.e., if the hidden layer is single, then it is denoted as vanilla LSTM (VLSTM) model while more than one hidden layer was stacked, then it is denoted as stacked LSTM (SLSTM). And the bidirectional model follows a two-layered model in which one layer performed operation in the forward direction of the data sequence and another layer applied operation in the reverse direction of the data sequence, and then the final output was generated by combining both interpretations (Althelaya et al. 2018). This bidirectional model is an extended variation of RNN proposed by Schuster and Paliwal (1997).

Other than this, two well renowned LSTM models (CNN and ConvLSTM) were mainly designed for sequence prediction in two-dimensional spatial data. However, it can be modified for univariate/multivariate time series forecasting data. These two model structures mainly differ by their inputs, in which the CNNLSTM model can interpret each subsequence of two-time steps and provide a time series of interpretations of the subsequences to the LSTM model to process as input. The input data can then be reshaped to have the required structure [samples, subsequences, timesteps, features]. While, ConvLSTM layer expects input as a sequence of two-dimensional images (rows and columns); therefore, the shape of input data must be [samples, timesteps, rows, columns, features]. More detailed information on the CNNLSTM and ConvLSTM were discussed by Donahue et al. (2017) and Shi et al. (2015). In the present study, we have used five different LSTM model structures to quantify the best-fitted model over the selected basin.

Moreover, the value of multiple input variables was presented an extensive range that affects the learning skills and the convergence of the LSTM network during training. Therefore, for efficient learning and faster convergence, input and target variables normalized between 0 and 1, without any changes in the shape of original variables. The normalized procedure is given by Equation 8.8:

$$x_n = \frac{x - x_{min}}{x_{max} - x_{min}} \qquad \textbf{Eq. 8.8}$$

Where, x is the original vector, x_n is the normalized vector, x_{min} and x_{max} are the minimum and maximum values of vector x, respectively.

8.6.5. PRINCIPAL COMPONENT ANALYSIS

PCA is the statistical approach that will help to reduce the covariance amount in the set of variables. Suppose a set of orthogonal vectors is found in the test space; in that case, the original data of M dimensional space is projected into the N dimension sub-space expended by this set of orthogonal vectors (M > N). This projection coefficient comprises a new features vector which helps in completing the dimensionality reduction. The PCA identifies the principal directions from which the data start varying to the maximum. This principal direction helps for obtaining the features having higher discriminative and can give useful information about the data patterns (Rasheed et al. 2020). In this study, the model-5 dataset was selected and converted into the standardized format ($\frac{x-\mu}{\sigma}$, where x is the sequence of data, μ and σ is the mean and standard deviation of the sequence) before applying the PCA. We have selected the three principal components to analyze the variation in model accuracy by dimensionality reduction.

8.6.6. OPEN-SOURCE SOFTWARE USED

This study was carried out using python programming language version 3.7.6. open-source software, i.e., Scientific Python Development Environment (Spyder) 4.0.1. We have installed different libraries in the software such as WhiteboxTools v1.4.0 (Lindsay 2020) and Gdal v3.2.0 (Warmerdam and Rouault 1998) for spatial data pre-processing and Numpy (Van Der Walt et al. 2011), Pandas (McKinney 2010), Scikit-Learn (Pedregosa et al. 2011) for data management, and Matplotlib v3.1.1 was used for preparing the graphs (Hunter 2007). We use the Deep-Learning frameworks TensorFlow (Abadi et al. 2016) and Keras (Chollet 2016).

8.6.7. PERFORMANCE METRICS

The model performance was tested based on the Root Mean Square Error (RMSE) and Nash-Sutcliffe Efficiency (NSE) (Nash and Sutcliffe 1970) statistical approaches. These methods are widely used to evaluate the machine learning model (Fan et al. 2020). The RMSE value equals zero, indicating the perfect match of predicted values with observed values while NSE values vary from –∞ to 1. The RMSE value should be small or near zero for reliable model performance and the NSE value close to one. The following Equations 8.9 and 8.10 are used for estimating the statistical matrices as follows:

$$RMSE = \sqrt{\frac{\sum_{t=1}^{n}[y_o(t)-y_p(t)]^2}{n}} \quad \textbf{Eq. 8.9}$$

$$NSE = 1 - \frac{\sum_{t=1}^{n}[y_o(t)-y_p(t)]^2}{\sum_{i=1}^{n}[y_o(t)-\underline{y_o}]^2} \quad \textbf{Eq. 8.10}$$

Where y_o and y_p are observed and predicted discharge at time t. $\underline{y_o}$ and $\underline{y_p}$ represent the average observed and predicted discharge at time t. n indicates the total number of observations.

8.6.8. EFFECT OF HYPERPARAMETERS ON MODEL PERFORMANCE

The accuracy of the prediction model was significantly affected by the selection of hyperparameters such as activation function, number of LSTM layers, hidden units, loss function, learning rate, optimization algorithm, batch size, dropout rate, and time steps. Several authors previously discussed the dependency of hyperparameters on model prediction (Kratzert et al. 2018, 2019b; Fan et al. 2020; Thapa et al. 2020). Therefore, we have performed a test to quantify the best suitable hyperparameters using the model-4 dataset and applied them to the VLSTM model over the Rampur discharge site.

Table 8.3. Performance of the different activation functions and their estimated mean (standard deviation) of NSE and RMSE during the training and testing stages for ten iterations (repeating model).

Activation functions	Training		Testing	
	NSE	RMSE	NSE	RMSE
elu	0.78 (0.00)	120.9 (0.3)	0.85 (0.00)	112.4 (1.4)
relu	0.78 (0.00)	119.5 (1.2)	0.86 (0.01)	108.4 (2.4)
selu	0.78 (0.00)	119.9 (1.0)	0.85 (0.01)	112.7 (2.9)
sigmoid	0.74 (0.00)	129.4 (1.0)	0.81 (0.01)	128.1 (1.8)
softmax	0.75 (0.00)	127.3 (0.3)	0.83 (0.00)	121.6 (0.5)
softplus	0.76 (0.00)	125.7 (1.1)	0.84 (0.01)	118.7 (3.0)
softsign	0.78 (0.00)	119.5 (0.5)	0.86 (0.00)	108.6 (1.9)
tanh	0.78 (0.00)	120.5 (0.4)	0.86 (0.00)	111.2 (1.6)

The LSTM model obtained the current hidden out, by passing the current cell state through the tanh activation function. However, many other activation functions can use at a place of tanh function. Here, we have applied the most significant nonlinear activation functions for evaluating the model performance. Our results suggested that the softsign activation function

$[f(x) = x/(1 + |x|)]$ performed well in training and testing than other activation functions (Table 8.3). Lin and Shen (2018) have revealed that the softsign function is similar to the tanh, but it has a relatively slow and soft saturation, making it more robust to avoid vanishing gradients.

Further, we have varied the LSTM layer from 1 to 6 based on the model-4 dataset using SLSTM neural network. Results demonstrate that the shallow LSTM network (single layer) was performed well compared to the deep neural network (Figure 8.5a). Thapa et al. (2020) have also concluded that the shallow LSTM model with a single hidden layer achieved superior results than the deeper LSTM models with multiple hidden layers. Then, we have also altered the number of hidden units in the LSTM layer (number of LSTM units per time step) to evaluate the effect of forecast outcomes. Results suggested that the higher NSE was found in the 50 hidden units, and it varies with other hidden units (Figure 8.5b). Another parameter of interest in establishing a model structure is the learning rate and the number of epochs applied on VLSTM using the model-4 dataset. The NSE value was found maximum in 0.005 learning rate compared to the other learning rate (Figure 8.5c). It was also seen that this learning rate (0.005) was able to produce higher loss between observed and predicted data in starting and then converges down when the number of epochs was increased. Our results also revealed that the smaller value (0.0001) of the learning rate could make the model's training process slower, and the curve of loss function becomes smother. A similar pattern of small learning rate was found by Le et al. (2019). We have also increased the number of epochs from 20 to 180 (Figure 8.5d). The results revealed that the 160 and 180 epochs were found higher NSE during the testing stage; therefore, 180 epochs were selected for further model evaluation.

In the VLSTM model, we have applied seven different optimization algorithms other than Adaptive moment (Adam) using the model-4 dataset. However, one more optimization algorithm (Ftrl) was not considered because of their lower NSE value over the study area. Thapa et al. (2020) have compared the different optimizers and suggested that the Adadelta shows higher RMSE than other optimizers. Our results indicate that the Adam optimizer found higher NSE, followed by Nadam and Adamax (Figure 8.5e). Then, the RMSE value was measured by varying the dropout rate from 0.0 to 0.2 with an interval of 0.05. Our observation suggests a higher NSE in 0.0 or no dropout rate while it started decreasing when the dropout rate was increased (Figure 8.5f). This pattern indicates that the dropout rate and NSE value were inversely proportional to each other.

Further, the batch size of model prediction was analyzed over the VLSTM and model-4 dataset, as this parameter greatly influences the speed of the convergence of the training network. Many

authors have recommended a batch size of 32 (Bengio 2012; Thapa et al. 2020); however, we have tested different batch sizes and found a minimum error in value 8 (Figure 8.5g). And the time steps of the prediction model were varied from 1 to 15 days, and observed a higher NSE in 10-days time steps (Figure 8.5h). Based on the RMSE and model performance, we have set 50 hidden units, 0.005 learning rate, 180 epochs, softsign activation function, Adam optimizer, 0.0 dropout rate, eight batch size, and 10-day time steps for different model structures.

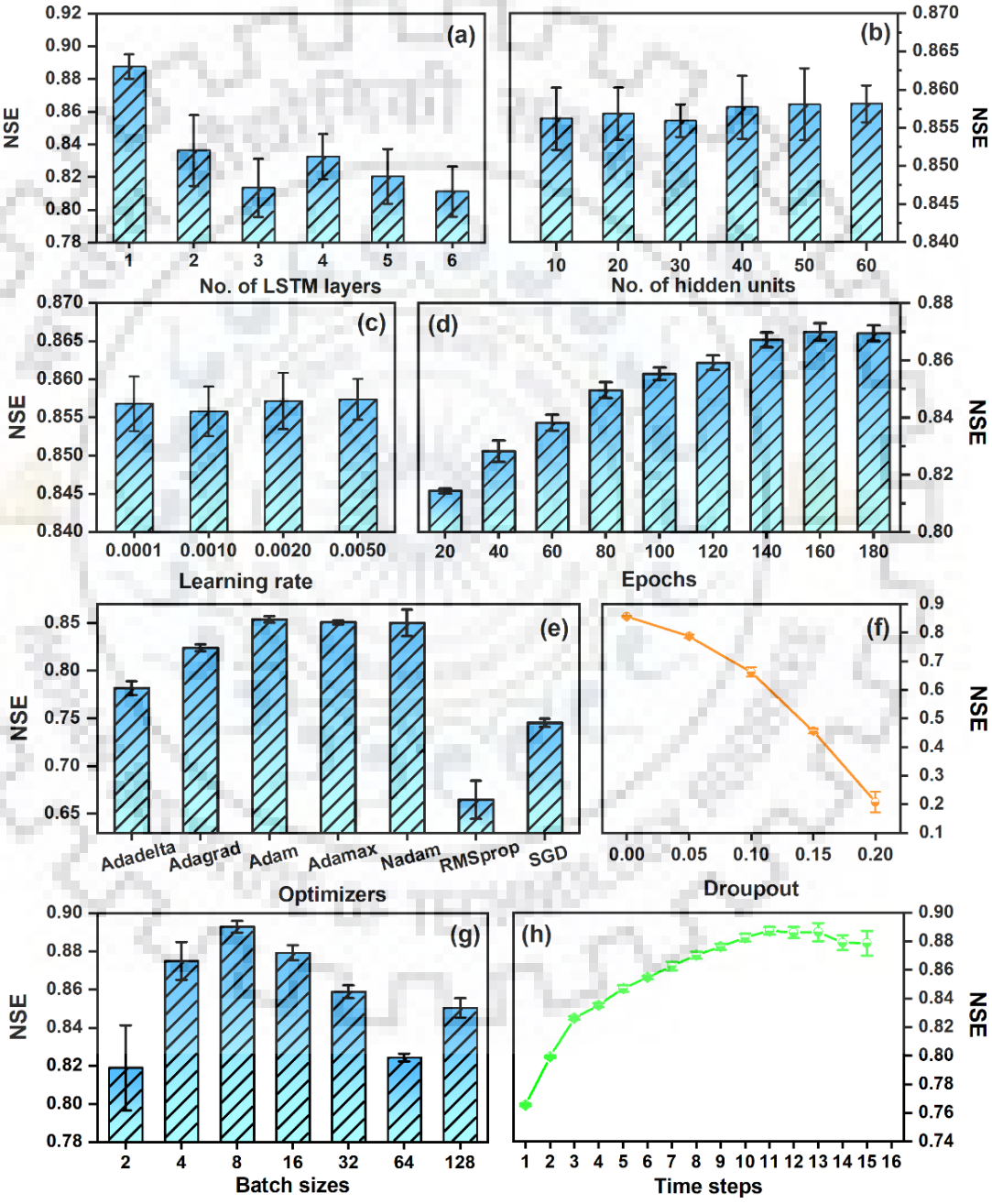

Figure 8.5. Hyperparameter tuning of the LSTM model and their performance are measured through NSE based on the observed and predicted discharge during the testing period using the model-4 dataset over the Rampur discharge site.

8.7. RESULTS

8.7.1. TEMPORAL VARIABILITY OF ESSENTIAL CLIMATIC VARIABLES

The meteorological variables were acquired hourly and converted into daily, monthly, and yearly time scales over the Sutlej River basin. The diurnal variation of T_a and T_s was minimum in 6:30 and 5:30 hours, while the maximum value was observed in 14:30 and 13:30 hours, respectively. Similarly, u was higher in the daytime compared to nighttime; however, RH shows an inverse pattern as of u. The mean monthly and yearly distribution of the selected variables (T_a, RH, rainfall, snowfall, and SCA) were measured upto the Bhakra discharge site from the 2000 to 2019 period (Figure 8.6**).** The selected variable shows a heterogeneous pattern for the studied period. The mean monthly T_a was positive from May to September, with the highest value attained in July and lowest in January (Figure 8.6a). The RH shows a higher value in monsoon (June to September) and a lower in the winter period (December to February) (Figure 8.6b). Similarly, rainfall mainly occurs during the monsoon period (Figure 8.6c), and snowfall receives throughout the year, with a maximum in January (Figure 8.6d). For further detailed analysis, the spatio-temporal distribution of SCA was monitored to map the monthly and yearly pattern of snow cover. The spatial distribution of SCA was maximum in February, and a minimum extent was observed in August. The temporal pattern of SCA shows a higher value from January to April and a lower value in July and August over the basin (Figure 8.6d). The spatial distribution of Snow Cover Day (SCD) anomalies also represented that the year 2000/01 was found a higher negative, and a higher positive value was noticed in 2018/19.

The monthly statistical value (minimum, maximum, mean, and standard deviation) and Sen's slope of meteorological variables along with SCA were estimated. The trends of the selected variables were not statistically significant at $p < 0.05$. The T_a shows a positive trend from February to May as well as September during the study period. The rainfall and snowfall decreased during March and April, while SCA showed a declining trend in December and January. On the other hand, the monthly rainfall trend was positively correlated (0.69) with the discharge trend; however, T_a and SCA trend was correlated with discharge at a delay of one month. Results also demonstrate that the region experienced higher discharge when the rainfall was increased in the monsoon season. This means the discharge variability is highly dependent on the rainfall amount and their intensity, as they contribute to both direct and rainfall-induced snow melting to the river discharge.

Further, the annual trend of snowfall, rainfall, and SCA was found increasing but not significant

at $p < 0.05$ (Table 8.4). In comparison, the T_a shows a declining trend for the study period, which is also not statistically significant ($p < 0.05$). This indicates that the precipitation in the form of liquid and solid was increased for the study area.

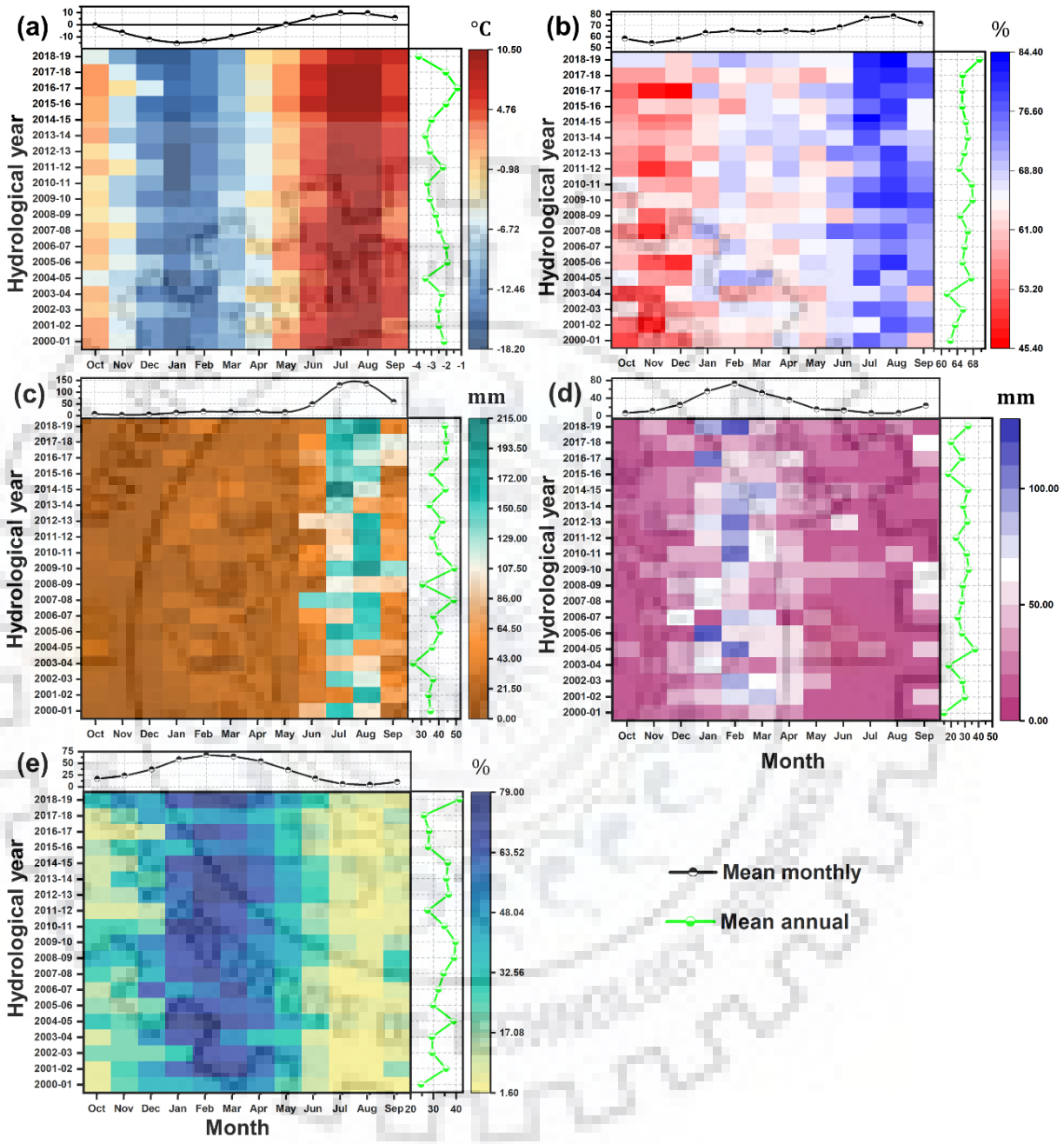

Figure 8.6. Heat map of (a) Air temperature (T_a), (b) Relative Humidity (RH), (c) Rainfall, (d) Snowfall, and Snow Cover Area (SCA) in the Sutlej River basin (upto Bhakra discharge site) during the hydrological year of 2000–2019.

However, the discharge was found a decreasing trend for Rampur and Sunni, whereas it was increasing in the Kasol and Bhakra locations. Overall, by the findings, we can conclude that the selected locations were experiencing a declining discharge with higher groundwater withdrawal.

The decreasing discharge trend also causes a significant implication on hydropower generation projects and the livelihood of the people living in the upstream and downstream regions. Therefore, reliable model development for discharge prediction is needed over the selected region to manage the future water resources.

Table 8.4. Sen's slope (in per year) of the meteorological variables along with discharge data over the different discharge sites. All trends are not significant at p < 0.05.

	T_a (℃)	Snowfall (mm)	Rainfall (mm)	SCA (%)	u ($m\,s^{-1}$)	RH (%)	Discharge ($m^3 s^{-1}$)
				2000–2006			
Bhakra	–0.05	30.06	8.21	1.07	–0.01	1.02	11.87
				2000–2012			
Kasol	–0.05	7.67	5.22	0.71	–0.01	0.40	2.02
Sunni	–0.05	7.90	4.99	0.74	–0.01	0.39	–0.98
Rampur	–0.06	8.71	2.67	0.81	–0.01	0.39	–1.85
				2000–2019			
Bhakra	–0.03	1.49	6.38	0.16	0.00	0.14	-
Kasol	–0.02	1.50	4.67	0.19	0.00	0.10	-
Sunni	–0.02	1.70	4.33	0.19	0.00	0.11	-
Rampur	–0.01	1.99	3.07	0.25	0.00	0.11	-

8.7.2. SELECTION OF BEST SUITED LSTM MODEL

The daily discharge to the Sutlej basin (upto the Rampur location) was simulated using various deep learning models. A network of different LSTM models was attempted to predict the daily discharge and assess how accurate the model can able to predict. The optimal model has higher NSE and lower RMSE in both the training and testing periods. In this study, a combination of datasets taken in model-4 (T_a, RH, Rainfall, and SCA) was utilized in all LSTM model architectures to select the best mode of prediction. For comparison, we have measured the mean NSE and RMSE of each model in both training and testing stages against observed discharge data among ten repetitions (Table 8.5). The models were performed differently during the training and testing stages. The SLSTM performed well during the training, whereas BLSTM was better during the testing stage. The observed RMSE in the testing stage varied between 98.3 and 134.6, with the maximum value in CNNLSTM while relatively lower in the BLSTM followed by VLSTM.

Table 8.5. Performance statistics of LSTM model architectures in one-day ahead prediction of discharge using model-4 data. The value represents the mean (standard deviation) of the NSE and the RMSE during the training and testing stages of the selected LSTM architectures.

LSTM types	Training		Testing	
	NSE	RMSE	NSE	RMSE
Vanilla	0.81 (0.01)	110.7 (1.6)	0.88 (0.02)	101.6 (6.4)
Stack	0.88 (0.03)	87.7 (9.3)	0.81 (0.02)	126.7 (6.0)
Bidirectional	0.83 (0.01)	110.7 (2.0)	0.90 (0.01)	98.3 (3.2)
CNN	0.85 (0.02)	98.4 (6.1)	0.79 (0.01)	134.6 (3.3)
Conv	0.82 (0.01)	108.0 (2.6)	0.86 (0.01)	110.1 (5.4)

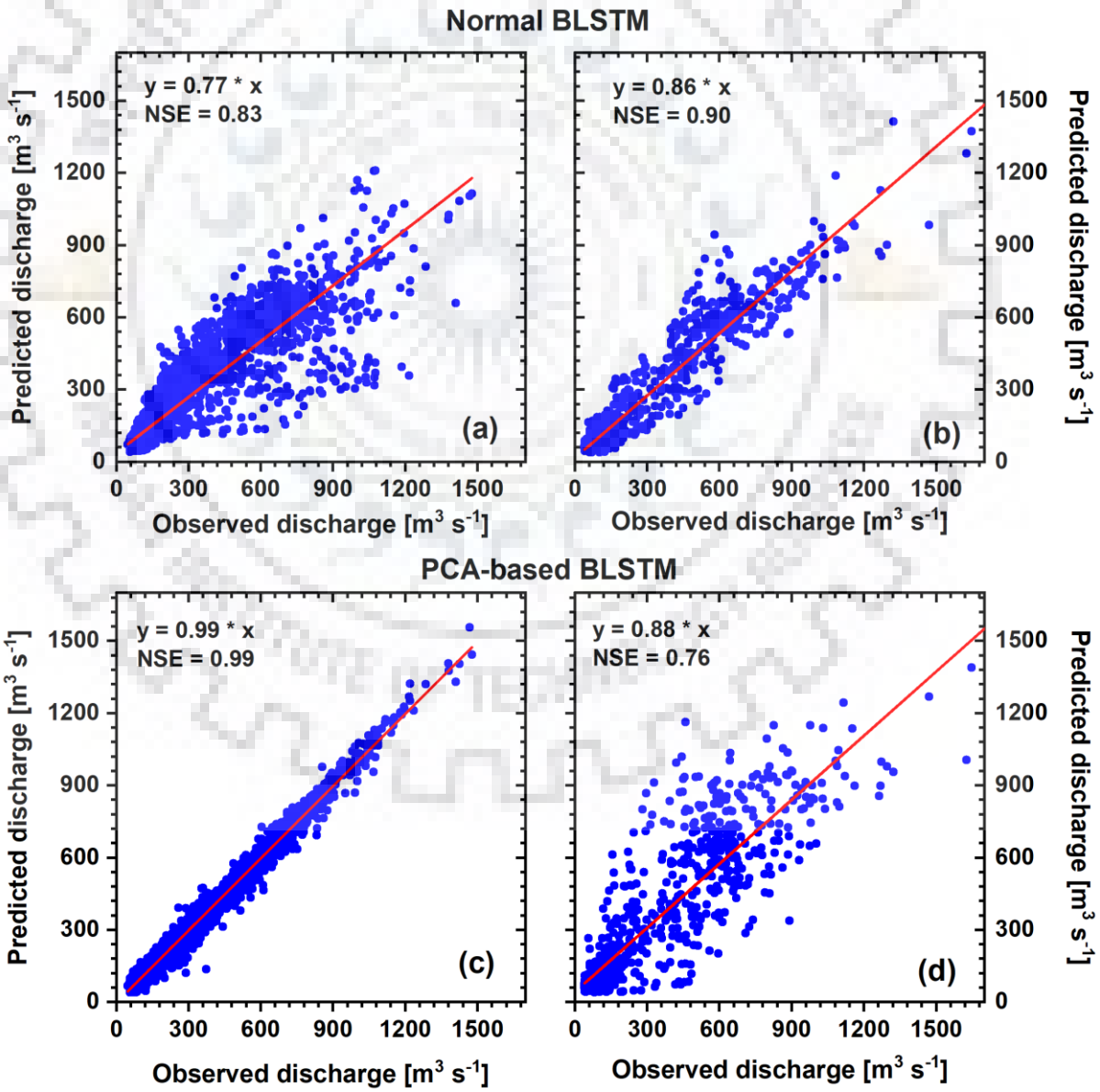

Figure 8.7. Scatter plot of the normal BLSTM during (a) training and (b) testing stages and PCA-based BLSTM during (c) training and (d) testing of the observed and predicted discharge over the Rampur discharge site from 2000–2012 period.

A different method based on their evaluation criteria suggests that BLSTM and VLSTM show higher NSE relative to other LSTM architectures during the testing period. However, the SLSTM and CNNLSTM experienced higher NSE during the training period. The higher value of NSE indicates that the predicted discharge was well-matched with the observed discharge. By combining the present output and previously published information, we can conclude the BLSTM and VLSTM are best suited for the Sutlej River basin. As per the LSTM architectures, the VLSTM uses a single hidden layer, while the BLSTM has the capability to process information at the present movement based on both past and future information. This characteristic of BLSTM can optimize the edge position and also have the anti-noise ability.

8.7.3. COMPARISON BETWEEN NORMAL BLSTM AND PCA-BASED BLSTM

The predictability performance of the BLSTM model and the n-dimensional reduction-based prediction model was tested for better discharge forecast modelling. The result over the training and testing stages represents that both the prediction model have the capability to simulate the future streamflow. It can be seen that the NSE for the normal BLSTM was 0.83 (Figure 8.7a**)** and 0.90 (Figure 8.7b**)** during the training and testing stages**,** respectively, while PCA-based BLSTM was 0.99 (Figure 8.7c) and 0.76 (Figure 8.7a) in training and testing periods, respectively. The NSE of the training period is more important than the testing period to better understand the performance of the prediction model. Another reason for considering the training NSE is that 80% of the study data was used to train the model, whereas only 20% of data was used for testing. Therefore, we have selected the PCA-based BLSTM for predicting the discharge data over the basin.

This higher reliability of the prediction model through PCA-based BLSTM was investigated by the effect of dimension reduction, and it also decreased computational complexity. However, the input of the data-driven model (normal BLSTM) was selected based on human knowledge. The obtained result based on NSE shows that the PCA-based BLSTM was performed well and has the applicability for matching the extreme events of the daily discharge. Therefore, we have concluded that the PCA-based BLSTM is the best-suited model for short-term discharge forecasting over the selected basin.

8.7.4. DAILY DISCHARGE PREDICTION BASED ON PCA BLSTM

The daily distribution of discharge prediction was analyzed using the PCA-based BLSTM model for four discharge sites (Bhakra, Kasol, Sunni, and Rampur) (Figure 8.8). This variability of discharge prediction at each site will help to understand the performance of forecasted data for shorter (2000–2006) and longer periods (2000–2012). The result at each gauging station was plotted for training and testing, then predicted from 2012 to 2019. In the training set, all the locations were showing a higher accuracy in the prediction with the maximum value of NSE in Rampur, while a lower value was observed in Kasol.

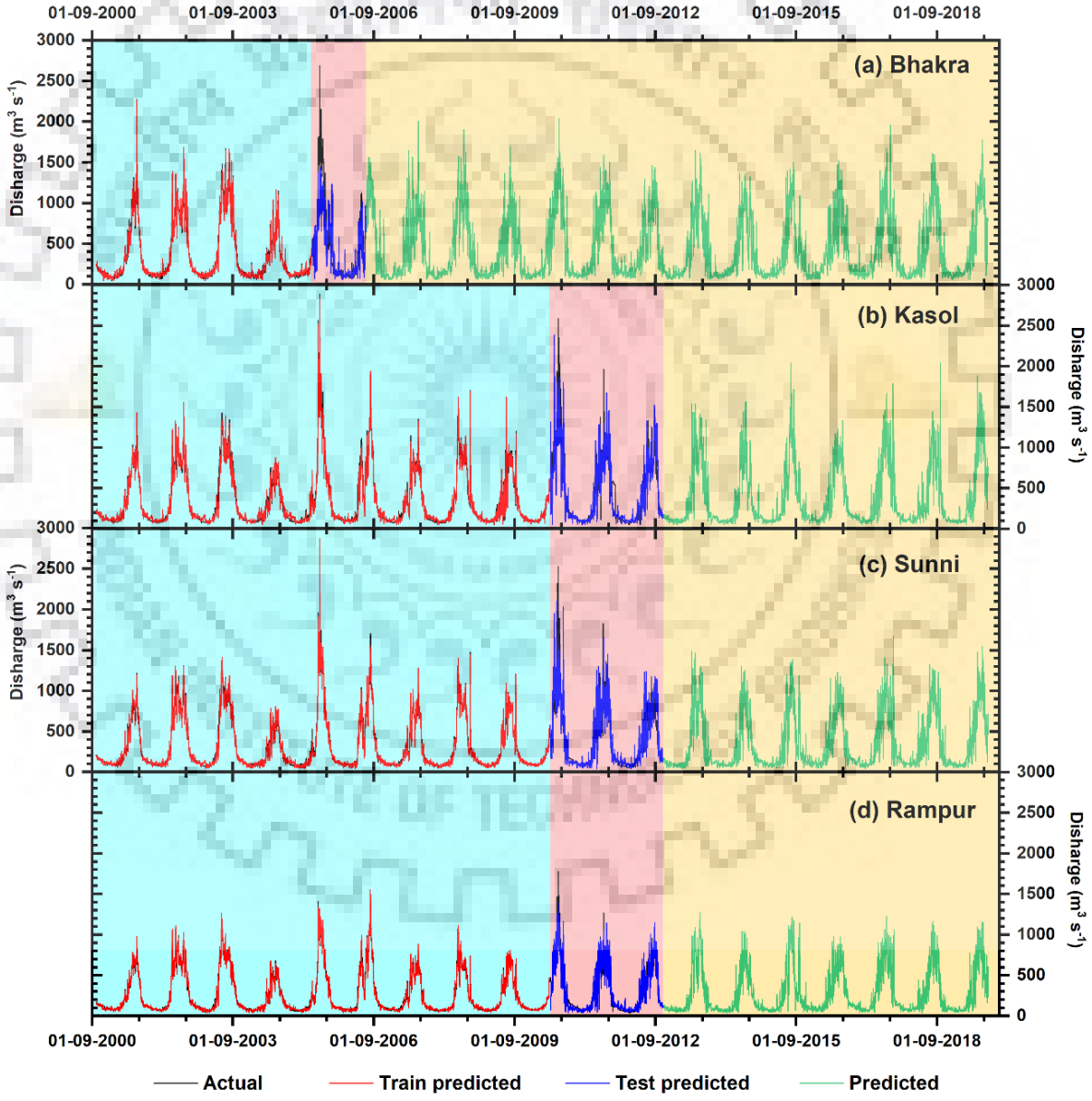

Figure 8.8. Performance of the PCA-based BLSTM model over the (a) Bhakra, (c) Kasol, (c) Sunni, and (d) Rampur. Cyan, pink and yellow colors represent the training, testing, and predicted stages of the model.

However, the testing period for all the locations experienced a relatively lower NSE than the training period. This may have been occurred due to the short period of the dataset for testing. This higher accuracy in Rampur may be occurred because of the input variables, which show a higher correlation with discharge than other selected locations.

8.8. DISCUSSION

The Sutlej River basin is the home for the highest potential hydropower generation project relative to other basins of Indus River systems. To sustain these hydropower projects, continuous monitoring, modelling, and prediction of discharge are needed at a higher temporal scale. Therefore, a prediction model was developed using machine learning approaches at a daily time scale. To quantify the best suitable prediction model for river discharge modelling, a direct comparison of five LSTM model architectures (Vanilla, Stacked, Bidirectional, CNN, and Con LSTM) has been carried out to assess their reliability based on the performance metrics. The performance of the LSTM model was high as compared to other existing models, described and compared by many authors (Fan et al. 2020; Thapa et al. 2020). And several authors have used different measures to evaluate the performance (Nourani et al. 2014; Yaseen et al. 2015; Hussain and Khan 2020). Apart from this, numerous authors have utilized the LSTM model for streamflow/river discharge forecast at various time scales (Kratzert et al. 2018; Thapa et al. 2020; Yao 2021).

The outcomes of this study revealed that the T_a and SCA trend was correlated with a delay of one month with discharge. Verdhen et al. (2013) have noticed that the melting of SCA in a warming climate impacted the discharge one month ahead. It was also seen that the discharge was higher in the monsoon season when the amount of rainfall was mainly dominant in the basin. The rainfall concentration only contributes to river discharge but also indirectly influences the rainfall-induced snow melting. Numerous authors have already noticed that rainfall-induced snow melting causes a significant change in streamflow (Zhang et al. 2011; Tang et al. 2019). This region also experienced an increasing precipitation trend in terms of snowfall and rainfall, but statistically insignificant at $p < 0.05$. A similar pattern of higher rainfall was observed by other authors (Singh et al. 2014; Gupta et al. 2020). However, discharge of the region shows a decreasing trend which means there may be an increase in groundwater due to the infiltration capacity of a region (Askar 2013). Patel et al. (2021) have highlighted that this region may have positive glacier mass change or other hydrological factors enhancing the groundwater of this region. Many authors also noticed that this region is over-exploited by the groundwater abstraction for agricultural purposes (Kaur and Kumar 2014; Sidhu et al. 2021).

After analysing the climatic condition of the basin, the selection of the best suitable model for discharge prediction was made. The first 80% of the data were used for the model generation, and the remaining 20% were used for validation purposes. Based on the RMSE, a higher value was obtained in the CNNLSTM model, while a lower value was found in BLSTM followed by VLSTM. The higher RMSE of CNNLSTM was well-matched with an observation of other authors (Bryant 2020; Cao et al., 2018). Similarly, Ma et al. (2019) have observed that the CNNLSTM was better performed in the spatial analysis, and BLSTM had higher accuracy for the temporal analysis. Hewage et al. (2020) have compared the BLSTM with other machine learning techniques and found that the model shows the more accurate result of rainfall for long-term forecasting. Also, Wang et al. (2019) have highlighted that the Bidirectional achieve the best accuracy and the relative error is 40% lower than the VLSTM.

Then, the results of normal BLSTM were compared with the PCA-generated BLSTM discharge over the Sutlej river basin. Results indicate that the PCA-based BLSTM received higher NSE than normal BLSTM during the training period; however, the NSE was relatively lower in the testing period. Many authors have revealed that the higher NSE in the training period is important, because the prediction model needs to be trained and then tested (Vu et al. 2016; Lin et al. 2021). Therefore, the NSE of the training period needs to be considered for the high-performance prediction model. Many authors have shown that the PCA-based LSTM provides better results with other comparable LSTM models (Liu and Wang 2018; Rasheed et al. 2020). The present finding is well-matched with Rasheed et al. (2020). It was noticed by several authors that the impact of input variables and a short period of testing influences the accuracy of the prediction model (Arahal et al. 2002; Ding et al. 2018). Afterward, the PCA-based BLSTM model was used to predict the daily discharge over the four discharge locations during training and testing, showing that the discharge outcomes at the Rampur location outperformed other locations.

Overall, our findings suggest that the discharge of the Sutlej river basin was mainly controlled by T_a, rainfall, SCA, and RH. Additionally, the BLSTM model performed well compared to other LSTM architecture, while the comparison between normal BLSTM and PCA-based BLSTM shows higher accuracy in PCA-based BLSTM. This selected prediction model can forecast future changes in the discharge over the Sutlej River basin at a daily time scale. The outcomes of this study could be helpful for managing the water resources and also have the potential to forecast the upcoming disaster over the region.

8.9. CONCLUSIONS

A daily discharge prediction is significantly needed for the Himalayan terrain to map and monitor the extreme events that affect the infrastructure and cause ecological imbalance. To address this, we have applied five different LSTM models over the Sutlej River basin from 2000 to 2012 and then predicted for 2012–2019. Initially, the contribution of essential climate variables on discharge was quantified based on correlation and RFE techniques. Results demonstrate that Ta, RH, Rainfall, and SCA were the main contributing variables than others. Afterward, the tuning of hyperparameters was performed at 180 epochs, eight batch sizes, ten lag times, 0.0 dropout, Adam optimizer, and softsign activation function, which enhances the accuracy of the prediction model. Then, the selected input variables with hyperparameters values were implemented in the model for reliable prediction of discharge in both training and testing periods. Based on NSE and RMSE, we have concluded that BLSTM shows higher accuracy than other selected models for Rampur discharge location. After analyzing the best-suited LSTM model, the PCA-based model was analysed, and results were compared with the normal BLSTM. The outcomes suggest that the PCA-based BLSTM outperformed normal BLSTM.

Moreover, a daily discharge prediction for all four locations was carried out for training and testing, which shows that the Rampur gauging station model performed better than other locations for the testing period. Overall, this present study can convey that the developed prediction model outperformed for the location where the correlation coefficient of input variables was higher and has a sufficient dataset available for testing. This model can bridge the gap between daily discharge prediction and their influence on extreme events at a temporal scale.

CHAPTER 9

CONCLUSIONS AND RESEARCH CONTRIBUTION

9.1. ORIGINAL RESEARCH CONTRIBUTION

A central theme of this thesis is to provide reliable monitoring and modeling of cryosphere changes and their implication on the water availability of the region. For quantifying the snow cover changes, a large part of the problem stems from the limitation of cloud cover that produces a discontinuity in spatial and temporal scale for long-term snow cover monitoring. Therefore, a sequential non-spectral composite methodology (five successive steps) was applied to remove cloud obscuration. The cloud gap-filled SCPs were validated with the indirect method as well as high-resolution satellite data (Landsat-8). Results indicate that the cloud removed SCPs show an overall efficiency of 92.8 $\pm$ 1.6% by an indirect approach, while an overestimation (9.3%) was observed between Landsat and MODIS SCA along with a higher correlation (R = 0.99, $p < 0.001$). This composite methodology was calibrated and validated over the Chenab river basin and then applied to the KH region. In the KH region, the cloud-gap-filled SCA was compared with Landsat-8 and then established the relationship with in-situ observations (snowfall and temperature). The annual SCA shows an increasing trend for the entire KH except in the eastern Himalayas. The snow cover day and nine snow cover timing indexes were assessed to understand the snow cover characteristics. The relationship between SCA and meteorological variables was established, suggesting a higher correlation between temperature and shortwave radiation. The sensitivity test was performed to examine the potential contributors in snow cover variability.

After analyzing the snow cover distribution and their characteristics, the glacier energy and mass balance were measured over the glaciers of the cold-arid region. This region is mainly selected for glacier changes estimation because the glaciers of the region cause a significant concern towards the water supply and their associated future streamflow. The SEB components were measured point-scale over the Phuche glacier, upper Ganglass catchment, Ladakh range. The meteorological data were recorded at 5600 m a.s.l., indicating that air temperature and wind speed show an increasing linear trend with a declining RH for five consecutive years (2012–2017). The region witnessed a higher negative MB during 2015/16 (–1.8 m w.e.) followed by 2012/13 (–1.2 m w.e.), while the loss was comparatively less (–0.1 m w.e.) during 2016/17. The point-scale SEB ablation was validated with the stake measured total melt, indicating a higher correlation (R^2 = 0.91) between them for the period 2016/17. Also, we have estimated glacier MB from the glaciological method over the Phuche and Khardung glaciers during 2014–2017. A maximum

mass loss was observed during 2015/16 for both the glaciers, while a positive MB was found in 2014/15 and 2016/17 for the Phuche, and a negative MB was observed during the entire study period of the Khardung glacier.

Further, an imperative technique was developed that enables comprehensive identification and monitoring of drought over a large spatial extent. The CTEI identifies the occurrence of drought over the three major river basins, namely the Indus, Ganga, and Brahmaputra (IGB), originating from the Himalayas. The performance and accuracy of the proposed drought index (CTEI) were validated with the IGDI, which was derived from groundwater observation wells. Results illustrate an enhanced understanding of holistic conditions of drought compared to pre-existing drought indices. Other than this, we used six different methods to estimate the GR rate over the Ganga river basin from 2003 to 2016. The mean annual GR rates estimated from Wu, Henry, SWB, GWSC, Kumar, and RIF methods were 24.4, 16.1, 11.7, 15.8, 18.7, and 17.1 cm yr^{-1} or 23.5, 15.5, 11.3, 15.2, 18.0, and 16.5% of monsoonal averaged precipitation (~103.9 cm) respectively. The nonparametric trend test analysis of estimated GR shows a decline with statistically insignificant. The spatial distribution of GR indicates that the eastern region of the basin attains higher GR other than the western part.

Moreover, a prediction model was developed for the Sutlej river basin, which used five different LSTM architectures during 2000–2012. For this, we have first selected the best-fitted input variables based on correlation and RFE techniques, showing T_a, RH, rainfall, and SCA were the main influencing variables than other. The BLSTM model performed well compared to other selected LSTM models in both training and testing. Further, the normal BLSTM was compared with PCA-based BLSTM that outperformed from normal BLSTM. Therefore, the PCA-based BLSTM model was implemented for four gauging stations and predicted discharge during 2012–2019.

9.2. FUTURE RESEARCH DIRECTION

Overall, the presented studies prove the potential of various remote sensing and field-collected data for monitoring and modeling cryospheric processes in one of the world's major freshwater reservoir regions. It also addresses the contributing variables and their changing pattern with respect to time. The study includes the various model development in order to provide reliable outcomes from the study and further generate an error in the observation. These outcomes could be used to understand the potential importance of climatic variables on the snow cover distribution and glacier mass balance changes that cause regional water availability and

imbalance in the ecosystem. Furthermore, a reliable prediction of streamflow/river discharge is needed to quantify the future implication on the ecosystem and also have the capability to fill the inconsistency in time series data.

LIST OF PUBLICATIONS

JOURNAL PUBLICATION

1. **Jaydeo K Dharpure**, Akansha Patel, Ajanta Goswami, Anil V Kulkarni, and Snehmani. Spatiotemporal snow cover characterization and its linkage with climate change over the Chenab River basin, western Himalayas. *GIScience & Remote Sensing*, **2020**, *57(7)*, pp. 882-906. https://doi.org/10.1080/15481603.2020.1821150

2. **Jaydeo K Dharpure**, Ajanta Goswami, Akansha Patel, Anil V Kulkarni, and Thamban Meloth. Drought characterization using the Combined Terrestrial Evapotranspiration Index over the Indus, Ganga and Brahmaputra River basins. *Geocarto International*, **2020**, pp.1-25. *https://doi.org/10.1080/10106049.2020.1756462*

3. **Jaydeo K Dharpure**, Ajanta Goswami, Akansha Patel, and Anil V. Kulkarni. Quantification of groundwater recharge and its spatio-temporal variability over the Ganga River basin. *Geocarto International*, **2021**, pp. 1-24. https://doi.org/10.1080/10106049.2021.1914748

4. **Jaydeo K Dharpure**, Ajanta Goswami, Akansha Patel, Anil V. Kulkarni and Snehmani. Assessment of snow cover dynamics and its sensitivity with hydro-meteorological factors in the Karakoram and Himalayan region. *Hydrological Science Journal*, **2021**, *66(15)*, pp. 2198-2215**.** https://doi.org/10.1080/02626667.2021.1985125

5. **Jaydeo K Dharpure**, Ajanta Goswami, Akansha Patel, Sanjay Jain, and Anil V Kulkarni. Modeling of glacier energy and mass budget of the Phuche glacier, cold-arid trans-Himalayan region, Ladakh range, India. *Cold Region Science and Technology*, **2021** (Under review).

6. **Jaydeo K Dharpure**, Ajanta Goswami, Akansha Patel, Sanjay Jain, and Anil V Kulkarni. Estimation of glaciological based mass balance and its interrelationship with climate drivers over the Phuche and Khardung glaciers, Cold-arid Himalayan region, Ladakh range, India. *Regional Environmental Change*, **2021** (Under review).

7. **Jaydeo K Dharpure**, Ajanta Goswami, Akansha Patel, Sanjay Jain, and Anil V Kulkarni. Prediction of discharge using Long Short-Term Memory (LSTM) deep neural network in the Sutlej River basin (western Himalaya). *Hydrological Science Journal*, **2022** (Under review).

CONFERENCE PROCEEDINGS

1. **Jaydeo K Dharpure**, Ajanta Goswami and Anil V Kulkarni. Understanding the spatial differences in terrestrial water storage variations in the Indus, Ganga, and the Brahmaputra River basins. India-UK Water Centre's (IUKWC) workshop at ***University of Warwick, UK*, 2019**.

2. **Jaydeo K Dharpure**, Ajanta Goswami, and Anil V. Kulkarni. Drought characterization using the Combined Terrestrial Evapotranspiration Index over the Indus, Ganga and Brahmaputra River basins. In Proceedings of DwD-GCRF-UKADR-DRG-UKCDR International Conference, ***Northumbria University Newcastle, UK*, 2019**.

3. **Jaydeo K Dharpure**, Ajanta Goswami and Anil V Kulkarni. "Estimation of Snow Cover and climatic variability using MODIS data of Teesta River basin Sikkim, India. Theme- Cryospheric Processes and Dynamics, Session- Glacier processes and glacio-hydrological responses, registration no.- NCPS2019/64 at ***National Centre for Polar and Ocean Research, Goa*, 2019.**

4. **Jaydeo K Dharpure**, Ajanta Goswami, and Anil V. Kulkarni. Spatial and temporal variation of snow cover in the Himalayan and Karakorum region using MODIS data (2000–2019). In Proceedings of ***EGU General Assembly Conference Abstracts, Vienna*, 2020**, abstract no 3421. https://doi.org/10.5194/egusphere-egu2020-3421.

BIBLIOGRAPHY

1. Abeysingha NS, Singh M, Sehgal VK, et al (2016) Analysis of trends in streamflow and its linkages with rainfall and anthropogenic factors in Gomti River basin of North India. Theor Appl Climatol 123:785–799. https://doi.org/10.1007/s00704-015-1390-5
2. Acharya A, Kayastha RB (2018) Mass and energy balance estimation of Yala Glacier (2011-2017), Langtang Valley, Nepal. Water (Switzerland) 11:. https://doi.org/10.3390/w11010006
3. Agboma CO, Yirdaw SZ, Snelgrove KR (2009) Intercomparison of the total storage deficit index (TSDI) over two Canadian Prairie catchments. J Hydrol 374:351–359. https://doi.org/10.1016/j.jhydrol.2009.06.034
4. Ahmad S, Israr M, Liu S, et al (2018) Spatio-temporal trends in snow extent and their linkage to hydro-climatological and topographical factors in the Chitral River Basin (Hindukush, Pakistan). Geocarto Int 0:1–24. https://doi.org/10.1080/10106049.2018.1524517
5. Ahmed M, Abdelmohsen K (2018) Quantifying Modern Recharge and Depletion Rates of the Nubian Aquifer in Egypt. Surv Geophys 39:729–751. https://doi.org/10.1007/s10712-018-9465-3
6. Aizen VB, Aizen EM, Nikitin SA (2002) Glacier regime on the northern slope of the Himalaya (Xixibangma glaciers). Quat Int 97–98:27–39. https://doi.org/10.1016/S1040-6182(02)00049-6
7. Ajayi T, Lopez DL, Ayo-bali AE (2021) Using Artificial Neural Network to Model Water Discharge and Chemistry in a River Impacted by Acid Mine Drainage. Am J Water Resour 9:63–79. https://doi.org/10.12691/ajwr-9-2-4
8. Al-Hilphy ARS, Hassan A, Majeed GH, Yaqoob GY (2014) A practical study for incident solar radiation intensity in Basrah province and air temperature. IOSR J Eng 4:13–21. https://doi.org/10.9790/3021-04531321
9. Albergel C, Dutra E, Munier S, et al (2018) ERA-5 and ERA-Interim driven ISBA land surface model simulations: Which one performs better? Hydrol Earth Syst Sci 22:3515–3532. https://doi.org/10.5194/hess-22-3515-2018
10. Allen PM, Harmel RD, Dunbar JA, Arnold JG (2011) Upland contribution of sediment and runoff during extreme drought: A study of the 1947-1956 drought in the Blackland Prairie, Texas. J Hydrol 407:1–11. https://doi.org/10.1016/j.jhydrol.2011.04.039

11. Allen RG, Perieira LS, Raes D, Smith M (2006) Irrigation and Drainage Paper Crop No. 56

12. Allen SK, Rastner P, Arora M, et al (2016) Lake outburst and debris flow disaster at Kedarnath, June 2013: hydrometeorological triggering and topographic predisposition. Landslides 13:1479–1491. https://doi.org/10.1007/s10346-015-0584-3

13. Allison GB, Gee GW, Tyler SW (1994) Vadose-Zone Techniques for Estimating Groundwater Recharge in Arid and Semiarid Regions. Soil Sci Soc Am J 58:6–14. https://doi.org/10.2136/sssaj1994.03615995005800010002x

14. Amatya PM, Ma Y, Han C, et al (2015) Recent trends (2003-2013) of land surface heat fluxes on the southern side of the central Himalayas ,Nepal. J Geophys Res Atmos 120:957–970. https://doi.org/10.1002/2015JD023510

15. Anand J, Gosain AK, Khosa R, Srinivasan R (2018) Regional scale hydrologic modeling for prediction of water balance, analysis of trends in streamflow and variations in streamflow: The case study of the Ganga River basin. J Hydrol Reg Stud 16:32–53. https://doi.org/10.1016/j.ejrh.2018.02.007

16. Andersen OB, Seneviratne SI, Hinderer J, Viterbo P (2005) GRACE-derived terrestrial water storage depletion associated with the 2003 European heat wave. Geophys Res Lett 32:1–4. https://doi.org/10.1029/2005GL023574

17. Angchuk T (2021) Annual and seasonal glaciological mass balance of Patsio Glacier , western Himalaya (India) from 2010 to 2017

18. Anjum MN, Ding Y, Shangguan D, et al (2019) Quantification of spatial temporal variability of snow cover and hydro-climatic variables based on multi-source remote sensing data in the Swat watershed, Hindukush Mountains, Pakistan. Meteorol Atmos Phys 131:467–486. https://doi.org/10.1007/s00703-018-0584-7

19. Archer DR, Fowler HJ (2006) Conflicting Signals of Climatic Change in the Upper Indus Basin. J Clim 19:4276–4293. https://doi.org/10.1175/JCLI3860.1

20. Arfanuzzaman M (2018) Economics of transboundary water: An evaluation of a glacier and snowpack-dependent river basin of the Hindu Kush Himalayan region. Water Policy 20:90–108. https://doi.org/10.2166/wp.2017.071

21. Ashok K, Guan Z, Saji NH, Yamagata T (2004) Individual and combined influences of ENSO and the Indian Ocean Dipole on the Indian summer monsoon. J Clim 17:3141–3155. https://doi.org/10.1175/1520-0442(2004)017<3141:IACIOE>2.0.CO;2

22. Ashraf A, Naz R, Roohi R (2012) Glacial lake outburst flood hazards in Hindukush, Karakoram and Himalayan ranges of Pakistan: Implications and risk analysis. Geomatics, Nat Hazards Risk 3:113–132. https://doi.org/10.1080/19475705.2011.615344

23. Asoka A, Gleeson T, Wada Y, Mishra V (2017) Relative contribution of monsoon precipitation and pumping to changes in groundwater storage in India. Nat Geosci 10:109–117. https://doi.org/10.1038/ngeo2869

24. Atif I, Mahboob MA, Iqbal J (2015) Snow cover area change assessment in 2003 and 2013 using MODIS data of the upper Indus basin, Pakistan. J Himal Earth Sci 48:117–128

25. Ayad Ali Faris Beg, Ahmed H. Al-Sulttani, Adrian Ochtyra, et al (2016) Estimation of Evapotranspiration Using SEBAL Algorithm and Landsat-8 Data—A Case Study: Tatra Mountains Region. J Geol Resour Eng 4:. https://doi.org/10.17265/2328-2193/2016.06.002

26. Ayub S, Akhter G, Ashraf A, Iqbal M (2020) Snow and glacier melt runoff simulation under variable altitudes and climate scenarios in Gilgit River Basin, Karakoram region. Model Earth Syst Environ. https://doi.org/10.1007/s40808-020-00777-y

27. Azam MF, Ramanathan AL, Wagnon P, et al (2016) Meteorological conditions, seasonal and annual mass balances of Chhota Shigri Glacier, western Himalaya, India. Ann Glaciol 57:328–338. https://doi.org/10.3189/2016AoG71A570

28. Azam MF, Wagnon P, Berthier E, et al (2018) Review of the status and mass changes of Himalayan-Karakoram glaciers. J Glaciol 64:61–74. https://doi.org/10.1017/jog.2017.86

29. Azam MF, Wagnon P, Ramanathan A, et al (2012) From balance to imbalance: A shift in the dynamic behaviour of Chhota Shigri glacier, western Himalaya, India. J Glaciol 58:315–324. https://doi.org/10.3189/2012JoG11J123

30. Azam MF, Wagnon P, Vincent C, et al (2014) Processes governing the mass balance of Chhota Shigri Glacier (western Himalaya, India) assessed by point-scale surface energy balance measurements. Cryosphere 8:2195–2217. https://doi.org/10.5194/tc-8-2195-2014

31. Azmat M, Liaqat UW, Qamar MU, Awan UK (2017) Impacts of changing climate and snow cover on the flow regime of Jhelum River, Western Himalayas. Reg Environ Chang 17:813–825. https://doi.org/10.1007/s10113-016-1072-6

32. Bahadur J (1993) The Himalayas: a third polar region. Snow glacier Hydrol Proc Int Symp Kathmandu, 1992 181–190

33. Bajracharya SR, Shrestha B (2011) The Status of Glaciers in the Hindu Kush–Himalayan Region. Kathmandu: ICIMOD. https://doi.org/www.icimod.org/publications

34. Bandyopadhyay D, Singh G, Kulkarni A V. (2019) Spatial distribution of decadal ice-thickness change and glacier stored water loss in the Upper Ganga basin, India during 2000–2014. Sci Rep 9:1–9. https://doi.org/10.1038/s41598-019-53055-y

35. Banerjee A (2017) Brief communication: Thinning of debris-covered and debris-free glaciers in a warming climate. Cryosphere 11:133–138. https://doi.org/10.5194/tc-11-133-2017

36. Banerjee C, Kumar DN (2018) Analyzing Large-Scale Hydrologic Processes Using GRACE and Hydrometeorological Datasets. Water Resour Manag 4409–4423. https://doi.org/10.1007/s11269-018-2070-x

37. Baniya B, Tang Q, Huang Z, et al (2018) Spatial and temporal variation of NDVI in response to climate change and the implication for carbon dynamics in Nepal. Forests 9:1–18. https://doi.org/10.3390/f9060329

38. Barman S, Bhattacharjya RK (2015) Change in snow cover area of Brahmaputra river basin and its sensitivity to temperature. Environ Syst Res 4:. https://doi.org/10.1186/s40068-015-0043-0

39. Barnett TP, Adam JC, Lettenmaier DP (2005) Potential impacts of a warming climate on water availability in snow-dominated regions. Nature 438:303–309. https://doi.org/10.1038/nature04141

40. Basnett S, Kulkarni A V. (2019) Snow Cover Changes Observed Over Sikkim Himalaya. Springer International Publishing, Cham

41. Bastiaanssen WGM, Pelgrum H, Wang J, et al (1998) A remote sensing surface energy balance algorithm for land (SEBAL), Part 1: Formulation. J Hydrol 212–213:213–229. https://doi.org/10.1016/S0022-1694(98)00254-6

42. Beaudoing HK, Rodell M, NASA/GSFC/HSL (2020) LDAS Noah Land Surface Model L4 monthly 0.25 x 0.25 degree V2.1. Greenbelt, Maryland, USA, Goddard Earth Sci Data Inf Serv Cent (GES DISC) 10.5067/SXAVCZFAQLNO

43. Bhalme HN, Mooley DA (1980) Large-scale droughts/floods and monsoon circulation. Mon. Weather Rev. 108:1197–1211

44. Bhambri R, Hewitt K, Kawishwar P, et al (2019) Ice-dams, outburst floods, and movement heterogeneity of glaciers, Karakoram. Glob Planet Change 180:100–116. https://doi.org/10.1016/j.gloplacha.2019.05.004

45. Bhambri R, Misra A, Kumar A, et al (2018) Glacier Lake inventory of Himachal Pradesh. Himal Geol 39:1–32

46. Bhanja SN, Mukherjee A, Rangarajan R, et al (2019) Long-term groundwater recharge rates across India by in situ measurements. Hydrol Earth Syst Sci 23:711–722. https://doi.org/10.5194/hess-23-711-2019

47. Bhanja SN, Mukherjee A, Rodell M (2020) Groundwater storage change detection from in situ and GRACE-based estimates in major river basins across India. Hydrol Sci J 00:1–10. https://doi.org/10.1080/02626667.2020.1716238

48. Bhanja SN, Mukherjee A, Rodell M (2018) Groundwater Storage variations in India. In: ed. Groundwater of South Asia. Singapore: Springer. pp 49–59

49. Bhanja SN, Mukherjee A, Saha D, et al (2016) Validation of GRACE based groundwater storage anomaly using in-situ groundwater level measurements in India. J Hydrol 543:729–738. https://doi.org/10.1016/j.jhydrol.2016.10.042

50. Bhanja SN, Rodell M, Li B, et al (2017) Spatio-temporal variability of groundwater storage in India. J Hydrol 544:428–437. https://doi.org/10.1016/j.jhydrol.2016.11.052

51. Bhuiyan C, Singh RP, Kogan FN (2006) Monitoring drought dynamics in the Aravalli region (India) using different indices based on ground and remote sensing data. Int J Appl Earth Obs Geoinf 8:289–302. https://doi.org/10.1016/j.jag.2006.03.002

52. Bhutiyani MR (2014) Climate Change in the Northwestern Himalayas. In: Dynamics of climate change and water resources of Northwestern Himalaya. pp 85–96

53. Bhutiyani MR, Kale VS, Pawar NJ (2010) Climate change and the precipitation variations in the northwestern Himalaya: 1866-2006. Int J Climatol 30:535–548. https://doi.org/10.1002/joc.1920

54. Bhutiyani MR, Kale VS, Pawar NJ (2007) Long-term trends in maximum, minimum and mean annual air temperatures across the Northwestern Himalaya during the twentieth century. Clim Change 85:159–177. https://doi.org/10.1007/s10584-006-9196-1

55. Bilal H, Chamhuri S, Mokhtar M Bin, Kanniah KD (2019) Recent snow cover variation in the Upper Indus Basin of Gilgit Baltistan, Hindukush Karakoram Himalaya. J Mt Sci 16:296–308. https://doi.org/10.1007/s11629-018-5201-3

56. Bloomfield JP, Marchant BP (2013) Analysis of groundwater drought building on the standardised precipitation index approach. Hydrol Earth Syst Sci 17:4769–4787. https://doi.org/10.5194/hess-17-4769-2013

57. Blunden J, Arndt E (2017) State of the Climate in 2016

58. Bolch T, Kulkarni A, Kääb A, et al (2012a) The state and fate of himalayan glaciers. Science (80-) 336:310–314. https://doi.org/10.1126/science.1215828

59. Bolch T, Kulkarni A, Kääb A, et al (2012b) The state and fate of Himalayan glaciers. Science (80-) 336:310–314. https://doi.org/10.1126/science.1215828

60. Bolch T, Pieczonka T, Mukherjee K, Shea J (2017) Brief communication: Glaciers in the Hunza catchment (Karakoram) have been nearly in balance since the 1970s. Cryosphere 11:531–539. https://doi.org/10.5194/tc-11-531-2017

61. Bonekamp PNJ, de Kok RJ, Collier E, Immerzeel WW (2019) Contrasting meteorological drivers of the glacier mass balance between the Karakoram and central Himalaya. Front Earth Sci 7:1–14. https://doi.org/10.3389/feart.2019.00107

62. Bongartz K, Flügel WA, Pechstädt J, et al (2007) Analysis of climate change trend and possible impacts in the Upper Brahmaputra River Basin – the BRAHMATWINN Project. Environ Monit Assess 135:227–240. https://doi.org/10.1007/s10661-007-9645-y

63. Bons CA (2018) Ganga River Basin Planning Assessment Report. In: Main volume and Appendices. Deltares with AECOM and FutureWater for the World Bank and the Government of India

64. Bonsor HC, MacDonald AM, Ahmed KM, et al (2017) Typologies hydrogéologiques de l'aquifère alluvial du bassin de l'Indus et du Gange, Asie du Sud. Hydrogeol J 25:1377–1406. https://doi.org/10.1007/s10040-017-1550-z

65. Bookhagen B, Burbank DW (2010) Toward a complete Himalayan hydrological budget: Spatiotemporal distribution of snowmelt and rainfall and their impact on river discharge. J Geophys Res Earth Surf 115:1–25. https://doi.org/10.1029/2009JF001426

66. Brooks EB, Wynne RH, Thomas VA (2018) Using window regression to gap-fill landsat ETM+ post SLC-Off data. Remote Sens 10:. https://doi.org/10.3390/rs10101502

67. Brown JF, Wardlow BD, Tadesse T, et al (2008) The Vegetation Drought Response Index (VegDRI): A New Integrated Approach for Monitoring Drought Stress in Vegetation. GIScience Remote Sens 45:16–46. https://doi.org/10.2747/1548-1603.45.1.16

68. Brown RD, Brasnett B, Robinson D, et al (2010) Gridded North American monthly snow depth and snow water equivalent for GCM evaluation. Atmosphere-Ocean 5900:. https://doi.org/10.3137/ao.410101

69. Brown RD, Mote PW (2009) The response of Northern Hemisphere snow cover to a changing climate. J Clim 22:2124–2145. https://doi.org/10.1175/2008JCLI2665.1

70. Burbank DW, Bookhagen B, Gabet EJ, Putkonen J (2012) Modern climate and erosion in the Himalaya. Comptes Rendus - Geosci 344:610–626. https://doi.org/10.1016/j.crte.2012.10.010

71. Butt MJ, Assiri ME, Waqas A (2019) Spectral Albedo Estimation of Snow Covers in Pakistan Using Landsat Data. Earth Syst Environ 3:267–276. https://doi.org/10.1007/s41748-019-00104-1

72. C3S CCCS (2019) C3S ERA5-Land reanalysis. In: Copernicus Clim. Chang. Serv.

73. Callegari M, Mazzoli P, de Gregorio L, et al (2015) Seasonal river discharge forecasting using support vector regression: A case study in the Italian Alps. Water (Switzerland) 7:2494–2515. https://doi.org/10.3390/w7052494

74. Cao Y, Roy S Sen (2020) Spatial patterns of seasonal level trends of groundwater in India during 2002–2016. Weather 75:123–128. https://doi.org/10.1002/wea.3370

75. Cawkwell FGL, Bamber JL (2002) The impact of cloud cover on the net radiation budget of the Greenland ice sheet. Ann Glaciol 34:141–149. https://doi.org/10.3189/172756402781817789

76. CGWB (2017) Dynamic Ground Water Resources of India. https://doi.org/June 2017

77. CGWB (2011) Dynamic Groundwater Resources of India (As on March 31st 2011). Cent Gr Water Board Minist Water Resour River Dev Ganga Rejuvenation Gov India 299

78. CGWB (2016) Central Ground Water Board

79. Chang TJ, Kleopa XA (1991) A Proposed Method for Drought Monitoring. Water Resour Bull 27:275–281. https://doi.org/10.1111/j.1752-1688.1991.tb03132.x

80. Chaturvedi MC, Srivastava VK (1979) Induced Groundwater Recharge in the Ganges Basin. Water Resour Res 15:1156–1166

81. Chelamallu HP, Venkataraman G, Murti MVR (2014) Accuracy assessment of MODIS/Terra snow cover product for parts of Indian Himalayas. Geocarto Int 29:592–608. https://doi.org/10.1080/10106049.2013.819041

82. Chen F, Mitchell K, Schaake J, et al (1996) Modeling of land surface evaporation by four schemes and comparison with FIFE observations. J Geophys Res Atmos 101:7251–7268. https://doi.org/10.1029/95JD02165

83. Chen J, Li J, Zhang Z, Ni S (2014) Long-term groundwater variations in Northwest India from satellite gravity measurements. Glob Planet Change 116:130–138. https://doi.org/10.1016/j.gloplacha.2014.02.007

84. Chen S, Wang X, Guo H, et al (2020) Spatial and Temporal Adaptive Gap-Filling Method Producing Daily Cloud-Free NDSI Time Series. IEEE J Sel Top Appl Earth Obs Remote Sens 13:2251–2263. https://doi.org/10.1109/jstars.2020.2993037

85. Childs EC (1960) The nonsteady state of the water table in drained land. J Geophys Res 65:780–782. https://doi.org/10.1029/jz065i002p00780

86. Choudhury A, Yadav AC, Bonafoni S (2021) A response of snow cover to the climate in the northwest himalaya (Nwh) using satellite products. Remote Sens 13:1–22. https://doi.org/10.3390/rs13040655

87. Cogley JG (2011) Present and future states of Himalaya and Karakoram glaciers. Ann Glaciol 52:69–73. https://doi.org/10.3189/172756411799096277

88. Condon LE, Maxwell RM (2019) Simulating the sensitivity of evapotranspiration and streamflow to large-scale groundwater depletion. Sci Adv 5:eaav4574. https://doi.org/10.1126/sciadv.aav4574

89. Cosgrove WJ, Loucks DP (2015) Water management: Current and future challenges and research directions. Wyo Univ Water Resour Res Inst Water Resour Ser 51:4823–4839. https://doi.org/10.1002/2014WR016869.Received

90. DACFW (2016) Department of Agriculture, Cooperation & Farmers Welfare

91. Dadic R, Corripio JG, Burlando P (2008) Mass-balance estimates for Haut Glacier d' Arolla, Switzerland, from 2000 to 2006 using DEMs and distributed mass-balance modeling. Ann Glaciol 49:22–26. https://doi.org/10.3189/172756408787814816

92. Dahri ZH, Ahmad B, Leach JH, Ahmad S (2011) Satellite-based snowcover distribution and associated snowmelt runoff modeling in Swat River Basin of Pakistan. Proc Pakistan Acad Sci 48:19–32

93. Dahri ZH, Ludwig F, Moors E, et al (2016) An appraisal of precipitation distribution in the high-altitude catchments of the Indus basin. Sci Total Environ 548–549:289–306. https://doi.org/10.1016/j.scitotenv.2016.01.001

94. Dai Y, Zeng X, Dickinson RE, et al (2003) The common land model. Bull Am Meteorol Soc 84:1013–1023. https://doi.org/10.1175/BAMS-84-8-1013

95. Dankers R, De Jong SM (2004) Monitoring snow-cover dynamics in Northern Fennoscandia with SPOT VEGETATION images. Int J Remote Sens 25:2933–2949. https://doi.org/10.1080/01431160310001618374

96. Dariane AB, Khoramian A, Santi E (2017) Investigating spatiotemporal snow cover variability via cloud-free MODIS snow cover product in Central Alborz Region. Remote Sens Environ 202:152–165. https://doi.org/10.1016/j.rse.2017.05.042

97. Das S, Sharma MC (2019) Glacier changes between 1971 and 2016 in the Jankar Chhu Watershed, Lahaul Himalaya, India. J Glaciol 65:13–28. https://doi.org/10.1017/jog.2018.77

98. Davaze L, Rabatel A, Dufour A, et al (2020) Region-Wide Annual Glacier Surface Mass Balance for the European Alps From 2000 to 2016. Front Earth Sci 8:0–14. https://doi.org/10.3389/feart.2020.00149

99. de Vries JJ, Simmers I (2002) Groundwater recharge: An overview of process and challenges. Hydrogeol J 10:5–17. https://doi.org/10.1007/s10040-001-0171-7

100. Demlie M (2015) Assessment and estimation of groundwater recharge for a catchment located in highland tropical climate in central Ethiopia using catchment soil–water balance (SWB) and chloride mass balance (CMB) techniques. Environ Earth Sci 74:1137–1150. https://doi.org/10.1007/s12665-015-4099-y

101. Denby B, Smeets CJPP (2000) Derivation of Turbulent Flux Profiles and Roughness Lengths from Katabatic Flow Dynamics. J Appl Meteorol 39:1601–1612. https://doi.org/10.1175/1520-0450(2000)039<1601:DOTFPA>2.0.CO;2

102. Deng H, Pepin NC, Liu Q, Chen Y (2018a) Understanding the spatial differences in terrestrial water storage variations in the Tibetan Plateau from 2002 to 2016. Clim Change 1–15. https://doi.org/10.1007/s10584-018-2325-9

103. Deng W, Song J, Bai H, et al (2018b) Analyzing the Impacts of Climate Variability and Land Surface Changes on the Annual Water–Energy Balance in the Weihe River Basin of China. Water 10:1792. https://doi.org/10.3390/w10121792

104. Dharpure JK, Goswami A, Patel A, et al (2020a) Drought characterization using the Combined Terrestrial Evapotranspiration Index over the Indus, Ganga and Brahmaputra river basins. Geocarto Int 0:1–25. https://doi.org/10.1080/10106049.2020.1756462

105. Dharpure JK, Patel A, Goswami A, Kulkarni A V (2020b) Spatiotemporal snow cover characterization and its linkage with climate change over the Chenab river basin , western Himalayas. GIScience Remote Sens 00:1–25. https://doi.org/10.1080/15481603.2020.1821150

106. Dhungel S, Kathayat B, Mahata K, Panday A (2018) Transport of regional pollutants through a remote trans-Himalayan valley in Nepal. Atmos Chem Phys 18:1203–1216. https://doi.org/10.5194/acp-18-1203-2018

107. Dimri AP, Niyogi D, Barros AP, et al (2015) Western Disturbances: A review. Rev Geophys 53:225–246. https://doi.org/10.1002/2014RG000460.Received

108. Dobhal DP, Mehta M, Srivastava D (2013) Influence of debris cover on terminus retreat and mass changes of Chorabari Glacier, Garhwal region, central Himalaya, India. J Glaciol 59:961–971. https://doi.org/10.3189/2013JoG12J180

109. Dobson JE, Bright EA, Coleman PR, et al (2000) LandScan: A global population database for estimating populations at risk. Photogramm Eng Remote Sensing 66:849–857

110. Dozier J, Marks D (1987) Snow Mapping and Classification from Landsat Thematic Mapper Data. Ann Glaciol 9:97–103. https://doi.org/10.3189/s026030550000046x

111. Dripps WR, Bradbury KR (2007) A simple daily soil-water balance model for estimating the spatial and temporal distribution of groundwater recharge in temperate humid areas. Hydrogeol J 15:433–444. https://doi.org/10.1007/s10040-007-0160-6

112. Duan SB, Li ZL, Li H, et al (2019) Validation of Collection 6 MODIS land surface temperature product using in situ measurements. Remote Sens Environ 225:16–29. https://doi.org/10.1016/j.rse.2019.02.020

113. Ebrahimi S, Marshall SJ (2016) Surface energy balance sensitivity to meteorological variability on Haig Glacier, Canadian Rocky Mountains. Cryosphere 10:2799–2819. https://doi.org/10.5194/tc-10-2799-2016

114. ECMWF (2019) Essential Climate Variables for assessment of climate variability from 1979 to present

115. Ek MB, Mitchell KE, Y. L, et al (2003) Implementation of Noah land surface model advances in the National Centers for Environmental Prediction operational mesoscale Eta model. J Geophys Res 108:8851. https://doi.org/10.1029/2002JD003296

116. Engebretson C (2020) Landsat 8-9 Operational Land Imager (OLI) - Thermal Infrared Sensor (TIRS) Collection 2 Level 1 (L1) Data Format Control Book (DFCB). Dep Inter US Geol Surv 2:1–75

117. Eriksson M, Jianchu X, Shrestha, Arun Bhakta Vaidya, Ramesh Ananda Nepal, Santosh Sandström K (2009) The changing Himalayas: Impact of climate change on water resources and livelihoods in the greater Himalayas

118. Famiglietti JS, Lo M, Ho SL, et al (2011) Satellites measure recent rates of groundwater depletion in California's Central Valley. Geophys Res Lett 38:2–5. https://doi.org/10.1029/2010GL046442

119. Famiglietti JS, Rodell M (2013) Water in the Balance. Science (80-) 340:1300–1302

120. Fan H, Jiang M, Xu L, et al (2020) Comparison of long short term memory networks and the hydrological model in runoff simulation. Water (Switzerland) 12:1–15. https://doi.org/10.3390/w12010175

121. Farinotti D, Immerzeel WW, de Kok RJ, et al (2020a) Manifestations and mechanisms of the Karakoram glacier Anomaly. In: EGU General Assembly Conference Abstracts. pp 8–16

122. Farinotti D, Immerzeel WW, de Kok RJ, et al (2020b) Manifestations and mechanisms of the Karakoram glacier Anomaly. Nat Geosci 13:8–16. https://doi.org/10.1038/s41561-019-0513-5

123. Farr TG, Rosen PA, Caro E, et al (2007) The Shuttle Radar Topography Mission. Rev Geophys 45:RG2004. https://doi.org/10.1029/2005RG000183

124. Favier V, Agosta C, Genthon C, et al (2011) Modeling the mass and surface heat budgets in a coastal blue ice area of Adelie Land, Antarctica. J Geophys Res Earth Surf 116:1–14. https://doi.org/10.1029/2010JF001939

125. Favier V, Wagnon P, Chazarin JP, et al (2004) One-year measurements of surface heat budget on the ablation zone of Antizana Glacier 15, Ecuadorian Andes. J Geophys Res Atmos 109:1–15. https://doi.org/10.1029/2003JD004359

126. Feng W, Zhong M, Lemoine JM, et al (2013) Evaluation of groundwater depletion in North China using the Gravity Recovery and Climate Experiment (GRACE) data and ground-based measurements. Water Resour Res 49:2110–2118. https://doi.org/10.1002/wrcr.20192

127. Flechtner F, Dobslaw H, Fagiolini E (2007) Gravity Recovery and Climate Experiment AOD1B Product Description Document. AOD1b Prod Descr Doc Prod Release 05 750:1–33

128. Forsythe N, Fowler HJ, Kilsby CG, Archer DR (2012) Opportunities from remote sensing for supporting water resources ss in village/valley scale catchments in the Upper Indus Basin. Water Resour Manag 26:845–871. https://doi.org/10.1007/s11269-011-9933-8

129. Foster JL, Chang ATC, Hall DK (1995) Snow mass in boreal forests derived from a modified passive microwave algorithm. In: Multispectral and Microwave Sensing of Forestry, Hydrology, and Natural Resources. International Society for Optics and Photonics, pp 605–617

130. Francis PA, Gadgil S (2010) Towards understanding the unusual indian monsoon in 2009. J Earth Syst Sci 119:397–415. https://doi.org/10.1007/s12040-010-0033-6

131. Frey H, Machguth H, Huss M, et al (2014) Estimating the volume of glaciers in the Himalayan-Karakoram region using different methods. Cryosphere 8:2313–2333. https://doi.org/10.5194/tc-8-2313-2014

132. Fujita K, Ageta Y (2000) Effect of summer accumulation on glacier mass balance on the Tibetan Plateau revealed by mass-balance model. J Glaciol 46:244–252. https://doi.org/10.3189/172756500781832945

133. Gadgil S, Vinayachandran PN, Francis PA (2003) Droughts of the Indian summer monsoon: Role of clouds over the Indian Ocean. Curr Sci 85:1713–1719

134. Gafurov A, Bárdossy A (2009) Cloud removal methodology from MODIS snow cover product. Hydrol Earth Syst Sci 13:1361–1373. https://doi.org/10.5194/hess-13-1361-2009

135. Gafurov A, Vorogushyn S, Farinotti D, et al (2015) Snow-cover reconstruction methodology for mountainous regions based on historic in situ observations and recent remote sensing data. Cryosphere 9:451–463. https://doi.org/10.5194/tc-9-451-2015

136. Galewsky J (2009) Rain shadow development during the growth of mountain ranges: An atmospheric dynamics perspective. J Geophys Res Earth Surf 114:1–17. https://doi.org/10.1029/2008JF001085

137. Gao Y, Xie H, Lu N, et al (2010) Toward advanced daily cloud-free snow cover and snow water equivalent products from Terra–Aqua MODIS and Aqua AMSR-E measurements. J Hydrol 385:23–35

138. Gardelle J, Berthier E, Arnaud Y (2012) Slight mass gain of Karakoram glaciers in the early twenty-first century. Nat Geosci 5:1–4. https://doi.org/10.1038/ngeo1450

139. Gardelle J, Berthier E, Arnaud Y, Kääb A (2013) Region-wide glacier mass balances over the Pamir-Karakoram-Himalaya during 1999-2011. Cryosphere 7:1263–1286. https://doi.org/10.5194/tc-7-1263-2013

140. Gassert F, Landis M, Luck M, et al (2014) "Aqueduct Global Maps 2.1." Working Paper. World Resour Inst

141. Gauch M, Kratzert F, Klotz D, et al (2020) Rainfall–runoff prediction at multiple timescales with a single long short-term memory network. arXiv 2045–2062. https://doi.org/10.5194/hess-2020-540

142. Gautam MR, Timilsina GR, Acharya K (2013) Climate Change in the Himalayas: Current State of Knowledge

143. Gautam RC, Bana RS (2014) Drought in India: Its impact and mitigation strategies – A review. Indian J Agron 59:179–190

144. GEC (2017) Report of the Ground Water Resource Estimation Committee

145. Gee GW, Hillel D (1988) Groundwater recharge in arid regions: Review and critique of estimation methods. Hydrol Process 2:255–266. https://doi.org/10.1002/hyp.3360020306

146. Girotto M, De Lannoy GJM, Reichle RH, et al (2017) Benefits and pitfalls of GRACE data assimilation: A case study of terrestrial water storage depletion in India. Geophys Res Lett 44:4107–4115. https://doi.org/10.1002/2017GL072994

147. Goldin T (2016) Groundwater: India's drought below ground. Nat. Geosci. 9:98

148. Gonçalvès J, Petersen J, Deschamps P, et al (2013) Quantifying the modern recharge of the "fossil" Sahara aquifers. Geophys Res Lett 40:2673–2678. https://doi.org/10.1002/grl.50478

149. Graham RM, Cohen L, Ritzhaupt N, et al (2019) Evaluation of six atmospheric reanalyses over Arctic sea ice from winter to early summer. J Clim 32:4121–4143. https://doi.org/10.1175/JCLI-D-18-0643.1

150. Grippa M, Kergoat L, Frappart F, et al (2011) Land water storage variability over West Africa estimated by Gravity Recovery and Climate Experiment (GRACE) and land surface models. Water Resour Res 47:1–18. https://doi.org/10.1029/2009WR008856

151. Guhathakurta P (2003) Drought in districts of India during the recent all India normal monsoon years and its probability of occurrence. Mausam 542–545

152. Guhathakurta P, Rajeevan M, Sikka DR, Tyagi A (2015) Observed changes in southwest monsoon rainfall over India during 1901-2011. Int J Climatol 35:1881–1898. https://doi.org/10.1002/joc.4095

153. Gupta RP, Haritashya UK, Singh P (2005) Mapping dry/wet snow cover in the Indian Himalayas using IRS multispectral imagery. Remote Sens Environ 97:458–469. https://doi.org/10.1016/j.rse.2005.05.010

154. Gurung DR, Giriraj A, Aung KS, et al (2011a) Snow-cover mapping and monitoring in the Hindu Kush-Himalayas. International Centre for Integrated Mountain Development (ICIMOD)

155. Gurung DR, Kulkarni A V, Giriraj A, et al (2011b) Changes in seasonal snow cover in Hindu Kush-Himalayan region. Cryosph Discuss 5:755–777. https://doi.org/10.5194/tcd-5-755-2011

156. Gutzler DS, Rosen RD (1992) Interannual variability of wintertime snow cover across the Northern Hemisphere. J Clim 5:1441–1447

157. Hagman G (1984) Prevention Better than Cure: Report on Human and Natural Disasters in the Third World. 129–139

158. Hall DK, Foster JL, Chang ATC (1982) Measurement and modeling of microwave emission from forested snowfields in Michigan. Hydrol Res 13:129–138

159. Hall DK, Foster JL, Chien JYL, Riggs GA (1995a) Determination of actual snow-covered area using Landsat TM and digital elevation model data in Glacier National Park, Montana. Polar Rec (Gr Brit) 31:191–198. https://doi.org/10.1017/S0032247400017290

160. Hall DK, Riggs GA (2007) Accuracy assessment of the MODIS snow products. In: Hydrological Processes. pp 1534–1547

161. Hall DK, Riggs GA, Digirolamo NE, Román MO (2019) Evaluation of MODIS and VIIRS cloud-gap-filled snow-cover products for production of an Earth science data record. Hydrol Earth Syst Sci 23:5227–5241. https://doi.org/10.5194/hess-23-5227-2019

162. Hall DK, Riggs GA, Salomonson V V (1995b) Mapping Global Snow Cover using Moderate Resolution Imaging Spectroradiometer (MODIS) Data. Remote Sens Environ 54:127–140

163. Hamed KH (2009) Exact distribution of the Mann-Kendall trend test statistic for persistent data. J Hydrol 365:86–94. https://doi.org/10.1016/j.jhydrol.2008.11.024

164. Hamed KH (2008) Trend detection in hydrologic data: The Mann-Kendall trend test under the scaling hypothesis. J Hydrol 349:350–363. https://doi.org/10.1016/j.jhydrol.2007.11.009

165. Hao Z, AghaKouchak A (2013) A Nonparametric Multivariate Multi-Index Drought Monitoring Framework. J Hydrometeorol 15:89–101. https://doi.org/10.1175/jhm-d-12-0160.1

166. Hasson S, Lucarini V, Khan MR, et al (2014a) Early 21st century snow cover state over the western river basins of the Indus River system. Hydrol Earth Syst Sci 18:4077–4100. https://doi.org/10.5194/hess-18-4077-2014

167. Hasson S, Lucarini V, Pascale S, Böhner J (2014b) Seasonality of the hydrological cycle in major South and Southeast Asian river basins as simulated by PCMDI/CMIP3 experiments. Earth Syst Dyn 5:67–87. https://doi.org/10.5194/esd-5-67-2014

168. Hay JE, Fitzharris BB (1988) A comparison of the energy-balance and bulk-aerodynamic approaches for estimating glacier melt. J Glaciol 34:145–153

169. Hayes M, Svoboda M, Wall N, Widhalm M (2011) The Lincoln Declaration on Drought Indices: Universal Meteorological Drought Index Recommended. Bull Am Meteorol Soc 92:485–488. https://doi.org/10.1175/2010bams3103.1

170. Healy RW, Cook PG (2002) Using groundwater levels to estimate recharge. Hydrogeol J 10:91–109. https://doi.org/10.1007/s10040-001-0178-0

171. Heim Jr. RR (2002) A review of twentieth-century drought indices used in the United States. Bull Am Meteorol Soc 1149–1166. https://doi.org/, https://doi.org/10.1175/1520-0477-83.8.1149

172. Henry CM, Allen DM, Huang J (2011) Groundwater storage variability and annual recharge using well-hydrograph and GRACE satellite data. Hydrogeol J 19:741–755. https://doi.org/10.1007/s10040-011-0724-3

173. Heppner CS, Nimmo JR (2005) A Computer Program for Predicting Recharge with a Master Recession Curve. In: US Geological Survey. Washington, USA, pp 1–8

174. Hewitt K (2005) The Karakoram Anomaly? Glacier Expansion and the 'Elevation Effect,' Karakoram Himalaya. Mt Res Dev 25:332–340. https://doi.org/10.1659/0276-4741(2005)025

175. Heynen M, Miles E, Ragettli S, et al (2016) Air temperature variability in a high-elevation Himalayan catchment. Ann Glaciol 57:212–222. https://doi.org/10.3189/2016AoG71A076

176. Hock R (2005) Glacier melt : a review on processes and their modelling. Prog Phys Geogr 3:362–391

177. Hoffmann L, Günther G, Li D, et al (2019) From ERA-Interim to ERA5: the considerable impact of ECMWF's next-generation reanalysis on Lagrangian transport simulations. Atmos Chem Phys 19:3097–3124. https://doi.org/10.5194/acp-19-3097-2019

178. Hoinkes H (1954) Measurement of ablation and heat balance on alpine glaciers. J Glaciol 2:497–501

179. Huang X, Deng J, Wang W, et al (2017) Impact of climate and elevation on snow cover using integrated remote sensing snow products in Tibetan Plateau. Remote Sens Environ 190:274–288. https://doi.org/10.1016/j.rse.2016.12.028

180. Huang X, Hao X, Feng Q, et al (2014) A new MODIS daily cloud free snow cover mapping algorithm on the Tibetan Plateau. Sci Cold Reg 6:0116--123. https://doi.org/10.3724/SP.J.1226.2014.00116

181. Huang Z, Pan Y, Gong H, et al (2015) Subregional-scale groundwater depletion detected by GRACE for both shallow and deep aquifers in North China Plain. Geophys Res Lett 42:1791–1799. https://doi.org/10.1002/2014gl062498

182. Huffman GJ, Bolvin DT, Braithwaite D, et al (2018) Algorithm Theoretical Basis Document (ATBD) Version 5.2 NASA - NASA Global Precipitation Measurement (GPM) Integrated Multi-satellitE Retrievals for GPM (IMERG) - Algorithm Theoretical Basis Document (ATBD) Version 5.2. IMERG Algorithm Theor Basis Doc IMERG Algo:1–31. https://doi.org/https://pmm.nasa.gov/resources/documents/gpm-integrated-multi-satellite-retrievals-gpm-imerg-algorithm-theoretical-basis-

183. Huffman GJ, Bolvin DT, Nelkin EJ, et al (2007) The TRMM Multisatellite Precipitation Analysis (TMPA): Quasi-Global, Multiyear, Combined-Sensor Precipitation Estimates at Fine Scales. J Hydrometeorol 8:38–55. https://doi.org/10.1175/JHM560.1

184. Hugonnet R, McNabb R, Berthier E, et al (2021) Accelerated global glacier mass loss in the early twenty-first century. Nature 592:726–731. https://doi.org/10.1038/s41586-021-03436-z

185. Hussain D, Kao HC, Khan AA, et al (2020) Spatial and Temporal Variations of Terrestrial Water Storage in Upper Indus Basin Using GRACE and Altimetry Data. IEEE Access 8:65327–65339. https://doi.org/10.1109/ACCESS.2020.2984794

186. IITs (2015) Ganga River Basin Management Plan - 2015

187. Immerzeel WW, Bierkens MFP (2012) Asia's water balance. Nat Geosci 5:841–842. https://doi.org/10.1038/ngeo1643

188. Immerzeel WW, Droogers P, de Jong SM, Bierkens MFP (2009) Large-scale monitoring of snow cover and runoff simulation in Himalayan river basins using remote sensing. Remote Sens Environ 113:40–49. https://doi.org/10.1016/j.rse.2008.08.010

189. Immerzeel WW, Van Beek LPH, Bierkens MFP (2010) Climate change will affect the asian water towers. Science (80-) 328:1382–1385. https://doi.org/10.1126/science.1183188

190. India-WRIS (2012) River basin atlas of India. RRSC-West, NRSC, ISRO, Jodhpur, India

191. IPCC (2013) Technical Summary. In: Climate Change 2013: The Physical Science Basis. Contribution of Working Group I to the Fifth Assessment Report of the Intergovernmental Panel on Climate Change. Cambridge Univ Press Cambridge, United Kingdom New York, NY, USA 31–116. https://doi.org/10.1017/cbo9781107415324.005

192. Jain CK, Singh S (2020) Impact of climate change on the hydrological dynamics of River Ganga, India. J Water Clim Chang 11:274–290. https://doi.org/10.2166/wcc.2018.029

193. Jain SK, Goswami A, Saraf AK (2008) Accuracy assessment of MODIS, NOAA and IRS data in snow cover mapping under Himalayan conditions. Int J Remote Sens 29:5863–5878. https://doi.org/10.1080/01431160801908129

194. Järvinen O, Leppäranta M (2013) Solar radiation transfer in the surface snow layer in Dronning Maud Land, Antarctica. Polar Sci 7:1–17. https://doi.org/10.1016/j.polar.2013.03.002

195. Jarvis A, Reuter HI, Nelson A, Guevara E (2008) Hole-filled SRTM for the globe version 4, from the CGIAR-CSI SRTM 90m database. http//srtm csi cgiar org

196. Jaswal AK, Rao GSP (2010) Recent trends in meteorological parameters over Jammu and Kashmir. Mausam 61:369–382

197. Jia S, Zhu W, Lu A, Yan T (2011) A statistical spatial downscaling algorithm of TRMM precipitation based on NDVI and DEM in the Qaidam Basin of China. Remote Sens Environ 115:3069–3079. https://doi.org/10.1016/j.rse.2011.06.009

198. Jing Y, Shen H, Li X, Guan X (2019) A two-stage fusion framework to generate a spatio'temporally continuous MODIS NDSI product over the Tibetan Plateau. Remote Sens 11:1–21. https://doi.org/10.3390/rs11192261

199. Jowhar TN (2001) Geobarometric constraints on the depth of emplacement of granite from the Ladakh batholith, Northwest Himalaya,India. J. Mineral. Petrol. Sci. 96:256–264

200. Jury MW, Mendlik T, Tani S, et al (2019) Climate projections for glacier change modelling over the Himalayas. Int J Climatol 1–20. https://doi.org/10.1002/joc.6298

201. Kääb A, Berthier E, Nuth C, et al (2012) Contrasting patterns of early twenty-first-century glacier mass change in the Himalayas. Nature 488:495–498. https://doi.org/10.1038/nature11324

202. Kahl A, Dujardin J, Lehning M (2019) The bright side of PV production in snow-covered mountains. Proc Natl Acad Sci U S A 116:1162–1167. https://doi.org/10.1073/pnas.1720808116

203. Kan G, Li J, Zhang X, et al (2017) A new hybrid data-driven model for event-based rainfall–runoff simulation. Neural Comput Appl 28:2519–2534. https://doi.org/10.1007/s00521-016-2200-4

204. Kattel DB, Yao T, Yang W, et al (2015) Comparison of temperature lapse rates from the northern to the southern slopes of the Himalayas. Int J Climatol 35:4431–4443. https://doi.org/10.1002/joc.4297

205. Kayastha R, Ageta Y, Nakawo M, et al (2003) Positive degree-day factors for ice ablation on four glaciers in the Nepalese Himalayas and Qinghai-Tibetan Plateau. Bull Glaciol Res 20:7–14

206. Kayastha RB, Ohata T, Ageta Y (1999) Application of a mass-balance model to a Himalayan glacier. J Glaciol 45:559–567

207. Khan A, Koch M, Chinchilla K (2018) Evaluation of Gridded Multi-Satellite Precipitation Estimation (TRMM-3B42-V7) Performance in the Upper Indus Basin (UIB). Climate 6:76. https://doi.org/10.3390/cli6030076

208. Khan AA, Pant NC, Sarkar A, et al (2017) The Himalayan cryosphere: A critical assessment and evaluation of glacial melt fraction in the Bhagirathi basin. Geosci Front 8:107–115. https://doi.org/10.1016/j.gsf.2015.12.009

209. Klein AG, Barnett AC (2003) Validation of daily MODIS snow cover maps of the Upper Rio Grande River Basin for the 2000–2001 snow year. Remote Sens Environ 86:162–176

210. Klok EJ, Nolan M, Van Den Broeke MR (2005) Analysis od meteorological data and the surface energy balance of McCall Glacier, Alaska, USA. J Glaciol 51:451–461. https://doi.org/10.3189/172756505781829241

211. Klok EJ, Oerlemans J (2002) Model study of the spatial distribution of the energy and mass balance of Morteratschgletscher, Switzerland. J Glaciol 48:505–518. https://doi.org/10.3189/172756502781831133

212. Kogan FN (1997) Global drought watch from space. Bull Am Meteorol Soc 78:621. https://doi.org/10.1175/1520-0477(1997)078<0621:GDWFS>2.0.CO;2

213. Koster RD, Suarez MJ (1996) Energy and Water Balance Calculations in the Mosaic LSM. NASA Tech Memo 9:76

214. Kothawale DR, Rajeevan M (2016) Monthly, Seasonal and Annual Rainfall Time Series for All-India, Homogeneous Regions and Meteorological Subdivisions: 1871-2016. 02:1871–2016

215. Koul MN, Bahuguna IM, Rajawat AS, et al (2016) Glacier Area Change over Past 50 Years to Stable Phase in Drass Valley, Ladakh Himalaya (India). Am J Clim Chang Ladakh Himalaya (India) Am J Clim Chang 5:88–102

216. Kour R, Patel N, Krishna AP (2016a) Effects of terrain attributes on snow-cover dynamics in parts of Chenab basin, western Himalayas. Hydrol Sci J 61:1861–1876. https://doi.org/10.1080/02626667.2015.1052815

217. Kour R, Patel N, Krishna AP (2016b) Assessment of temporal dynamics of snow cover and its validation with hydro-meteorological data in parts of Chenab Basin, western Himalayas. Sci China Earth Sci 59:1081–1094. https://doi.org/10.1007/s11430-015-5243-y

218. Kratzert F, Herrnegger M, Klotz D, et al (2019) NeuralHydrology - Interpreting LSTMs in hydrology. arXiv

219. Kratzert F, Klotz D, Brenner C, et al (2018) Rainfall – runoff modelling using Long Short-Term Memory (LSTM) networks. Hydrol Earth Syst Sci 6005–6022

220. Kripalani RH, Kulkarni A, Sabade SS (2003) Western Himalayan snow cover and Indian monsoon rainfall: A re-examination with INSAT and NCEP/NCAR data. Theor Appl Climatol 74:1–18. https://doi.org/10.1007/s00704-002-0699-z

221. Krishnamurti TN, Bedi HS, Subramaniam M (1989) The Summer Monsoon of 1987. 321–340

222. Kulkarni A V., Rathore BP, Singh SK, Ajai (2010) Distribution of seasonal snow cover in central and western Himalaya. Ann Glaciol 51:123–128. https://doi.org/10.3189/172756410791386445

223. Kulkarni A V., Singh SK, Mathur P, Mishra VD (2006) Algorithm to monitor snow cover using AWiFS data of RESOURCESAT-1 for the Himalayan region. Int J Remote Sens 27:2449–2457. https://doi.org/10.1080/01431160500497820

224. Kulkarni A V, Rathore BP, Singh SK, Bahuguna IM (2011) Understanding changes in the Himalayan cryosphere using remote sensing techniques. Int J Remote Sens 32:601–615. https://doi.org/10.1080/01431161.2010.517802

225. Kumar A, Negi HS, Kumar K, et al (2019) Quantifying mass balance of East-Karakoram glaciers using geodetic technique. Polar Sci 19:24–39. https://doi.org/10.1016/j.polar.2018.11.005

226. Kumar A, Negi HS, Kumar K, et al (2018) Estimation of recent changes in thickness and mass balance of the Patsio glacier in the Great Himalayan region using geodetic technique and ancillary data. Geocarto Int 0:1–17. https://doi.org/10.1080/10106049.2018.1506506

227. Kumar CP (1997) Estimation of natural ground water recharge. ISH J Hydraul Eng 3:61–74. https://doi.org/10.1080/09715010.1997.10514603

228. Kumar CP, Seethapathi P V. (2002) Assessment of Natural Ground Water Recharge in Upper Ganga Canal Command Area. J Appl Hydrol Assoc Hydrol India 15:13–20

229. Kumar KK, Rajagopalan B, Hoerling M, et al (2006) Unraveling the Mystery of Indian Monsoon. Science (80-) 314:115–119. https://doi.org/10.1126/science.1131152

230. Kumar M, Kumar P (2016) Snow cover dynamics and geohazards: a case study of Bhilangna watershed, Uttarakhand Himalaya, India. Geoenvironmental Disasters 3:0–7. https://doi.org/10.1186/s40677-016-0035-z

231. Kumar V, Venkataraman G (2011) SAR interferometric coherence analysis for snow cover mapping in the western Himalayan region. Int J Digit Earth 4:78–90. https://doi.org/10.1080/17538940903521591

232. Landerer FW, Swenson SC (2012) Accuracy of scaled GRACE terrestrial water storage estimates. Water Resour Res 48:1–11. https://doi.org/10.1029/2011WR011453

233. Le XH, Ho HV, Lee G, Jung S (2019) Application of Long Short-Term Memory (LSTM) neural network for flood forecasting. Water (Switzerland) 11:. https://doi.org/10.3390/w11071387

234. Leblanc MJ, Tregoning P, Ramillien G, et al (2009) Basin-scale, integrated observations of the early 21st century multiyear drought in Southeast Australia. Water Resour Res 45:1–10. https://doi.org/10.1029/2008WR007333

235. Lettenmaier DP, Famiglietti JS (2006) Hydrology: Water from on high. Nature 444:562–563. https://doi.org/10.1029/2006GL027070

236. Li B, Rodell M (2015) Evaluation of a model-based groundwater drought indicator in the conterminous U.S. J Hydrol 526:78–88. https://doi.org/10.1016/j.jhydrol.2014.09.027

237. Li B, Zhou W, Zhao Y, et al (2015) Using the SPEI to assess recent climate change in the Yarlung Zangbo River Basin, South Tibet. Water (Switzerland) 7:5474–5486. https://doi.org/10.3390/w7105474

238. Li H, Li X, Xiao P (2016) Impact of sensor zenith angle on MOD10A1 data reliability and modification of snow cover data for the Tarim River Basin. Remote Sens 8:1–18. https://doi.org/10.3390/rs8090750

239. Li X, Fu W, Shen H, et al (2017) Monitoring snow cover variability (2000–2014) in the Hengduan Mountains based on cloud-removed MODIS products with an adaptive spatio-temporal weighted method. J Hydrol 551:314–327. https://doi.org/10.1016/j.jhydrol.2017.05.049

240. Li X, Jing Y, Shen H, Zhang L (2019a) The recent developments in cloud removal approaches of MODIS snow cover product. Hydrol Earth Syst Sci 23:2401–2416. https://doi.org/10.5194/hess-23-2401-2019

241. Li Y, Chen Y, Li Z (2019b) Developing Daily Cloud-Free Snow Composite Products From MODIS and IMS for the Tienshan Mountains. Earth Sp Sci 6:266–275. https://doi.org/10.1029/2018EA000460

242. Liang L, Cuo L, Liu Q (2018) The energy and mass balance of a continental glacier: Dongkemadi Glacier in central Tibetan Plateau. Sci Rep 8:1–8. https://doi.org/10.1038/s41598-018-31228-5

243. Liang TG, Huang XD, Wu CX, et al (2008) An application of MODIS data to snow cover monitoring in a pastoral area: A case study in Northern Xinjiang, China. Remote Sens Environ 112:1514–1526

244. Liang X, Lettenmaier DP, Wood EF, Burges SJ (1994) A simple hydrologically based model of land surface water and energy fluxes for general circulation models. J Geophys Res 99:14415. https://doi.org/10.1029/94JD00483

245. Lin H, Li G, Cuo L, et al (2017) A decreasing glacier mass balance gradient from the edge of the Upper Tarim Basin to the Karakoram during 2000-2014. Sci Rep 7:1–9. https://doi.org/10.1038/s41598-017-07133-8

246. Lin X, Wen J, Liu Q, et al (2020) Spatiotemporal variability of land surface Albedo over the Tibet Plateau from 2001 to 2019. Remote Sens 12:1–18. https://doi.org/10.3390/rs12071188

247. Liu M, Xiong C, Pan J, et al (2020) High-resolution reconstruction of the maximum snow water equivalent based on remote sensing data in a mountainous area. Remote Sens 12:. https://doi.org/10.3390/rs12030460

248. Liu S, Zhang Y, Han H (2010) Surface Energy Balance of Keqicar Glacier, Tianshan Mountains China During Ablation Period. In: Geophysical Research Abstract. p 7546

249. Long D, Chen X, Scanlon BR, et al (2016) Have GRACE satellites overestimated groundwater depletion in the Northwest India Aquifer? Sci Rep 6:1–11. https://doi.org/10.1038/srep24398

250. Long D, Scanlon BR, Longuevergne L, et al (2013) GRACE satellite monitoring of large depletion in water storage in response to the 2011 drought in Texas. Geophys Res Lett 40:3395–3401. https://doi.org/10.1002/grl.50655

251. Long D, Yang Y, Wada Y, et al (2015) Deriving scaling factors using a global hydrological model to restore GRACE total water storage changes for China's Yangtze River Basin. Remote Sens Environ 168:177–193. https://doi.org/10.1016/j.rse.2015.07.003

252. Lopez-Burgos V, Gupta H V., Clark M (2013) Reducing cloud obscuration of MODIS snow cover area products by combining spatio-temporal techniques with a probability of snow approach. Hydrol Earth Syst Sci 17:1809–1823. https://doi.org/10.5194/hess-17-1809-2013

253. Luqman M, Shah UUH, Khan S, Akmal F (2018) River channel dynamics detection using Remote Sensing and GIS technologies: A case study of River Chenab in Indo-Pak Region. 2017 5th Int Conf Aerosp Sci Eng ICASE 2017 1–5. https://doi.org/10.1109/ICASE.2017.8374275

254. Lutz AF, Immerzeel WW, Shrestha AB, Bierkens MFP (2014) Consistent increase in High Asia's runoff due to increasing glacier melt and precipitation. Nat Clim Chang 4:587–592. https://doi.org/10.1038/nclimate2237

255. MacDonald AM, Bonsor HC, Ahmed KM, et al (2016) Groundwater quality and depletion in the Indo-Gangetic Basin mapped from in situ observations. Nat Geosci 9:762–766. https://doi.org/10.1038/ngeo2791

256. Mahto SS, Mishra V (2019) Does ERA-5 Outperform Other Reanalysis Products for Hydrologic Applications in India? J Geophys Res Atmos 124:9423–9441. https://doi.org/10.1029/2019JD031155

257. Mandal A, Ramanathan A, Angchuk T, et al (2016) Unsteady state of glaciers (Chhota Shigri and Hamtah) and climate in Lahaul and Spiti region, western Himalayas: a review of recent mass loss. Environ Earth Sci 75:1–12. https://doi.org/10.1007/s12665-016-6023-5

258. Mandal A, Ramanathan A, Azam MF, et al (2020) Understanding the interrelationships among mass balance, meteorology, discharge and surface velocity on Chhota Shigri Glacier over 2002–2019 using in situ measurements. J Glaciol 66:727–741. https://doi.org/10.1017/jog.2020.42

259. Mandal A, Ramanathan A, Farooq Azam M, et al (2015) Annual and seasonal mass balances of Chhota Shigri Glacier (benchmark glacier, Western Himalaya), India. EGU Gen Assem Conf Abstr 17:14078

260. Mann HB (1945) Nonparametric Tests Against Trend. Econometrica 13:245–259. https://doi.org/10.1016/j.annrmp.2004.07.001

261. Marchane A, Jarlan L, Hanich L, et al (2015) Remote Sensing of Environment Assessment of daily MODIS snow cover products to monitor snow cover dynamics over the Moroccan Atlas mountain range. Remote Sens Environ 160:72–86. https://doi.org/10.1016/j.rse.2015.01.002

262. Marzeion B, Cogley JG, Richter K, Parkes D (2014) Attribution of global glacier mass loss to anthropogenic and natural causes. Science 345:919–921. https://doi.org/10.1126/science.1254702

263. Marzeion B, Leclercq PW, Cogley JG, Jarosch AH (2015) Brief Communication: Global reconstructions of glacier mass change during the 20th century are consistent. Cryosphere 9:2399–2404. https://doi.org/10.5194/tc-9-2399-2015

264. Maskey S, Uhlenbrook S, Ojha S (2011) An analysis of snow cover changes in the Himalayan region using MODIS snow products and in-situ temperature data. Clim Change 108:391–400. https://doi.org/10.1007/s10584-011-0181-y

265. Matiu M, Jacob A, Notarnicola C (2020) Daily MODIS snow cover maps for the european alps from 2002 onwards at 250 m horizontal resolution along with a nearly cloud-free version. Data 5:1–11. https://doi.org/10.3390/data5010001

266. Maurer JM, Schaefer JM, Rupper S, Corley A (2019) Acceleration of ice loss across the Himalayas over the past 40 years. Sci Adv 5:. https://doi.org/10.1126/sciadv.aav7266

267. McGrath D, Sass L, O'Neel S, et al (2018) Interannual snow accumulation variability on glaciers derived from repeat, spatially extensive ground-penetrating radar surveys. Cryosph 12:3617–3633. https://doi.org/10.5194/tc-12-3617-2018

268. McKee TB, Doesken NJ, Kleist J (1993) The relationship of drought frequency and duration to time scales. Eighth Conf Appl Climatol 22:1571–1592. https://doi.org/10.1002/joc.846

269. Mechal A, Wagner T, Birk S (2015) Recharge variability and sensitivity to climate: The example of Gidabo River Basin, Main Ethiopian Rift. J Hydrol Reg Stud 4:644–660. https://doi.org/10.1016/j.ejrh.2015.09.001

270. Meena HM, Tewari JC, Pandey CB (2015) Influence of Weather Variation on Cropping Pattern of Leh District of Ladakh Region. Curr World Environ 10:489–493. https://doi.org/10.12944/cwe.10.2.13

271. Menon S, Koch D, Beig G, et al (2010) Black carbon aerosols and the third polar ice cap. Atmos Chem Phys 10:4559–4571. https://doi.org/10.5194/acp-10-4559-2010

272. Min L, Shen Y, Pei H (2015) Estimating groundwater recharge using deep vadose zone data under typical irrigated cropland in the piedmont region of the North China Plain. J Hydrol 527:305–315. https://doi.org/10.1016/j.jhydrol.2015.04.064

273. Mir RA, Jain SK, Saraf AK, Goswami A (2015) Decline in snowfall in response to temperature in Satluj basin, western Himalaya. J Earth Syst Sci 124:365–382. https://doi.org/10.1007/s12040-015-0539-z

274. Mishra B, Babel MS, Tripathi NK (2014a) Analysis of climatic variability and snow cover in the Kaligandaki River Basin, Himalaya, Nepal. Theor Appl Climatol 116:681–694. https://doi.org/10.1007/s00704-013-0966-1

275. Mishra B, Tripathi NK, Babel MS (2014b) An artificial neural network-based snow cover predictive modeling in the higher Himalayas. J Mt Sci 11:825–837. https://doi.org/10.1007/s11629-014-2985-5

276. Mishra V, Smoliak B V., Lettenmaier DP, Wallace JM (2012) A prominent pattern of year-to-year variability in Indian Summer Monsoon Rainfall. Proc Natl Acad Sci 109:7213–7217. https://doi.org/10.1073/pnas.1119150109

277. Moiwo JP, Yang Y, Li H, et al (2009) Comparison of GRACE with in situ hydrological measurement data shows storage depletion in Hai River Basin, Northern China. Water SA 35:663–670. https://doi.org/10.4314/wsa.v35i5.49192

278. Mölg T, Hardy DR (2004) Ablation and associated energy balance of a horizontal glacier surface on Kilimanjaro. J Geophys Res D Atmos 109:1–13. https://doi.org/10.1029/2003JD004338

279. Moore RD (1983) On the use of bulk aerodynamic formulae over melting snow. Nord Hydrol 14:193–206. https://doi.org/10.2166/nh.1983.016

280. Mott R, Vionnet V, Grünewald T (2018) The Seasonal Snow Cover Dynamics: Review on Wind-Driven Coupling Processes. Front Earth Sci 6:. https://doi.org/10.3389/feart.2018.00197

281. Muhammad S, Thapa A (2020) An improved Terra-Aqua MODIS snow cover and Randolph Glacier Inventory 6.0 combined product (MOYDGL06∗) for high-mountain Asia between 2002 and 2018. Earth Syst Sci Data 12:345–356. https://doi.org/10.5194/essd-12-345-2020

282. Muhammad S, Tian L, Khan A (2019a) Early twenty-first century glacier mass losses in the Indus Basin constrained by density assumptions. J Hydrol 574:467–475. https://doi.org/10.1016/j.jhydrol.2019.04.057

283. Muhammad S, Tian L, Khan A (2019b) Early twenty-first century glacier mass losses in the Indus Basin constrained by density assumptions. J Hydrol 574:467–475. https://doi.org/10.1016/j.jhydrol.2019.04.057

284. Mukherjee A, Bhanja SN, Wada Y (2018) Groundwater depletion causing reduction of baseflow triggering Ganges river summer drying. Sci Rep 8:1–9. https://doi.org/10.1038/s41598-018-30246-7

285. Mukherjee A, Saha D, Harvey CF, et al (2015) Groundwater systems of the Indian Sub-Continent. J Hydrol Reg Stud 4:1–14. https://doi.org/10.1016/j.ejrh.2015.03.005

286. Mukherji A, Molden D, Nepal S, et al (2015) Himalayan waters at the crossroads: issues and challenges. Int J Water Resour Dev 31:151–160. https://doi.org/10.1080/07900627.2015.1040871

287. Mukherji A, Sinisalo A, Nüsser M, et al (2019) Contributions of the cryosphere to mountain communities in the Hindu Kush Himalaya: a review. Reg Environ Chang 1311–1326. https://doi.org/10.1007/s10113-019-01484-w

288. Mukhopadhyay B (2012) Detection of dual effects of degradation of perennial snow and ice covers on the hydrologic regime of a Himalayan river basin by stream water availability modeling. J Hydrol 412–413:14–33. https://doi.org/10.1016/j.jhydrol.2011.06.005

289. Mukhopadhyay B, Khan A (2014) Rising river flows and glacial mass balance in central Karakoram. J Hydrol 513:192–203. https://doi.org/10.1016/j.jhydrol.2014.03.042

290. Mukhopadhyay B, Khan A, Gautam R (2015) Rising and falling river flows: contrasting signals of climate change and glacier mass balance from the eastern and western Karakoram. Hydrol Sci J 60:2062–2085. https://doi.org/10.1080/02626667.2014.947291

291. Murtaza KO, Romshoo SA (2017) Recent glacier changes in the Kashmir Alpine Himalayas, India. Geocarto Int 32:188–205. https://doi.org/10.1080/10106049.2015.1132482

292. Nalbantis I, Tsakiris G (2009) Assessment of hydrological drought revisited. Water Resour Manag 23:881–897. https://doi.org/10.1007/s11269-008-9305-1

293. Nandargi SS, Shelar A (2018) Rainfall and Flood Studies of the Ganga River Basin in India. Ann Geogr Stud 1:34–50

294. NCERT (2020) Atmospheric circulation and weather systems

295. Ndehedehe C, Awange J, Agutu N, et al (2016) Understanding changes in terrestrial water storage over West Africa between 2002 and 2014. Adv Water Resour 88:211–230. https://doi.org/10.1016/j.advwatres.2015.12.009

296. Negi HS, Datt P, Thakur NK, et al (2017) Observed spatio-temporal changes of winter snow albedo over the north-west Himalaya. Int J Climatol 37:2304–2317. https://doi.org/10.1002/joc.4846

297. Negi HS, Kulkarni A V., Semwal BS (2009) Estimation of snow cover distribution in Beas basin, Indian Himalaya using satellite data and ground measurements. J Earth Syst Sci 118:525–538. https://doi.org/10.1007/s12040-009-0039-0

298. Negi HS, Kumar A, Kanda N, et al (2020) Status of glaciers and climate change of East Karakoram in early twenty-first century. Sci Total Environ 753:141914. https://doi.org/10.1016/j.scitotenv.2020.141914

299. Nicholson LI, Prinz R, Mölg T, Kaser G (2013) Micrometeorological conditions and surface mass and energy fluxes on Lewis Glacier, Mt Kenya, in relation to other tropical glaciers. Cryosphere 7:1205–1225. https://doi.org/10.5194/tc-7-1205-2013

300. Nie Y, Pritchard HD, Liu Q, et al (2021) Glacial change and hydrological implications in the Himalaya and Karakoram. Nat Rev Earth Environ 2:91–106. https://doi.org/10.1038/s43017-020-00124-w

301. Nimmo JR, Horowitz C, Mitchell L (2015) Discrete-storm water-table fluctuation method to estimate episodic recharge. Groundwater 53:282–292. https://doi.org/10.1111/gwat.12177

302. NRAA (2009) Drought Management Strategies-2009. Draft Pap Natl Rainfed Area Auth Minist Agric Gov India New Delhi

303. Nüsser M, Schmidt S, Dame J (2012) Irrigation and Development in the Upper Indus Basin. Mt Res Dev 32:51–61. https://doi.org/10.1659/MRD-JOURNAL-D-11-00091.1

304. Oerlemans J (2001) Glaciers and climate change. CRC Press

305. Oerlemans J, Anderson B, Hubbard A, et al (1998) Modelling the response of glaciers to climate warming. Clim Dyn 14:267–274. https://doi.org/10.1007/s003820050222

306. Oerlemans J, Klok EJ (2002) Energy Balance of a Glacier Surface: Analysis of Automatic Weather Station Data from the Morteratschgletscher, Switzerland. Arctic, Antarct Alp Res 34:477. https://doi.org/10.2307/1552206

307. Oke TR (1987) Boundary layer climates, 2nd edn. Taylor & Francis e-Library

308. Owuor SO, Butterbach-Bahl K, Guzha AC, et al (2016) Groundwater recharge rates and surface runoff response to land use and land cover changes in semi-arid environments. Ecol Process 5:1–21. https://doi.org/10.1186/s13717-016-0060-6

309. Padma Kumari B, Goswami BN (2010) Seminal role of clouds on solar dimming over the Indian monsoon region. Geophys Res Lett 37:1–5. https://doi.org/10.1029/2009GL042133

310. Pai DS, Sridhar L, Guhathakurta P, Hatwar HR (2011) District-wide drought climatology of the southwest monsoon season over India based on standardized precipitation index (SPI). Nat Hazards 59:1797–1813. https://doi.org/10.1007/s11069-011-9867-8

311. Palmer WC (1965) Meteorological droughts. 58

312. Panda DK, Wahr J (2016) Spatiotemporal evolution of water storage changes in India from the updated GRACE-derived gravity records. Water Resour Res 52:135–149. https://doi.org/10.1002/2015WR017797

313. Panday PK, Frey KE, Ghimire B (2011) Detection of the timing and duration of snowmelt in the Hindu Kush-Himalaya using QuikSCAT, 2000-2008. Environ Res Lett 6:2000–2008. https://doi.org/10.1088/1748-9326/6/2/024007

314. Parajka J, Blöschl G (2008) Spatio-temporal combination of MODIS images - Potential for snow cover mapping. Water Resour Res 44:. https://doi.org/10.1029/2007WR006204

315. Parajka J, Pepe M, Rampini A, et al (2010) A regional snow-line method for estimating snow cover from MODIS during cloud cover. J Hydrol 381:203–212

316. Patel A, Goswami A, Dharpure JK, et al (2021a) Estimation of mass and energy balance of glaciers using a distributed energy balance model over the Chandra river basin (Western Himalaya). Hydrol Process 35:1–22. https://doi.org/10.1002/hyp.14058

317. Patel A, Goswami A, Dharpure JK, et al (2021b) Regional mass variations and its sensitivity to climate drivers over glaciers of Karakoram and Himalayas. GIScience Remote Sens 00:1–23. https://doi.org/10.1080/15481603.2021.1930730

318. Patel A, Goswami A, Dharpure JK, Meloth T (2020) Rainfall variability over the Indus, Ganga, and Brahmaputra river basins: A spatio-temporal characterisation. Quat Int. https://doi.org/10.1016/j.quaint.2020.06.010

319. Patel LK, Sharma P, Singh AT, et al (2021c) Spatial surface velocity pattern in the glaciers of Chandra Basin, Western Himalaya. Geocarto Int 0:1–18. https://doi.org/10.1080/10106049.2021.1920627

320. Paudel KP, Andersen P (2011) Monitoring snow cover variability in an agropastoral area in the Trans Himalayan region of Nepal using MODIS data with improved cloud removal methodology. Remote Sens Environ 115:1234–1246

321. Paul F, Kotlarski S (2010) Forcing a distributed glacier mass balance model with the regional climate model REMO. Part II: Downscaling strategy and results for two swiss glaciers. J Clim 23:1607–1620. https://doi.org/10.1175/2009JCLI3345.1

322. Pearce CM (1991) Mapping muskox habitat in the Canadian High Arctic with SPOT satellite data. Arctic 44:49–57. https://doi.org/10.14430/arctic1570

323. Pellicciotti F, Brock B, Strasser U, et al (2005) An enhanced temperature-index glacier melt model including the shortwave radiation balance : development and testing for Haut Glacier d ' Arolla , Switzerland. 51:573–587

324. Petheram C, Walker G, Grayson R, et al (2002) Towards a framework for predicting impacts of land-use on recharge: 1. A review of recharge studies in Australia. Aust J Soil Res 40:397–417. https://doi.org/10.1071/SR00057

325. PMD (2015) Drought Bulletin of Pakistan Drought Bulletin

326. Prasad YS, Rao BV (2018) Groundwater recharge estimation studies in a khondalitic terrain of India. Appl Water Sci 8:1–9. https://doi.org/10.1007/s13201-018-0738-2

327. Pratap B, Sharma P, Patel L, et al (2019) Reconciling high glacier surface melting in summer with air temperature in the semi-arid zone of Western Himalaya. Water (Switzerland) 11:1–18. https://doi.org/10.3390/w11081561

328. Pratap Singh UKHKSR and NK (2005) Prevailing weather conditions during summer\nseasons around Gangotri Glacier. Curr Sci 88:753–760

329. Preethi B, Revadekar J V., Kripalani RH (2011) Anomalous behaviour of the Indian summer monsoon 2009. J Earth Syst Sci 120:783–794. https://doi.org/10.1007/s12040-011-0112-3

330. Pu Z, Xu L (2009) MODIS/Terra observed snow cover over the Tibet Plateau: Distribution, variation and possible connection with the East Asian Summer Monsoon (EASM). Theor Appl Climatol 97:265–278. https://doi.org/10.1007/s00704-008-0074-9

331. Qian Y, Wang W, Leung LR, Kaiser DP (2007) Variability of solar radiation under cloud-free skies in China: The role of aerosols. Geophys Res Lett 34:1–5. https://doi.org/10.1029/2006GL028800

332. Qin D, Liu S, Li P (2006) Snow cover distribution, variability, and response to climate change in western China. J Clim 19:1820–1833. https://doi.org/10.1175/jcli3694.1

333. Rabus B, Eineder M, Roth A, Bamler R (2003) The shuttle radar topography mission - A new class of digital elevation models acquired by spaceborne radar. ISPRS J Photogramm Remote Sens 57:241–262. https://doi.org/10.1016/S0924-2716(02)00124-7

334. Radić V, Hock R (2011) Regionally differentiated contribution of mountain glaciers and ice caps to future sea-level rise. Nat Geosci 4:91–94. https://doi.org/10.1038/ngeo1052

335. Rajmohan N, Prathapar SA (2013) Hydrogeology of the Eastern Ganges Basin: An overview

336. Randhawa SS., Gautam N (2019) Assessment of Spatial Distribution of Seasonal Snow Cover During the Year 2018-19 in Himachal Pradesh Using Space Data

337. Randhawa SS, Rathore BP, Ishant R (2016) Assessment of seasonal snow cover variation during the year 2015-16 in Himachal Pradesh using space data

338. Rao SVN, Rao M V., Ramasastri KS, Singh RNP (1997) A study of sedimentation in Chenab basin in western Himalayas. Nord Hydrol 28:201–216. https://doi.org/10.2166/nh.1997.0012

339. Rathore BMS, Sud R, Saxena V, et al (2013) Drought Conditions and Management Strategies in India. Meteorol Serv Dep 1–6

340. Rathore BP, Bahuguna IM, Singh SK, et al (2018a) Trends of snow cover in Western and West-Central Himalayas during 2004-2014. Curr Sci 114:800–807. https://doi.org/10.18520/cs/v114/i04/800-807

341. Rathore BP, Singh SK, Brahmbhatt R, et al (2015) Monitoring of moraine-dammed lakes: A remote sensing-based study in the Western Himalaya. Curr Sci 109:1843–1849. https://doi.org/10.18520/v109/i10/1843-1849

342. Rathore BP, Singh SK, Jani P, et al (2018b) Monitoring of Snow Cover Variability in Chenab Basin Using IRS AWiFS Sensor. J Indian Soc Remote Sens 46:1497–1506. https://doi.org/10.1007/s12524-018-0797-8

343. Ren YY, Ren GY, Sun XB, et al (2017) Observed changes in surface air temperature and precipitation in the Hindu Kush Himalayan region over the last 100-plus years. Adv Clim Chang Res 8:148–156. https://doi.org/10.1016/j.accre.2017.08.001

344. RGI Consortium (2017) Randolph Glacier Inventory – A Dataset of Global Glacier Outlines: Version 6.0. echnical Report, Glob L Ice Meas from Space, Color USA Digit Media 1–14. https://doi.org/https://doi.org/10.7265/N5-RGI-60

345. Richard K, Agyei AW, Nicholas K-B, et al (2015) Development of Groundwater Recharge Model for the Sumanpa Catchment at Ashanti-Mampong-Ashanti Area in Ghana. Sci Res 3:289–295. https://doi.org/10.11648/j.sr.20150306.14

346. Richardson SD, Reynolds JM (2000) An overview of glacial hazards in the Himalayas. Quat Int 65–66:31–47. https://doi.org/10.1016/S1040-6182(99)00035-X

347. Riggs GA, Hall DK, Roman MO (2016) MODIS Snow Products Collection 6 User Guide. Natl Snow Ice Data Cent Boulder, CO, USA 6:1–80

348. Riggs GA, Hall DK, Román MO (2017) Overview of NASA's MODIS and Visible Infrared Imaging Radiometer Suite (VIIRS) snow-cover Earth System Data Records. Earth Syst Sci Data 9:765–777. https://doi.org/10.5194/essd-9-765-2017

349. Rizwan M, Li X, Jamal K, et al (2019) Precipitation variations under a changing climate from 1961-2015 in the source region of the Indus River. Water (Switzerland) 11:. https://doi.org/10.3390/w11071366

350. Rodell M, Chen J, Kato H, et al (2007) Estimating groundwater storage changes in the Mississippi River basin (USA) using GRACE. Hydrogeol J 15:159–166. https://doi.org/10.1007/s10040-006-0103-7

351. Rodell M, Famiglietti JS (2001) An analysis of terrestrial water storage variations in Illinois with implications for the Gravity Recovery and Climate Experiment (GRACE). Water Resour Res 37:1327–1339. https://doi.org/10.1029/2000WR900306

352. Rodell M, Houser PR, Jambor U, et al (2004) The Global Land Data Assimilation System. Am Meteorol Soc

353. Rodell M, Velicogna I, Famiglietti JS (2009) Satellite-based estimates of groundwater depletion in India. Nature 460:999–1002. https://doi.org/10.1038/nature08238

354. Rui H, Beaudoing HK (2018) README Document for GLDAS Version 2 Data Products. Goddard Earth Sci Data Inf Serv Cent (GES DISC) 1–32.

https://doi.org/http://hydro1.sci.gsfc.nasa.gov/data/s4pa/GLDAS/GLDAS_NOAH10_M.2.0/doc/README_ GLDAS2.pdf

355. Rukundo E, Doğan A (2019) Dominant influencing factors of groundwater recharge spatial patterns in Ergene river catchment, Turkey. Water (Switzerland) 11:. https://doi.org/10.3390/w11040653

356. Rushton KR, Ward C (1979) The estimation of groundwater recharge. J Hydrol 41:345–361. https://doi.org/10.1016/0022-1694(79)90070-2

357. Ryan JC, Smith LC, Van As D, et al (2019) Greenland Ice Sheet surface melt amplified by snowline migration and bare ice exposure. Sci Adv 5:1–10. https://doi.org/10.1126/sciadv.aav3738

358. Sabin TP, Krishnan R, Vellore R, et al (2020) Climate Change Over the Himalayas. In: Krishnan R, Sanjay J, Gnanaseelan C, et al. (eds) Assessment of Climate Change over the Indian Region: A Report of the Ministry of Earth Sciences (MoES), Government of India. Springer Singapore, Singapore, pp 207–222

359. Sahu R, Gupta RD (2020) Snow Cover Analysis in Chandra Basin ofWestern Himalaya from 2001 to 2016. Springer Singapore

360. Sakthivadivel R (2007) The groundwater recharge movement in India. Agric Groundw Revolut Oppor Threat to Dev 3:195–210

361. Sakumura C, Bettadpur S, Bruinsma S (2014) Ensemble prediction and intercomparison analysis of GRACE time-variable gravity field models. Geophys Res Lett 41:1389–1397. https://doi.org/10.1002/2013GL058632

362. Sattar A, Goswami A, Kulkarni A V., Das P (2019) Glacier-surface velocity derived ice volume and retreat assessment in the dhauliganga basin, central himalaya – A remote sensing and modeling based approach. Front Earth Sci 7:1–15. https://doi.org/10.3389/feart.2019.00105

363. Savoskul OS, Smakhtin V (2013) Glacier systems and seasonal snow cover in six major Asian river basins: Water storage properties under changing climate

364. Scanlon BR, Cook PG (2002) Theme issue on groundwater recharge. Hydrogeol J 10:3–4. https://doi.org/10.1007/s10040-001-0175-3

365. Scanlon BR, Healy RW, Cook PG (2002) Choosing appropriate techniques for quantifying groundwater recharge. Hydrogeol J 10:18–39. https://doi.org/10.1007/s10040-0010176-2

366. Scanlon BR, Keese KE, Flint AL, et al (2006) Global synthesis of groundwater recharge in semiarid andaridregions. Hydrol Process 20:3335–3370. https://doi.org/10.1002/hyp

367. Scanlon BR, Longuevergne L, Long D (2012) Ground referencing GRACE satellite estimates of groundwater storage changes in the California Central Valley, USA. Water Resour Res 48:1–9. https://doi.org/10.1029/2011WR011312

368. Schaefer M, Fonseca-Gallardo D, Fariás-Barahona D, Casassa G (2020) Surface energy fluxes on Chilean glaciers: Measurements and models. Cryosphere 14:2545–2565. https://doi.org/10.5194/tc-14-2545-2020

369. Schmidt S, Nüsser M (2017) Changes of High Altitude Glaciers in the Trans-Himalaya of Ladakh over the Past Five Decades (1969–2016). Geosciences 7:27. https://doi.org/10.3390/geosciences7020027

370. Sen PK (1968) Estimates of the Regression Coefficient Based on Kendall's Tau. J Am Stat Assoc 63:1379–1389

371. Senthilkumar M, Gnanasundar D, Arumugam R (2019) Identifying groundwater recharge zones using remote sensing & GIS techniques in Amaravathi aquifer system, Tamil Nadu, South India. Sustain Environ Res 1:1–9. https://doi.org/10.1186/s42834-019-0014-7

372. Seyednasrollah B, Kumar M (2014) Net radiation in a snow-covered discontinuous forest gap for a range of gap sizes and topographic configurations. J Geophys Res 119:10,323-10,342. https://doi.org/10.1002/2014JD021809

373. Shafiq M ul, Ahmed P, Islam Z ul, et al (2018) Snow cover area change and its relations with climatic variability in Kashmir Himalayas, India. Geocarto Int 6049:1–15. https://doi.org/10.1080/10106049.2018.1469675

374. Shafiq MU, Bhat MS, Rasool M (2016) Variability of Precipitation regime in Ladakh region of India from 1901-2000. J Climatol Weather Forecast 4:8–11. https://doi.org/10.4172/2332-2594.1000165

375. Shah T (2008) India's master plan for groundwater recharge: An assessment and some suggestions for revision. Econ Polit Wkly 43:41–49

376. Shamsudduha M, Taylor RG, Longuevergne L (2012) Monitoring groundwater storage changes in the highly seasonal humid tropics: Validation of GRACE measurements in the Bengal Basin. Water Resour Res 48:1–12. https://doi.org/10.1029/2011WR010993

377. Shang H, Letu H, Nakajima TY, et al (2018) Diurnal cycle and seasonal variation of cloud cover over the Tibetan Plateau as determined from Himawari-8 new-generation geostationary satellite data. Sci Rep 8:1105

378. Sharma P, Patel LK, Ravindra R, et al (2016) Role of debris cover to control specific ablation of adjoining batal and sutri dhaka glaciers in chandra basin (Himachal Pradesh) during peak ablation season. J Earth Syst Sci 125:459–473. https://doi.org/10.1007/s12040-016-0681-2

379. Sharma SS, Ganju A (2000) Complexities of avalanche forecasting in Western Himalaya - an overview. Cold Reg Sci Technol 31:95–102. https://doi.org/10.1016/S0165-232X(99)00034-8

380. Sharma V, Mishra VD, Joshi PK (2013) Erratum to: Snow cover variation and streamflow simulation in a snow-fed river basin of the Northwest Himalaya (J. Mt. Sci., (2012), 9, (853-868), 10.1007/s11629-012-2419-1). J Mt Sci 10:494. https://doi.org/10.1007/s11629-012-2800-0

381. Sheffer NA, Dafny E, Gvirtzman H, et al (2010) Hydrometeorological daily recharge assessment model (DREAM) for the Western Mountain Aquifer, Israel: Model application and effects of temporal patterns. Water Resour Res 46:1–16. https://doi.org/10.1029/2008WR007607

382. Shekhar MS, Chand H, Kumar S, et al (2010) Climate-change studies in the western Himalaya. Ann Glaciol 51:105–112. https://doi.org/10.3189/172756410791386508

383. Shen M, Cong N, Cao R (2015) Temperature sensitivity as an explanation of the latitudinal pattern of green-up date trend in Northern Hemisphere vegetation during 1982-2008. Int J Climatol 35:3707–3712. https://doi.org/10.1002/joc.4227

384. Sherpa SF, Wagnon P, Brun F, et al (2017) Contrasted surface mass balances of debris-free glaciers observed between the southern and the inner parts of the Everest region (2007-15). J Glaciol 63:637–651. https://doi.org/10.1017/jog.2017.30

385. Shewale MP, Kumar S (2005) Climatological Features of Drought Incidences in India. Meteorol Monogr Natonal Clim Centre, Indian Meteorol Dep

386. Shresth Tayal (2017) Snow cover variability in Western Himalayas and its implications on socio-economic status and livelihood of local communities. In: Br. Antarct. Surv. https://talks.cam.ac.uk/talk/index/72562

387. Shrestha AB, Agrawal NK, Alfthan B, et al (2015) The Himalayan Climate and Water Atlas

388. Shrestha AB, Wake CP, Mayewski PA, Dibb JE (2000) Precipitation fluctuations in the Himalaya and its vicinity: An analysis based on temperature records from Nepal. Int J Clim 20:317–327. https://doi.org/doi:10.1175/1520-0442(1999)012<2775:MTTITH>2.0.CO;2

389. Shrivastava D, Sangewar C V., Kaul MK, Jamwal KS (1999) Mass balance of Rulung Glacier-a Trans-Himalayan glacier, Indus basin, Ladak. In: Snow, Ice and Glacier. pp 41–46

390. Shukla S, Wood AW (2008) Use of a standardized runoff index for characterizing hydrologic drought. Geophys Res Lett 35:1–7. https://doi.org/10.1029/2007GL032487

391. Shuttlewor WJ (1992) Evaporation

392. Siebert S, Burke J, Faures JM, et al (2010) Groundwater use for irrigation - A global inventory. Hydrol Earth Syst Sci 14:1863–1880. https://doi.org/10.5194/hess-14-1863-2010

393. Sikka DR (2003) Evaluation of monitoring and forecasting of summer monsoon over India and a review of monsoon drought of 2002. Proc Indian Natn Sci Acad 69:479–504

394. Simic A, Fernandes R, Brown R, et al (2004) Validation of VEGETATION, MODIS, and GOES+ SSM/I snow-cover products over Canada based on surface snow depth observations. Hydrol Process 18:1089–1104

395. Singh DK, Gusain HS, Mishra V, Gupta N (2018a) Snow cover variability in North-West Himalaya during last decade. Arab J Geosci 11:. https://doi.org/10.1007/s12517-018-3926-3

396. Singh MK, Thayyen RJ, Jain SK (2019) Snow cover change assessment in the Upper Bhagirathi basin using an enhanced cloud removal algorithm. Geocarto Int 0:1–24. https://doi.org/10.1080/10106049.2019.1704069

397. Singh P, Arora M, Goel NK (2006) Effect of climate change on runoff of a glacierized Himalayan basin. Hydrol Process 20:1979–1992. https://doi.org/10.1002/hyp.5991

398. Singh P, Bengtsson L (2004) Hydrological sensitivity of a large Himalayan basin to climate change. Hydrol Process 18:2363–2385. https://doi.org/10.1002/hyp.1468

399. Singh P, Haritashya UK, Kumar N (2007) Meteorological study for Gangotri Glacier and its comparison with other high altitude meteorological stations in central Himalayan region. Nord Hydrol 38:59. https://doi.org/10.2166/nh.2007.028

400. Singh P, Jain SK, Naresh K (1997) Estimation of Snow and Glacier-Melt Contribution to the Chenab River , Western Himalaya. Mt Res Dev 17:49–56

401. Singh RP, Roy S, Kogan F (2003) Vegetation and temperature condition indices from NOAA AVHRR data for drought monitoring over India. Int J Remote Sens 24:4393–4402. https://doi.org/10.1080/0143116031000084323

402. Singh S, Kumar R, Dimri AP (2018b) Mass balance status of Indian Himalayan glaciers: A brief review. Front Environ Sci 6:. https://doi.org/10.3389/fenvs.2018.00030

403. Singh SK, Rathore BP, Bahuguna IM, Ajai (2014) Snow cover variability in the Himalayan-Tibetan region. Int J Climatol 34:446–452. https://doi.org/10.1002/joc.3697

404. Singh VB, Ramanathan A, Angchuk T, et al (2018c) Meteorological Characteristics of the Chhota Shigri Glacier, Lahaul-Spiti Valley, Himachal Pradesh, Northern India. J Clim Chang 4:41–49. https://doi.org/10.3233/JCC-1800012

405. Sinha D, Syed TH, Famiglietti JS, et al (2016) Characterizing Drought in India Using GRACE Observations of Terrestrial Water Storage Deficit. J Hydrometeorol 18:381–396. https://doi.org/10.1175/jhm-d-16-0047.1

406. Sinha D, Syed TH, Reager JT (2019) Utilizing combined deviations of precipitation and GRACE-based terrestrial water storage as a metric for drought characterization: A case study over major Indian river basins. J Hydrol 572:294–307. https://doi.org/10.1016/j.jhydrol.2019.02.053

407. Snehmani, Dharpure JK, Kochhar I, et al (2016) Analysis of snow cover and climatic variability in Bhaga basin located in western Himalaya. Geocarto Int 31:1094–1107. https://doi.org/10.1080/10106049.2015.1120350

408. Soheb M, Ramanathan A, Angchuk T, et al (2020) Mass-balance observation, reconstruction and sensitivity of Stok glacier, Ladakh region, India, between 1978 and 2019. J Glaciol. https://doi.org/10.1017/jog.2020.34

409. Soheb M, Ramanathan A, Mandal A, et al (2018) Wintertime surface energy balance of a high-altitude seasonal snow surface in Chhota Shigri glacier basin, Western Himalaya. Geol Soc Spec Publ 462:155–168. https://doi.org/10.1144/SP462.10

410. Soheb M, Ramanathan A, Mandal A, et al (2017) Wintertime surface energy balance of a high-altitude seasonal snow surface in Chhota Shigri glacier basin, Western Himalaya. Geol Soc London, Spec Publ SP462.10. https://doi.org/10.1144/SP462.10

411. Sood V, Singh S, Taloor AK, et al (2020) Monitoring and mapping of snow cover variability using topographically derived NDSI model over north Indian Himalayas during the period 2008–19. Appl Comput Geosci 8:100040. https://doi.org/10.1016/j.acags.2020.100040

412. Sophocleous MA (1991) Combining the soilwater balance and water-level fluctuation methods to estimate natural groundwater recharge: Practical aspects. J Hydrol 124:229–241. https://doi.org/10.1016/0022-1694(91)90016-B

413. Stephens DB (1994) A Perspective on Diffuse Natural Recharge Mechanisms in Areas of Low Precipitation. Soil Sci Soc Am J 58:40–48. https://doi.org/10.2136/sssaj1994.03615995005800010006x

414. Stillinger T, Roberts DA, Collar NM, Dozier J (2019) Cloud Masking for Landsat 8 and MODIS Terra Over Snow-Covered Terrain: Error Analysis and Spectral Similarity Between Snow and Cloud. Water Resour Res 55:6169–6184. https://doi.org/10.1029/2019WR024932

415. Strassberg G, Scanlon BR, Rodell M (2007) Comparison of seasonal terrestrial water storage variations from GRACE with groundwater-level measurements from the High Plains Aquifer (USA). Geophys Res Lett 34:1–5. https://doi.org/10.1029/2007GL030139

416. Stumm D, Joshi SP, Gurung TR, Silwal G (2020) Mass balances of Yala and Rikha Samba Glacier, Nepal from 2000 to 2017. Earth Syst Sci Data Discuss 1–37. https://doi.org/10.5194/essd-2020-272

417. Sumioka SS, Bauer HH (2003) Estimating Ground-Water Recharge from Precipitation on Whidbey and Camano Islands, Island County, Washington, Water Years 1998 and 1999. US Dep. Inter. US Geol. Surv. 3(4101):1–49

418. Sun AY, Scanlon BR, Zhang Z, et al (2019) Combining Physically Based Modeling and Deep Learning for Fusing GRACE Satellite Data: Can We Learn From Mismatch? Water Resour Res 1179–1195. https://doi.org/10.1029/2018WR023333

419. Sun W, Qin X, Du W, et al (2014) Ablation modeling and surface energy budget in the ablation zone of Laohugou glacier No. 12, western Qilian mountains, China. Ann Glaciol 55:111–120. https://doi.org/10.3189/2014AoG66A902

420. Sun Z, Zhu X, Pan Y, et al (2018) Drought evaluation using the GRACE terrestrial water storage deficit over the Yangtze River Basin, China. Sci Total Environ 634:727–738. https://doi.org/10.1016/j.scitotenv.2018.03.292

421. Swenson S, Wahr J (2006) Estimating large-scale precipitation minus evapotranspiration from GRACE satellite gravity measurements. J Hydrometeorol 7:252–270. https://doi.org/10.1175/JHM478.1

422. Swenson S, Yeh PJF, Wahr J, Famiglietti J (2006) A comparison of terrestrial water storage variations from GRACE with in situ measurements from Illinois. Geophys Res Lett 33:1–5. https://doi.org/10.1029/2006GL026962

423. Syed TH, Famiglietti JS, Rodell M, et al (2008) Analysis of terrestrial water storage changes from GRACE and GLDAS. Water Resour Res 44:1–15. https://doi.org/10.1029/2006WR005779

424. Tahir AA, Adamowski JF, Chevallier P, et al (2016) Comparative assessment of spatiotemporal snow cover changes and hydrological behavior of the Gilgit, Astore and Hunza River basins (Hindukush–Karakoram–Himalaya region, Pakistan). Meteorol Atmos Phys 128:793–811. https://doi.org/10.1007/s00703-016-0440-6

425. Tahir AA, Chevallier P, Arnaud Y, et al (2015) Snow cover trend and hydrological characteristics of the Astore River basin (Western Himalayas) and its comparison to the Hunza basin (Karakoram region). Sci Total Environ 505:748–761. https://doi.org/10.1016/j.scitotenv.2014.10.065

426. Tahir AA, Chevallier P, Arnaud Y, Ahmad B (2011) Snow cover dynamics and hydrological regime of the Hunza River basin, Karakoram Range, Northern Pakistan. Hydrol Earth Syst Sci 15:2275–2290. https://doi.org/10.5194/hess-15-2275-2011

427. Tang BH, Shrestha B, Li ZL, et al (2012) Determination of snow cover from MODIS data for the Tibetan Plateau region. Int J Appl Earth Obs Geoinf 21:356–365. https://doi.org/10.1016/j.jag.2012.07.014

428. Tapley BD, Bettadpur S, Ries J, et al (2004a) Grace measurements of Mass variability in the Earth system: supporting online material. Science (80-) 503–505:503–506

429. Tapley BD, Bettadpur S, Watkins M, Reigber C (2004b) The gravity recovery and climate experiment: Mission overview and early results. Geophys Res Lett 31:1–4. https://doi.org/10.1029/2004GL019920

430. Tawde SA, Kulkarni A V., Bala G (2017) An estimate of glacier mass balance for the Chandra basin, western Himalaya, for the period 1984-2012. Ann Glaciol 58:99–109. https://doi.org/10.1017/aog.2017.18

431. Thakur K, Asher M (2015) Changing the Colours of Chenab Narratives on hydropower ' development ' from Lahaul Valley

432. Thapa S, Li B, Fu D, et al (2020a) Trend analysis of climatic variables and their relation to snow cover and water availability in the Central Himalayas: a case study of Langtang Basin, Nepal. Theor Appl Climatol 140:891–903. https://doi.org/10.1007/s00704-020-03096-5

433. Thapa S, Zhao Z, Li B, et al (2020b) Snowmelt-driven streamflow prediction using machine learning techniques (LSTM, NARX, GPR, and SVR). Water (Switzerland) 12:. https://doi.org/10.3390/w12061734

434. Thayyen RJ, Dimri AP (2018) Slope Environmental Lapse Rate (SELR) of temperature in the monsoon regime of the western Himalaya. Front Environ Sci 6:1–20. https://doi.org/10.3389/fenvs.2018.00042

435. Thayyen RJ, Dimri AP, Kumar P, Agnihotri G (2013) Study of cloudburst and flash floods around Leh, India, during August 4-6, 2010. Nat Hazards 65:2175–2204. https://doi.org/10.1007/s11069-012-0464-2

436. Thayyen RJ, Gergan JT (2010) Role of glaciers in watershed hydrology: A preliminary study of a "himalayan catchment." Cryosphere 4:115–128. https://doi.org/10.5194/tc-4-115-2010

437. Thayyen RJ, Singh MK, Dimri AP (2020) Visual Evidence of Constrained Area of a Cloudburst, 12 June 2018, Tirisha Village, Nubra Valley, Ladakh, India. J Clim Chang 6:47–57. https://doi.org/10.3233/jcc200011

438. Thomas AC, Reager JT, Famiglietti JS, Rodell M (2014) A GRACE-based water storage deficit approach for hydrological drought characterization Alys. Geophys Prospect 41:3307–3314. https://doi.org/10.1002/2014GL061184.Received

439. Thomas BF, Famiglietti JS, Landerer FW, et al (2017) GRACE Groundwater Drought Index: Evaluation of California Central Valley groundwater drought. Remote Sens Environ 198:384–392. https://doi.org/10.1016/j.rse.2017.06.026

440. Thornthwaite CW (1948) An Approach toward a Rational Classification of Climate. Geogr Rev 38:55–94. https://doi.org/10.2307/210739

441. Thornthwaite CW, Mather JR (1955) Water Balance (Publications in Climatology). Drexel Institute of Technology Laboratory of Climatology, Centerdon, New Jersey

442. Tiwari VM, Wahr J, Swenson S (2009) Dwindling groundwater resources in northern India, from satellite gravity observations. Geophys Res Lett 36:1–5. https://doi.org/10.1029/2009GL039401

443. Torres CA (2015) Drought in Tharparkar: From Seasonal to Forced Migration. 65–76

444. Tran H, Nguyen P, Ombadi M, et al (2019) A cloud-free modis snow cover dataset for the contiguous United States from 2000 to 2017. Sci Data 6:1–13. https://doi.org/10.1038/sdata.2018.300

445. Tsakiris G, Pangalou D, Vangelis H (2007) Regional drought assessment based on the Reconnaissance Drought Index (RDI). Water Resour Manag 21:821–833. https://doi.org/10.1007/s11269-006-9105-4

446. Tsakiris G, Vangelis H (2005) Establishing a drought index incorporating evapotranspiration. Eur Water 9:3–11. https://doi.org/10.1111/j.1600-0609.2009.01288.x

447. Turkeltaub T, Kurtzman D, Bel G, Dahan O (2015) Examination of groundwater recharge with a calibrated/validated flow model of the deep vadose zone. J Hydrol 522:618–627. https://doi.org/10.1016/j.jhydrol.2015.01.026

448. Valero CV, Wever N, Christen M, Bartelt P (2018) Modeling the influence of snow cover temperature and water content on wet-snow avalanche runout. Nat Hazards Earth Syst Sci 18:869–887. https://doi.org/10.5194/nhess-18-869-2018

449. van den Broeke M, van As D, Reijmer C, van de Wal R (2004) Assessing and improving the quality of unattended radiation observations in Antarctica. J Atmos Ocean Technol 21:1417–1431. https://doi.org/10.1175/1520-0426(2004)021<1417:AAITQO>2.0.CO;2

450. van der Vat M, Boderie P, Bons K, et al (2019) Participatory Modelling of Surface and Groundwater to Support Strategic Planning in the Ganga Basin in India. Water 11:2443. https://doi.org/10.3390/w11122443

451. Vicente-Serrano SM, Begueria S, Lepez-Moreno JI (2009) A multiscalar drought index sensitive to global warming: The standardized precipitation evapotranspiration index. J Clim 23:1696–1718. https://doi.org/10.1175/2009JCLI2909.1

452. Vicente-Serrano SM, Beguería S, López-Moreno JI (2010) A multiscalar drought index sensitive to global warming: the standardized precipitation evapotranspiration index. J Clim 23:1696–1718

453. Vijay S, Braun M (2016) Elevation change rates of glaciers in the Lahaul-Spiti (Western Himalaya, India) during 2000-2012 and 2012-2013. Remote Sens 8:1–16. https://doi.org/10.3390/rs8121038

454. Vuille M, Carey M, Huggel C, et al (2018) Rapid decline of snow and ice in the tropical Andes – Impacts, uncertainties and challenges ahead. Earth-Science Rev 176:195–213. https://doi.org/10.1016/j.earscirev.2017.09.019

455. Wagnon P, Brun F, Khadka A, et al (2021) Reanalysing the 2007-19 glaciological mass-balance series of Mera Glacier, Nepal, Central Himalaya, using geodetic mass balance. J Glaciol 67:117–125. https://doi.org/10.1017/jog.2020.88

456. Wagnon P, Vincent C, Arnaud Y, et al (2013) Seasonal and annual mass balances of Mera and Pokalde glaciers (Nepal Himalaya) since 2007. Cryosphere 7:1769–1786. https://doi.org/10.5194/tc-7-1769-2013

457. Wahr J, Swenson S, Velicogna I (2006) Accuracy of GRACE mass estimates. Geophys Res Lett 33:1–5. https://doi.org/10.1029/2005GL025305

458. Wan Z (2014) New refinements and validation of the collection-6 MODIS land-surface temperature/emissivity product. Remote Sens Environ 140:36–45. https://doi.org/10.1016/j.rse.2013.08.027

459. Wan Z, Wang Y, Hou S, et al (2021) A doubling of glacier mass loss in the Karlik Range, easternmost Tien Shan, between the periods 1972-2000 and 2000-2015. J Glaciol 67:1–12. https://doi.org/10.1017/jog.2020.76

460. Wang X, Xie H, Liang T (2008) Evaluation of MODIS snow cover and cloud mask and its application in Northern Xinjiang, China. Remote Sens Environ 112:1497–1513

461. Wang X, Xie H, Liang T, Huang X (2009) Comparison and validation of MODIS standard and new combination of Terra and Aqua snow cover products in northern Xinjiang, China. Hydrol Process 23:419

462. Wang X, Zheng H, Chen Y, et al (2014) Mapping snow cover variations using a MODIS daily cloud-free snow cover product in northeast China. J Appl Remote Sens 8:084681. https://doi.org/10.1117/1.JRS.8.084681

463. Wang Y, Yang J, Chen Y, et al (2018) Detecting the Causal Effect of Soil Moisture on Precipitation Using Convergent Cross Mapping. Sci Rep 8:1–8. https://doi.org/10.1038/s41598-018-30669-2

464. Wani JM, Thayyen RJ, Gruber S, et al (2020) Single-year thermal regime and inferred permafrost occurrence in the upper Ganglass catchment of the cold-arid Himalaya, Ladakh, India. Sci Total Environ 703:134631. https://doi.org/10.1016/j.scitotenv.2019.134631

465. Wani JM, Thayyen RJ, Ojha CSP, Gruber S (2021) The surface energy balance in a cold and arid permafrost environment, Ladakh, Himalayas, India. Cryosphere 15:2273–2293. https://doi.org/10.5194/tc-15-2273-2021

466. Waqas A, Athar H (2019) Spatiotemporal variability in daily observed precipitation and its relationship with snow cover of Hindukush, Karakoram and Himalaya region in northern Pakistan. Atmos Res 228:196–205. https://doi.org/10.1016/j.atmosres.2019.06.002

467. Wester P, Mishra A, Mukherji A, et al (2019) The Hindu Kush Himalaya Assessment. Springer Nature Switzerland

468. Wiese DN, Landerer FW, Watkins MM (2016) Quantifying and reducing leakage errors in the JPL RL05M GRACE mascon solution. Water Resour Res 52:7490–7502. https://doi.org/10.1002/2016WR019344

469. Wijngaard RR, Lutz AF, Nepal S, et al (2017) Future changes in hydro-climatic extremes in the Upper Indus, Ganges, and Brahmaputra River basins. J Auton Nerv Syst 34:1–26. https://doi.org/10.1016/0165-1838(91)90005-N

470. Wilhite DA (2000) Drought as a Natural Hazard. Drought A Glob Assess 1:3–18

471. Wiltshire AJ (2014) Climate change implications for the glaciers of the Hindu Kush, Karakoram and Himalayan region. Cryosphere 8:941–958. https://doi.org/10.5194/tc-8-941-2014

472. Wood LR, Neumann K, Nicholson KN, et al (2020) Melting Himalayan Glaciers Threaten Domestic Water Resources in the Mount Everest Region, Nepal. Front Earth Sci 8:1–8. https://doi.org/10.3389/feart.2020.00128

473. World Bank (2011) Water Systems Modeling for Ganga Basin

474. Wu Q, Si B, He H, Wu P (2019) Determining Regional-Scale Groundwater Recharge with GRACE and GLDAS. Remote Sens 11:154. https://doi.org/10.3390/rs11020154

475. Xiao C, Liu S, Zhao L, et al (2007) Observed changes of cryosphere in China over the second half of the 20th century: An overview. Ann Glaciol 46:382–390. https://doi.org/10.3189/172756407782871396

476. Xiao R, He X, Zhang Y, et al (2015) Monitoring groundwater variations from satellite gravimetry and hydrological models: A comparison with in-situ measurements in the mid-atlantic region of the United States. Remote Sens 7:686–703. https://doi.org/10.3390/rs70100686

477. Xu W, Ma H, Wu D, Yuan W (2017) Assessment of the daily cloud-free MODIS Snow-cover product for monitoring the snow-cover phenology over the Qinghai-Tibetan Plateau. Remote Sens 9:585. https://doi.org/10.3390/rs9060585

478. Xue Y, Houser PR, Maggioni V, et al (2019) Assimilation of Satellite-Based Snow Cover and Freeze/Thaw Observations Over High Mountain Asia. Front Earth Sci 7:1–21. https://doi.org/10.3389/feart.2019.00115

479. Yang P, Xia J, Zhan C, et al (2017) Monitoring the spatio-temporal changes of terrestrial water storage using GRACE data in the Tarim River basin between 2002 and 2015. Sci Total Environ 595:218–228. https://doi.org/10.1016/j.scitotenv.2017.03.268

480. Yao X (2021) Daily Streamflow Prediction Using Deep Learning : A Case Study on Russian River , CA. In: Deep learning. Springer

481. Yeh PJF, Swenson SC, Famiglietti JS, Rodell M (2006) Remote sensing of groundwater storage changes in Illinois using the Gravity Recovery and Climate Experiment (GRACE). Water Resour Res 42:1–7. https://doi.org/10.1029/2006WR005374

482. Yeo SR, Kim WM, Kim KY (2017) Eurasian snow cover variability in relation to warming trend and Arctic Oscillation. Clim Dyn 48:499–511. https://doi.org/10.1007/s00382-016-3089-4

483. Yevjevich V (1969) An objective approach to definitions and investigations of continental hydrologic droughts. Hydrol Pap no 23. https://doi.org/10.1016/0022-1694(69)90110-3

484. Yirdaw SZ, Snelgrove KR, Agboma CO (2008) GRACE satellite observations of terrestrial moisture changes for drought characterization in the Canadian Prairie. J Hydrol 356:84–92. https://doi.org/10.1016/j.jhydrol.2008.04.004

485. Young WJ, Anwar A, Bhatti T, et al (2019) Pakistan: Getting More from Water. World Bank 163

486. Zhang F, Thapa S, Immerzeel W, et al (2019a) Water availability on the Third Pole: A review. Water Secur 7:. https://doi.org/10.1016/j.wasec.2019.100033

487. Zhang G, Kang S, Fujita K, et al (2013) Energy and mass balance of Zhadang glacier surface, central Tibetan Plateau. J Glaciol 59:137–148. https://doi.org/10.3189/2013JoG12J152

488. Zhang H, Zhang F, Zhang G, et al (2019b) Ground-based evaluation of MODIS snow cover product V6 across China: Implications for the selection of NDSI threshold. Sci Total Environ 651:2712–2726. https://doi.org/10.1016/j.scitotenv.2018.10.128

489. Zhang S, Gao H, Naz BS (2014) Monitoring reservoir storage in South Asia from multisatellite remote sensing. Water Resour Res 50:8927–8943. https://doi.org/10.1002/2014WR015829

490. Zhang Y (2015) Changing in glacier and snow cover of Karakorum and Western Himalaya and impacts on hydrologic regimes. EGU Gen Assem Conf Abstr 17:1686

491. Zhang Y, Yan S, Lu Y (2010) Snow cover monitoring using MODIS data in liaoning province, Northeastern China. Remote Sens 2:777–793. https://doi.org/10.3390/rs2030777

492. Zhang Z, Dong Y, Yuan Y (2020) Temperature Forecasting via Convolutional Recurrent Neural Networks Based on Time-Series Data. Complexity 2020:. https://doi.org/10.1155/2020/3536572

493. Zhao M, Geruo A, Velicogna I, Kimball JS (2017a) Satellite observations of regional drought severity in the continental United States using GRACE-based terrestrial water storage changes. J Clim 30:6297–6308. https://doi.org/10.1175/JCLI-D-16-0458.1

494. Zhao M, Geruo A, Velicogna I, Kimball JS (2017b) A Global Gridded Dataset of GRACE Drought Severity Index for 2002–14: Comparison with PDSI and SPEI and a Case Study of the Australia Millennium Drought. J Hydrometeorol 18:2117–2129. https://doi.org/10.1175/JHM-D-16-0182.1

495. Zhu T, Ringler C (2012) Climate change impacts on water availability and use in the Limpopo River Basin. Water (Switzerland) 4:63–84. https://doi.org/10.3390/w4010063

496. Zomlot Z, Verbeiren B, Huysmans M, Batelaan O (2015) Spatial distribution of groundwater recharge and base flow: Assessment of controlling factors. J Hydrol Reg Stud 4:349–368. https://doi.org/10.1016/j.ejrh.2015.07.005